UNIVERSITY OF SALERNO
DEPARTMENT OF CIVIL ENGINEERING

PhD Course in
Risk and Sustainability in Civil Engineering, Architecture, Environmental and Territory Protection
Cycle XXXIII - (2019-2020)

CFD ANALYSIS OF COASTAL FLOOD RISK: OVERTOPPING RELATED PHENOMENA

ANGELA DI LEO

Tutor:
PROF. **FABIO DENTALE**

PhD Coordinator:
PROF. **FERNANDO FRATERNALI**

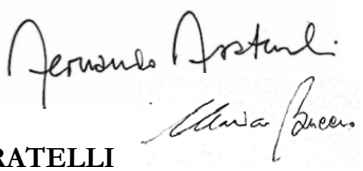

Co.Tutor:
PROF. **MARIANO BUCCINO**
PROF. **EUGENIO PUGLIESE CARRATELLI**

CFD ANALYSIS OF COASTAL FLOOD RISK: OVERTOPPING RELATED PHENOMENA

Finito di stampare il 14/06/2021.

A mia madre e mio padre

GENERAL INDEX

LIST OF SYMBOLS

A	[m^2]	source region area
a	[-]	Coefficient
b	[-]	Coefficient
c	[s^{-1}]	damping coefficient
Cv	[%]	coefficient of variation
$Cr_{1/3}$	[m]	the highest third of the wave crest
c	[m/s]	wave celerity
C_{D10}	[-]	wind shear coefficient (or drag coefficient)
c_μ	[-]	empirical constant
d	[m]	water depth
E_{LR}	[-]	mean of Log-Residuals
E_{mean}	[m]	mean height of wave envelope
E_{rms}	[m]	quadratic mean height of wave envelope
F	[-]	fractional function
f_{wind}	[-]	wind factor expressed as ratio q_{wind}/q
f_{NY}	[Hz]	Nyquist frequency
f_{max}	[Hz]	Spectral peck frequency
f_μ		damping factor
g	[m/s^2]	Gravitational acceleration
h	[m]	water depth in front of toe of structure

H_{m0}	[m]	Significant (spectral) wave height
$H_{m0,deep}$	[m]	H_{m0} determined at deep water
Hm	[m]	mean wave height
Hs	[m]	significant wave height
$H_{1/3}$	[m]	significant wave height defined as highest one-third of wave heights
$H_{1/10}$	[m]	One-Tenth Highest wave
H_n	[m]	significant wave height nearshore
k_{bn}	[-]	multiplier for mean discharge giving effect of recurve wall
L	[m]	wavelength
$L_{m-1,0}$	[m]	spectral wavelength in deep water = $gT^2_{m-1,0}/2\pi$
LR	[-]	Log- Residuals
L_p	[m]	local wavelength
M_D	[%]	maximum distance between two overtopping curves
m	[-]	Foreshore slope
M_X	[-]	maximum semi-band amplitude
Max_{LR}	[-]	maximum value of Log-Residuals
N_{ow}	[-]	number of overtopping waves
N_w	[-]	number of incident waves
p	[N/m^2]	pressure
P_V	[-]	probability of the overtopping volume V* being larger or equal to V

Pow	[-]	probability of overtopping per wave = Now/ Nw
q	[mc/s/m]	Wave overtopping discharge per time unit and per unit length of breakwater
q_{wind}	[m^3/s/m]	overtopping discharge including the effect of the wind
R_c	[m]	Crest freeboard of structure relative to sea water level (SWL)
Rc_{eff}	[m]	Crest freeboard of structure relative to surge on SWL
$R_T=k^2/\nu\varepsilon$	[-]	turbulence Reynolds number
$s_{m-1,0}$	[-]	wave steepness with Lo, based on $T_{m-1,0}$ = $H_{m0}/L_{m-1,0} = 2\pi\ H_{mo}/(gT^2_{m-1,0})$
SD_{LR}	[-]	Standard deviation of Log-Residuals
s_p (t)	[m^3/s]	mass source flow rate
t	[s]	time
T_m	[s]	average wave period
T_p	[s]	Peak period
T_R	[years]	Storm Return Period
ui	[m/s]	cartesian component of the velocity
$\vec{u}_{str}$	[m/s]	background stream velocity
$\overline{u_i}$	[m/s]	averaged velocity
u_i'	[m/s]	turbulence velocity
U_{10}	[m/s]	wind speed at 10 m above sea level
Ur	[-]	Ursell number

V	$[m^3/m]$	Volume of overtopping wave per unit crest width
$V_{f,}$	$[m^3/m]$	final overtopping volume
V_E	[%]	relative volume error between two consecutive grids
V_w	$[m^3]$	volume of water inside a cell
V_c	$[m^3]$	volume of the cell
V_{max}	$[m^3/m]$	Maximum individual overtopping wave volume per unit crest width
W		source region
Γ	[-]	Mathematical gamma function
τ	$[N/m^2]$	viscous stress tensor
μ	$[N*s/m^2]$	dynamic viscosity
ν	$[m^2/s]$	kinematic viscosity
ν_T	$[m^2/s]$	Eddy viscosity
ϱ	$[Kg/m^3]$	Fluid density
k	$[m^2/s^2]$	Turbulent kinetic energy
ε	$[m^2/s^3]$	Turbulent dissipation rate
$c\mu$, $c1$, σk, $\sigma\varepsilon$	[-]	Constant of turbulence model
m	[unit of x]	mean
σ^2	[unit of x]	Variance
σ (st.dev)	[unit of x]	Standard deviation
s	[unit of x]	Skewness

η	[m]	water surface elevation to the mean water level
$\Delta x, \Delta y, \Delta z$	[m]	Grid size in x (horizontal), y (transversal), and z (vertical) directions
ρ_a	[kg/m^3]	density of air
τ	[N/m^2]	wind shear stress
φ_i	[rad]	is the phase angle
ω	[Hz]	angular frequency

LIST OF ABBREVIATION

ANN Artificial Neural Network
CFD Computational Fluid Dynamics
CFL Courant-Friedrichs-Levy
CLASH Crest Level Assessment of Coastal Structures by Full-scale Monitoring, Neural Network Prediction and Hazard Analysis on Permissible Wave Overtopping
FAVOR Fractional Area/Volume Obstacle Representation
GMRES Generalized Minimum RESidual method
MWL Mean Water Level
NS Navier Stokes
RANS Reynolds-Averaged Navier Stokes
Re Reynolds Number
RMS Root Mean Square
RNG Renormalization-Group
STL STereo Lithography interface format
SWL Still water level
TKE Turbulent Kinetic Energy
VOF Volume-Of-Fluid

LIST OF FIGURES

LIST OF TABLES

SOMMARIO

La presente tesi di dottorato intende presentare i risultati della validazione di una procedura numerica innovativa per la simulazione dell'interazione tra il moto ondoso e strutture radenti a parete verticale. I fenomeni di tracimazione ondosa sono le cause più frequenti di rischio associate a queste tipologie di strutture. Infatti, in molti casi queste opere sono preposte alla protezione di strade, lungo mare e edifici prospicienti la costa.

Prima di entrare nel merito di tale procedura si è ritenuto necessario introdurre i fenomeni connaturati all'ambiente costiero, indotti dai cambiamenti climatici e che sono causa di inondazioni.

Le inondazioni rappresentano una minaccia per gli insediamenti urbani prospicienti la riva, in cui sono messe a rischio abitazioni, infrastrutture e attività economiche.

In questo spirito la presente tesi sarà articolata come segue:

In primo luogo, si presenta il rischio costiero connesso ai fenomeni di tracimazione su cui è incentrato il lavoro di ricerca.

Viene poi illustrato lo stato dell'arte relativo alla stima della portata di tracimazione e della modellazione numerica per ciò che attiene l'analisi di questo fenomeno nella letteratura scientifica.

Inoltre, particolare attenzione è stata rivolta alle varie fonti di incertezza di stima di cui diversi autori hanno discusso nei loro lavori.

La prima parte del lavoro è stata svolta guardando alle criticità delle analisi CFD e all'estrema variabilità del fenomeno analizzato. Ci si è soffermati sulle problematiche relative alla griglia di calcolo e alla convergenza del modello. I test sono stati definiti sulla base di una medesima campagna sperimentale sviluppata presso l'Università "Federico II" di Napoli e coordinata dal Prof. Ing. Mariano Buccino nell'ambito di un progetto

svolto in collaborazione con il Prof. Luis Cordova e il C.U.G.RI. (*Physical model tests for the design of the seawall "Malecón Tradicional", Habana, CUBA*)
La seconda parte del lavoro, con attenzione rivolta al fenomeno in oggetto, è stata incentrata sulla analisi di diversi metodi di stima della portata di overtopping (Eurotop Manual, Reti Neurali). Inoltre, la validazione dei risultati numerici è stata svolta con riferimento a medesimi test di laboratorio.
Sono state analizzate inoltre diverse soluzioni progettuali per la mitigazione della portata tracimante sotto l'azione di diverse forzanti meteomarine.
Infine, è stato analizzato numericamente l'effetto indotto dall'azione del vento sull' overtopping.
L'obiettivo di tali analisi è fornire strumenti validi nella pratica ingegneristica ma che consentono in maniera spedita di analizzare i fenomeni di interesse almeno nelle fasi iniziali della progettazione. In questa fase, infatti, è spesso richiesto lo studio di diverse forzanti meteomarine su diverse soluzioni progettuali.

ABSTRACT

This PhD thesis aims to present the results of the validation of an innovative numerical procedure for simulating the interaction between wave motion and vertical structures. Wave overflow phenomena are the most frequent causes of risk associated with these types of structures. In fact, in many cases these structures are designed to protect roads, social activity and buildings overlooking the coast.
The potential impact on coastal structure induced by climate change is exposed. The main problem is the risk associated to coastal flooding induced by wave overtopping processes.
The thesis will be structured as follows:
First, there is the coastal risk linked to the overtopping phenomena on which the research work is focused.
The state of the art relating to the estimation of the overflow rate and numerical modelling is then illustrated. Some references are also discussed; particular attention is addressed to the uncertainty of wave overtopping prediction.
The first part of the work was carried out by looking at critical issues of the numerical approach and at the extreme variability of the phenomenon analysed. The focus is on grid effects and the convergence of the model.
The tests were based on the same experimental campaign developed at the University of Naples "Federico II" and coordinated by Prof. Ing. Mariano Buccino as part of a project carried out in collaboration with Prof. Luis Cordova and C.U.G.RI. (Physical model tests for the design of the seawall "Malecón Tradicional", Habana city, CUBA).
The second part of the work was focused on the analysis of different predictive methods for wave overtopping. Also, the validation of numerical results has been carried out comparing with analogous laboratory results.

Different design solutions for wave overtopping mitigation have been also simulated.
Finally, through numerical simulations, the effect of wind action on overtopping discharge has been studied.
The goal of these analysis is to provide valid tools for engineering practice, thus allowing an expedite analysis of the phenomena of interest at early stages of design, in which the comparison of different wave forcing on different design solutions is often required.

ACKNOWLEDGMENT

I would like to express my gratitude to the people mentioned hereafter, in no order of importance.
Wholehearted thanks my PhD supervisor Prof. Fabio Dentale, first of all for inviting me to join the 'MEDUS' Lab and for providing me with the encouragement and the enthusiasm I needed for the research work.
I wish to gratefully acknowledge the help provided by my co-supervisor, Prof. Mariano Buccino, for the continuous support he gave me during my PhD study and related research, for his patience and motivation.
In addition, I am grateful to Prof. Eugenio Pugliese Carratelli for providing scientific assistance.

ABOUT THE AUTHOR

Angela Di Leo è nata a Bisaccia (Avellino) il 24/09/1989.
Si laurea in Ingegneria Civile presso l'Università degli Studi di Salerno il 29 febbraio 2016 con una tesi in Idraulica Marittima.
Nel dicembre 2016 risulta vincitrice del concorso per incarico di collaborazione per " Supporto all'attività di ricerca per la modellazione numerica delle interazioni tra onde e strutture marittime in collaborazione con il gruppo di Ingegneria Marittima del DICIV, sotto la responsabilità del Dott. Ing. Fabio Dentale".
Nel novembre 2017 è risultata vincitrice del concorso per il Dottorato di Ricerca in "Rischio e sostenibilità nei sistemi dell'ingegneria civile, edile e ambientale" – curriculum: "Interventi ed Infrastrutture per la Difesa Del Suolo, Sistemi e Infrastrutture per l'ambiente", dell'Università degli Studi di Salerno (XXXIII ciclo). Ha partecipato a numerose attività di studio e consulenza a supporto di enti territoriali. É stata correlatrice di numerose tesi di laurea. Ha svolto attività di supporto alla didattica per i corsi universitari di "Idraulica e fluidodinamica ambientale", "Idraulica Marittima" e "Coastal Management", presso l'Università degli Studi di Salerno. Ha pubblicato 8 articoli scientifici indicizzati in Scopus di 4 su riviste internazionali.

Angela Di Leo was born in Bisaccia (AV) on 24 September 1989.
She graduated in Civil Engineering at University of Salerno on February 29, 2016, with Thesis in Maritime Hydraulics.
In 2016, following a public competition, she earned a research contract for Support of research activity of numerical modelling of wave structures interactions in collaboration with DICIV Maritime Engineering Group, under the responsibility of Eng. Fabio Dentale".

In 2017, she was admitted, following a public selection to XXXIII cycle of PhD in Risk and Sustainability in Civil, Architectural, and Environmental Engineering (cycle XXXIII) of the University of Salerno. In this capacity, she participated in numerous applied research activities in support of local authorities. She supervised several graduate theses of students of Civil Engineering Department and worked as teaching assistant for various University courses at the Civil Engineering Syllabus: Hydraulics and environmental Fluid Dynamics, Maritime Hydraulics, "River and Coastal Management".
She has been co-authoring 8 scientific papers listed in Scopus database (4 of them published on scientific journal).

1 INTRODUCTION

1.1 RESEARCH OBJECTIVES

A reliable estimate of wave overtopping is necessary for the design and safety assessment of coastal structures. The most-widely used tools for predicting wave overtopping are empirical formula based on hydraulic model tests of simplified cross-sections or field measurements.
The range of structure configurations and wave conditions is however very wide while the empirical methods are often only based upon specific applicable conditions. In order to extend the applicability of the empirical methods, numerical modelling techniques have been developed to predict the wave overtopping discharge.
Numerical models can simulate the overtopping process at prototype scale, thus avoiding scale effects. Besides, they can deal with complicated configurations and a wide range of wave conditions.
The focus of the present work is to demonstrate the applicability of numerical CFD techniques for these types of problem by comparing it for various geometrical configurations with other numerical tools, experimental results, formulas from scientific literature and neural network method.
The case study analysed in this research activity concerns a vertical seawall named Malecòn Traditional (Cuba) with a significant effect of the foreshore on wave transformation and consequently on wave overtopping.
The analysis was supported by analogous experiments developed in the hydraulics laboratory at the University of Naples, conducted jointly by Prof. Mariano Buccino and Prof. Louis Cordova.

A wide and detailed grid sensitivity study has been developed in the initial part of the work with the aim of obtaining a preliminary estimate of the error linked to the grid by knowing the main parameters of the problem studied with CFD approach.
Furthermore, a wide numerical test campaign was carried out with the aim of showing the potential of CFD and the possibility of using regular waves at an early stage of the design, simplifying the computational effort.
The possibility of using regular waves for the study of the effects of wind on the overtopping phenomenon was also addressed.
Finally, the wind effects on wave overtopping were investigated with numerical CFD approach and compared with the reference literature. Furthermore, the numerical calculation has allowed to overcome the scale effects that limiting the laboratory experiments for the study of the wind effects.

1.2 CONTEXT OF THE RESEARCH

The thesis addresses the problems of coastal flooding focusing on estimate the quantities that may be the cause of damage by means of numerical modeling. Despite the large scientific literature available, there are still knowledge gaps to be covered to improve the understanding of wave overtopping under different conditions.

However, the process of wave overtopping on sea dikes with shallow and very shallow foreshore is not yet fully understood. Gentle foreshores in combination with (very) shallow water conditions lead to heavy wave breaking and a significant change of the wave spectra from offshore to the toe of the dike.

1.3 METHODOLOGY

The present work is primarily based on the numerical integration of the two-dimensional analysis of the RANS/VOF equations to investigate the problem of wave overtopping taking also into consideration the surf zone processes.
The work aims thus to demonstrate the capability of CFD techniques by comparing its performance with laboratory observations and literature formulae and other prediction tools available to quantify mean overtopping discharge and maximum individual wave overtopping.

1.4 OUTLINE OF THE THESIS

The thesis is organized as follows: section 2 focuses on the state of art of different problems addressed in this work as method to estimate wave overtopping and relative uncertainty on overtopping measurements by taking also into account the ways though which climate change might impact on the design of coastal structures in the future.
Section 3 describes the numerical methodology of RANS/VOF and the numerical techniques used in this work.
Section 4 presents a discussion on grid sensitivity study based on analysis of regular waves transformation in the surf zone and based on mean overtopping discharge, with particular attention to the effect of turbulence closure models and free surface boundary condition. The results are considered for both non-breaking and breaking waves.
In section 5, the CFD study with regular and irregular wave conditions on different seawall configuration is presented.
Section 6 is about the analysis of laboratory tests and the validation of numerical method with laboratory data, literature formulas, artificial neural network techniques. Also, the effect of spectral amplitude on the estimation of the mean overtopping discharge is discussed.

Section 7 presents the effect of wind stress on wave overtopping studied through numerical methods. Finally, the concluding remarks of this study are presented in section 8.

2 STATE OF ART

2.1 CLIMATE CHANGE

Climate change is responsible for sea level rise and increase in the storminess (i.e. more frequent and more severe storms), posing risks to coastal communities. Floods on the coastline are expected to increase, leading to potential human life losses and significant economic damage. In this climate change scenario, the existing coastal structures protecting the coastline against wave attack should at least provide the same degree of protection against future storms as they do today. Therefore, a good knowledge of the coastal processes is required to correctly assess the safety of the existing coastal structures in future scenarios and to improve design guidelines. The main coastal processes involved are, among others, wave overtopping over the crest of the structures, wave run-up on sea dikes and wave forces and pressures exerted by the waves on the structures.

2.1.1 Potential impacts on coastal structures

Besides coasts, ports are the infrastructure most likely to be affected by changes in wave climate.

The potential impacts of climate change can affect wave parameters on main coastal structures processes: stability, overtopping, washing, wave reflection and wave transmission. These processes can influence the structures situated on the coasts or in the ports and are mainly controlled from the extreme wave climate, except for the last two, for which the average also the climate of the waves is important.

2.2 WAVE OVERTOPPING PROCESSES AND COASTAL RISK

The term overtopping refers to the flow of water that crosses the crest of a breakwater which during storms may make the area behind the crest inaccessible and dangerous for people, vehicles, and boats (Schuttrumpf et al. 1998).
Wave overtopping is influenced by several parameters which can be identified and classified in the following way:

- Structural Parameters: Structure Type, crest height and width, berm width, height, and slope.
- Wave parameters and water depth: wave height, period and direction, spectral quantities, water depth in front of the structure.
- Wind parameters: Wind velocity and direction.
- Scale and model effects.
- Measured quantities: average overtopping rate, individual overtopping rate, number of overtopping waves.

The overtopping can only be tolerated if it does not cause harmful waves to the rear of the structure and will depend on the height of the wave (run-up), the characteristics of the wave at toe of the structure (influenced eventually by foreshore) and geometrical parameters of the seawall.
The need to avoid substantial overflow of a seawall translates into the search optimal geometry of the wall always considering both the necessity of reducing the risks and the need keep cost ant the impact on the environment within reasonable limits.
The risks associated with overtopping phenomena can be linked to many parameters, such as:

- mean overtopping flow rate q [mc/s/m] and relative limits tolerable.
- individual overtopping volume V_{max} [mc/m] and the relative limits.

Both these parameters have to be kept with limits stated by legal constraints or, otherwise, by widely accepted research results.

The first EurOtop Manual (2007) gave four tables with estimated tolerable overtopping for specific hazards, like limits for pedestrians, vehicles, property behind the defence and structural damage to the crest and rear slope.

The overtopping limits suggested in Table 2.2.1 to Table 2.2.3 therefore derive from a generally precautionary principle informed by previous guidance and by observations and measurements made by the CLASH partners and other researchers.

Table 2.2.1 Limits for overtopping for pedestrians (Eurotop Manual 2007).

Hazard type and reason	Mean discharge	Max volume[1]
	q (l/s/m)	V_{max} (l/m)
Trained staff, well shod and protected, expecting to get wet, overtopping flows at lower levels only, no falling jet, low danger of fall from walkway	1–10	500 at low level
Aware pedestrian, clear view of the sea, not easily upset or frightened, able to tolerate getting wet, wider walkway[2].	0.1	20–50 at high level or velocity

[1] *Note: These limits relate to overtopping velocities well below $v_c \approx 10$ m/s. Lower volumes may be required if the overtopping process is violent and/or overtopping velocities are higher.*

[2] *Note: Not all of these conditions are required, nor should failure of one condition on its own require the use of a more severe limit.*

Table 2.2.2 Limits for overtopping for vehicles (Eurotop Manual 2007).

Hazard type and reason	Mean discharge	Max volume
	q (l/s/m)	V_{max} (l/m)
Driving at low speed, overtopping by pulsating flows at low flow depths, no falling jets, vehicle not immersed	10–50[1]	100–1,000
Driving at moderate or high speed, impulsive overtopping giving falling or high velocity jets	0.01–0.05[2]	5–50[2] at high level or velocity

[1] *Note: These limits probably relate to overtopping defined at highway.*

[2] *Note: These limits relate to overtopping defined at the defence, but assumes the highway to be immediately behind the defence.*

Table 2.2.3 Limits for overtopping for property behind the defence (Eurotop Manual 2007).

Hazard type and reason	Mean discharge	Max volume
	q (l/s/m)	V_{max} (l/m)
Significant damage or sinking of larger yachts	50	5,000–50,000
Sinking small boats set 5–10 m from wall. Damage to larger yachts	10(1)	1,000–10,000
Building structure elements	1(2)	~
Damage to equipment set back 5–10 m	0.4(1)	~

(1) *Note: These limits relate to overtopping defined at the defence.*
(2) *Note: This limit relates to the effective overtopping defined at the building.*

One of the main insights developed since EurOtop (2007) is that tolerable overtopping depends very strongly on the peak volume, and hence on the wave height that causes the overtopping.
A mean tolerable overtopping discharge should be coupled to a wave height causing that discharge.

Table 2.2.4 Limits for wave overtopping for structural design of breakwaters, seawalls, dikes and dams (Eurotop Manual 2018).

Hazard type and reason	Mean discharge q (l/s per m)	Max volume Vmax (l per m)
Rubble mound breakwaters; Hm0 > 5 m; no damage	1	2,000-3,000
Rubble mound breakwaters; Hm0 > 5 m; rear side designed for wave overtopping	5-10	10,000-20,000
Grass covered crest and landward slope; maintained and closed grass cover; Hm0 = 1 – 3 m	5	2,000-3,000
Grass covered crest and landward slope; not maintained grass cover, open spots, moss, bare patches; Hm0 = 0.5 – 3 m	0.1	500
Grass covered crest and landward slope; Hm0 < 1 m	5-10	500
Grass covered crest and landward slope; Hm0 < 0.3 m	No limit	No limit

Wave overtopping over a breakwater or sea defence structure may hit anything behind the structure crest. The level of tolerable overtopping will be very site and structure specific.

Table 2.2.5 Limits for wave overtopping for property behind the defence (Eurotop Manual 2018).

Hazard type and reason	Mean discharge q (l/s per m)	Max volume Vmax (l per m)
Significant damage or sinking of larger yachts; Hm0 > 5 m	>10	>5,000-30,000
Significant damage or sinking of larger yachts; Hm0 = 3-5 m	>20	>5,000-30,000
Sinking small boats set 5-10 m from wall; Hm0 = 3-5 m Damage to larger yachts	>5	>3,000-5,000
Safe for larger yachts; Hm0 > 5 m	<5	<5,000
Safe for smaller boats set 5-10 m from wall; Hm0 = 3-5 m	<1	<2,000
Building structure elements; Hm0 = 1-3 m	≤1	<1,000
Damage to equipment set back 5-10m	≤1	<1,000

Breakwaters may be particularly dangerous in storms where people can be washed off. In some instances, an operating authority may be able to exclude access, but at others the public may still be able to access under

severe wave conditions, even when such overtopping could be dangerous for people.

Table 2.2.6 Limits for wave overtopping for people and vehicles (Eurotop Manual 2018).

Hazard type and reason	Mean discharge q (l/s per m)	Max volume Vmax (l per m)
People at structures with possible violent overtopping, mostly vertical structures	No access for any predicted overtopping	No access for any predicted overtopping
People at seawall / dike crest. Clear view of the sea.		
Hm0 = 3 m	0.3	600
Hm0 = 2 m	1	600
Hm0 = 1 m	10-20	600
Hm0 < 0.5 m	No limit	No limit
Cars on seawall / dike crest, or railway close behind crest		
Hm0 = 3 m	<5	2000
Hm0 = 2 m	10-20	2000
Hm0 = 1 m	<75	2000
Highways and roads, fast traffic	Close before debris in spray becomes dangerous	Close before debris in spray becomes dangerous

2.3 PREDICTION OF WAVE OVERTOPPING

As stated in the previous paragraph, wave overtopping is a key design parameter; the geometry and the crest level of coastal structures must thus be carefully chosen to limit the amount of water passing over the structure during wave attack.

Due to the irregular wave action, wave overtopping is a phenomenon which is clearly unevenly distributed in both time and space.

Consequently, it is not a simple problem to predict overtopping amounts and to assess or design the crest level of a coastal structure. However, different prediction formulae to predict the (average) overtopping discharge at coastal structures exist.

As discussed above, hazards induced by overtopping phenomenon can be related to many flow parameters, among the most important there are:
• mean overtopping discharge, q;
• individual maximum overtopping volume V_{max}.

There are three possible approaches for the prediction of wave overtopping. Physical modelling give accurate results (although scale effects could be an issue), but it is expensive and time consuming. Alternatively, there exist a range of empirical tools and formulae, based on data from numerous physical model and field experiments; the EurOtop Manual (Pullen et al., 2007) gives guidance on many such tools. However, some of the tools may be difficult to use with input parameters being open to interpretation.
Also, some tools and formulae are only suited to certain shapes of structure.
The third approach is through numerical modelling. Ideally, a numerical model may provide- within limits - the accuracy of a physical model test, but with increased flexibility and reduced expense. (McCabe et al. 2013)

2.3.1 EurOtop,2018 empirical formula for mean overtopping discharge

The Eurotop Manual (van der Meer et al. 2018) is widely used as design tool for various coastal structures. In this paragraph a discussion will be given about mean overtopping discharge calculation for vertical seawalls, as well as the effects of wave return structure or bullnose at the top of the wall, treated in research activity.
The general scheme of wave overtopping analysis in Eurotop, 2018 for vertical wall is the following.

The main factors that are addressed in Eurotop are:

- Influence of foreshore
- Possible wave breaking
- Impulsive condition
- Low freeboard

The principal formula used for wave overtopping is:

$$\frac{q}{\sqrt{gH_{m0}^3}} = aexp(-b\,R_c/H_{m0}) \quad (1)$$

It is an exponential function connecting the dimensionless overtopping discharge $q/(gH^3_{m0})^{1/2}$ and the relative crest freeboard R_c/H_{m0}. This type of equation plotted on a log-linear graph gives a straight line, thus making it easy to compare the formulae for various structures.
In the case of vertical wall structures, overflows depend on the type of interaction between wall and wave, which can be classified in two different regimes:
1)non-impulsive
2)impulsive
the two cases give rise to two very different response in terms of overtopping.
In order to proceed with assessment of wave overtopping and to identify the wave processes at wall, it is necessary first to determine the dominant overtopping regime (impulsive or non-impulsive) for a given structure and sea state. An "impulsiveness" parameter must be defined:

$$\frac{h^2}{H_{m0}L_{m-1,0}} \quad (2)$$

If this quantity is greater than 0.23 the condition will be assumed to be non-impulsive otherwise it will be considered impulsive.

Impulsive condition

General formula for mean overtopping discharge for vertical wall:

$$\frac{q}{\sqrt{gH_{m0}^3}} = 0.011 \left(\frac{H_{m0}}{h\, s_{m-1,0}}\right)^{0.5} exp\left[\left(2.2\frac{R_c}{H_{m0}}\right)\right] \quad (3)$$

Valid for R_c/H_{m0} within the range 0 - 1.35

$$\frac{q}{\sqrt{gH_{m0}^3}} = 0.0014 \left(\frac{H_{m0}}{h\, s_{m-1,0}}\right)^{0.5} \left(\frac{R_c}{H_{m0}}\right)^{-3} \quad (4)$$

Valid for R_c/H_{m0} greater than1.35

Non-Impulsive condition

For the case of simple vertical walls, with influencing foreshore, under non-impulsive conditions, the Equation (5) is used to evaluate overtopping discharge for mean value approach. For a design or assessment approach, it is strongly recommended to increase the average discharge by about one standard deviation (Equation (6)).

$$\frac{q}{\sqrt{gH_{m0}^3}} = 0.05\, exp\left(-2.78\frac{R_c}{H_{m0}}\right) \quad (5)$$

$$\frac{q}{\sqrt{gH_{m0}^3}} = 0.062 exp\left(-2.61\frac{R_c}{H_{m0}}\right) \quad (6)$$

Effect of bullnose

EurOtop,2018 also provides a decision chart to assess the effect of the curvature of the seaward face of the wall as shown in the Figure 2.3.1;

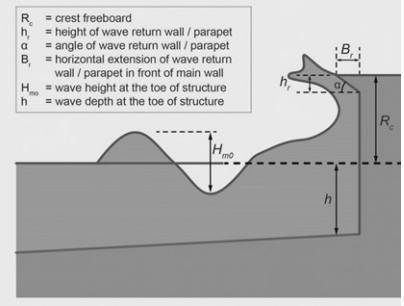

Figure 2.3.1 Configuration of a vertical plain seawall with bullnose (EurOtop,2018)

The reduction factor is defined as:

$$k_{bn} = \frac{q_{curve}}{q_{vertical}} \tag{7}$$

and it can be calculated as a function of the non-dimensional crest freeboard Rc /H_{m0} as well as on the main geometric features of the curved structure.

2.3.2 EurOtop,2018 empirical formula for individual overtopping volume V_{max}

The first step in the estimation of a maximum expected individual wave overtopping volume is to estimate the proportion of waves overtopping (Now/Nw) in a sequence of Nw incident waves.

To estimate the number of overtopping waves, EurOtop, 2018 proposed Eqs. (8)(9) for vertical structure and for non-impulsive and impulsive condition, respectively.

$$\frac{N_{ow}}{N_w} = \exp\left[-1.21\left(\frac{R_c}{H_{m0}}\right)\right]^2 \quad for\ non\ impulsive\ conditions \tag{8}$$

$$\frac{N_{ow}}{N_w} = \max\begin{cases} exp\left[-1.21\left(\frac{R_c}{H_{m0}}\right)\right]^2 \\ 0.024\left(\frac{h^2}{H_{m0}L_{m-1,0}}\frac{R_c}{H_{m0}}\right)^{-1} \end{cases} for\ impulsive\ conditions \tag{9}$$

The distribution of individual overtopping volumes in a sequence is generally well-described by a two-parameter Weibull distribution:

$$P_V = 1 - exp\left[-\left(\frac{V}{a}\right)\right]^b \tag{10}$$

where P_V is the probability that an individual event volume will not exceed V, and a and b are Weibull scale and shape parameters, respectively.
So, to estimate the largest the equation becomes:

$$V_{max} = a\,[ln(N_{ow})]^{1/b} \tag{11}$$

In the equation (11) to evaluate V_{max} there are two parameter of distribution *a* and *b*.
The equation to calculate *a* is given by:

$$a = \left(\frac{1}{\Gamma\left(1+\frac{1}{b}\right)}\right)\left(\frac{qT_m}{P_{ov}}\right) \tag{12}$$

where Γ is the mathematical gamma function and $P_{ov}=N_{ow}/N_w$ is the probability of overtopping.
Note that for vertical structures, there is not yet an equivalent of Equation for the shape parameter b as a function of the mean overtopping discharge and wave characteristics, so the discrete values given should be used for non-impulsive condition.
For non-impulsive conditions, $h^2/(H_{m0}\ L_{m-1,0})> 0.23$, there is a weak steepness dependency for the shape parameter:

$$\begin{aligned} b &= 0.66 \quad for\ s_{m-1,0} = 0.02 \\ b &= 0.82 \quad for\ s_{m-1,0} = 0.04 \end{aligned} \tag{13}$$

For impulsive conditions, (EA, 1999 and Pearson et al., 2002) for $h^2/(H_{m0}\ L_{m-1,0}) \leq 0.23$ the value becomes b = 0.85.

2.3.3 Artificial Neural Network

New techniques to predict wave overtopping at seawalls, flood embankments, breakwaters, and another shoreline structure are represented by Artificial Neural Network.

Artificial Neural Networks (ANNs) fall in the field of artificial intelligence and can in this context be defined as systems that simulate intelligence by attempting to reproduce the structure of human brains. ANNs are organised in the form of layers and within each layer there are one or more processing elements called 'neurons'.
The input layer is composed by 14 input parameters, while the output layer consists of one of the three possible outputs (Kr or Kt or q), see Figure 2.3.2. The full list of the ANN input parameters is given in Table 2.3.1
This new ANN tool allows to accurately estimate q, Kr and Kt by using consistently the same input parameters and ANN-architecture.

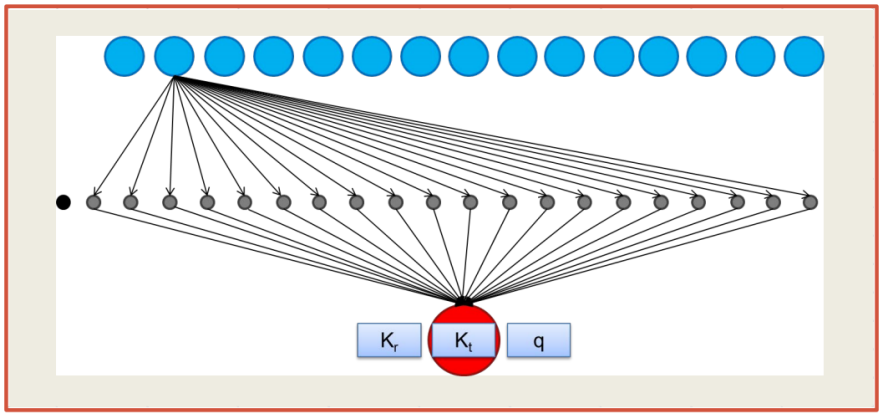

Figure 2.3.2 Schematization of the ANN architecture. The first layer consists of 15 dimensionless input parameters, the hidden layer of 20 hidden neurons and 1 bias. The output layer consists of 1 output neuron that can be q, Kr or Kt (from Eurotop 2018).

With reference to Table 2.3.1, the input parameters of the ANN tool are made dimensionless, to reproduce the relevance of specific key geometrical and physically based parameters.

Table 2.3.1 The 15 dimensionless input parameters of ANN.

Parameter	Type	Representation of
$H_{m0,t}$ /$L_{m-1,0,t}$	Wave condition	Wave steepness (Breaking)
β [rad]	Wave condition	Wave obliquity
$h/L_{m-1,0,t}$	Wave condition	Shoaling
h_t /$H_{m0,t}$	Geometry	Effect of toe submergence
$B_t/L_{m-1,0,t}$	Geometry	Effect of toe width
$d_b/H_{m0,t}$	Geometry	Effect of the berm level
$B/L_{m-1,0,t}$	Geometry	Effect of the berm width
$R_c/H_{m0,t}$	Geometry	Effect of the relative crest height (including the crown wall if present)
$A_c/H_{m0,t}$	Geometry	Effect of the relative crest height
$G_c/L_{m-1,0,t}$	Geometry	Effect of the crest width
$\cot\alpha_d$	Geometry	Downstream slope
$\cot\alpha_{incl}$	Geometry	Average slope in the run-up/down area
m		Cotangent of the foreshore slope
$D/H_{m0,t}$	Structure characteristics	Indication of structure permeability and/or roughness
γ_f	Structure characteristics	Dissipation induced by structure roughness and permeability

The wave length $L_{m-1,0,t}$,used as scale parameter for the structure widths, is computed on the basis of the wave period at the structure toe ($L_{m-1,0,t} = (g \cdot T^2_{m-1,0,t})/2\pi$) instead of using the local wave length reconstructed with specific procedures based on h and $T_{m-1,0,t}$.

The database used to train the ANN tool consists of about 13,000 tests on wave overtopping, more than 7,000 tests on wave reflection and 3,500 tests on wave transmission, for a total amount of almost 18,000 tests (Zanuttigh et al., 2016; Formentin et al., 2017). This database is an update and integration of the datasets collected within the CLASH (2004) and the DELOS projects, joined with a number of further datasets, partially derived from people involved in preparation of EurOtop (2016) or from private communication.

All the Outputs are provided in terms of average values and percentiles (5% and 95%) as reported in Table 2.3.2

Table 2.3.2 Example of an Outputs table of the NN Tool.

Test-ID	Average	Prototype	5.0%	95.0%	E
1_1	5.36e-01	5.36e-01	2.37e-01	1.12e+00	0.1074
1_2	1.34e-03	1.34e-03	2.84e-04	6.01e-03	0.3976
1_3	1.13e-01	1.13e-01	7.65e-02	1.71e-01	0.0826

The previous table is delivered to the User and printed at the Results page after the run NN Tool, it contains the average values of the predictions, the percentiles 5% and 95% to derive the 90% confidence bands, the values of the Euclidean distance E between the configuration of the User Scenario(s) and the NN domain of validity and, when the Output is q, an extra column including the corrected average prediction of q accounting for the model effects.
The ANN tool is free to use– upon registration – from the website of the EurOtop ANN tool, www.unibo.it/overtopping-neuralnetwork.

2.3.4 Numerical modelling of wave overtopping

Numerical techniques are at a very advanced stage of development, to the point that they are now a fundamental element of engineering practice.
Many CFD software packages have been developed in the last decades and used to study wave overtopping as FLOW-3D® (Flow Science Inc. (USA)(Dentale et al 2014a, Dentale et al 2014b, Buccino et al. 2016, Buccino et al. 2019), SWASH (Martínez Pés (2013). The availability of open-sources codes with wave generation capabilities such as OpenFoamR© (Jacobsen et al.,2012; Higuera et al., 2013) has increased the application of detailed computational fluid-dynamics for marine, maritime, and coastal engineering.

Recently, Borsboom and Jacobsen (2021) presented a new absorbing boundary condition with a complete analytical framework to predict its performance.
Furthermore, the methods based on non-Eulerian approaches should also be mentioned e.g. DualSPHysics an open-source CFD software package, developed based on the Smoothed Particle Hydrodynamics method -SPH (Akbari et al.2017, Viccione et al. 2012, Didier and Neves, 2009).
The performance of numerical models depends on the governing equations, on the solving technique and on validation procedures and tests.
Some models have high computational efficiency but have difficulty in modelling wave breaking and free surfaces tracking. On the contrary other method has excellent capability to track free surface deformations but computationally expensive.
Flow-3D® package, which was selected for this research project, is based on RANS, and is capable of simulating wave breaking and large free surface deformations; it also has reasonable computational efficiency in comparison to other software systems.
In FLOW-3D, the mesh is structured, meaning that the volume elements or cells are well ordered. Both Cartesian and cylindrical meshes can be defined in FLOW-3D, and cell dimensions can be uniform or non-uniform. Therefore, it has the advantages of easy mesh generation, regularity for improved numerical accuracy. In numerical domain of Flow3D the geometry, is defined within the grid by computing the fractional face areas and fractional volumes of each element that are blocked by obstacles (FAVOR method). The use of a multiple and nested meshes, and the re-run capability available in FLOW-3D software are other options that make the numerical model suitable for hydraulic structure modeling.
Flow-3D allows either one or two fluid flow, with or without a free surface, and a multitude of available physics options to suit the specific application. A large selection of boundary conditions is also available to properly model each specific application. Another benefit of Flow3D is

the ability to select from several different implicit and explicit numerical solver options.
The program is based on the fundamental laws of mass, momentum, and energy conservation and applicable to almost any type of flow process.

2.4 UNCERTAINTY ON THE OVERTOPPING DISCHARGE MEASUREMENTS

A high degree of uncertainty is inevitable in engineering measurements and modelling, so a brief discussion is necessary.
The uncertainties of input parameters and models generally fall into certain categories as described in *Eurotop,2018:*

- Fundamental or statistical uncertainties
- Data uncertainty
- Model uncertainty
- Human errors

It is known that overtopping flow rate is very sensitive to small variation in the geometry of the structures, the wave climate and the local bathymetry and, as consequence, empirical formulas derived from general cases does not provide the same reliability as a specific model experiment.
As referred in Goda 2009, when random waves are generated under a specified wave spectrum, several runs of generated waves have different combinations of wave heights and periods, thus producing different volumes of total wave overtopping. Such difference increases as the overtopping volume decreases.
In Romano et al. 2014 is also shown the variability in 25 tests with the same energy density spectrum (H_{m0} = 0.081 m, T_p = 1.42 s) but with different seeds for the starting phases distributions. With these conditions the total overtopped volume varied in the range 0.5–1.5 l for storm duration of 1250s.

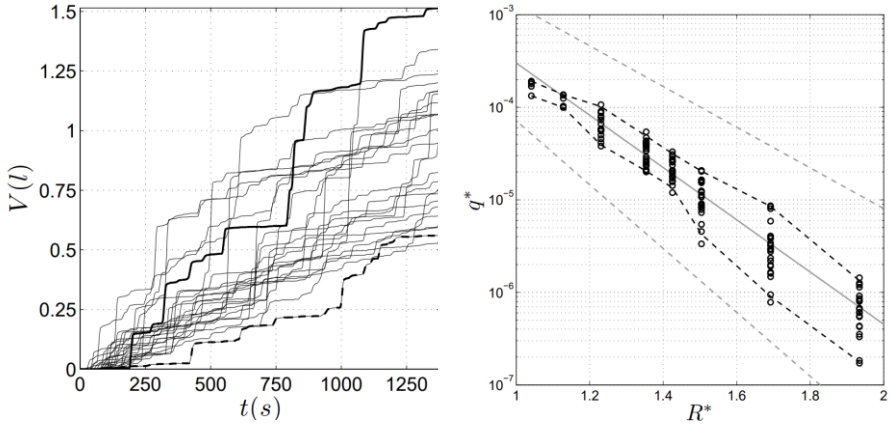

Figure 2.4.1 Overtopping volume time series obtained for 25 repetitions of the same sea state (Hm0 = 0.081 m, Tp = 1.42 s) with varying the seeding number. (Romano et al. 2014).

As plotted in the Figure 2.4.1 (b) the laboratory tests, carried out on a simple rubble mound breakwater, have shown that this variability is one order of magnitude smaller than the confidence intervals of the Pullen et al. (2007) formula (dotted grey lines).

McCabe et al. 2013 in their work discuss about overtopping agreement between model, field, and flume.

The agreement was generally good but the repeatability of two nominally identical flume experiments was only within 25%. In addition, they show that the different distributions of random phase between spectral components can cause differences overall overtopping rates.

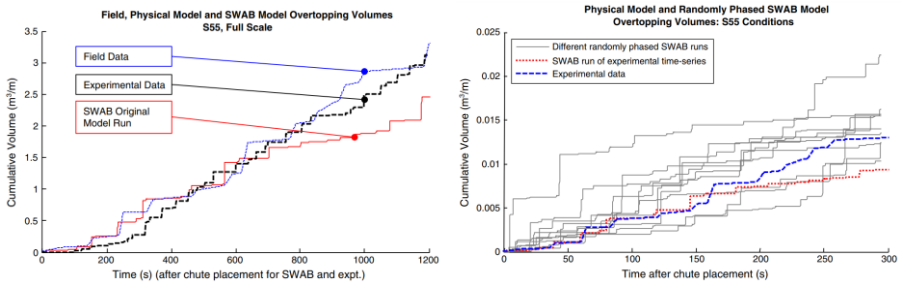

Figure 2.4.2 Cumulative overtopping as derived from experimental, field, and numerical model and different randomly phased of numerical model. (McCabe et al. 2013).

As phase distribution cannot be predicted, this increases the uncertainty of any method used to make overtopping predictions.
In addition, Pearson et al. (2002) highlighted the question of the relationship between the length of time series and the accuracy of the overtopping estimate.
Pearson et al. 2002 also discusses variabilities and uncertainties inherent in the overtopping processes it can be seen that as expected the standard deviations of mean discharge have the lowest deviations: < 5% for same-seed, and ~ 8% for varying-seed, and the largest scatter is in maximum volume which is typically ~ 15 - 20%. Furthermore, they discuss about the sequence length, showing higher variability of mean discharge in sequences with lower number overtopping events.

2.5 Convergence Analysis - A Brief Review of Literature Data

Basic grid convergence study on surface elevation η and velocity profile is addressed in Dieter Vanneste 2013. The Author suggests some indication of grid dimension as function of wave height and wavelength.
Also, Yazid Maliki et al. 2017, carry out mesh convergence studies of volumetric overtopping discharge against time as shown in Figure 2.5.1

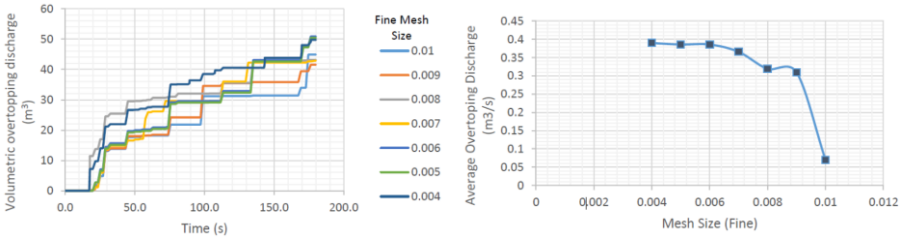

Figure 2.5.1 Volumetric overtopping and mean discharge with different mesh size of numerical model. (YAZID MALIKI et al. 2017).

It should be noted how the convergence is related to the simulation time. As you can see in the Figure 2.5.1, the volume curves appear generally distant during simulation and then converge at certain instant.

S.I.O Scholte, 2020 investigate whether CFD (OpenFoam) can be used to assess safety of structures. The author discusses about strange behaviour shown in the Figure 2.5.2.

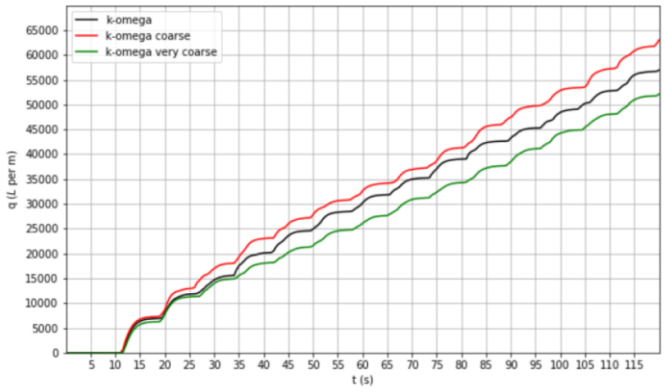

Figure 2.5.2 Overtopping volume as computed with three different mesh sizes (S.I.O Scholte, 2020).

At first, the amount of overtopping in the two coarser grids have approximately a difference of around 10 percent. Those percentages are not the most worrying, however. It was expected that the overtopping showed a convergent behaviour when the grid size becomes finer, e.g. a finer mesh result in consistently more or less overtopping. Instead, the line of the finest grid lies in the middle of the three lines.

2.6 MOTIVATION

As is it shown by some Authors in the recent research literature, there is an extreme intrinsic variability of the phenomenon and the uncertainties of estimation have been shown by some authors. Moreover, systematic studies of convergence on this phenomenon have not been found in the literature.

Therefore, the main objective of this work is to analyze the phenomenon and possible uncertainties linked to numerical modeling.

The main objective of this work is to investigate the possibility to use numerical simulations as an alternative or complimentary tool for

prediction of overtopping, by considering numerical model results in connection with specific laboratory experiments and with existing empirical formulas.
The analysis is focused on the case of a seawall with a significant effect of the foreshore on wave transformation not fully investigated in literature. In order to do so, the influence of low frequencies component of spectral amplitude is also studied by using both regular and irregular wave conditions.
Finally, the effect of the wind on wave overtopping has been also discussed.

3 NUMERICAL METHOD

3.1 RANS MODELS

In the last ten years, advances of Computational Fluid Dynamics (CFD) have led to a decisive step in the simulation of wave actions on coastal structures. While physical tank models and formulas derived from them are still the main design coastal structures, 2D or even 3D flow simulation is quickly becoming standard practice; a typical procedure involves the numerical integration of Reynolds Averaged Navier-Stokes (RANS/VOF) equations on a fixed grid, with one of the traditional turbulence models (K-eps, K-ω, RNG) and a free surface tracking procedure - this latter generally based on the now classical Volume of Fluid Method.
There are several CFD codes available, but in this study the model Flow-3D® was selected, a commercial code developed by Flow Science Inc. (Bradford, 2000; Chopakatla et al, 2008), due to the long-standing experience that our research group has gained over the years.
FLOW-3D® is based on the RANS (Reynolds Averaged Navier-Stokes) equations combined with the Volume of Fluid (VOF) method to track the location of the fluid surfaces and various turbulence techniques such as k-ε, RNG or LES (Hirt and Nichols, 1981)

Flow-3D® is a multi-physics solver with options for a broad wide range of flow problems. The physical background (basic equations) of the model is presented hereafter, together with a description of the numerical implementation.

3.2 GOVERNING EQUATIONS AND TURBULENCE CLOSURE MODEL

The flow in general is described by the general Navier-Stokes equations that are the fundamental equations for fluid dynamics, which reflect the conservation of mass and momentum.
The general equation of mass conservation for incompressible fluid reads:

$$\frac{\partial u_i}{\partial x_i} = 0 \tag{14}$$

and u_i is the cartesian component of the velocity.
The conservation of momentum establishes that the change in momentum in a control volume is equal to all the acting forces on the control volume:

$$\frac{\partial u_i}{\partial t} + u_j \frac{\partial u_i}{\partial x_i} = g_{ij} - \frac{1}{\rho}\frac{\partial p}{\partial x_i} + \frac{1}{\rho}\frac{\partial \tau_{ij}}{\partial x_j} \tag{15}$$

where (g) is the gravity force, (p) pressure forces and viscous stress tensor (τ). The momentum equations, often referred to as the Navier-Stokes equations, describe the fluid motion with full consideration of nonlinear effects.
The solution of the momentum conservation equation required constitutive equations that relate the stress tensor to the velocity field. For Newtonian fluids, shear stresses are directly proportional to velocity gradient; when the fluid is incompressible, the shear stresses read:

$$\tau_{ij} = \mu\left(\frac{\partial u_i}{\partial x_j} + \frac{\partial u_j}{\partial x_i}\right) \tag{16}$$

The basic tool required for the derivation of the RANS equations from the instantaneous Navier–Stokes equations is the Reynolds decomposition.

The Reynolds-decomposition technique leads to the so-called RANS equations, where an all-dependent time signal quantity (in this case velocity) can be decomposed into a mean term and a fluctuating term:

$$u_i = \overline{u_\iota} + u_i' \tag{17}$$

The most natural way to describe the dynamics of a turbulent motion is to start from Navier-Stokes equations in their classical form of laminar motion and adapt them to the turbulent case according to the Reynolds decomposition method.
The RANS equations for an incompressible fluid read:

$$\frac{\partial \overline{u_\iota}}{\partial x_i} = 0 \tag{18}$$

$$\frac{\partial \overline{u_\iota}}{\partial t} + \overline{u_j}\,\frac{\partial \overline{u_\iota}}{\partial x_j} = g_i - \frac{1}{\rho}\frac{\partial \bar{p}}{\partial x_i} + \frac{1}{\rho}\frac{\partial}{\partial x_j}\left[\mu\left(\frac{\partial \overline{u_\iota}}{\partial x_j} + \frac{\partial \overline{u_j}}{\partial x_i}\right) - \rho\overline{u_i' u_j'}\right] \tag{19}$$

The turbulent shear stresses $-\rho\overline{u_i' u_j'}$, often referred to as the Reynolds shear stresses, require additional modelling to close the RANS equation for solving. The main difficulty in studying turbulence is the simultaneous presence into the fluid of many vortical structures with different characteristic size that mutually interact each other; they are due to nonlinear terms in the Navier-Stokes equations and make difficult the analytical implementation.
Closure assumptions are necessary to relate the higher-order correlations of the turbulent flow field to the characteristics of the mean flow field.
However, there are algebraic models, which directly provide the turbulent viscosity in function of the mean variables, without resorting to differential equations, but they often contain empirical parameters constitute ad hoc models for specific problems. There are differential models of greater generality, in which one or more characteristic quantities of turbulence (kinetic energy turbulent or the dissipation rate) are obtained by solving suitable transport equations. The purpose of this approach is

to obtain equations of greater generality, having less dependence on empirical assumptions, although with mayor complexity and computational effort.
In Flow-3D, there are six turbulence models available: the Prandtl mixing length model, the one-equation, the two-equation k-ε, the ReNormalization Group (RNG) and k-ω models, and a large eddy simulation, LES, model.

For practical engineering problems, the most successful computational turbulence models are based upon two or more additional conservation and transport equations. A minimum of two equations is desirable because it allows to take into account both the turbulent energy and the length and time scales of turbulent processes.

- The standard k-ε model (Harlow & Nakayama 1967) is a two-equation model that calculates both turbulent kinetic energy, k and dissipation rate, ε, and finds the turbulent mixing length LT dynamically.
- The Renormalized Group (RNG)(Yakhot & Orszag 1986, Yakhot & Smith 1992) is a more robust version of the two-equation k-ε model, and it is recommended for most industrial problems. It extends the capabilities of the standard k-ε model to provide better coverage of transitionally turbulent flows, curving flows, wall heat transfer, and mass transfer.
- The k-ω model (Wilcox 1998, 2008) defines the second variable not as turbulent dissipation ε but as $\omega \equiv \varepsilon/k$ (Kolmogorov 1942). The k-ω two-equation model in FLOW-3D is thus suitable for modelling free shear flows with streamwise pressure gradients like spreading jets, wakes, and plumes.

3.2.1 k-e Model

As the name suggests, this model is based on two differential equations: one for the turbulent kinetic energy k, the other for the dissipation ε.

To determine k and ε, two additional transport equations must be solved, for the turbulent kinetic energy k and dissipation rate ε respectively:

$$\frac{\partial k}{\partial t} + u\frac{\partial k}{\partial x} + w\frac{\partial k}{\partial z} - \frac{\partial}{dx}\left[\frac{(\nu + \nu_T)}{\sigma_k}\frac{\partial k}{\partial x}\right] - \frac{\partial}{dz}\left[\frac{(\nu + \nu_T)}{\sigma_k}\frac{\partial k}{\partial z}\right] + \varepsilon - P = 0 \quad (20)$$

$$\frac{\partial \varepsilon}{\partial t} + u\frac{\partial \varepsilon}{\partial x} + w\frac{\partial \varepsilon}{\partial z} - \frac{\partial}{dx}\left[\frac{(\nu + \nu_T)}{\sigma_\varepsilon}\frac{\partial \varepsilon}{\partial x}\right] - \frac{\partial}{dz}\left[\frac{(\nu + \nu_T)}{\sigma_\varepsilon}\frac{\partial \varepsilon}{\partial z}\right] + c_2\frac{\varepsilon^2}{k} - c_1\frac{\varepsilon}{k}\nu_T P = 0 \quad (21)$$

Where the shear production, P, is defined as:

$$P = \frac{(\nu + \nu_T)}{\rho}\left\{2\left(\frac{\partial \mathrm{u}}{\partial x}\right)^2 + \left(\frac{\partial \mathrm{u}}{\partial z} + \frac{\partial w}{\partial x}\right)^2 + 2\left(\frac{\partial \mathrm{w}}{\partial z}\right)^2\right\} \quad (22)$$

Eqs. (20)–(22) represent the widely known standard k-ε turbulence model, where σk, σε, c_1 and c_2 are additional constants (Launder and Spalding, 1974).

3.2.1 RNG Model

The RNG method, like the k-ε model, accounts for the effects of smaller scales of motion by applying a renormalization technique to the Navier-Stokes equations, see e.g. Yakhot et al. (1992).
One of the major advantages of the RNG method is that by scale expansion, the important turbulence coefficients can be theoretically determined rather than being adjusted empirically. The RNG approach results in the same k equation but a modified form of the ε equation:

$$\frac{\partial \varepsilon}{\partial t} + u\frac{\partial \varepsilon}{\partial x} + w\frac{\partial \varepsilon}{\partial z} - \frac{\partial}{dx}\left[\frac{(\nu + \nu_T)}{\sigma_\varepsilon}\frac{\partial \varepsilon}{\partial x}\right] - \frac{\partial}{dz}\left[\frac{(\nu + \nu_T)}{\sigma_\varepsilon}\frac{\partial \varepsilon}{\partial z}\right] + c_2\frac{\varepsilon^2}{k} - c_1\frac{\varepsilon}{k}\nu_T P + R = 0 \quad (23)$$

This modification makes the RNG model more sensitive to flows having strong shear regions, due to the presence of the source term R.

In this study, a ReNormalized Group (RNG) has been used; here, the parameters cμ, c1, σk and σε still remain constant (cμ=0.085, c1=1.42, σk=σε=1.39), whereas c_2 is assumed to vary with P according to the formula (Yakhot et al., 1992):

$$c_2 = 1.68 + \frac{c_\mu \beta^3 (1 - 0.2283\beta)}{1 + 0.012\beta^3} \tag{24}$$

$$\beta = \frac{k}{\varepsilon}\sqrt{\frac{P}{(\nu + \nu_T)}} \tag{25}$$

3.2.1 k-ω Model

The k-equation can be combined directly with a time-scale equation. It turns out to be more suitable to use a quantity, ω, that has dimensions of inverse time. Then the eddy viscosity is represented as $\nu T = k/\omega$. The $k-\omega$ model of Wilcox (1998) can be written as:

$$\frac{\partial k}{\partial t} + u\frac{\partial k}{\partial x} + w\frac{\partial k}{\partial z} - \frac{\partial}{dx}\left[\frac{(\nu + \nu_T)}{\sigma_k}\frac{\partial k}{\partial x}\right] - \frac{\partial}{dz}\left[\frac{(\nu + \nu_T)}{\sigma_k}\frac{\partial k}{\partial z}\right] + C_\mu k\omega - P = 0 \tag{26}$$

$$\frac{\partial \omega}{\partial t} + u\frac{\partial \omega}{\partial x} + w\frac{\partial \omega}{\partial z} - \frac{\partial}{dx}\left[\frac{(\nu + \nu_T)}{\sigma_\omega}\frac{\partial \omega}{\partial x}\right] - \frac{\partial}{dz}\left[\frac{(\nu + \nu_T)}{\sigma_\omega}\frac{\partial \omega}{\partial z}\right] + C_{\omega 2}\omega^2 - C_{\omega 1}\frac{\omega}{k}P = 0 \tag{27}$$

The k-equation is altered only by changing ε to $k\omega$. The ω-equation is quite similar to the ε-equation. The standard constants are $C_{\omega 1} = 5/9$, $C_{\omega 2} = 3/40$, $\sigma_\omega = \sigma_k = 2$, and $C_\mu = 0.09$.

3.2.2 Turbulence Model Boundary Conditions

Near the wall the dynamic of turbulence is significantly far from the hypothesis of homogeneity and isotropy, and this implies significant

changes in the turbulence patterns and in the evaluation of the computational resources. So, for a long time, application of turbulence closure model is limited to region without the presence of a solid wall. Most practical flows, however, are wall bounded.

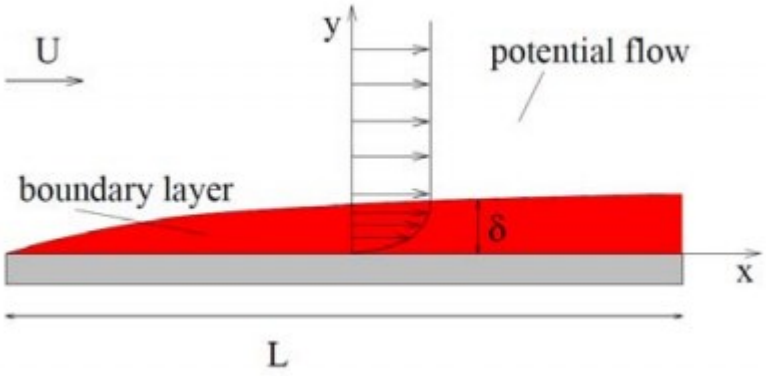

Figure 3.2.1 Wall bounded flow.

Boundary layers, the viscous flow region attached to solid boundaries, require special treatment. The so-called universal law of the wall (Von Karman, 1930) describes the flow profiles in such regions.

The dimensionless velocity u^+, and dimensionless wall distance y^+, as a function of shear velocity (u_τ) and viscosity (ν) are defined as:

$$u^+ = \frac{U}{u_\tau} \qquad y^+ = d\,\frac{u_\tau}{\nu} \tag{28}$$

Generally, wall models are based on the "existence" of a logarithmic velocity profile in a turbulent boundary layer and the f(y) has unit value far from the walls and tends exponentially to zero near a solid surface.

The Law of the wall can be described:

$$u^+ = \frac{1}{k}\ln(y^+) + C \tag{29}$$

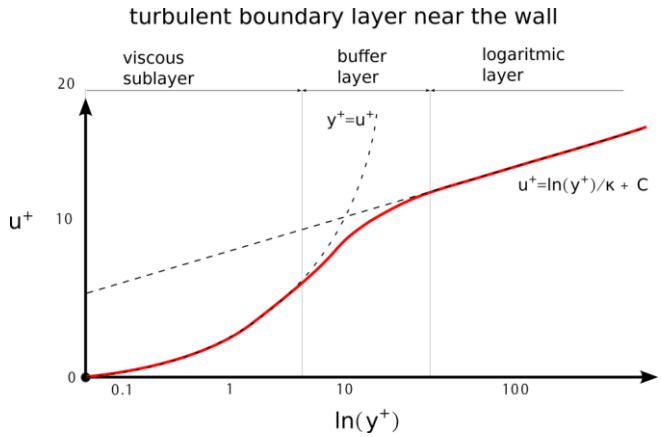

Figure 3.2.2 A sketch of near wall detail of developed turbulent boundary layer in dimensionless coordinates u^+ and y^+. (k is vin Karman's constant ≅ 0.41 and C are a constant ≅ 5.1) (Schultz, et al. 2003).

The fully developed boundary layer can be viewed as divided into four regions:

Viscous sublayer is a region closest to the wall. In this region $y^+=u^+$ The fluid flow is always laminar here. The Viscous sublayer region is typically where $y^+<10$.

Buffer layer is a region, where neither law holds. The Buffer layer region is typically where $5<y^+<30$.

Logarithmic (Log-law) layer is a region, where the Law of the wall holds. The Log-law layer region is typically where $30<y^+<300$.

Outer (Defect) layer is a region, where the free stream is taking over. The Outer layer region is typically where $y^+>300$.

In this way it is possible to express the average velocity parallel to the wall and the turbulence outside the viscous substrate as a function of the distance from the wall.

Wall functions can be used to define the boundary conditions near the wall for momentum and turbulence; so as not to resolve the viscous layer thus avoiding using an extremely finer mesh.

3.3 FREE SURFACE TRACKING

It is necessary to impose proper boundary conditions at the free surface in single-fluid modelling.
Regardless of the method employed, there are three essential features needed to properly model free surfaces:

- a scheme is needed to describe the shape and location of a surface;
- an algorithm is required to evolve the shape and location with time;
- free-surface boundary conditions must be applied at the surface.

In the literature many methods for free surface tracking are described; the most popular one is the Volume-of-Fluid (VOF) method (Hirt and Nichols, 1981), which is adopted in the present work.
The VOF method introduces a volume of fluid function F(x, y, z, t) to define the water region. The physical meaning of the F function is the fractional volume of a cell occupied by water. A unit value of F corresponds to a cell full of water, while a zero value indicates that the cell contains no water (void region). Cells with F value between zero and unity must then contain the free surface.
A free surface is a sharp interface used in *one-fluid* flows with void regions. (ref. Flow3d-Manual)

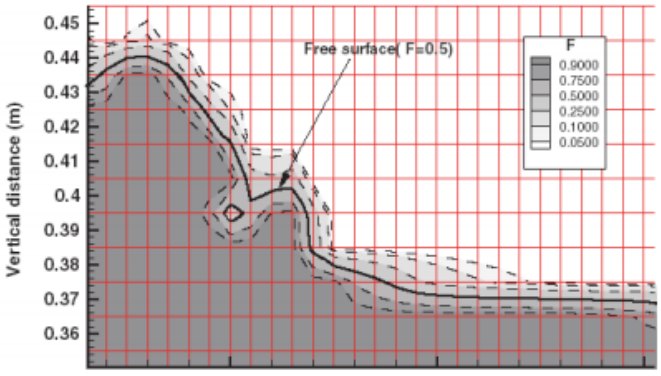

Figure 3.3.1 VOF Function near free surface.

The fractional function F can be evaluated as follows:

$$F = \frac{V_w}{V_c} \tag{30}$$

where V_w is the volume of water inside a cell and V_c is volume of the cell. This function represents the volume of fluid per unit volume; the fluid interface is plotted by solving the equation that describes the evolution of the fractional function F.

The two-dimensional transport equation for the fractional function is given by:

$$\frac{\partial F}{\partial t} + \frac{\partial uF}{\partial x} + \frac{\partial wF}{\partial z} = 0 \tag{31}$$

It is necessary to impose proper boundary conditions at the free surface in single-fluid modelling.

The VOF method is extremely suitable in fixed grid simulation methods, where the free surface should be able to have an arbitrary complex topology.

3.4 BOUNDARY CONDITIONS

The wave problem governed by the equations discussed above, forms an initial-boundary value problem, the initial and boundary conditions need to be prescribed correctly.

These boundary conditions depend on specific problem and so that will be addressed for specific simulation from time to time.

In this paragraph typical boundary and initial conditions utilized in this work are briefly discussed.

Free surface boundary condition

In this specific case the experiments have been conducted with a single fluid (water), i.e. neglecting any effect of air. Thus, fluid exists where F = 1, and void regions correspond to locations where F = 0.

This aspect has been treated in the previous paragraph.

Inflow boundary

In a wave simulation set up, the most important problem is the definition of the wave generation at one end of the domain, i.e. of the wave generator; different theories are available (Periodic Linear Wave Generator, Stokes Wave Generator, Stokes and Cnoidal Waves Generator (Fourier Series Method), Solitary Wave Generator, Random Wave) and are implemented in most software systems.

For **outflow boundary conditions**, in wave propagation problems, special boundary treatments have been devised that try to determine the speed and direction of waves approaching the boundary and then set boundary conditions in such a way as to allow their continuation through the boundary with a minimum of reflection. For wave propagation problems, it is natural to seek a boundary condition that will allow outgoing waves to smoothly leave the computational mesh with minimum reflection. This problem is analogous to wave absorption in experimental wave tanks, where one wants to eliminate the reflection of waves from the downstream end of the tank. In these tanks a variety of techniques are used, but nearly all of them employ some sort of energy dissipation (e.g., porous beaches).

In numerical model the sponge layer method uses a wave-damping region called a sponge, or wave-absorbing, layer to absorb waves before they reach an open boundary.

A wave-absorbing layer or sponge layer is a special region installed before an outflow boundary to absorb wave motion, which reduces wave reflection from the boundary (Figure 3.4.1.).

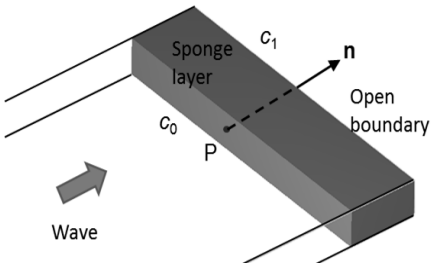

Figure 3.4.1 Sketch of wave absorbing layer.

In the sponge layer, defined by a special geometry component called the wave-absorbing component, the Navier-Stokes equation is modified as:

$$\frac{\partial \vec{u}}{\partial t} + \vec{u} \cdot \nabla \vec{u} = -\frac{1}{\rho} \nabla p + \nabla \cdot \nabla (v\vec{u}) - c(\vec{u} - \vec{u}_{str}) \tag{32}$$

where $-c(\vec{u} - \vec{u}_{str})$ is the artificial damping force that dissipates the wave motion, c is the damping coefficient in units of (time)$^{-1}$, and $\vec{u}_{str}$ is the background stream velocity that is exempted from damping.

Wave damping occurs only in the region covered by the absorbing component between the two planes; the values of the damping coefficient are defined at both the starting and end planes of the wave-absorbing layer.

The coefficient c can be constant inside the sponge layer or increase linearly in the wave propagation direction. It is evaluated using the expression:

$$c = c_0 + l \cdot \frac{c_1 - c_0}{d} \tag{33}$$

where c_0 and c_1 ($c_1 \geq c_0$) are the values of k at the starting side of the sponge layer and the open boundary, respectively. The distance l is measured from the starting side of the wave-absorbing layer toward the open boundary. Finally, d is the length of the sponge layer. The developers suggest the length of absorption must be at least as long as the longest waves to be trapped.

The values of c_0 and c_1 are 0.0 and 1.0 , respectively; the value of d is one wavelength. A previous application of this method is shown in Di Leo et al. 2017.

Lateral and upper limits of the numerical flume are treated as "Symmetry boundaries" (S), where the velocity gradient vanishes, and the turbulence production is zero.

The numerical wave channel is considered impermeable at the bottom, the normal velocity component $\mathbf{u_n}$ and the velocity component along the

surface $\mathbf{u}_s$ are zero, where n and s are the coordinate in the normal direction and tangential direction of the impermeable surface, respectively.

Internal obstacle boundaries

The definition of obstacles within a mesh is accomplished by defining the fractional cell areas and volumes of these cells partially occupied by obstacles (the FAVOR method) and by flagging those mesh cells that are entirely occupied by obstacles. (Flow 3D manual)

When obstacles are defined in the input file, using the FLOW-3D geometry builder or STL data, the area/volume fractions are automatically calculated before the hydrodynamic calculations are carried out.

3.5 NUMERICAL IMPLEMENTATION

3.5.1 Numerical solution

Following Hirt and Nichols (1981), the computational solutions of the above equations are obtained on a staggered grid. Fig.3 shows the locations of the velocity components, pressure, F function, as well as the turbulent kinetic energy $k^n_{i,j}$ and eddy viscosity $\nu^n_{i,j}$. The pressure $p_{i,j}$, volume of fluid function $F_{i,j}$, turbulent kinetic energy $k^n_{i,j}$ and eddy viscosity $\nu^n_{i,j}$ are cell-centered quantities, while the velocity components are defined at the cell faces. Δxi and Δzj are the mesh size at ith column and jth row.

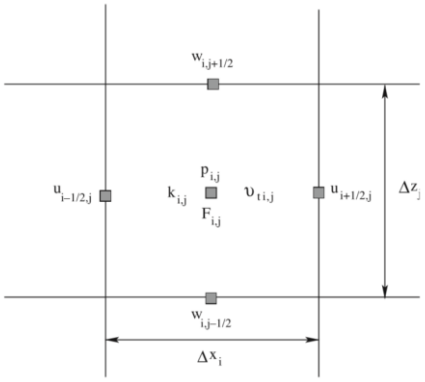

Figure 3.5.1. Stagger grid and locations of variables

The equations above described have been finite-difference solved, via the commercially available multi-physics CFD software "FLOW-3D". Developed by Flow Science Inc. (2009), FLOW-3D has been recently employed, with satisfactory results, in a number of wave-structure interaction problems, including both impermeable walls and permeable breakwaters (e.g. Buccino et al., 2016; Vicinanza et al., 2015, Dentale et al., 2014a, 2014b). The flow region is subdivided into a mesh of fixed rectangular cells, at centre of which are located all the variables but velocities, which are situated, instead, at the cell–faces (staggered grid arrangement) as shown in Figure 3.5.1. Curved obstacles, wall boundaries, or other geometric features are embedded in the mesh by defining the fractional areas of the cells that are open to flow (FAVOR™ method (Hirt and Sicilian, 1985). The governing equations are discretized as follows:

$$\frac{u_{i+1\,j}^{n+1} - u_{ij}^{n+1}}{\Delta x} + \frac{w_{ij+0.5}^{n+1} - w_{ij}^{n+1}}{\Delta z} = 0 \tag{34}$$

$$\frac{u_{ij}^{n+1} - u_{ij}^{n}}{\Delta t^{n+1}} = -\left(A_{ux} + A_{uy} + A_{uz}\right)_{ij}^{n} - (VIS_x)_{ij}^{n} - \frac{2}{\rho_{ij}^{n} + \rho_{i+1\,j}^{n}}\left(\frac{p_{i+1\,j}^{n+1} - p_{i\,j}^{n+1}}{\Delta x}\right) \tag{35}$$

$$\frac{w_{ij}^{n+1} - w_{ij}^{n}}{\Delta t^{n+1}} = -\left(A_{wx} + A_{wy} + A_{wz}\right)_{ij}^{n} - (VIS_z)_{ij}^{n} - \frac{2}{\rho_{ij}^{n} + \rho_{i\,j+1}^{n}}\left(\frac{p_{i+1\,j}^{n+1} - p_{i\,j}^{n+1}}{\Delta z}\right) \quad (36)$$

where the subscripts indicate the cell coordinates, and the superscripts indicate time step. Δx and Δz represent the cell length and height respectively, while Δt is the time step size (see subsection 3.5.2). In the momentum equations, both the advective fluxes($A_{\alpha\beta}$) and the viscous terms (VISx,z) are calculated explicitly, using the old time level n, according to the first order donor cell approximation method. As far as the fluid density (ϱ) is concerned, a single value is used in case of one incompressible fluid flow, whereas a weighted average over the VOF function F is employed for two incompressible fluids. Since in Eq. (34)-(36) pressures and velocities are coupled implicitly, an iteration solution procedure is needed. To this purpose, the momentum balance is firstly solved using the pressure gradient at the time level n; this gives an intermediate velocity vector, $\overrightarrow{U^*}$, which is linked to the real velocity at the time step n+1 $(\overrightarrow{U^{n+1}})$, by the following relationship:

$$\overrightarrow{U^{n+1}} = \overrightarrow{U^*} + \frac{2 \cdot \Delta t^{n+1}}{\rho_{ij}^{n} + \rho_{i+1\,j}^{n}} \nabla p' \quad (37)$$

Where $p' = p^{n+1} - p^{n}$. By inserting Eq. (37) in Eq. (34), a Poisson equation in p' is obtained, which is solved through the Generalized Minimum RESidual method (GMRES; Saad,1996).

After obtaining $(\overrightarrow{U^{n+1}})$, the new free surface configuration is computed with the VOF method.

3.5.2 Stability Considerations

Flow-3D uses variable time stepping to maintain the stability and accuracy of the solution. In particular, the n-th time step size, Δtn, is automatically adjusted to:

$$\Delta t^n = \min(\Delta t^n_{CON}, \Delta t_s) \tag{38}$$

where Δt_s is a user defined sampling rate, which depends on the frequency spectrum of the phenomenon under study, and Δt^n_{CON} is a convergence time step size, that is needed to avoid numerical instabilities. Since the advective fluxes have been computed using a simple first order donor cell, Δt^n_{CON} is required to meet the following criterion:

$$\Delta t^n_{CON} = \min(0.5 \cdot \Delta t_{CFL}, 0.5\frac{\Delta x}{\sqrt{\Delta z \Delta az}}) \tag{39}$$

where Δt_{CFL} is the time step to satisfy the Courant–Friedrichs–Lewy (CFL) stability criterion and the second quantity at the right-hand side of Eq. (39) ensures surface waves cannot propagate more than one cell in one time step (az indicates vertical acceleration).

3.5.3 Numerical solution and Geometry representations

FLOW-3D numerically solves the equations described in the previous sections using finite-difference (or finite-volume) approximations. The flow region is subdivided into a mesh of fixed rectangular cells (Eulerian approach). With each cell there are associated local average values of all dependent variables. As explained in the following, all variables are located at the centres of the cells except for velocities, which are located at cell-faces (staggered grid arrangement). Curved obstacles, wall boundaries, or other geometric features are embedded in the mesh by defining the fractional face areas and fractional volumes of the cells that are open to flow (the FAVOR method, Hirt and Sicilian,1985). All equations are formulated with area and volume porosity functions. This formulation, called FAVOR for Fractional Area/Volume Obstacle Representation Method (Hirt and Sicilian,1985) is used to model complex geometric regions.

4 DISCUSSION ON GRID SENSITIVITY STUDY

4.1 INTRODUCTION

As stated above the simulations have been carried out via numerical experiments conducted in a Computational Fluid Dynamics (CFD) wave flume, based on the commercial code FLOW-3D (Flow Science Inc., 2009). The CFD technique, which solves numerically the Navier-Stokes equations, is recently growing popular in the field of coastal and ocean engineering (e.g. Antonini et al. 2017; Miquel et al., 2018).

One of the obvious problems of the CFD is that the results may depend on the grid. What is needed is a result which does not depend on the grid, which might be attained by repeating the calculations with ever small grids until the variability of the results is limited under specific value - this is called *convergence analysis*. However, it postulates that there is a region, however, that varies from experiment to experiment where the results are grid independent. This region is called the convergence region in which the results variability is limited.

In this specific case, there are *two variables* of which we are interested to study the convergence: the **wave heights** (in some cases subject to breaking) and the **overtopping**. A convergence analysis has therefore been conducted to evaluate the influence of grid accuracy on wave height (wave transformation in the surf zone) and on wave overtopping. To do this a series of grids and several regular waves have been introduced.

To do so, the Flow3D code is tested with several meshes with different cell sizes using wave profile and volume of wave overtopping as indicators and following the ASME's criteria (Celik et al., 2008).

Both rectangular (non-uniform) and square grids (uniform) have been employed. The mesh cell sizes employed are indicated in the following

paragraph, the global refinement ratio being 5, well above the recommended minimum value of 1.3 (Celik et al., 2008).
This study is conducted on a real case study also analysed in laboratory. Further detail on geometry and laboratory arrangements has been shown in the follow paragraph.

4.2 CASE STUDY – EXPERIMENTAL CAMPAIGN

La Habana, capital of the Republic of Cuba, extends on an area of 740 Km^2, with a population of over 2 million people.
The northern part of the city centre is protected from the wave action by a vertical seawall, the Malecòn (Figure 4.2.1).
However, climate change has caused both the frequency and magnitude of more severe weather events to increase, causing more and more frequent Malecón overflow events. For this reason, the Cuban Government has long been looking for a solution which reduces the risk of flooding and respects the enormous value of the site.

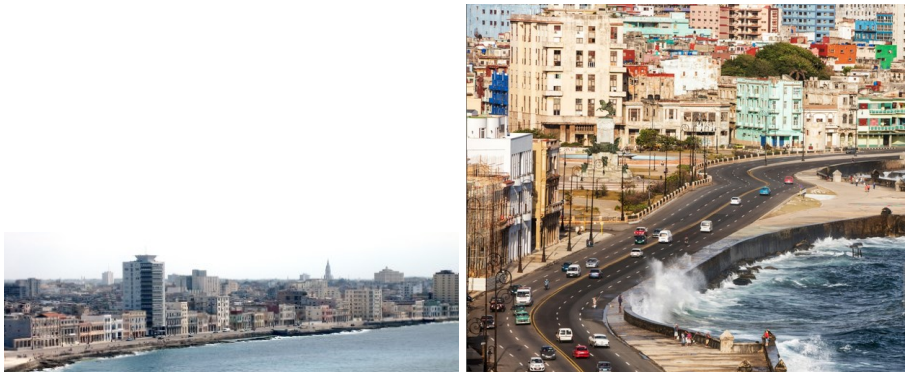

Figure 4.2.1 Malecòn Traditional Cuba.

In particular, at the beginning of 2013, scientists and engineers of the Centro de Investigaciones Hydraulicàs (CiH) of the Instituto Superior Politècnico "Jose Antonio Echevarria" have presented a desk study where a number of solutions are considered, including a weak increase of the wall

freeboard, curvature of the outer profile and placement of protective structures, such as berms and detached low-crested breakwaters.
To have a deeper insight on the effect of each solution, a wide physical model study was commissioned to the Consorzio interUniversitario per la previsione e prevenzione dei Grandi RIschi (CUGRI), which joins the Universities of Napoli Federico II and Salerno (Italy).
The experimental campaign and preliminary results of the tests was discussed in *Lopez et al. 2015*.
The tests were aimed to compare the performances of different structural solutions for the reduction of the mean rate of overtopping.
Hereafter, some details about laboratory study are explained on which our numerical study was based.

Facility

1:30 physical model tests have been conducted at the RAndom wave TAnk of the Dept. of Civil, Architectural and Environmental Engineering (DICEA) of the University of Naples "Federico II". The facility is 36m long, 18m wide, 1.2m deep and is provided with 16 independent piston type wavemakers, capable of simulating both regular and irregular wave trains with different angles of propagation and (for random waves) directional spreading. The basin has been partitioned to form a 18.37m x 1.54m channel with concrete walls, where the experiments have been carried out.

The foreshore

A "flat area", 180m long, allows the waves to develop properly prior evolving over the slopes; then, the topography starts from a position corresponding to 18.72m below the MSL to the toe of the Malecón seawall, which is nearly at 1.70m. After a long flat area, the bathymetry encompasses a mild stretch with a 4.1% slope, followed by a step inclined by 1:3 and an upper zone made up on 2 parts with a slope of 8.6% and 6% respectively. The overall length of the slopes is 230m.
At the end of the channel there is the Malecón seawall which is a simple vertical wall with a crest freeboard, R_c, of +3.96m relative to the MWL.

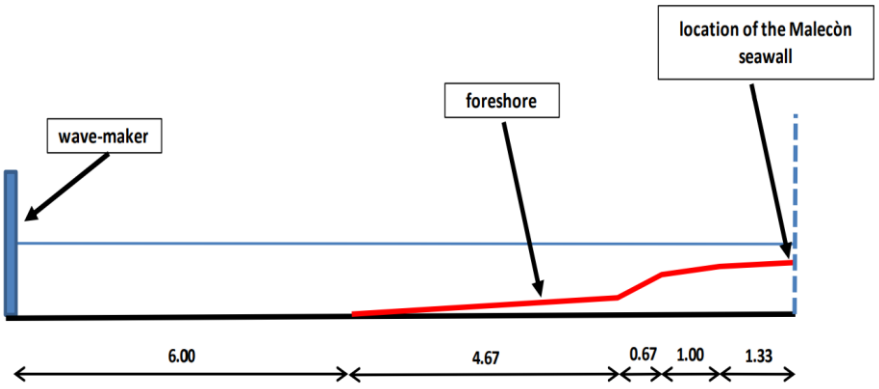

Figure 4.2.2 View of experimental tank and foreshore (Lopez et al. 2015).

Wave conditions

A rise of the mean sea level associated with 50 years return period storm has been considered (S). For this value of the still water depth, 8 JONSWAP driven random sea states have been run, with a duration of 1000 waves. 4 values of the spectral significant wave height at the paddle have been used, with two peak periods as shown in Table 4.2.1.

Table 4.2.1 Laboratory wave conditions.

Test	Hs (m)	Tp (s)	S (m)
9	2.7	12	1.73
10	4.0	12	1.73
11	5.4	12	1.73
12	6.5	12	1.73
13	2.7	10	1.73
14	4.0	10	1.73
15	5.4	10	1.73
16	6.5	10	1.73

The experimental campaign on Malecòn Seawall represents the starting point on which to base numerical investigation. Furthermore, the

laboratory results are fundamental to validate the numerical results and to compare with other tools available for the evaluation of overtopping.

The laboratory experiments however only provide the mean overtopping discharge (maximum overtopping volume Vmax is not provided) and the results have been reported in the follow from time to time, for the comparison with CFD results.

4.2.1 Details about grid constructions

In CFD, one of the most basic approximations lies in the type of cells used for the simulation.
Once a meshing decision is made, it affects not only the types, number, orientation, and placement of grid elements, but also simulation stability, convergence, and accuracy.
The basic assumption to define the grid dimension along the wave direction is based on points numbers of wavelength defined as:

$$Lmin = T\sqrt{gh} \tag{40}$$

Aspect ratio, i.e. the ratio between cell length and height, is a measure of the stretching of the cell. For highly anisotropic flows, extreme aspect ratios may yield accurate results with fewer cells. However, a general rule of thumb is to avoid aspect ratios more than 3.

In detail three value of wavelength has been used in the study, a value of wavelength obtained for two period used and a minimum value of wavelength in numerical domain calculated at wall.

Table 4.2.2 Value of wavelength used for grid definition.

L(T=10s) (m)	58.00
L(T=12s) (m)	69.61
$L/2_{min,seawall}$ (m)	34.80 ≈ 40

To examine the convergence of the solution on different computational grids, a mesh refinement study has been undertaken.
The 2Dimensional domain is discretized with "structured grid"; the basic assumption of discretization is the relaxion with wavelength. Three stages of grid refinement are involved in this study.

- *Grid refinement analysis Level_1*

In the first step the grids have been defined as function of wavelength; two values of L for two different period analysed 10 and 12 seconds, respectively. Δz, on the other hand has been defined as function of maximum ratio between mesh size in x and z direction. Maximum ratio has been fixed as 2.5 to ensure numerical stability (Table 4.2.3 and Table 4.2.4).

Table 4.2.3 Grid dimensions and characteristics for T=10s.

L(m) T(10s)]	Grid type	Δx (m)	Δz (m)	n.cells (x_{dir})	n.cells (z_{dir})	Total cells
58.00	A20	2.9	**1.2**	141	30	4254
	A30	1.9	**0.8**	212	45	9572
	A40	1.5	**0.6**	282	60	17017
	A60	1.0	**0.4**	423	91	38289
	A80	0.7	**0.3**	564	121	68069
	A160	0.4	**0.15**	1128	241	272275

The representation of different grids for wave period T=10s is shown in Figure 4.2.3.

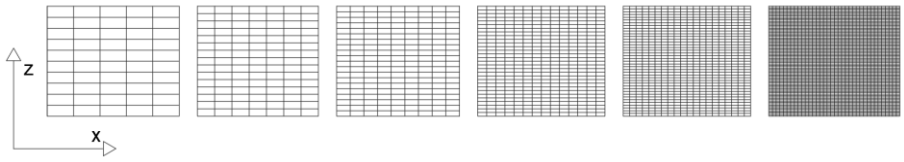

Figure 4.2.3 Non-uniform grid in X and Z directions (T=10s).

Also, the characteristics of grids related to wave period 12 s are summarized in the follow table.

Table 4.2.4 Grid dimensions and characteristics for T=12s.

L(m) [T(12s)]	Grid type	Δx (m)	Δz (m)	n.cells (x_{dir})	n.cells (z_{dir})	Total cells
69.61	B20	3.5	**1.4**	118	25	2954
	B30	2.3	**0.9**	176	38	6647
	B40	1.7	**0.7**	235	50	11818
	B60	1.2	**0.5**	353	75	26589
	B80	0.9	**0.35**	470	101	47270
	B160	0.4	**0.17**	940	201	189080

The graphic representation of different grids of wave period T=12s has been reported in the follow figure.

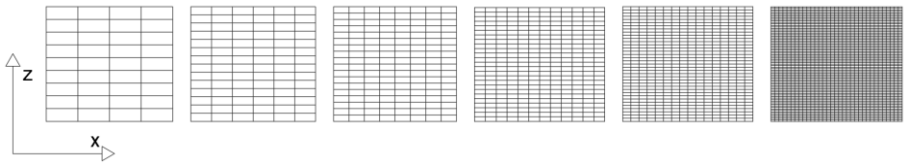

Figure 4.2.4 Non-uniform grid in X and Z directions (T=12s).

- *Grid refinement analysis Level_2*

In the second step the grid refinement is in one of the 2 directions. Δx has been fixed as defined in the previous step as function of wave length but of minimum value of wavelength in the experiments ($L_{min,seawall}$) and one-directional refinement normal to flow direction has been conducted.

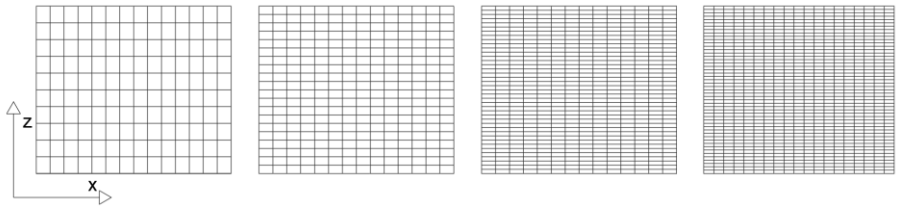

Figure 4.2.5 Non-uniform refinement in Z direction.

The characteristics of grids related to Level_2 of grid refinement are summarized in the follow table.

Table 4.2.5 Dimensions and characteristics of Level_2 of grid refinement.

Grid type	Δx (m)	Δz (m)	n.cells (x_{dir})	n.cells (z_{dir})	Total cells
Coarse C278	0.25	0.30	1640	117	191333
Medium M278	0.25	0.15	1640	233	382667
Fine F278	0.25	0.08	1640	438	717500

- *Grid refinement analysis Level_3*

The final refinement method is uniform, in this case four grid has been selected with all cells refined equally in all directions, with finest and coarsest grids shown in Figure 4.2.6.

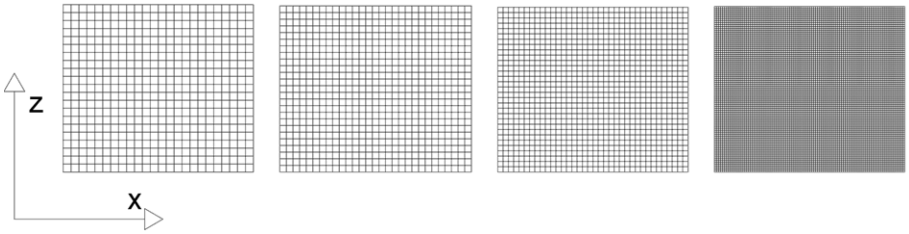

Figure 4.2.6 Uniform refinement in X and Z directions.

The specific details about grids of Level_3 of grid refinement are summarized in the Table 4.2.6

Table 4.2.6 Dimensions and characteristics of Level_3 of grid refinement.

Grid type	Δx (m)	Δz (m)	n.cells (x_{dir})	n.cells (z_{dir})	Total cells
Q1	0.15	0.15	2735	233	637255
Q2	0.4	0.4	1027	87	89349
Q3	0.5	0.5	822	70	57540
Q4	0.6	0.6	685	58	39730

4.2.1 Wave condition

In all simulations a rise of the mean sea level at the entry of the simulation domain (18.72m in calm water) has been considered that is associated with 50 years return period storm surge (Table 4.2.7) so the still water level was fixed at 20.45m for all the tests.

Table 4.2.7. Setup of sea level.

Scenario	Storm surge [m]	Tide [m]	Climatic change [m]	Total [m]
50 years	1.06	0.40	0.27	1.73

The simulations are carried out with regular input waves, thus highlighting hydrodynamic aspects that could be hidden when using random wave trains.

The wave conditions are summarized in the follow table:

Table 4.2.8. Wave condition of grid sensitivity study.

SCENARIO T_R=50 YEARS			
ID SIM	**DEPTH (m)**	**H (m)**	**T(s)**
TEST1	**20.45**	**8.00**	**10.00**
TEST2	**20.45**	**8.00**	**12.00**
TEST3	**20.45**	**1.50**	**10.00**
TEST4	**20.45**	**1.50**	**12.00**

Each sea state has been run for approximately 40 waves.

Numerical waves have been generated using the Stokes and cnoidal wave generator available in FLOW-3D. The waves were determined by the specification of the wave period, T, wave height, H, and local still water depth, d.

Cnoidal wave is a nonlinear oscillatory wave in shallow water, which has sharper crests and flatter troughs than a Stokes wave. In FLOW - 3D, it is generated using Fenton's Fourier series method (Fenton 1999).

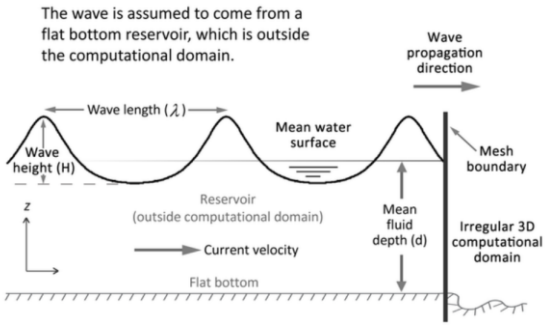

Figure 4.2.7 Stokes and Cnoidal wave definition (Flow3D Manual).

The wave conditions to be simulated, have been reported on the diagram of applicability ranges of various wave theories.

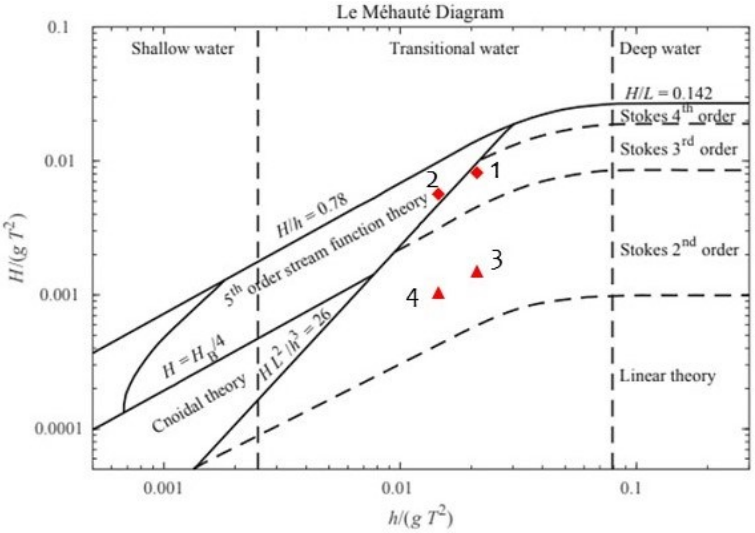

Figure 4.2.8 Diagram of wave theories (Le Méhauté, 1976).

In order to prevent the problem of fluid accumulation through the wave boundary, the code provides a default option that eliminates the net volume influx through the wave boundary.

4.2.2 Numerical framework

A 2D-numerical wave flume was set up to carry out the numerical simulation. The geometry was generated using AutoCAD, based on the dimensions of the physical model; it was then imported into the code as an STL file. In the computational domain (410 m in the x direction and 40 m in the z direction) have only general mesh block which represents the area where the fluid is flowing.
The profile of the sea bottom (Figure 4.2.9) has been reproduced at full-scale with the same characteristic of laboratory experiments (paragraph 4.2)

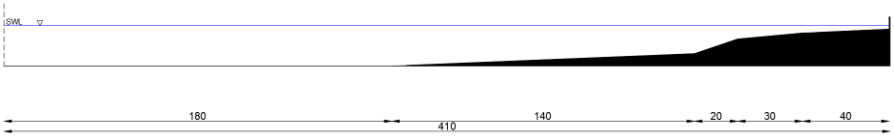

Figure 4.2.9. Characteristic of beach profile - prototype scale.

- *Boundary and initial conditions*

Setting the appropriate boundary condition is important to describe a real problem trough numerical method, reducing error and computational effort.
Offshore, the incident waves are sent to the computation domain by wave generator at boundary condition.

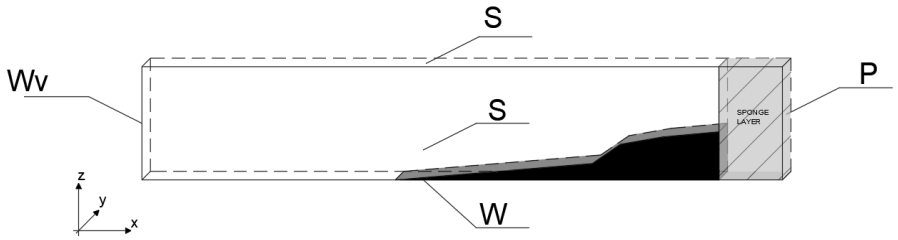

Figure 4.2.10 Boundary condition of 2D-numerical domain without seawall for analysis of wave transformation in the surf zone.

In Figure 4.2.10 boundary regions have been shown in where "S" representing symmetry, "WV" representing wave generation system, "W" standing for wall and "P" shows pressure condition that allows fluid to

outflow but with specific distribution (elevation), this is necessary to keep constant fluid level in the flume.

The figure below, however, shows the boundary conditions applied in the second part of the study, in which the seawall has been considered at the end of the numerical domain.

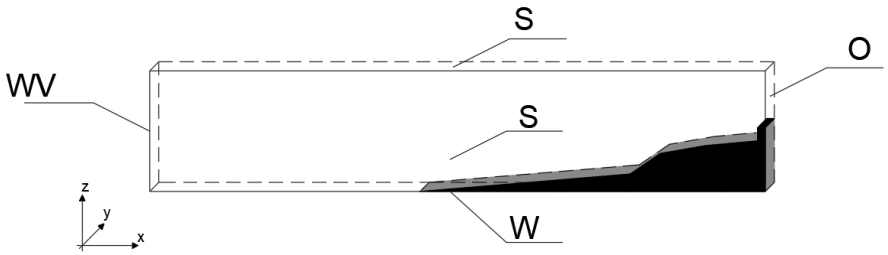

Figure 4.2.11 boundary condition of 2D-numerical domain with seawall to evaluate wave overtopping.

The only difference in this case is represented by the "O" that shows outflow boundary without a specific fluid elevation.
At boundary "Wv", a surface wave enters the computational domain and propagates in the direction normal to the boundary. At the opposite side, rear the structure, an 'outflow' condition has been imposed, which let the waves to flow out the computational domain without any reflections.
In all simulations conducted in this study, initial fluid elevation was specified with hydrostatic pressure.

- *Temporal discretization*

To choose an appropriate sampling time for the inflow input to avoid excessive approximations on the boundary conditions in the simulation.
The sampling frequency was set at 2 Hz, according to Nyquist condition:

$$f_{NY} = \frac{1}{2\,\Delta t} > f_{max} \tag{41}$$

Where f_{NY} is Nyquist frequency, Δt the sampling interval (set to 0.5s), f_{max} spectral peck frequency.

Table 4.2.9 Parameters of temporal discretization

T	$f_P=1/T$	ΔT (s)	fc (Hz)	F_{NY}
10	0.10	0.5	2	1
12	0.08	0.5	2	1

- *Numerical Implementation*

For computational mesh, FLOW3D adopted a structured grid system with a FAVOR (Fractional Area/Volume Obstacle Representation) scheme. The FAVOR scheme is capable of very efficient and flexible grid generation only with CAD files.
Fluid properties were set by loading through a Fluids Database those of water at 20°C. Turbulence was simulated using RNG model, but a further study on the other turbulence models will be shown below.

Table 4.2.10. General Parameter settings in convergence study

Parameter	Setting
Fluid	Water (20°C), incompressible
Turbulence	RNG
Pressure Solver	GMRES
VOF advection	Split Lagrangian method (TruVof)
Time step control	Automatic (stability and convergence)

4.3 ANALYSIS OF WAVE TRANSFORMATION IN THE SURF ZONE

When a wave train propagates from deep water into shallow water region, the wave profile becomes steeper and eventually breaks at a certain depth. Wave breaking is the most interesting phenomenon of the wave transformation in the nearshore region.

The numerical scheme analyzed in this part is presented in the Figure 4.3.1 and the setting parameters of numerical model have been discussed in the previous paragraph.

Figure 4.3.1 2D-Numerical layout of beach profile

Each model tests were also run without the sea wall (calibration runs) to check the wave conditions without reflections. For this purpose, a sponge layer was added at the end of the numerical domain (for further details see section 3.4).
For the analysis, objective of this paragraph, two sections have been considered in the numerical flume. In these sections the follows parameters have been estimated.

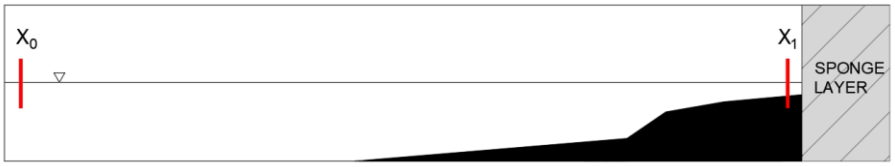

Figure 4.3.2 Section to wave measure in 2D-Numerical layout of beach profile

- X_0 standing for a section close to boundary wave maker also indicates as "nearshore".
- X_1 standing for a section close to position of the wall that is absent is this part of the study. This position is also indicated as "inshore".

Therefore, in the follow the symbol X_0 and X_1 is have been used to point out the two sections where the statistical parameters of the wave motion and the statistics of the wave profile will be evaluated.

Wave Statistics parameters

Mean Wave Height

The mean wave height is the simplest statistical parameters to define. It is found in the usual way as:

$$H_m = \frac{1}{N}\sum_{j=1}^{N} H_j \tag{42}$$

Significant Wave Height

The most widely used statistical wave height for a short-term wave record is the so-called significant height, denoted as either Hs or as $H_{1/3}$ or as H_{33}. The significant wave height is defined as the mean or average of the largest one-third of the waves in the wave record, hence the notation $H_{1/3}$ or H_{33} symbolizing the average of the largest 33% of the waves in the record.

$$H_s = \frac{1}{N/3}\sum_{j=1}^{N/3} H_j \tag{43}$$

One-Tenth Highest Wave

Another widely used descriptor of the short-term wave statistics is the One-Tenth Highest wave, denoted as $H_{1/10}$ or as H_{10}. Again, this symbolizes the average of the one-tenth (or ten percent) largest waves in the wave record.

$$H_{1/10} = \frac{1}{N/10}\sum_{j=1}^{N/10} H_j \tag{44}$$

Statistical indicators

In statistics the "moments" are parameters that characterize the distribution. Let us now use the first three moments around the mean.

The moment (m) of order k with respect to a point c (origin) is defined as the average of the k-th power of the deviation from point c and is therefore equal to:

$$m_k = \frac{\sum(x_i - c)^k}{n} \tag{45}$$

It is called "central moment" when the point is the mean μ.

- The central moment of order 1 (k = 1) is the sum of the deviations from the mean, so it is equal to 0.
- The central moment of order 2 (k = 2) is the variance or standard deviation.
- The odd-order central moments (m3, m5, ...) are used for symmetry indices.

The first order moment (mean) indicates the central tendency of the observations. It is the sum of the products of observations and their probabilities of occurrence, the average value.

$$m_1 = m = \frac{\sum_{i=1}^{N}(x_i - \mu)}{N} \tag{46}$$

The first central moment is zero when defined with reference to the mean, so that centered moments may in effect be used to "correct" for a non-zero mean.

Second Central Moment (Variance): Spread of the observations from the average value i.e., the squared deviation of the variable from its mean. Defined the variance as follow:

$$\sigma^2 = \frac{\sum_{i=1}^{N}(x_i - \mu)^2}{N} \tag{47}$$

The square root of the variance is known as the *standard deviation* and has the advantage of having the same unit of measurement as the observed quantity:

$$m_2 = \sigma = \sqrt{\frac{\sum_{i=1}^{N}(x_i - \mu)^2}{N}} \tag{48}$$

Since "root mean square" standard deviation σ is the square root of the variance, it is also considered a "second moment" quantity.
Third Standardized Moment (*Skewness*) gives an idea of the symmetry of the probability distribution around the mean and is given by:

$$m_3 = s = \frac{\sum_{i=1}^{N}(x_i - \mu)^3}{N} \tag{49}$$

4.3.1 Breaking wave analysis

Mesh convergence was assessed in order to determine the independence of the results.
As an ocean swell propagates out of deep water and into shallow water environments, the waves will undergo transformations through the effects of refraction, diffraction, and/or shoaling until the wave becomes unstable. The most important aspect of this wave transformation process occurs when the wave reaches a critical height, overturns on itself and breaks.
In the follow breaking wave tests for rectangular and square grid are analysed in detail.

Test 1 with rectangular grid

The Figure 4.3.3(a) shows the crests and trough envelope; the Figure 4.3.3(b) wave set-up across the flume, as a function of the x to wavelength ratio.

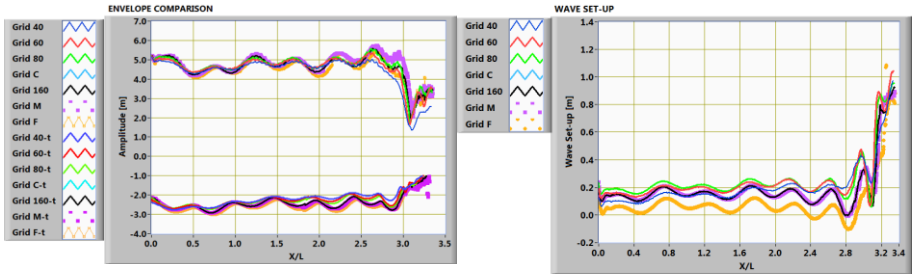

(a) **(b)**

Figure 4.3.3 comparison of all rectangular grid for Test 1: (a) envelope, (b) wave set-up

Wave breaking is occurring at the abscissa 3.3. The strange behaviour of the finer grid is also observed; tend to produce spikes corresponding to high waves in the nearshore.
The Figure 4.3.3(b) reports the wave-set up, which tends to increase in the surf zone reaching nearly 1.0m at the wall. The finer grid gives the maximum set-up.
A fluctuation of the water heigh around the initial value can be observed (Figure 4.3.3b). The fluctuation is probably due to reflection at outflow boundary.

- Wave PROFILE at X_0

Wave profile at X_0 is rather consistent among the grids. This is shown in the Figure 4.3.4.

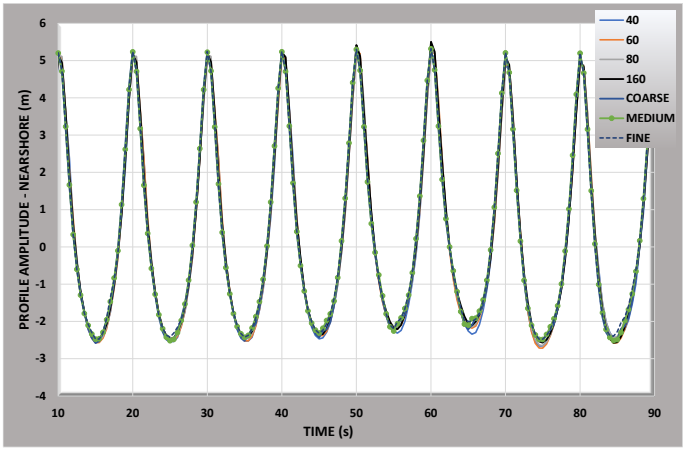

Figure 4.3.4 Numerical surface elevation η as function of time at X_0 (Test 1 H=8m T=10s)

Wave profile characteristics are analyzed via both the first 3 moments (mean, st.dev, skewness) and zero-crossing wave heights. Values are reported below.

Table 4.3.1 Wave heights statistics at at X_0 (TEST 1)

TEST1				
ID_{grid}	**H_{MEAN_N} [m]**	**$H_{(1/3)\_N}$ [m]**	**$H_{(1/10)\_N}$ [m]**	**$H_{(MAX)\_N}$ [m]**
A40	7.60	7.70	7.80	7.80
A60	7.60	7.80	7.90	7.90
A80	7.60	7.70	7.80	7.80
A160	7.60	7.80	7.90	7.90
Coarse	7.40	7.80	7.90	7.90
Medium	7.50	7.70	7.80	7.80
Fine	7.50	8.10	8.70	8.80

The results are stable across the different grids, same holds for profile statistics.

Table 4.3.2 profile statistics at X_0 (TEST 1)

TEST_1			
ID_{grid}	**Mean**	**St.dev**	**Skewness**
A40	0.12	2.5	0.74
A60	0.19	2.5	0.74
A80	0.23	2.5	0.74
A160	0.20	2.5	0.75
Coarse	0.20	2.5	0.75
Medium	0.24	2.4	0.76
Fine	0.19	2.5	0.71

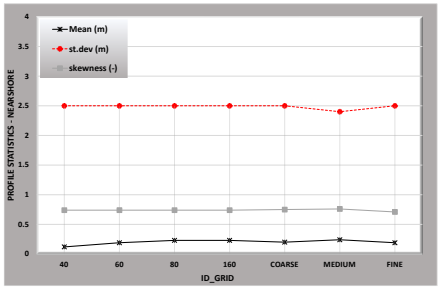

The skewness parameter will equal zero for linear waves but will become positive when the crests steepen, and the troughs become flatter. The results are consistent with the cnoidal wave theory used for the generation in the present study.

- Wave PROFILE at X_1

Wave profile at X_1 shows greater variability among the grids. This is shown in the Figure 4.3.5 a small phase lag between profiles.

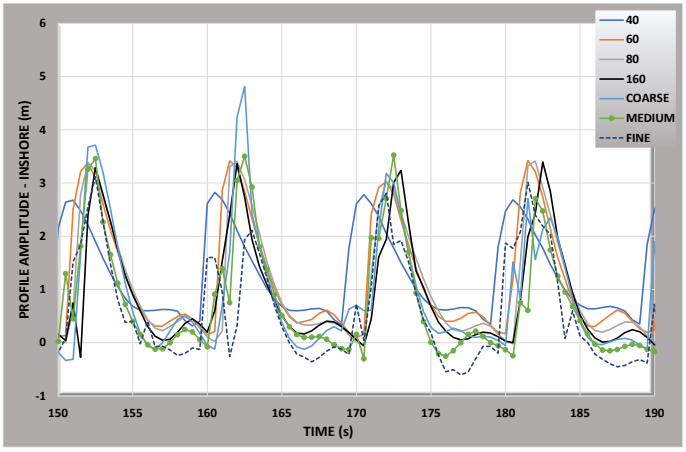

Figure 4.3.5 Numerical surface elevation η as function of time at X_1 for Test 1: H=8m T=10s

Profiles at "the wall" exhibit an intense variation as the results in Table 4.3.3 also show; unexpected no rigorous convergence has been observed. The second observation about the finest grid not resulting in the most or least water height of the seven grid sizes is of more concern.

Table 4.3.3 Wave heights statistics at X_1 (TEST 1)

TEST1				
ID_{grid}	H_{MEAN_i} [m]	$H_{(1/3)\_i}$ [m]	$H_{(1/10)\_i}$ [m]	$H_{(MAX)\_i}$ [m]
A40	2.35	2.73	3.31	3.53
A60	3.15	3.55	3.65	3.66
A80	3.16	3.65	3.81	3.84
A160	3.08	3.70	3.83	3.85
Coarse	2.94	4.22	4.67	4.85
Medium	3.42	4.42	4.75	4.94
Fine	3.31	4.06	4.30	4.52

The skewness value shows how the wave become non-linear due to breaking process.

Table 4.3.4 profile statistics at X_1 (TEST 1)

TEST_1			
ID_{grid}	Mean	St.dev	Skewness
A40	1.01	0.85	0.81
A60	1.04	1.06	1.11
A80	0.96	0.99	1.25
A160	0.93	1.05	1.60
Coarse	0.93	1.04	1.31
Medium	0.90	1.03	1.61
Fine	0.83	1.16	1.40

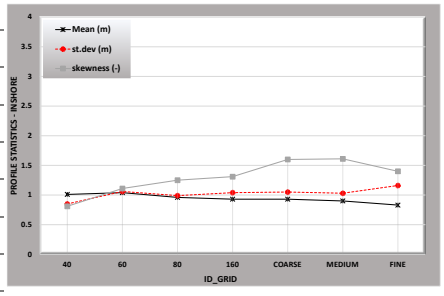

TEST 2 with rectangular grid

The Figure 4.3.6(a) and Figure 4.3.7(a) show the crests and trough envelope and Figure 4.3.6(b) and Figure 4.3.7(b) wave set-up across the flume, as a function of the x to wavelength ratio.

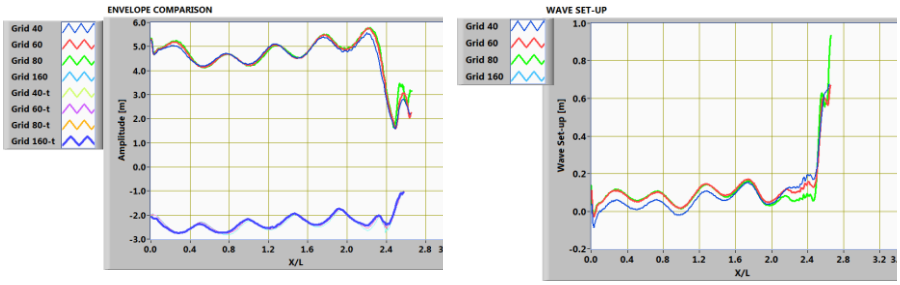

(a) **(b)**

Figure 4.3.6 comparison of grid Level_1 for Test 1: (a) envelope, (b) wave set-up

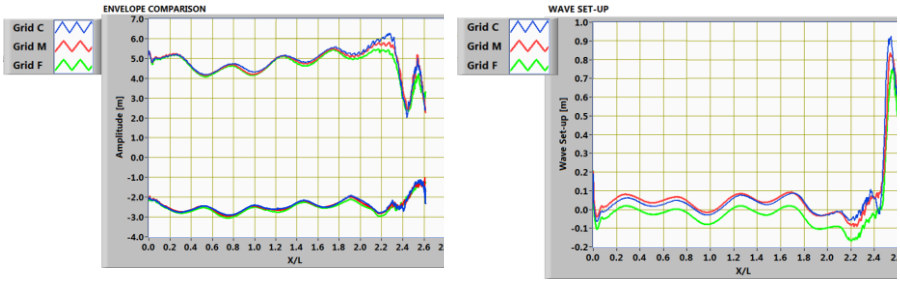

(a) **(b)**

Figure 4.3.7 comparison of grid Level_2 for Test 1: (a) envelope, (b) wave set-up

There is no convergence around the breaking point. It is possible to recognize an effect on wave reforming and re-breaking as shown in the follow figures.

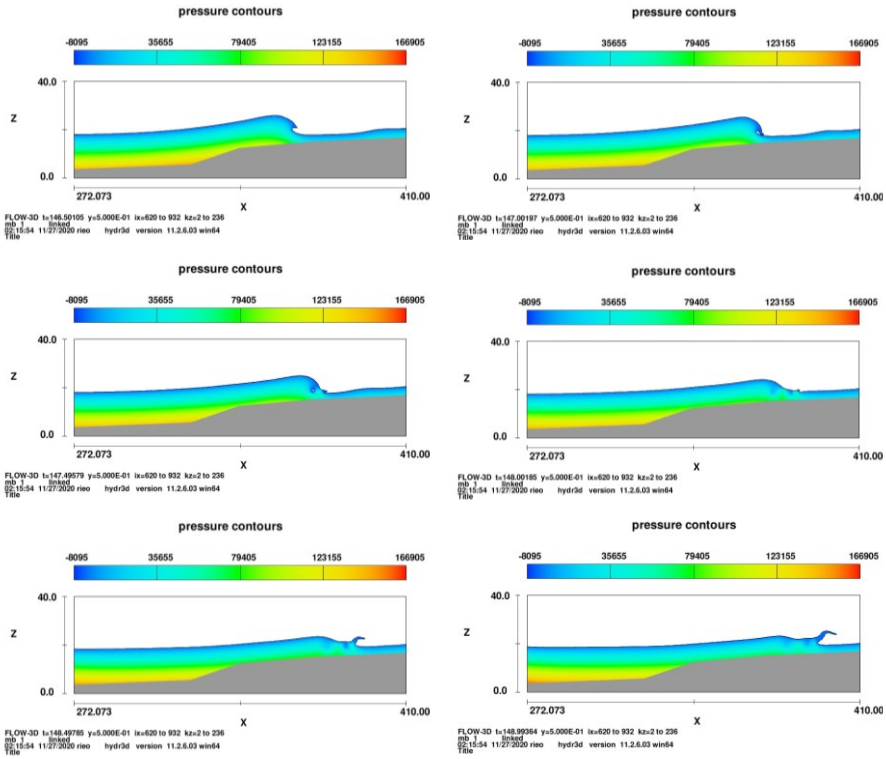

Figure 4.3.8 Example of wave breaking and reforming process.

- Wave PROFILE at X_0

Wave profile at X_0 is rather consistent among the grids. This is shown in the Figure 4.3.9 and the relative wave statistics reported in Table 4.3.5.

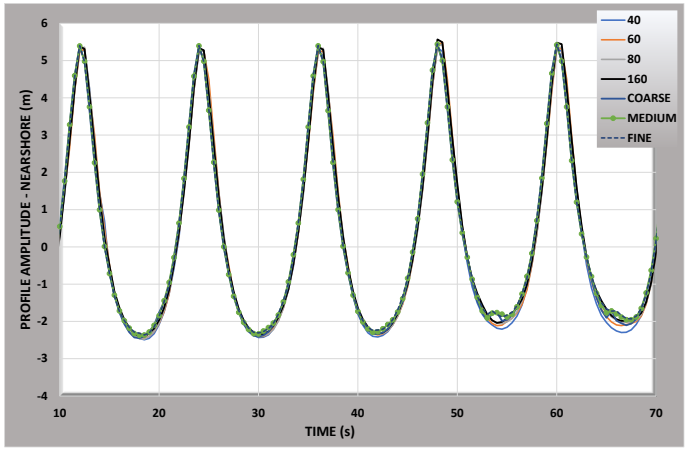

Figure 4.3.9 Numerical surface elevation η as a function of time at X_0 for Test 2 H=8m T=12s

Zero up-crossing wave characteristics also show good consistency among the grids.

Table 4.3.5 Nearshore wave characteristics (TEST 2)

TEST2				
ID_{grid}	**H_{MEAN_N} [m]**	**$H_{(1/3)\_N}$ [m]**	**$H_{(1/10)\_N}$ [m]**	**$H_{(MAX)\_N}$ [m]**
B40	7.47	7.74	7.83	7.86
B60	7.41	7.65	7.78	7.80
B80	7.36	7.67	7.81	7.84
B160	7.48	7.77	7.84	7.92
Coarse	7.51	7.82	7.92	8.00
Medium	7.49	7.83	7.91	7.92
Fine	7.60	7.95	8.19	8.25

Wave profile statistics also are constant among the grids.

Table 4.3.6 nearshore profile statistics (TEST 2)

TEST_2			
ID_{grid}	**Mean**	**St.dev**	**Skewness**
A40	0.04	2.47	0.90
A60	0.11	2.44	0.92
A80	0.05	2.38	0.99
A160	0.05	2.43	0.94
Coarse	0.02	2.46	0.91
Medium	0.04	2.45	0.92
Fine	-0.01	2.48	0.91

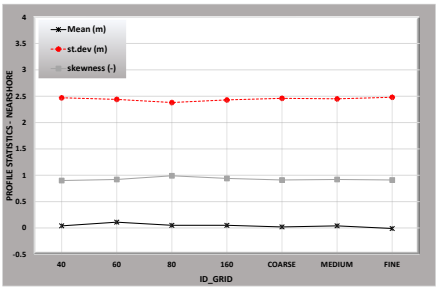

- Wave PROFILE at X_1

Wave profile at X_1 exhibit a much intense variation; no rigorous convergence has been observed. The finer grid produce spike.

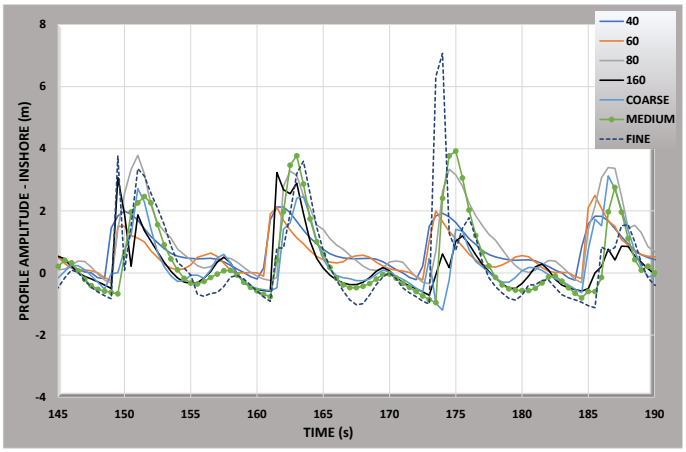

Figure 4.3.10 Numerical surface elevation η as a function of time at X_1 for Test 2: H=8m T=12s

Table 4.3.7 inshore wave heights statistics (TEST 2)

TEST2				
ID_{grid}	H_{MEAN_i} [m]	$H_{(1/3)\_i}$ [m]	$H_{(1/10)\_i}$ [m]	$H_{(MAX)\_i}$ [m]
B40	1.85	2.45	2.75	3.07
B60	1.92	3.04	3.70	3.94
B80	3.29	3.98	4.06	4.11
B160	2.08	3.28	3.54	3.67
Coarse	2.36	4.35	5.94	6.01
Medium	2.50	3.91	4.53	4.58
Fine	3.00	5.24	7.94	7.99

The variation of finer grid is also shown by the higher value of skewness.

Table 4.3.8 inshore profile statistics (TEST 2)

TEST_2			
ID_{grid}	Mean	St.dev	Skewness
A40	0.71	0.70	0.98
A60	0.75	0.78	1.51
A80	0.97	1.09	1.22
A160	0.59	0.85	1.57
Coarse	0.65	0.96	1.59
Medium	0.58	0.94	1.36
Fine	0.64	1.27	2.15

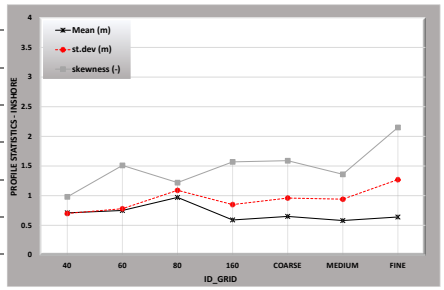

Wave profile statistics exhibit a much intense variation with a peak of the finer grid.

Test 1 with square grid

The analysis is also developed with square grid to evaluate the performance of accuracy.

The Figure 4.3.11 (a) shows the crests and trough envelope and Figure 4.3.11 (b) wave set-up across the flume, as a function of the x to wavelength ratio.

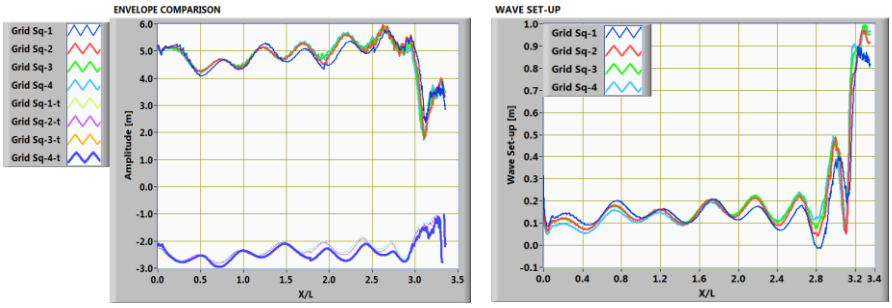

(a) **(b)**

Figure 4.3.11 comparison of grid Level_3 for Test 1 square: (a) envelopee, (b) wave set-up

- Wave PROFILE at X_0

Wave profile at X_0 is rather consistent among the grids. This is shown in the Figure 4.3.12.

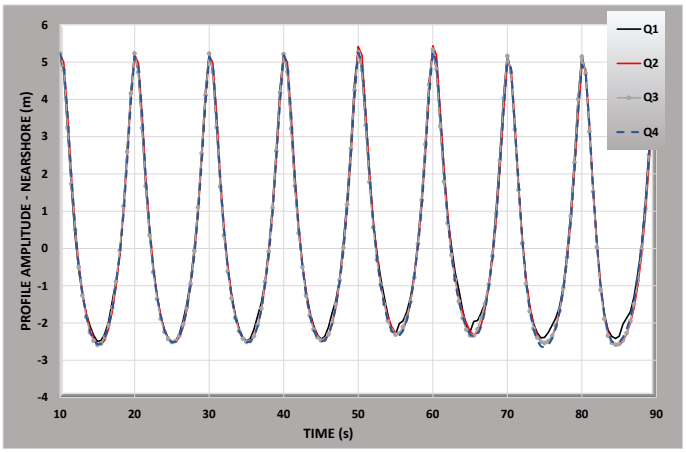

Figure 4.3.12 Numerical surface elevation η as a function of time at X_0 for Test 1_square grid: H=8m T=10s

Zero up-crossing wave characteristics also show good consistency among the grids.

Table 4.3.9 Nearshore wave characteristics (TEST 1_ square grid)

TEST1				
ID_{grid}	H_{MEAN_N} [m]	$H_{(1/3)\_N}$ [m]	$H_{(1/10)\_N}$ [m]	$H_{(MAX)\_N}$ [m]
Q1	7.49	7.75	7.78	7.79
Q2	7.62	7.79	7.81	7.82
Q3	7.62	7.78	7.81	7.81
Q4	7.68	7.81	7.87	7.88

Wave heights statistics also are constant among the grids. Same holds for wave profile statistics.

Table 4.3.10 Nearshore profile statistics (TEST 1_ square grid)

TEST_1_SQUARE GRID			
ID_{grid}	Mean	St.dev	Skewness
Q1	0.19	2.44	0.80
Q2	0.14	2.47	0.79
Q3	0.16	2.48	0.77
Q4	0.14	2.50	0.76

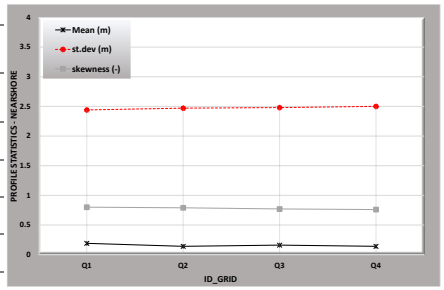

- Wave PROFILE at X_1

Wave profile at X_1 exhibit limited variation; no rigorous convergence has been observed.

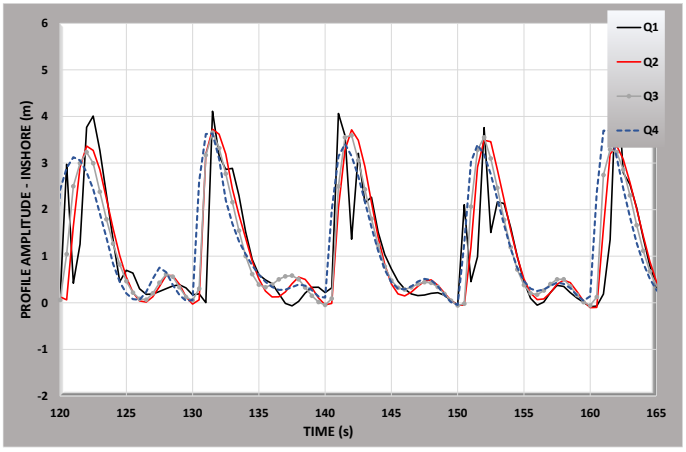

Figure 4.3.13 Numerical surface elevation η as a function of time at X_1 for Test 1_square grid: H=8m T=10s

Table 4.3.11 Inshore wave heights statistics (TEST 1_ square grid)

TEST1				
ID_{grid}	H_{MEAN_i} [m]	$H_{(1/3)\_i}$ [m]	$H_{(1/10)\_i}$ [m]	$H_{(MAX)\_i}$ [m]
Q1	2.84	4.20	4.39	4.44
Q2	3.05	3.71	4.02	4.15
Q3	3.29	3.74	4.02	4.29
Q4	3.29	3.71	4.04	4.37

Wave profile statistics are more consistent among the grid compared to rectangular grid.

Table 4.3.12 Inshore profile statistics (TEST 1_ square grid)

TEST_1_SQUARE GRID			
ID_{grid}	Mean	St.dev	Skewness
Q1	0.82	1.05	1.47
Q2	0.92	1.01	1.32
Q3	0.95	1.04	1.33
Q4	0.97	1.04	1.28

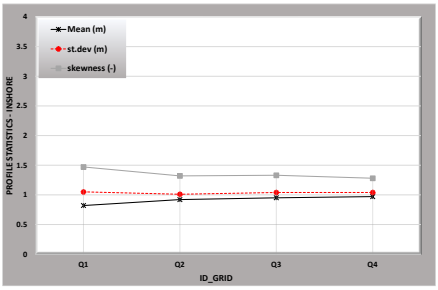

Test 2 with square grid

The analysis is also developed with square grid to evaluate the performance of accuracy.

The Figure 4.3.14(a) shows the crests and trough envelope and Figure 4.3.14 (b) wave set-up across the flume, as a function of the x to wavelength ratio.

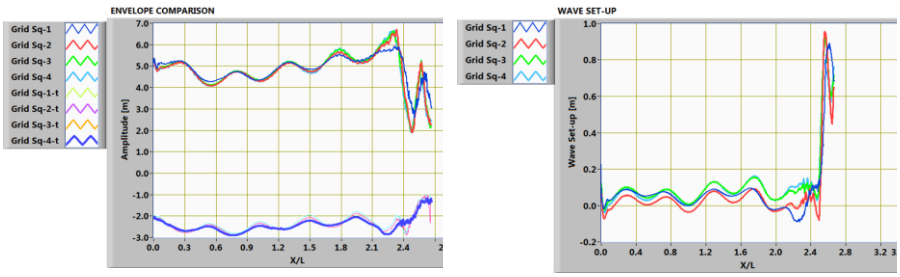

(a) **(b)**

Figure 4.3.14 comparison of grid Level_3 for Test 1 square: (a) envelope, (b) wave set-up

Grid square Sq-1 (finer grid) shows a different upper envelope; some scatter is observed in the wave set up profile.

- Wave PROFILE at X_0

Wave profile at X_0 is rather consistent among the grids. This is shown in the Figure 4.3.15.

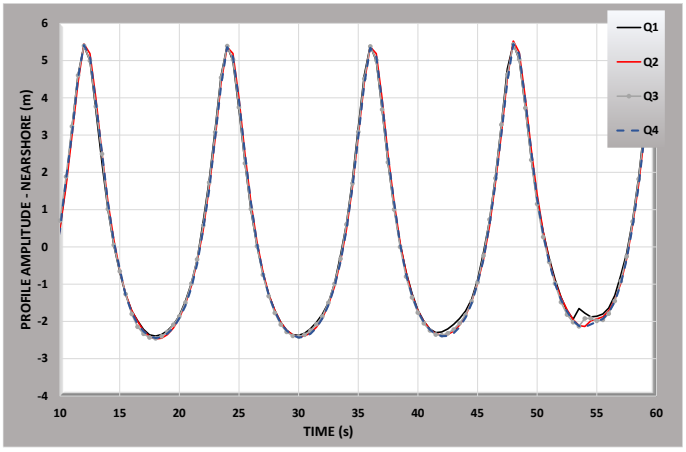

Figure 4.3.15 Numerical surface elevation η as a function of time at X_0 for Test 2_square grid: H=8m T=12s

Zero up-crossing wave characteristics also show good consistency among the grids.

Table 4.3.13 Nearshore wave characteristics (TEST 2_ square grid)

TEST2				
ID_{grid}	H_{MEAN_N} [m]	$H_{(1/3)\_N}$ [m]	$H_{(1/10)\_N}$ [m]	$H_{(MAX)\_N}$ [m]
Q1	7.42	8.00	8.26	8.38
Q2	7.31	7.92	8.06	8.20
Q3	7.54	7.81	7.87	7.87
Q4	7.60	7.84	7.92	8.02

Wave profile statistics are consistent among the grids.

Table 4.3.14 Nearshore profile statistics (TEST 2_ square grid)

TEST_2_SQUARE GRID			
ID_{grid}	Mean	St.dev	Skewness
Q1	0.09	2.48	0.87
Q2	0.04	2.47	0.91
Q3	0.12	2.45	0.90
Q4	0.12	2.45	0.91

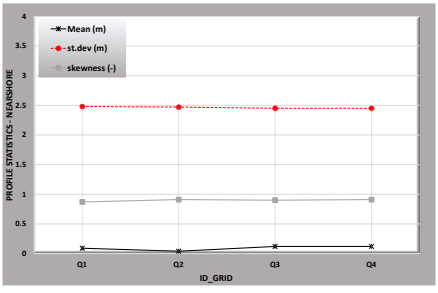

- Wave PROFILE at X_1

Wave profile at X_1 exhibit much intense variation; may be no rigorous convergence has been observed. The results do not show a different behaviour compared to rectangular grid.

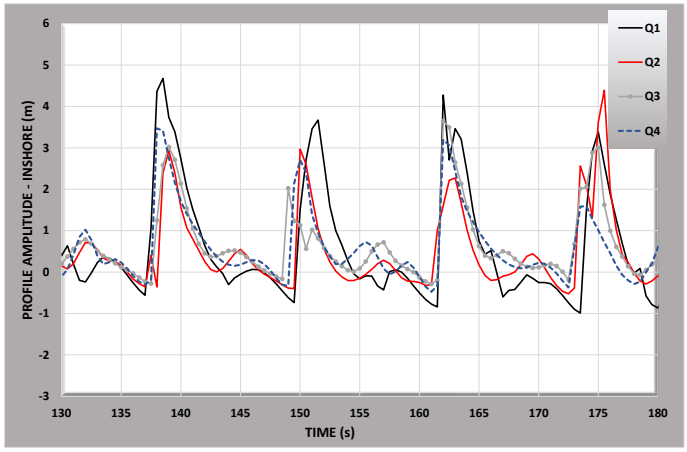

Figure 4.3.4.3 Numerical surface elevation η as a function of time at X_1 for Test 2_square grid: H=8m T=12s

Zero up-crossing wave characteristics show a low variability among the grids.

Table 4.3.15 Inshore wave heights statistics (TEST 2_ square grid)

TEST2				
ID_{grid}	**H_{MEAN_i} [m]**	**$H_{(1/3)\_i}$ [m]**	**$H_{(1/10)\_i}$ [m]**	**$H_{(MAX)\_i}$ [m]**
Q1	3.20	4.93	5.52	5.54
Q2	2.54	3.78	4.47	5.00
Q3	2.28	3.53	4.28	4.29
Q4	2.17	3.88	4.38	4.50

Wave profile statistics are consistent among the grids.

Table 4.3.16 Inshore profile statistics (TEST 2_ square grid)

TEST_2_SQUARE GRID			
ID_{grid}	Mean	St.dev	Skewness
Q1	0.68	1.11	1.47
Q2	0.68	0.88	1.47
Q3	0.75	0.84	1.54
Q4	0.76	0.90	1.78

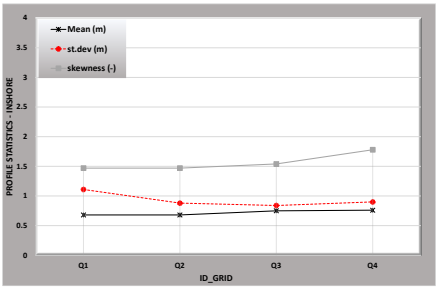

The grid effects do not appear negligible for the wave height evaluated in the section near the wall.
The complicated nonlinear phenomena due to breaking that occurs in the cases just described probably influence the results. The behaviour of finer grid is abnormal and required a further verification.

4.3.2 Non-breaking wave analysis

In this paragraph we discuss about non-breaking wave and their behaviour respect to grid sensitivity study.

Test 3 with rectangular grid

The Figure 4.3.16(a) shows the crests and trough envelope and Figure 4.3.16(b) wave set-up across the flume, as a function of the x to wavelength ratio.

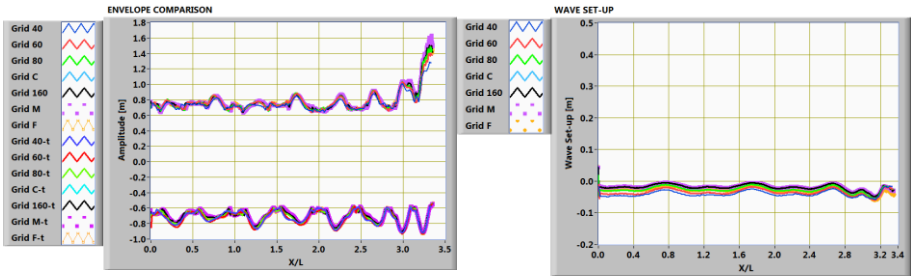

(a) **(b)**

Figure 4.3.16 comparison of all rectangular grid for Test 3: (a) envelope, (b) wave set-up

- Wave PROFILE at X_0

The surface profile generated by the boundary wave maker appear consistence among grids and the wave train appears to be stable in time.

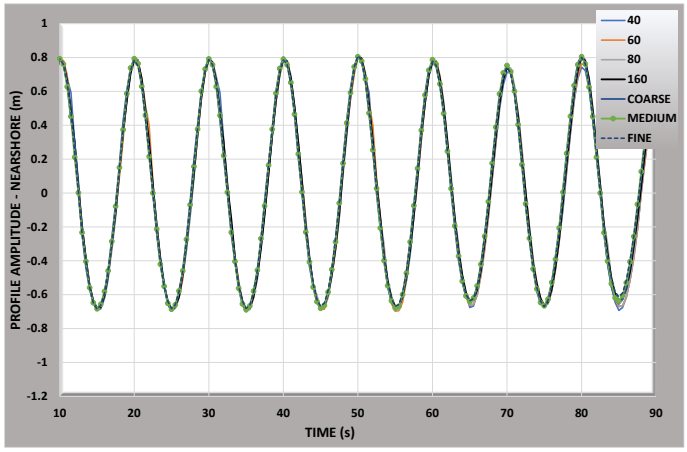

Figure 4.3.17 Numerical surface elevation η as a function of time at X_0 for Test 3_rectangular grid: H=1.5m T=10s

Zero up-crossing wave characteristics also show good consistency among the grids.

Table 4.3.17 nearshore wave characteristics (TEST 3)

TEST3				
ID_{grid}	**H_{MEAN_N} [m]**	**$H_{(1/3)\_N}$ [m]**	**$H_{(1/10)\_N}$ [m]**	**$H_{(MAX)\_N}$ [m]**
A40	1.23	1.49	1.50	1.50
A60	1.17	1.61	1.96	2.40
A80	1.30	1.58	1.79	2.06
A160	1.26	1.48	1.50	1.50
Coarse	1.30	1.48	1.49	1.49
Medium	1.31	1.47	1.48	1.48
Fine	1.31	1.46	1.48	1.48

The results are stable across the different grids, same holds for profile statistics.

Table 4.3.18 nearshore profile statistics (TEST 3)

TEST_3			
ID_{grid}	**Mean**	**St.dev**	**Skewness**
A40	-0.02	0.44	0.33
A60	-0.01	0.44	-0.20
A80	0.02	0.45	0.05
A160	0.04	0.45	0.21
Coarse	0.03	0.45	0.20
Medium	0.04	0.45	0.19
Fine	0.05	0.47	0.14

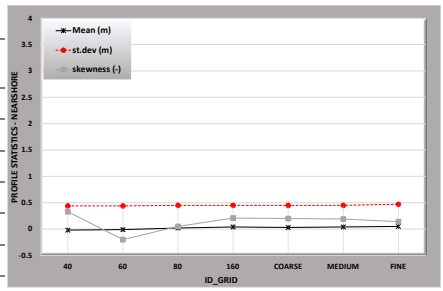

- Wave PROFILE at X_1

Wave profile at X_1 is rather consistent among the grids. This is shown in the Figure 4.3.18

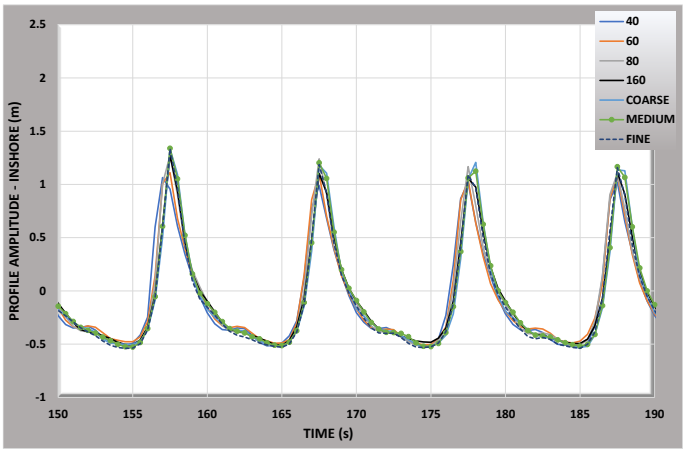

Figure 4.3.18 Numerical surface elevation η as a function of time at X_1 for Test 3_rectangular grid: H=1.5m T=10s

No significant differences between all grids are observed.

Table 4.3.19 inshore wave heights statistics (TEST 3)

TEST3				
ID_{grid}	**H_{MEAN_i} [m]**	**$H_{(1/3)\_i}$ [m]**	**$H_{(1/10)\_i}$ [m]**	**$H_{(MAX)\_i}$ [m]**
A40	1.82	2.11	2.23	2.37
A60	1.84	2.17	2.25	2.33
A80	1.94	2.23	2.29	2.36
A160	1.94	2.26	2.34	2.40
Coarse	1.85	2.20	2.32	2.32
Medium	2.03	2.41	2.55	2.63
Fine	1.91	2.22	2.27	2.28

The results are quite stable across the different grids, same holds for profile statistics.

Table 4.3.20 inshore profile statistics (TEST 3)

TEST_3			
ID_{grid}	**Mean**	**St.dev**	**Skewness**
A40	-0.02	0.49	1.39
A60	-0.02	0.48	1.58
A80	-0.03	0.47	1.78
A160	-0.04	0.46	1.99
Coarse	-0.03	0.46	1.83
Medium	-0.03	0.47	2.05
Fine	-0.04	0.46	1.91

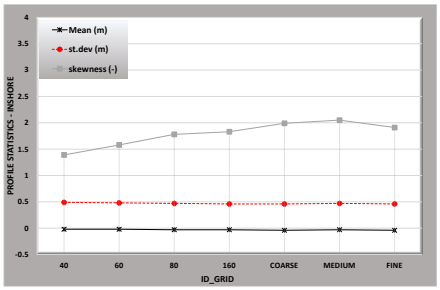

- **Test 4 with rectangular grid**

The Figure 4.3.19(a) and Figure 4.3.20(a) show the signal envelope and Figure 4.3.19 (b) and Figure 4.3.20(b) wave set-up across the flume, as a function of the x to wavelength ratio.

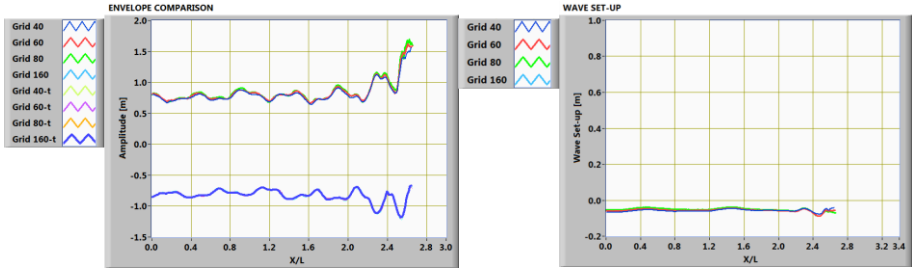

(a) **(b)**

Figure 4.3.19 comparison of grid Level_1 for Test 4: (a) envelope, (b) wave set-up

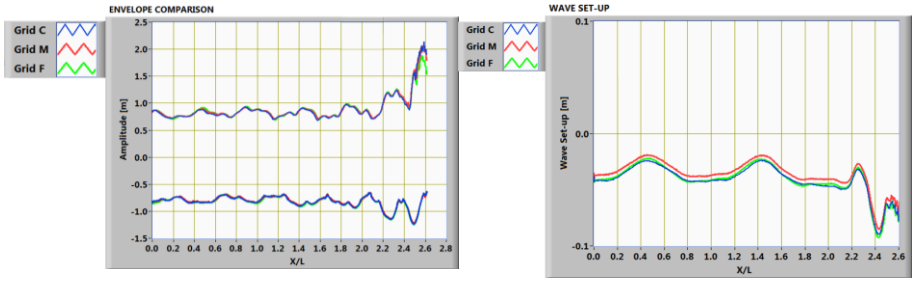

(a) (b)

Figure 4.3.20 comparison of grid Level_2 for Test 4: (a) envelope, (b) wave set-up

The figures show no breaking occurring for this experiment.

- Wave PROFILE at X_0

Wave profile at X_0 is rather consistent among the grids as is shown in the Figure 4.3.21.

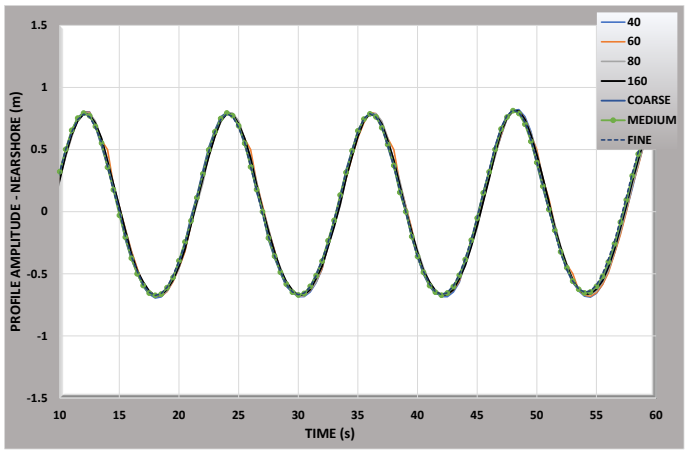

Figure 4.3.21 Numerical surface elevation η as a function of time at X_0 for Test 4 rectangular grid: H=1.5m T=12s

Zero up-crossing wave characteristics also show good consistency among the grids.

Table 4.3.21 nearshore wave characteristics (TEST 4)

TEST4				
ID_{grid}	**H_{MEAN_N} [m]**	**$H_{(1/3)\_N}$ [m]**	**$H_{(1/10)\_N}$ [m]**	**$H_{(MAX)\_N}$ [m]**
A40	1.65	1.85	1.85	1.87
A60	1.66	1.87	1.9	1.91
A80	1.66	1.89	1.92	1.92
A160	1.69	1.95	1.96	1.96
Coarse	1.67	1.90	1.91	1.92
Medium	1.69	1.94	1.96	1.99
Fine	1.72	1.99	2.00	2.01

The wave height statistics are stable among the different grids, same holds for profile statistics.

Table 4.3.22 nearshore profile statistics (TEST 4)

TEST_4			
ID_{grid}	**Mean**	**St.dev**	**Skewness**
A40	-0.07	0.59	0.04
A60	-0.06	0.59	0.05
A80	-0.05	0.59	0.05
A160	-0.05	0.61	0.05
Coarse	-0.04	0.60	0.10
Medium	-0.04	0.60	0.07
Fine	-0.04	0.62	0.02

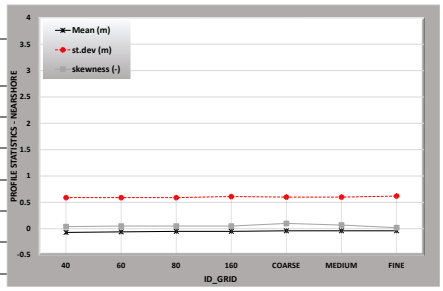

- Wave PROFILE at X_1

Wave profile at X_1 is rather consistent among the grids, as is shown in the Figure 4.3.22.

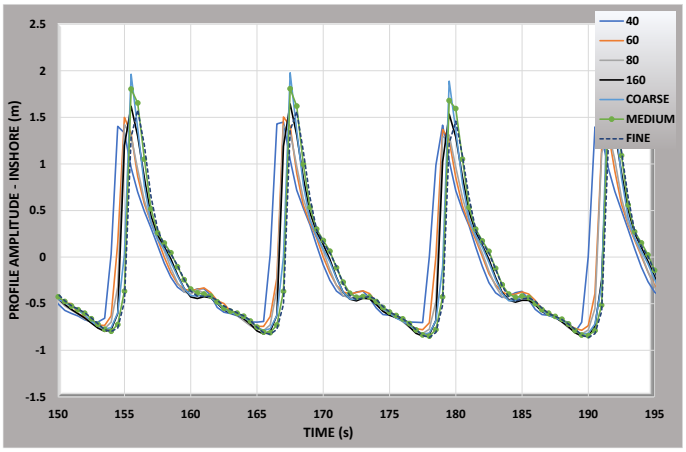

Figure 4.3.22 Numerical surface elevation η as a function of time at X_1 for Test 4 rectangular grid: H=1.5m T=12s

Zero up-crossing wave characteristics also show good consistency among the grids.

Table 4.3.23 inshore wave heights statistics (TEST 4)

TEST4				
ID_{grid}	H_{MEAN_i} [m]	$H_{(1/3)\_i}$ [m]	$H_{(1/10)\_i}$ [m]	$H_{(MAX)\_i}$ [m]
A40	2.12	2.21	2.26	2.26
A60	2.18	2.30	2.34	2.34
A80	2.12	2.23	2.30	2.30
A160	2.19	2.36	2.47	2.47
Coarse	2.28	2.75	2.86	2.86
Medium	2.36	2.55	2.59	2.59
Fine	1.98	2.30	2.40	2.40

The results are quite stable across the different grids, same holds for profile statistics.

Table 4.3.24 inshore profile statistics (TEST 4)

TEST_4			
ID_{grid}	Mean	St.dev	Skewness
A40	-0.04	0.55	1.23
A60	-0.05	0.54	1.36
A80	-0.06	0.52	1.42
A160	-0.07	0.51	1.67
Coarse	-0.05	0.54	2.03
Medium	-0.06	0.52	1.87
Fine	-0.06	0.49	1.64

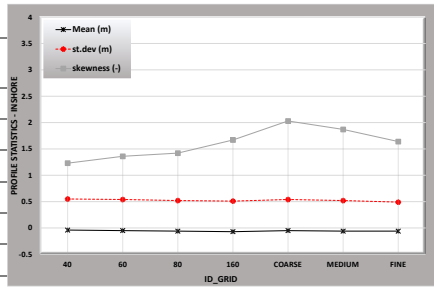

- **Test 4 with square grid**

The Figure 4.3.23(a) show the signal envelope and Figure 4.3.23(b) wave set-up across the flume, as a function of the x to wavelength ratio.

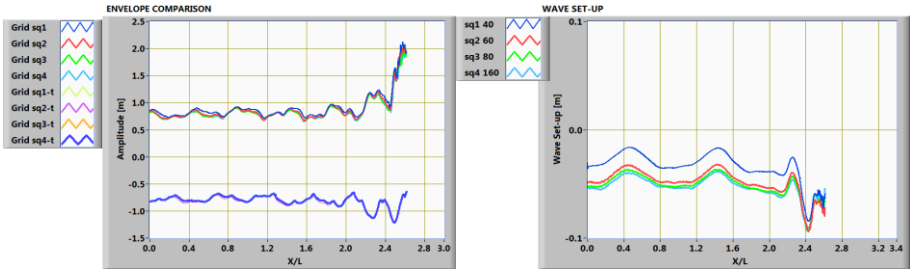

(a) **(b)**

Figure 4.3.23 comparison of grid Level_3 for Test 4: (a) envelope, (b) wave set-up

- Wave PROFILE at X_0

Wave profile at X_0 is rather consistent among the grids. This is shown in the Figure 4.3.24.

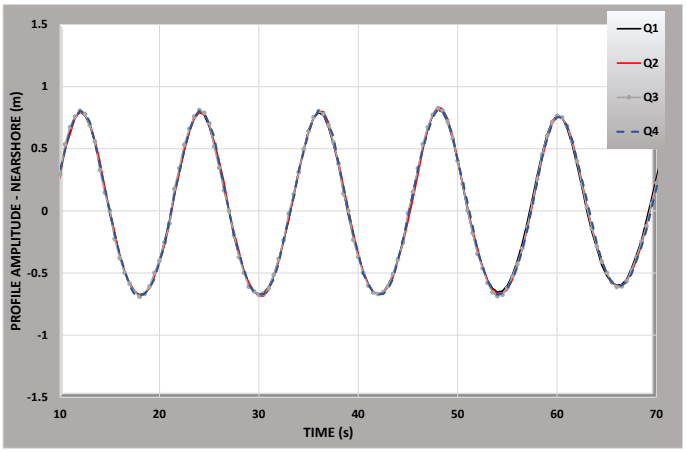

Figure 4.3.24 Numerical surface elevation η as a function of time at X_0 for Test 4 square grid: H=1.5m T=12s

Zero up-crossing wave characteristics also show good consistency among the grids.

Table 4.3.25 Nearshore wave characteristics (TEST 4_ square grid)

TEST4				
ID_{grid}	H_{MEAN_N} [m]	$H_{(1/3)\_N}$ [m]	$H_{(1/10)\_N}$ [m]	$H_{(MAX)\_N}$ [m]
Q1	1.68	1.92	1.94	1.94
Q2	1.67	1.90	1.91	1.91
Q3	1.63	1.84	1.84	1.84
Q4	1.65	1.88	1.90	1.91

The results are stable across the different grids, same holds for profile statistics.

Table 4.3.26 Nearshore profile statistics (TEST 4_ square grid

TEST_4_SQUARE GRID			
ID_{grid}	Mean	St.dev	Skewness
Q1	-0.03	0.60	0.07
Q2	-0.05	0.59	0.09
Q3	-0.05	0.58	0.09
Q4	-0.05	0.59	0.08

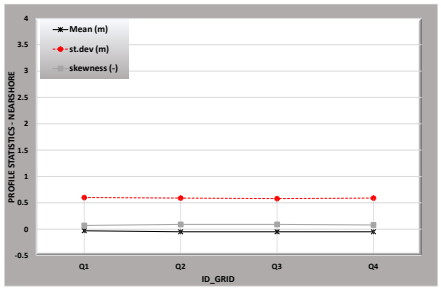

- Wave PROFILE at X_1

Wave profile at X_1 is rather consistent among the grids. This is shown in the Figure 4.3.25.

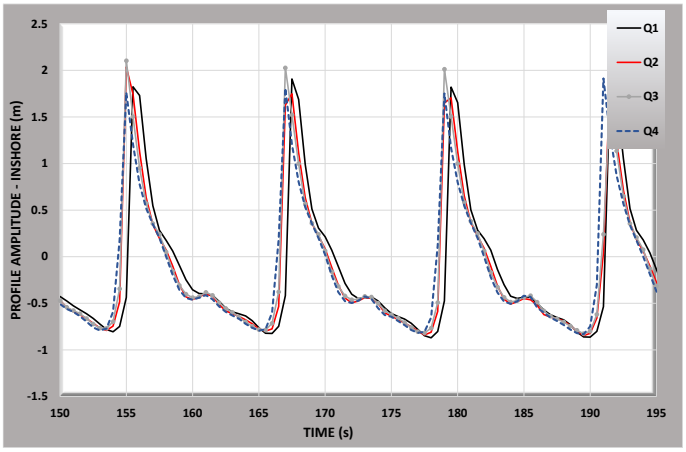

Figure 4.3.25 Numerical surface elevation η as a function of time at X_1 Test 4 square grid: H=1.5m T=12s

Zero up-crossing wave characteristics also show good consistency among the grids.

Table 4.3.27 Inshore wave heights statistics (TEST 4_ square grid)

TEST4				
ID_{grid}	**H_{MEAN_i} [m]**	**$H_{(1/3)\_i}$ [m]**	**$H_{(1/10)\_i}$ [m]**	**$H_{(MAX)\_i}$ [m]**
Q1	2.24	2.46	2.47	2.47
Q2	2.27	2.47	2.50	2.50
Q3	2.25	2.43	2.44	2.44
Q4	2.26	2.44	2.45	2.45

The results are stable across the different grids, same holds for profile statistics.

Table 4.3.28 Inshore profile statistics (TEST 4_ square grid)

TEST_4_SQUARE GRID			
ID_{grid}	**Mean**	**St.dev**	**Skewness**
Q1	-0.03	0.7	0.11
Q2	-0.04	0.7	0.11
Q3	-0.04	0.7	0.10
Q4	-0.05	0.7	0.07

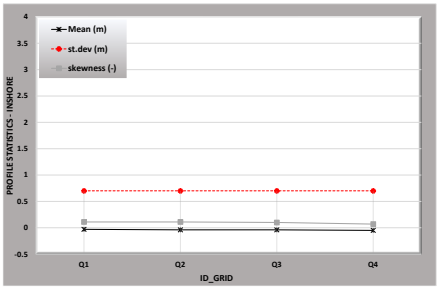

4.3.3 Discuss on results of grid sensitivity related to wave height.

Rectangular grid

The grid dependence on results has been studied trough a regression analysis that use as independent variable the geometric mean of grid dimension (Δx*Δz)^0.5, and as dependent variable has been studied the wave profile statistics(m, σ, s) and the zero up-crossing waves (H_m, $H_{1/3}$). In the follow the mean m will also be referred to as *wave set-up*, the standard deviation σ as *energy*.

For reasons that will be discussed later, the regressions were conducted without the value of finer grid. These often affect the trend as influential point.

The significance level of F-test was set equal to 5% and the results are shown in the Table 4.3.29.

Table 4.3.29 F-Test for rectangular grid

	F- Test(5 % significance level)				
ID_SIM	m	σ	s	H_m	$H_{1/3}$
TEST1	<	-	< ↑	-	< ↑
TEST2	-	-	-	-	-
TEST3	-	< ↓	< ↑	-	-
TEST4	-	-	< ↑	-	-

**Note: arrow represents the slope or the increasing or decreasing trend.*

The results do not indicate a clear grid effect except for "skewness- s". For this reason, it was concluded that the results are grid independent, and fluctuate around the mean value in a random way.

For each of the quantities studied, the coefficient of variation Cv was calculated as:

$$Cv = \frac{st.dev}{\mu}$$
$$Cv = \frac{\max() - \min()}{2} \quad \textit{valid for mean "m" and skewness "s"} \tag{50}$$

The analysis showed that Cv is function of Ursell number calculated as:

$$Ur = \frac{H_n L_p}{h^3} \tag{51}$$

in which H_n is the significant wave height nearshore and L_p is the local wavelength, obtained by the linear dispersion relationship using the peak period T_p, h is the water depth at X_1.

In this way the Ursell number it also considers the breaking of the wave.

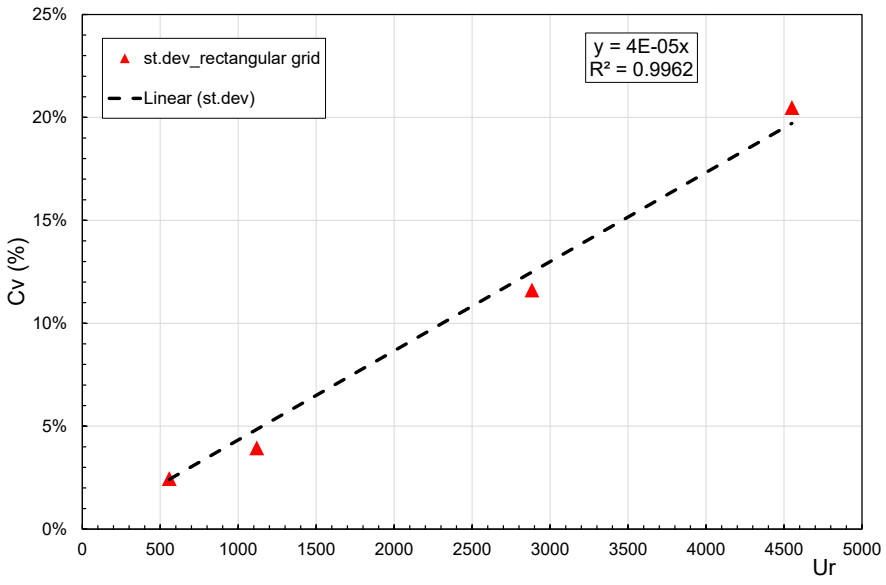

Figure 4.3.26 Coefficient of variation as function of Ursell number of statistical indicator "σ" (standard deviation).

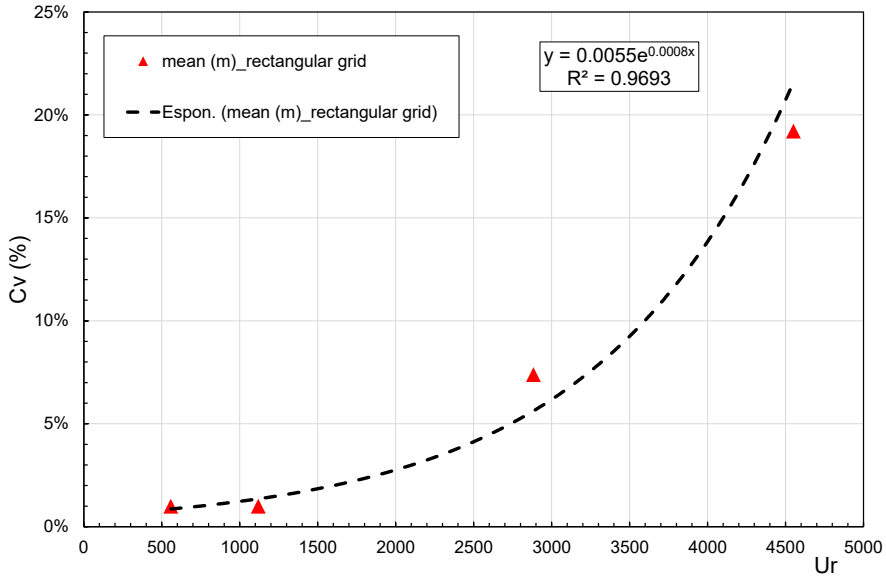

Figure 4.3.27 Coefficient of variation as function of Ursell number of statistical indicator "m" (mean or set-up).

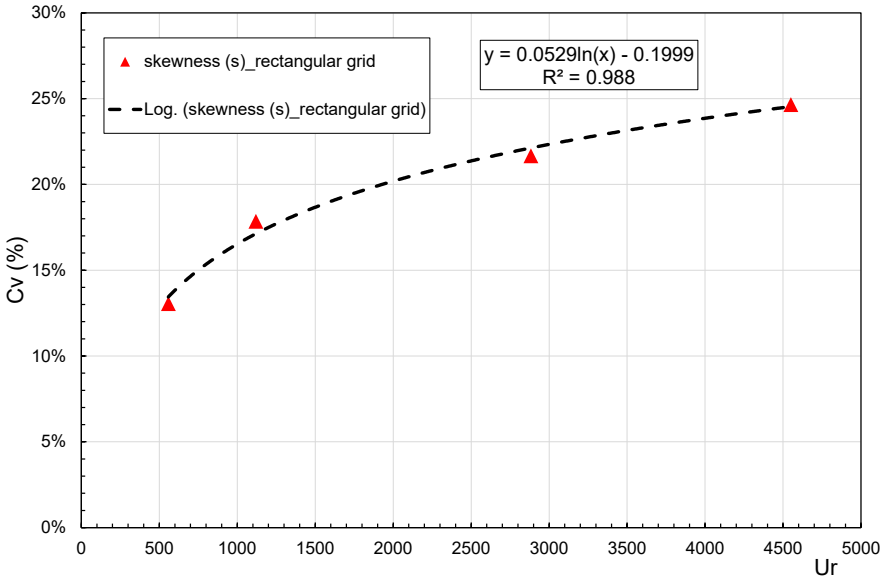

Figure 4.3.28 Coefficient of variation as function of Ursell number of statistical indicator "s" (skewness).

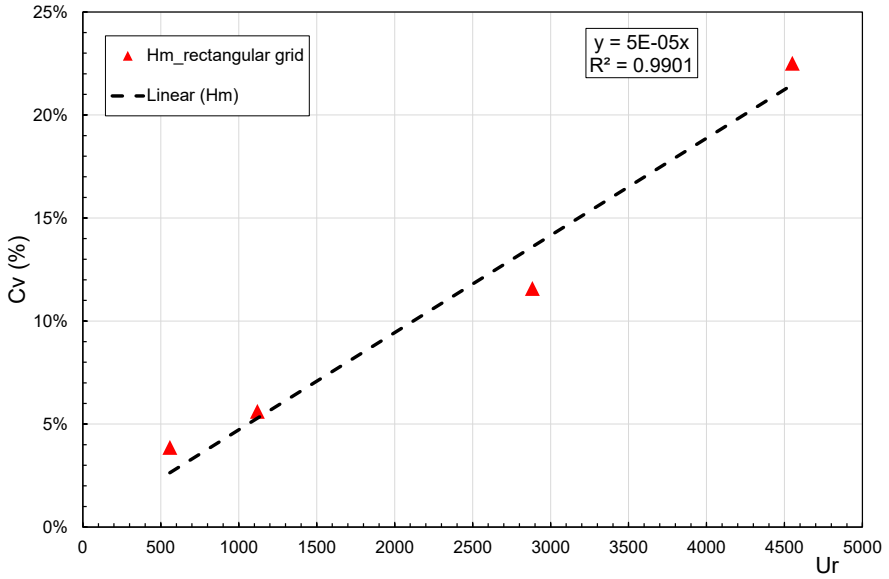

Figure 4.3.29 Coefficient of variation as function of Ursell number of statistical indicator "H_m".

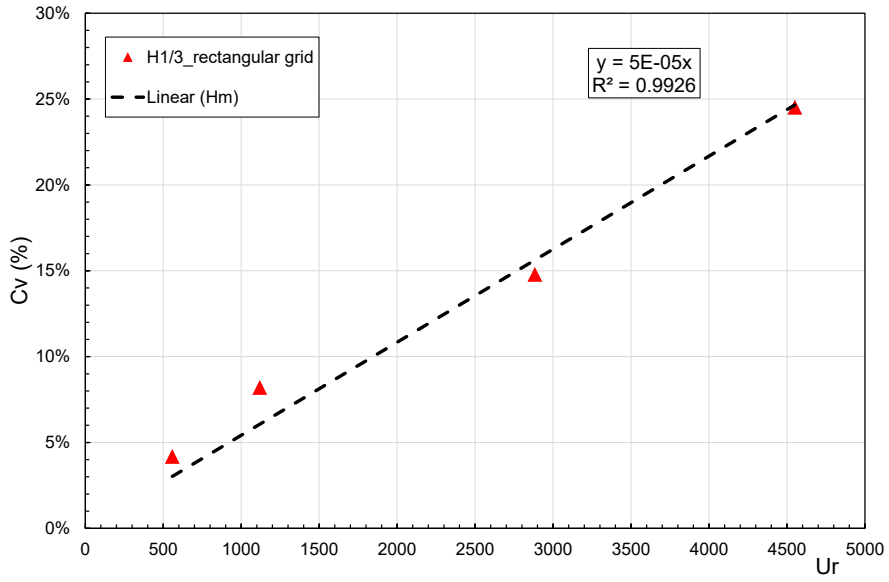

Figure 4.3.30 Figure 4.3.31 Coefficient of variation as function of Ursell number of statistical indicator "$H_{1/3}$".

As shown in the previous figures increasing Ur (nonlinear higher wave) increases the variability of the result expressed as Cv.
It also emphasizes the difference between non-breaking waves and breaking waves in terms of grid dependence.
At the wavemaker, the mesh resolution has low impact on the solution. The results on the wave height statistics show that the grid effects are negligible.
However, is possible to identify two different behaviours on breaking (Tests 1-2) and non-breaking wave (Tests 3-4) at section X_1 and therefore on mean wave height "at wall" also indicated as H_m

The value of H_m is plotted as function of grid dimension expressed as $(\Delta x*\Delta z)^{0.5}$. Are also plot the amplitudes of fluctuation expressed as $\mu\pm\sigma$ and $\mu\pm2\sigma$.

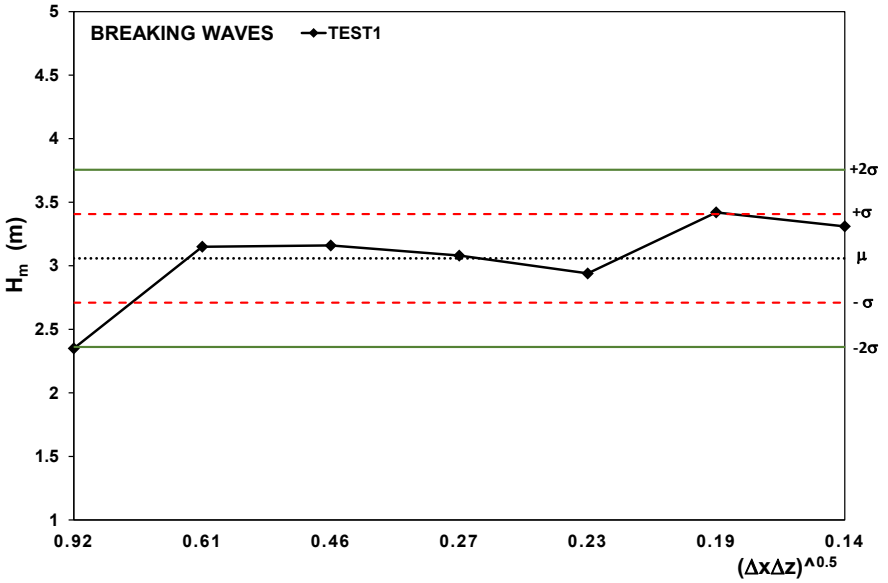

Figure 4.3.32 Results of the mesh convergence analysis on H_m for breaking wave Test_1.

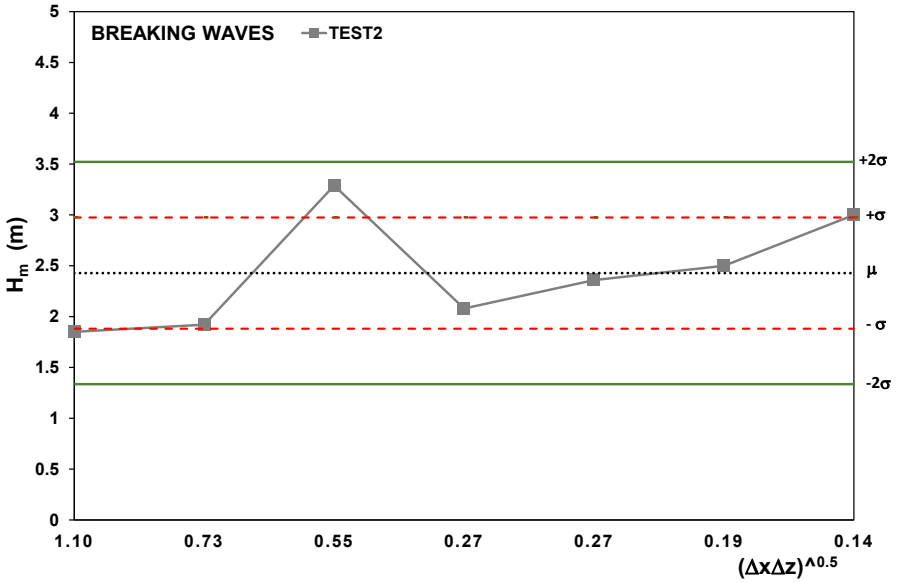

Figure 4.3.33 Results of the mesh convergence analysis on H_m for breaking wave Test_2.

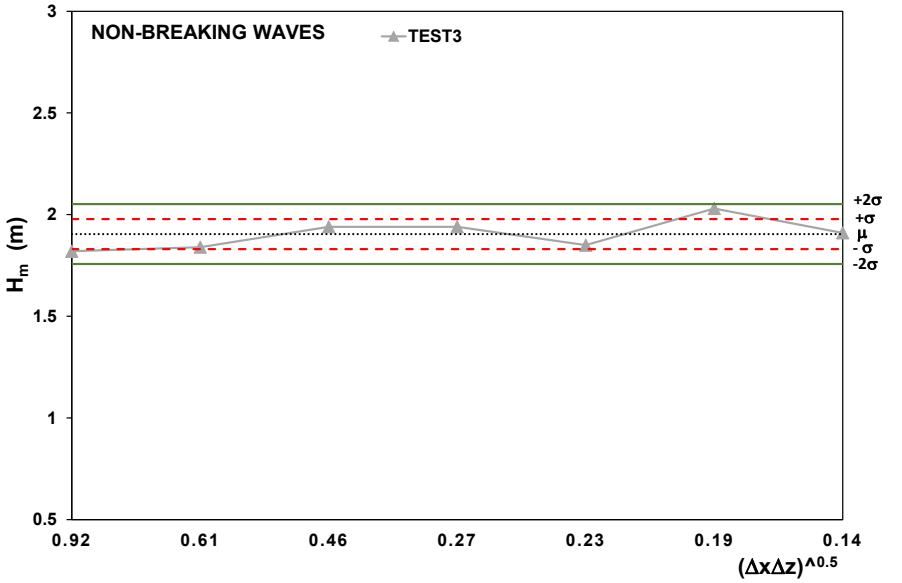

Figure 4.3.34 Results of the mesh convergence analysis on H_m for non-breaking wave Test_3.

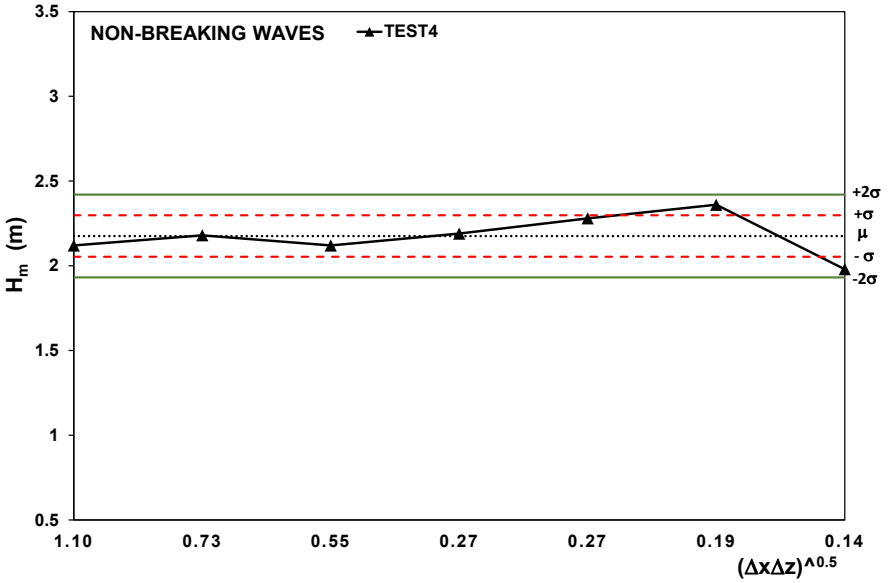

Figure 4.3.35 Results of the mesh convergence analysis on H_m for non-breaking wave Test_4.

In the first case the grid dependency on wave profile is narrower, and the amplitude of fluctuation is greater on the contrary for non-breaking wave the oscillatory convergence is small.

It is possible to conclude that results are on average grid independent but there is a fluctuation more or less wide, function of the breaking process, around the mean.

Comparison rectangular vs square grids

The convergence is function of a fluctuation around the mean value different for breaking and non-breaking waves. This fluctuation is evaluable with the coefficient of variation Cv as defined above (equation (50)).

Table 4.3.30 Cv value of significant statistics indicators.

	Breaking wave		**Non-breaking wave**	
	Cv(%)		**Cv(%)**	
	Rectangular grid	**Square Grid**	Rectangular grid	**Square Grid**
St.dv	16	**10**	7	**0**
skewness	24	**9**	16	**2**
MEAN	20	**-**	14	**-**
H_m	20	**16**	8	**1**
$H_{1/3}$	19	**11**	7	**1**

The results in the previous table show as the fluctuation increase for rectangular grid for breaking wave condition although to a lesser extent, the oscillation is also found for square grids.

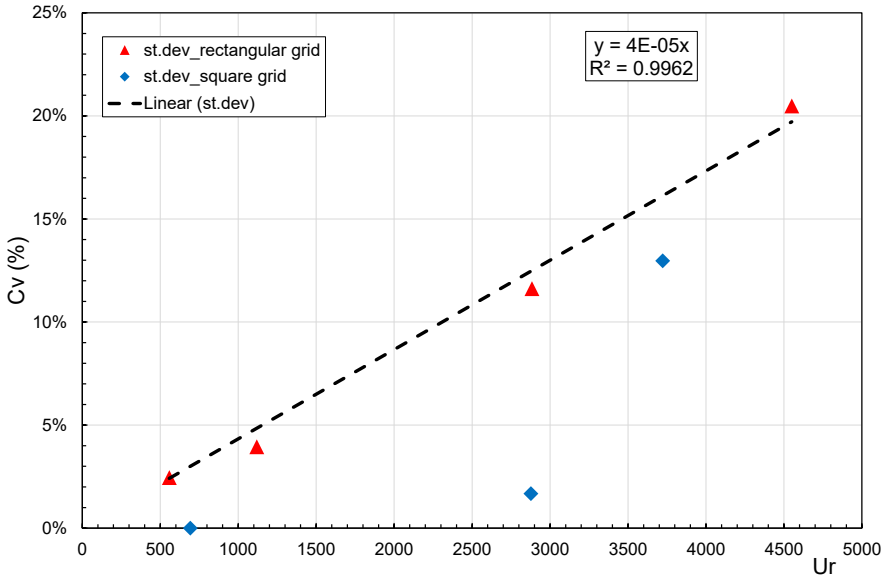

Figure 4.3.36 Comparison of Coefficient of variation of standard deviation "σ" for rectangular and square grids.

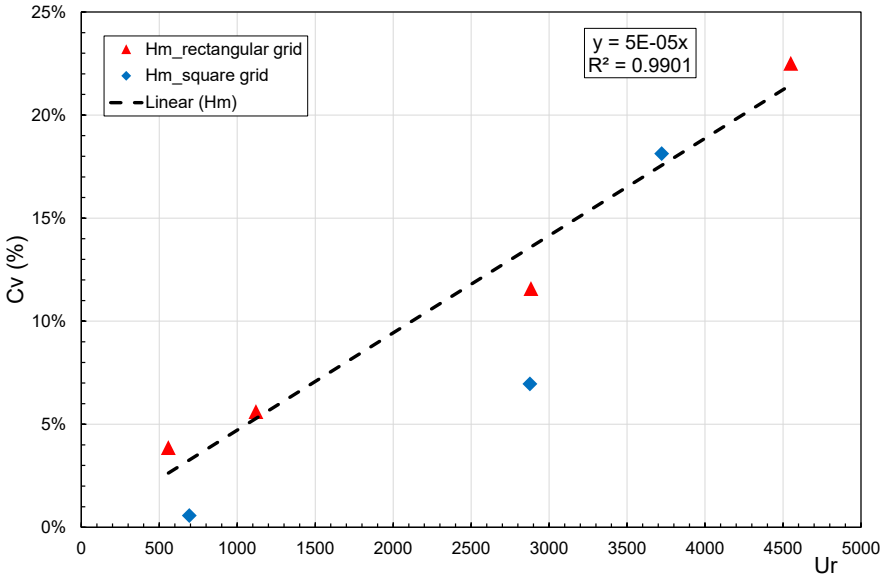

Figure 4.3.37 Comparison of Coefficient of variation of statistical indicator "H_m" for rectangular and square grids.

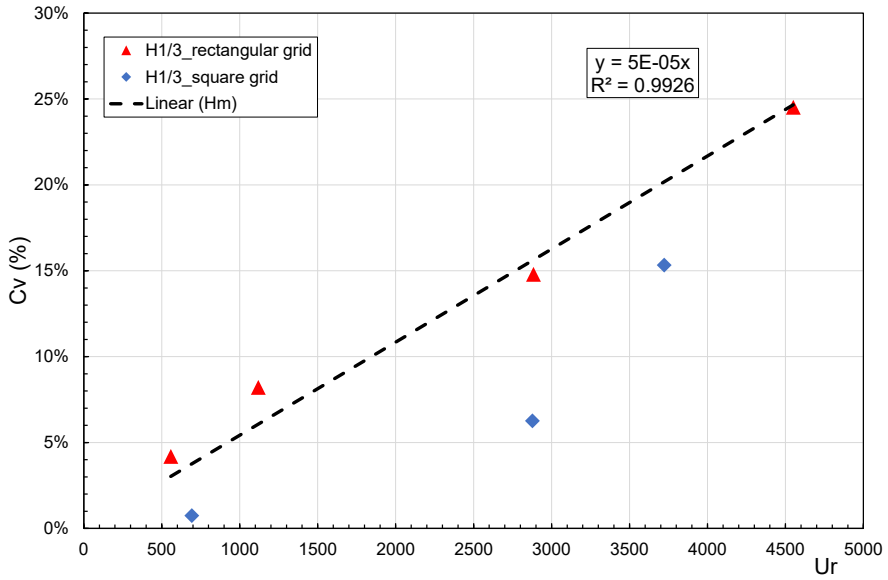

Figure 4.3.38 Comparison of Coefficient of variation of statistical indicator "$H_{1/3}$" for rectangular and square grids.

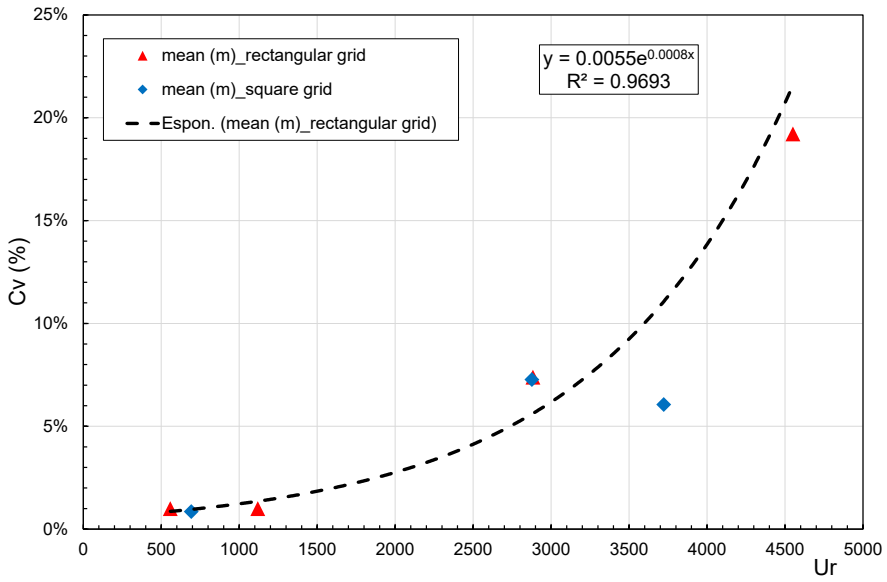

Figure 4.3.39 Comparison of Coefficient of variation of statistical indicator "m" (mean or set-up) for rectangular and square grids.

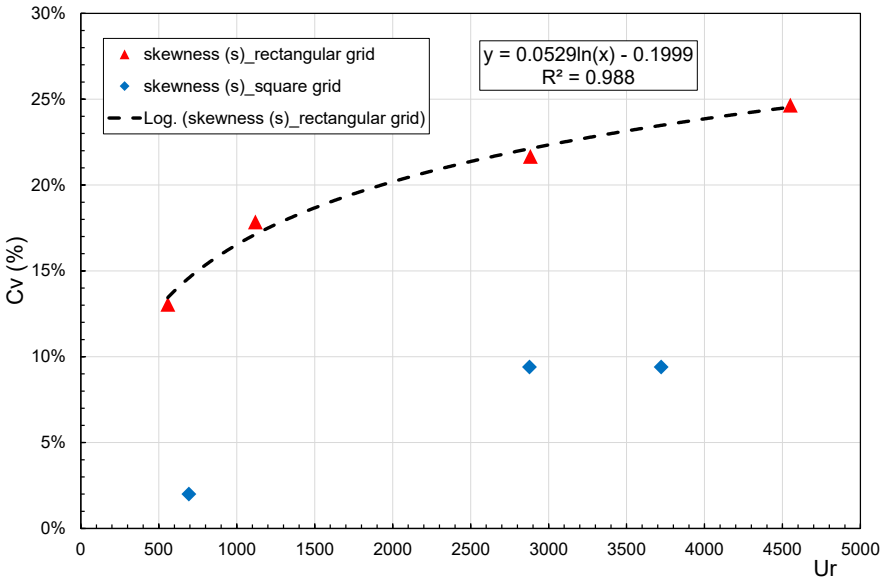

Figure 4.3.40 Comparison of Coefficient of variation of statistical indicator "s" (skewness) for rectangular and square grids.

The comparison shown in Figure 4.3.38 and in Figure 4.3.40 suggests square grids reduce, generally, variability of results. As an exception, results on wave set-up are basically similar for rectangular and square grids. Moreover, for the most relevant engineering quantities (wave energy and zero-up crossing waves) using square grids resulted beneficial only at low Ursell numbers.

Finer grid

The problem of finer grid is more pronounced for breaking waves as shown in the Figure 4.3.33 and as discussed in the paragraph 4.3.1 in which an unusual behaviour of the finer grid was found.

In situations with medium or high turbulence, the convective term clearly prevails over the diffusive one; this convective term is the cause of the non-linear behavior of the equations. The equations stability is compromised when nonlinear effects occur.

However, for a coarse grid, the "truncation error" is large; when we refine the mesh to a special size and beyond, the "round off error" becomes significant and may cause instability in the solution algorithm.

Furthermore, it is necessary to investigate whether the boundary condition or the absorber had an influence and order of accuracy.

4.4 GRID SENSITIVITY STUDY BASED ON MEAN OVERTOPPING RATE

Overtopping will be the key parameter to validate the results of the CFD model.

In this case the Malecòn Seawall is placed at the end of the numerical domain and a specific flux surface (Figure 4.4.1) is added to measure wave overtopping as plotted in the Figure 4.4.2 (a).

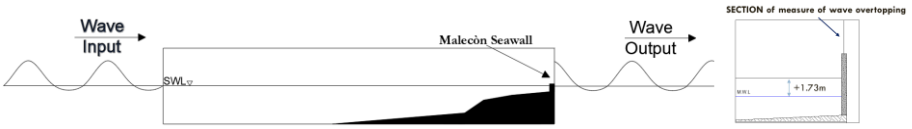

Figure 4.4.1 2D-Numerical layout of beach profile with Malecòn seawall and flux surface to measure wave overtopping.

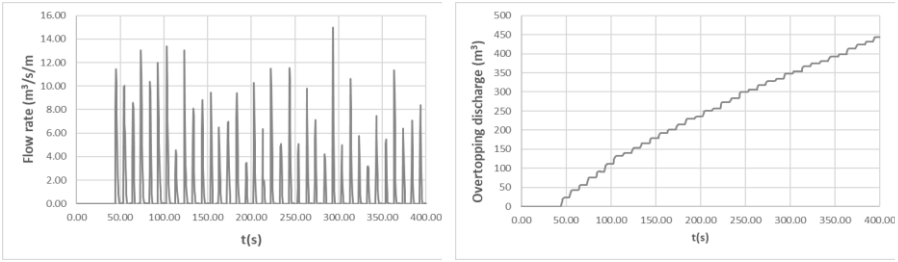

(a) **(b)**

Figure 4.4.2 Time series of overtopping flow rate (a) and overtopping discharge (b) (Test1_A80).

To discuss grid effects on the overtopping process, it useful to draw attention to the curves of cumulative overtopping volume as function of simulation time for different grid sizes (Figure 4.4.3 to Figure 4.4.6.). The graphs show as the convergence is function of simulation time.

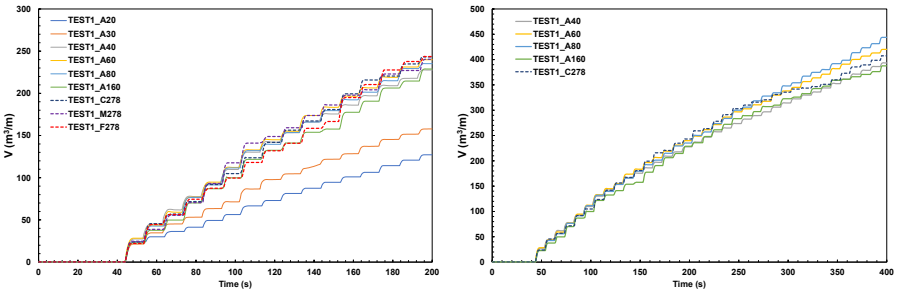

Figure 4.4.3 Time series of overtopping discharge of case Test1(H=8m T=10s).

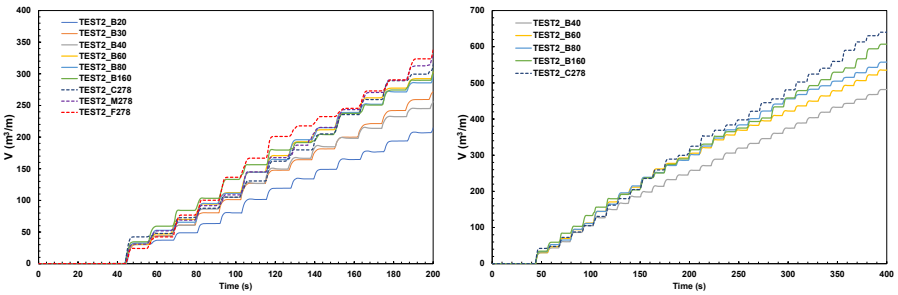

Figure 4.4.4 Time series of overtopping discharge of case Test2(H=8m T=12s).

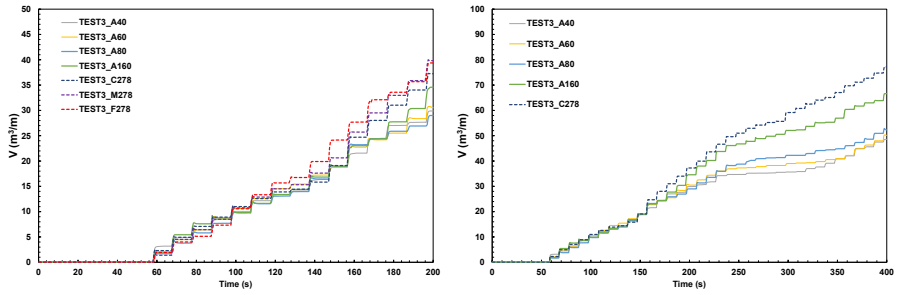

Figure 4.4.5 Time series of overtopping discharge of case Test3(H=1.5m T=10s).

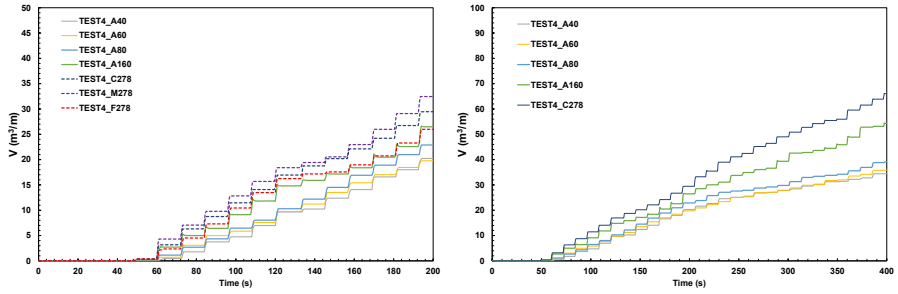

Figure 4.4.6 Time series of overtopping discharge of case Test4(H=1.5m T=12s).

The analysis of the results appears complex, a convergence of the results typical of other processes simulated by CFD is not always observed and furthermore the results tend to change with the simulation time.
Starting from the analysis of the final overtopping volume or similarly the mean overtopping flow rate, a study with different step is proposed.
The grid effect was measured using the quantity $\left|\frac{V_{ff}-V_{fc}}{V_{fc}}\right|$ (also indicated as relative error between two consecutive grids) V_E, defined as follow:

$$V_E = \left|\frac{Vf_{finer} - Vf_{Coarser}}{Vf_{Coarser}}\right| \tag{52}$$

where $V_{f,finer}$ represents the final overtopping volume relative to the finer grid and $V_{f,coarser}$ is the analogous value for the coarse grid used as reference value.
The graphs below show the geometric mean of two dimensions of the cell on the abscissa, and the absolute value of the relative error V_E on the ordinates.

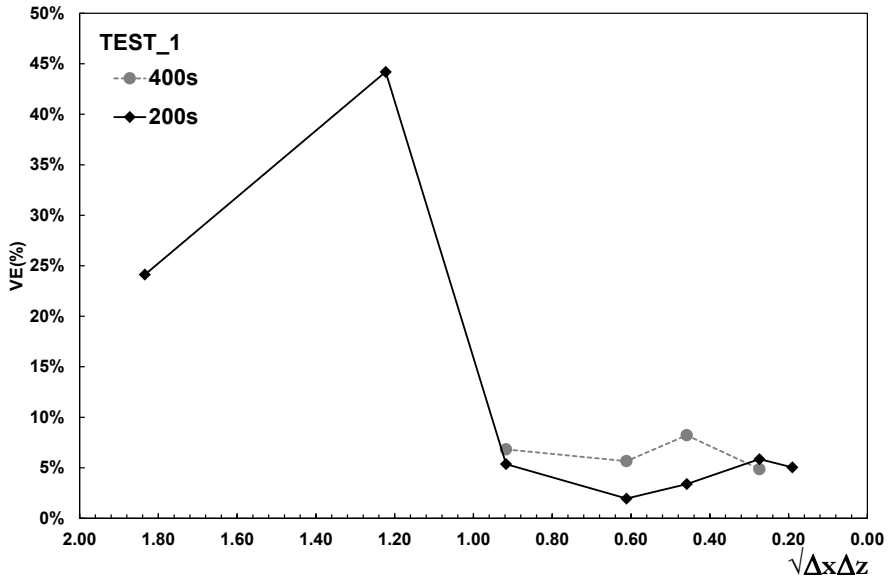

Figure 4.4.7 Relative volume error with refining grid of Test1(H=8.0m T=10s).

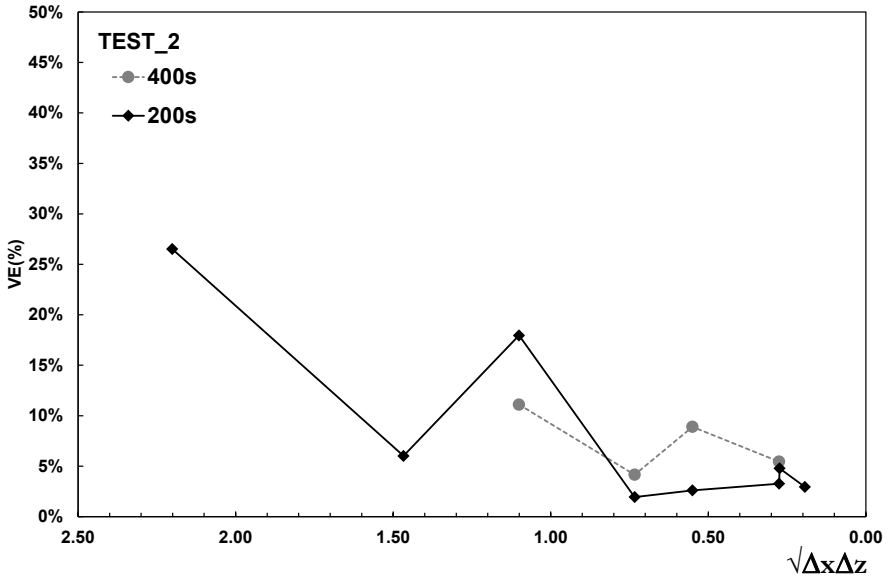

Figure 4.4.8 Relative volume error increasing grid of Test2(H=8.0m T=12s).

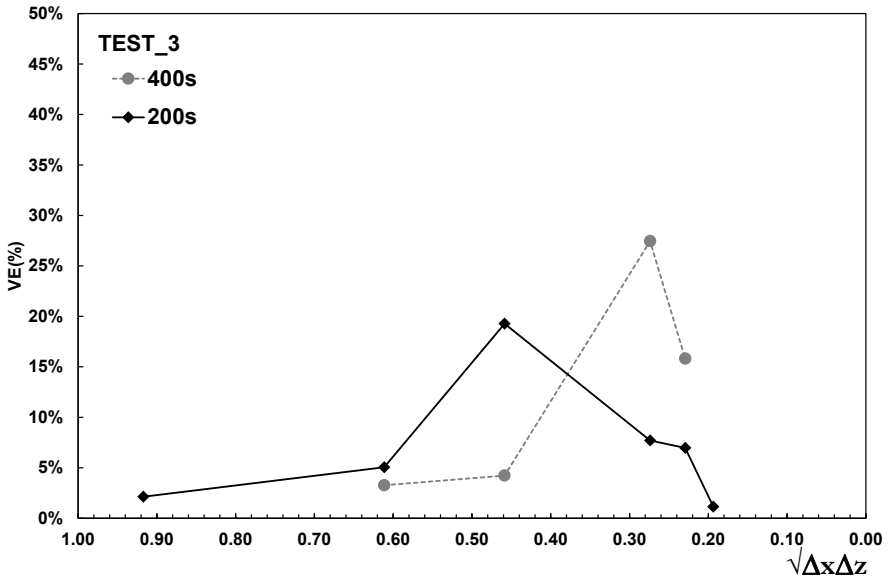

Figure 4.4.9 Relative volume error increasing grid of Test3(H=1.5m T=10s).

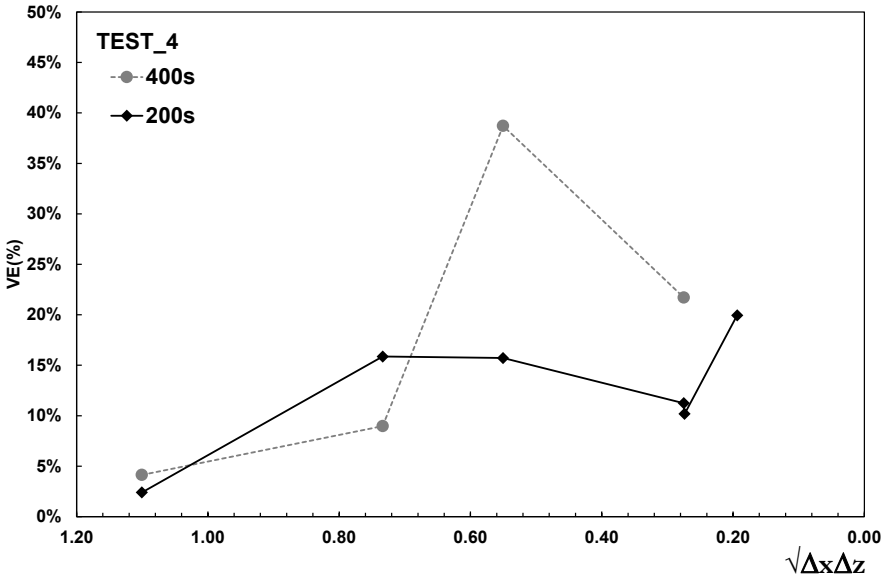

Figure 4.4.10 Relative volume error increasing grid of Test4(H=1.5m T=12s).

The comparison between the plots indicated 3 main aspects:

- an area of increasing error as the grid decreases.
- a progressively decreasing phase of the error with reducing grid size.
- finally grid independence area.

The initial increasing trend could be interpreted as a consequence of the grid being too coarse to properly represent wave overtopping.
Above a certain threshold the error suddenly increases and then progressively decreases.
However, it seen that:

(1). Results for a given grid could be in the increasing part, in the decreasing part or in the stationary part of the error curve basically depending on the value of the overtopping volume. For example, the grid representing by value of abscissa 0.6 is in the stationary

part for TEST1 (Figure 4.4.7 conversely in the increasing part for TEST3 (Figure 4.4.9).
(2). for 400s error tends to increase with simulation time and order of magnitude in the stationary zone is about 10% as also found in (S.I.O Scholte, 2020) that indicate the same order of magnitude of a typical error.

The behaviour explain in the point (1) can be explained by noticing that the final overtopping volume of Test1_200s (230 m^3/m) is nearly 7 times larger than in Test3_200s (35 m^3/m); thus it could be hypothesized that for coarse grids the numerical discretization of such a small volume is so poor to induce negligible effects when grid size reduces from Δx=1.5 Δz=0.6 m to Δx=0.18 Δz=0.06 m.

The quantity V_E previous defined can be related to the variable $\frac{qT}{\Delta x \Delta z}$ where the term "qT" represents the volume overflowed by a single wave and ΔxΔz represents the area of the mesh relative to the coarser grid. It represents the number of cells necessary to cover a unit volume equal to the average overflow volume in the period. In other words, for a proper analysis of convergence, the area of cells should be somehow compared to the overtopping phenomenon. To this purpose, a variable has been employed:

$$\frac{qT}{\Delta x \Delta z} = \exp\left(-2.61 \left(\frac{R_c}{H}\right)\left(\frac{\sqrt{gH^3}\, T}{\Delta x\, \Delta z}\right)\right. \tag{53}$$

The quantity qT specified in the equations (53) represents the average overtopping volume per wave, as order of magnitude; however, the effect of crest freeboard is considered in the equation, via the exponential term which coincides with Van der Meer and Janssen (1995) equation originally proposed for rubble mound breakwaters and then used in EurOtop Manual 2018 for vertical walls.

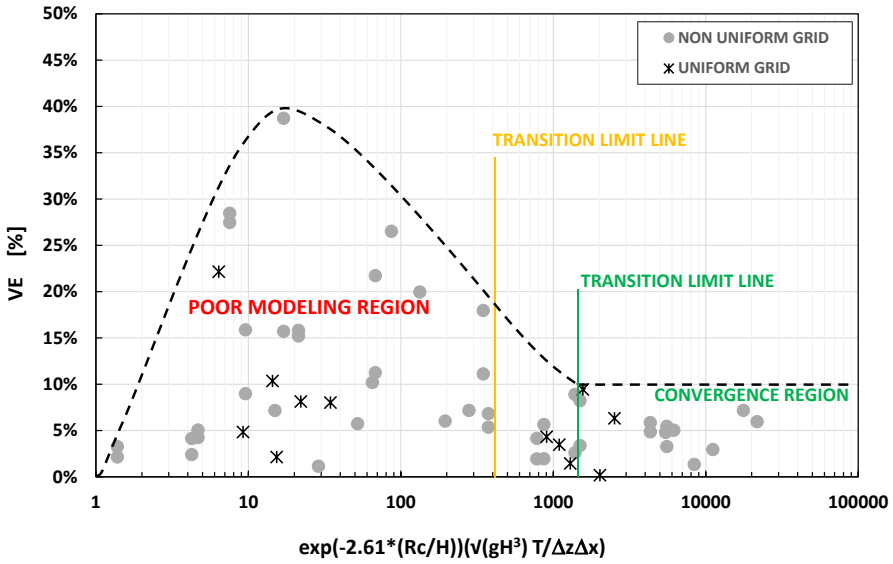

Figure 4.4.11 Envelope region relative of volume error V_E(%).

In Figure 4.4.11 the variable of the equations (53) are reported on the abscissa, while the relative error of the final overtopping volume is on the ordinates.

It should be noted that the analysis was carried out as before also for the square grids. The results are shown together with the rectangular grids in the previous and following figures.

Although the data appear to be dispersed, experimental data are enveloped by a bell-shaped region; the increasing part of the envelope at the left of the graph, represents the area of "poor modeling" where the overtopping volume is discretized in a number of cells too low. On the other hand, a convergence area is recognizable for value of variable ~1000.

The results suggest variable effectively represents numerical data, considering also relative crest freeboard.

Maximum distance between volume curves

So far, the problem of convergence has been addressed with reference to the total overtopping volume in a given time or, equivalently, the mean overtopping discharge. However, volume curves have been observed to not converge uniformly; Figure 4.4.12 compares results of Test_2 for grids M278 and F278, which belong to the convergence area of Figure 4.4.11. It is seen the final overtopping volumes to differ each other by 9.67cubic meters, corresponding to nearly 3% of the total overtopped volume (333 m^3 on average). Nevertheless, the curves exhibit a maximum distance as large as 34 cubic meters (at around 130 s), which is increased by a factor of four (nearly 10% of the total volume).

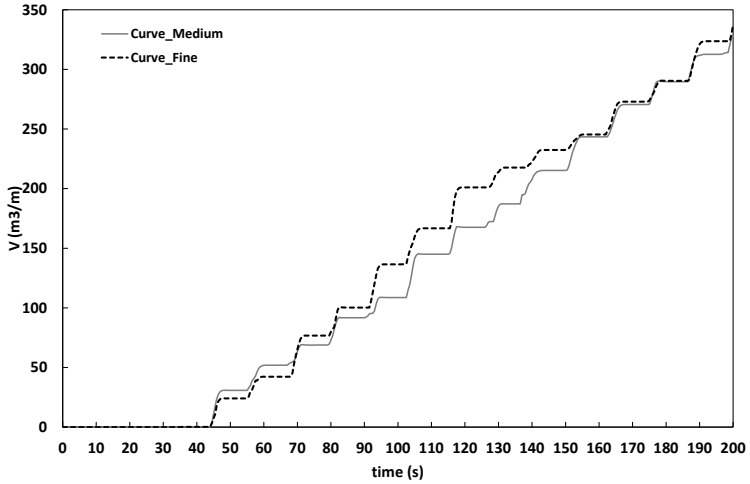

Figure 4.4.12 Example of volume curve of two consecutive grid of TEST2 (H=8m T=12s).

Analogous response can be found in the literature work (Yazid Maliki et al. 2017) and described in paragraph 2.5.

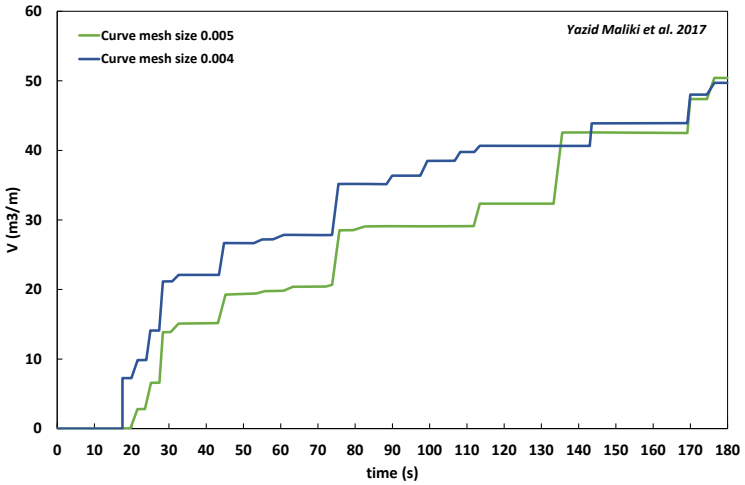

Figure 4.4.13 Volumetric overtopping curve of different mesh size of YAZID MALIKI et al. 2017.

The curves in Figure 4.4.13 redrawn from the Figure 2.5.1 (Yazid at al. 2017) show the same mean overtopping rate, but a maximum distance of about 10 cubic meters (at around 108s), that is 20% of the overtopping magnitude.

To investigate this interesting phenomenon the maximum distance between two overtopping curves has been calculated and divided by the total overtopped volume of the coarser grid:

$$M_D = \left| \frac{max\left[V_{coarse}(t) - V_{fine}(t)\right]}{V_{coarse}(\mathrm{t})} \right| \tag{54}$$

The variable M_D is plotted in the follow figures against equation (53).

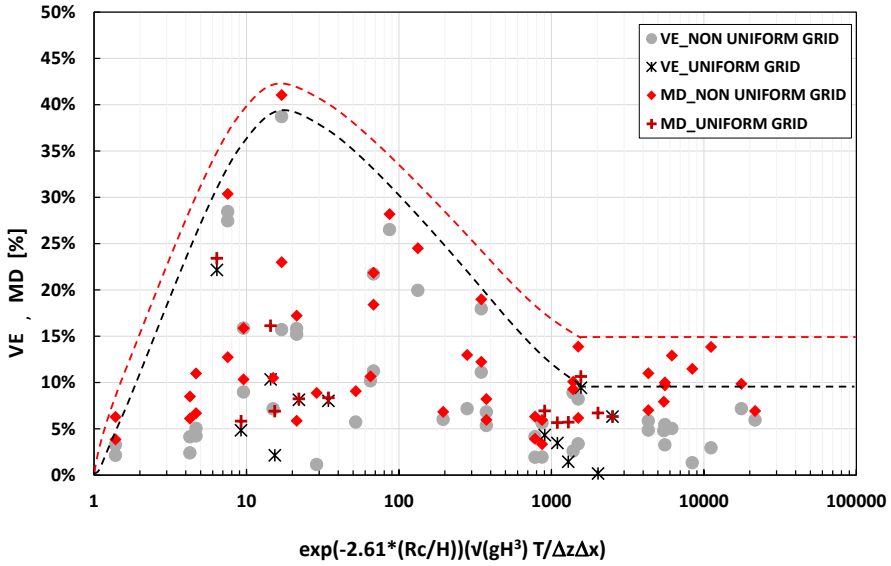

Figure 4.4.14 Envelope region relative of volume error VE(%) and maximum distance MD(%).

The envelope curve of MD exceeds that of the mean overtopping rate VE; however, while differences appear relatively small for the high error area, they are significant for the convergence zone where the limit expected distance between volume curves increases from less than 10% for the mean overtopping rate to nearly 15% for MD.
Note that this value is reasonably in agreement with results of Yazid et al. 2017).
The procedure descripted above induce dependence on number of wave or in other word on simulation time.

Volume error as Random variable

The error relative between two consecutive grids was considered as a random variable distributed approximately as a log-normal.
A log-normal (or lognormal) distribution is a continuous probability distribution of a random variable whose logarithm is normally distributed.

If relative error (X=Er) is considered as random variable with lognormal distribution (LogN) then N=ln X follows normal distribution N(μ,σ)

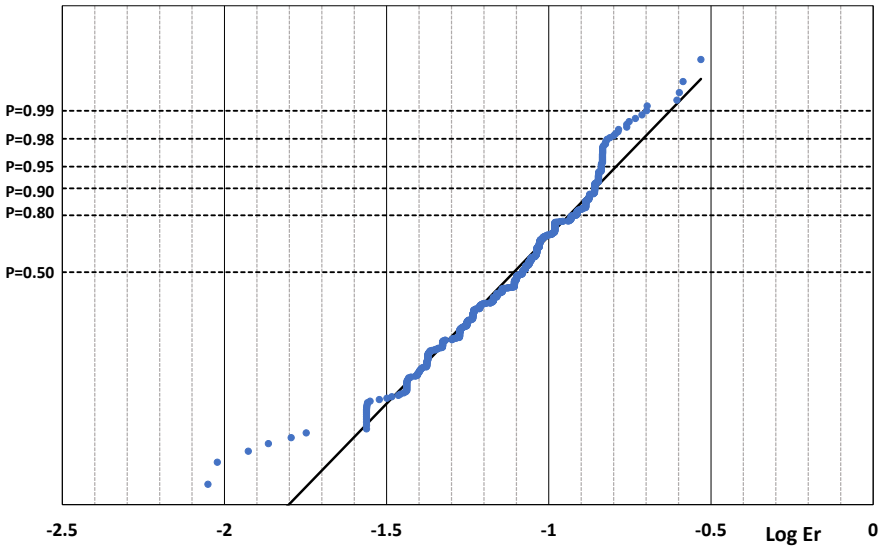

Figure 4.4.15 Log normal distribution plot of relative error of TEST1 grid 80-160.

As shown in Figure 4.4.15 the relative error between two consecutive grids during simulation time are approximately Lognormal distributed.
Therefore, the envelope regions have been updated taking into account the value of mean and standard deviation of distribution.

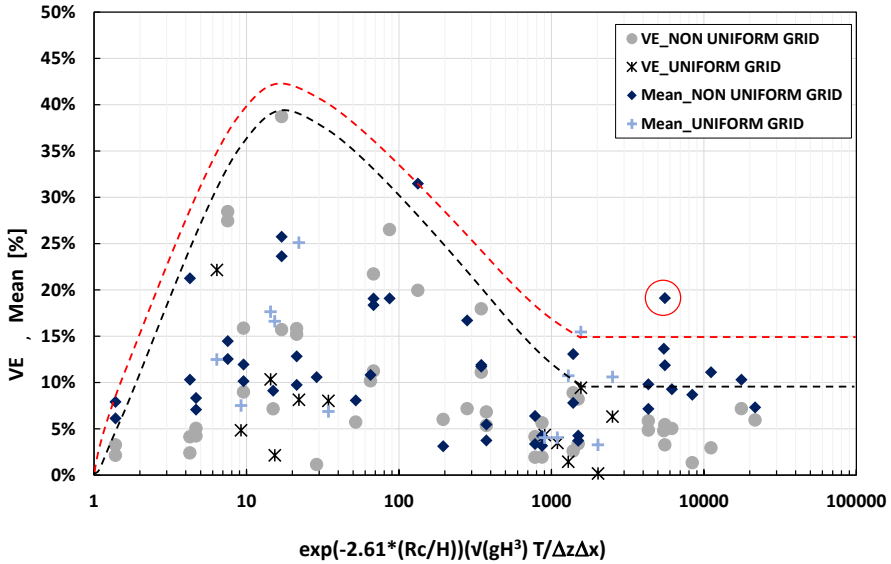

Figure 4.4.16 Envelope region relative of volume error VE (%) and mean error ME (%).

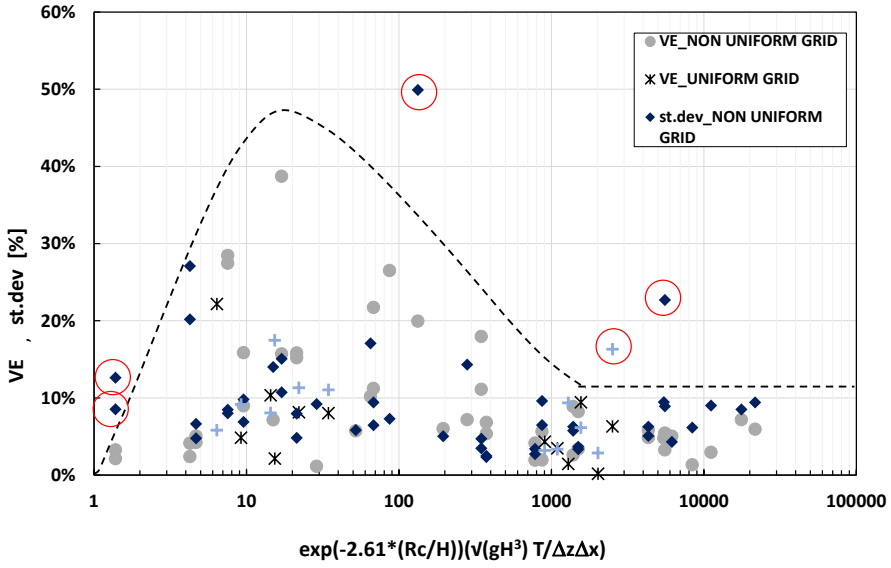

Figure 4.4.17 Envelope region relative of volume error VE (%) and st.dev.

Knowing the main parameter of the distribution is useful predetermined the random error with the graph of mean and standard deviation.

In conclusion with the nearshore quantities, the geometry of the wall is possible to evaluate the error relative to the grid through the graphs previously plotted.
Considering the various phenomena that can occur, as just discussed, in the convergence area an error between 10 and 15% is expected.

4.5 CONSISTENCY ANALYSIS WITH LABORATORY TESTS FOR GRID SENSITIVITY STUDY

To analyze to what extent the choice of the grid can influence the results relating to the mean overtopping flow rate, it is useful to compare the observed grid variability with the variability of the EurOtop database (which includes the outcomes of other EU projects, such as CLASH).
The analysis of all EurOtop data revealed a mean value of standard deviation of the Log-residuals approximately equal to 0.2.

The uncertainty related to the grid valuable as Log-Residual can be compared with standard deviation of the EurOtop dataset.
In this case, Log-residuals are defined as the logarithm of the q_{iGRID} (of i-th grid) to q_{mean}(of all grid) where q is the mean overtopping discharge:

$$LR = log_{10} \frac{q_{iGRID}}{q_{mean}} \tag{55}$$

On the other hand, Figure 4.5.1 plots the standardized *log-residuals* versus the abscissa calculated with equation (53).

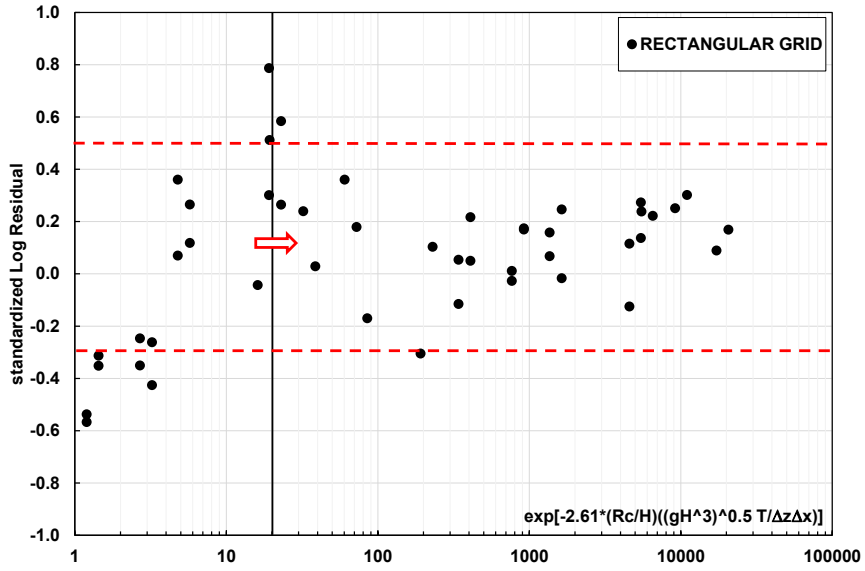

Figure 4.5.1 Log Residual of relative error between two consecutive grids.

These results show that the error estimated in laboratory is greater than the error relative to the grid.

The graph identifies a region for abscissa >20 in which the variability of standardized LR is included in interval ±0.5 times standard deviation of laboratory dataset that represent an acceptable value to choose the grid.

However, it is possible to see that as the abscissa increase the dispersion of the data is reduced and it is still contained with respect to the variability obtained in the laboratory.

Furthermore, the values of *standardized Log-Residuals* of square grids are added on the previous plot obtaining the Figure 4.5.2

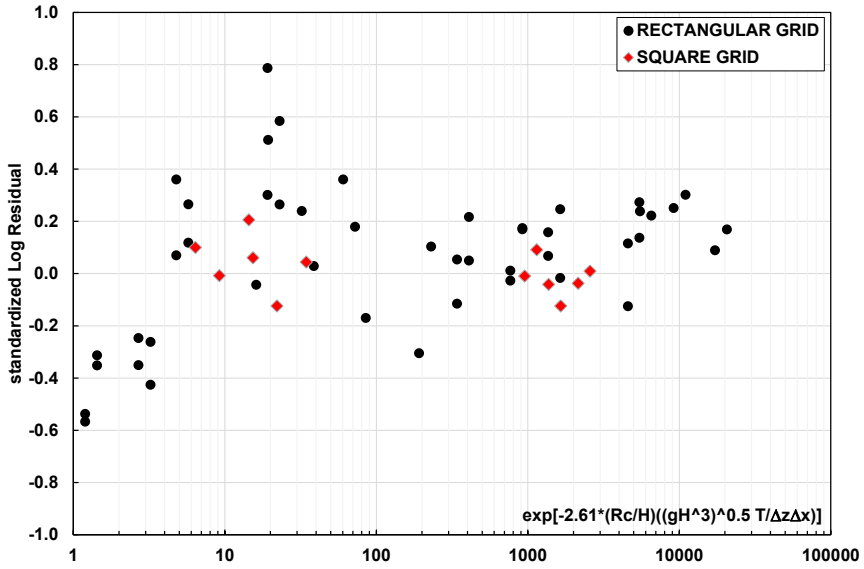

Figure 4.5.2 Log Residual of relative error between two consecutive grids (rectangular vs square grids).

The square grid data dispersion is limited in the interval ±0.2 times the standard deviation of laboratory dataset and for the convergence region identified with the abscissa greater than 1000 it shows a lower variability compared to the results obtained with rectangular grids.
An error of the same order of magnitude as the standard deviation of laboratory is to be avoided (even if in the specific case it never occurs) and so in order to keep on the safe side the chosen grid was the rectangular GRID 160, whose results lay within ±0.4 times standard deviation of laboratory measurement.
Furthermore, the choice of the rectangular grid derives from the compromise between accuracy of the result and computational cost, given the large extension of the numerical domain.

4.6 RESULTS DISCUSSION

The analysis of wave transformation in the surf zone without the presence of seawall showed in the paragraph 4.3 has yielded two different responses in term of convergence of wave statistic parameter.
However, the same behaviour was not observed for overtopping.
The relative error "E_r", calculated as relative difference between two grids, is represented as a function of the resolution of the finer mesh compared to the coarser one $((\Delta x\ \Delta z)_{coarser}/(\Delta x\ \Delta z)_{finer})$ to evaluate improving accuracy. The mesh resolution ($\Delta x\ \Delta z$) considered in the graph is the product of grid resolution in x and in z direction, respectively.
The error on the wave profile at generation (X_0) is in both cases less than 10% for each grid, so the different behaviour at X_1 of the breaking and non-breaking waves and the related errors on the volume and wave profile are analysed in detail.
As plotted in the figure the error on inshore wave profile shows a greater variability for the breaking wave which instead shows limited errors on the overflow volume.

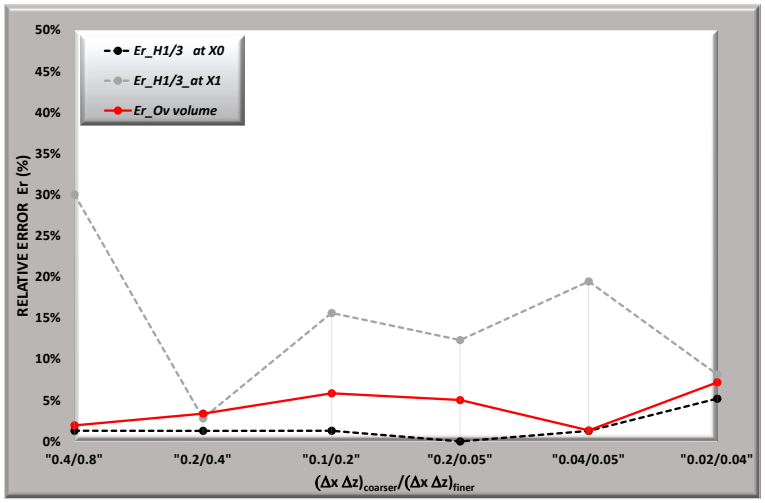

Figure 4.6.1 Relative error of wave statistics and overtopping volume for breaking wave Test1: H=8m, T=10s.

On the contrary for non-breaking waves the results as shown in the Figure 4.6.2.

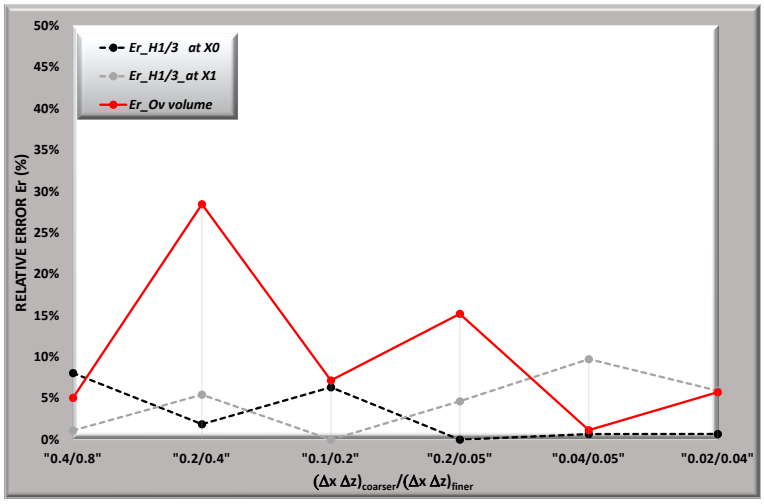

Figure 4.6.2 Relative error of wave statistics and overtopping volume for non-breaking wave Test3: H=1.5m, T=10s.

For lower mesh resolution non-breaking waves show higher value of relative error on overtopping volume, on the contrary, error on wave height statistics at X_1 is lower than 10%.

However, the uncertainties related to the grid are contained compared to the uncertainties of the laboratory measurements as discussed in the paragraph 4.5 and therefore, for the above considerations, the grid_160 [0.4x0.15(Tp10) and 0.4x0.17(Tp12)] is adequate for the objective of the work.

4.7 FURTHER TESTS OF THE NUMERICAL OPTIONS

During the process of wave breaking, the position of the free surface must be precisely tracked, so that the dynamics of the surface are well reproduced.
Secondly, the physical process of turbulence production, its transport and its dissipation during the entire breaking process must be properly modelled. In addition, computational cost must be kept within reasonable limits.

4.7.1 Effect of turbulence closure

The effects of the turbulence model have been evaluated in relation to the overtopping phenomenon.
The turbulence models tested are the k −ε, RNG and the k −ω model for the tests in which wave breaking occurs and for fixed GRID_160.

- analysis of TEST1

the figures show at same instant the different distribution of turbulent kinetic energy (TKE) for three models.

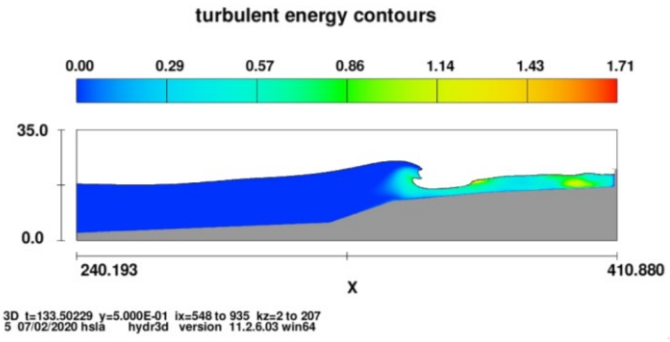

Figure 4.7.1 turbulent energy of TEST1 at instant t=133.5s (k-ε Model)

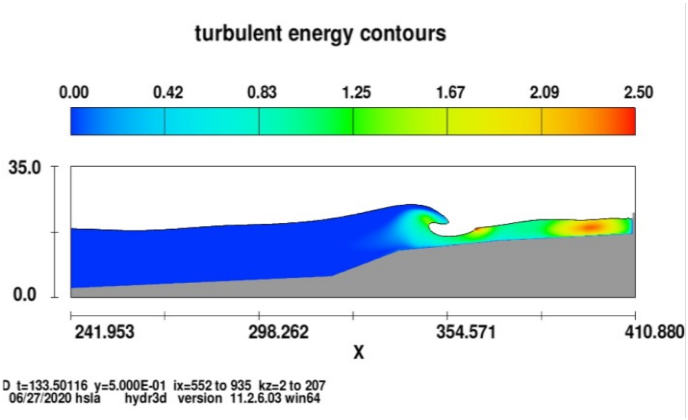

Figure 4.7.2 turbulent energy of TEST1 at instant t=133.5s (RNG Model)

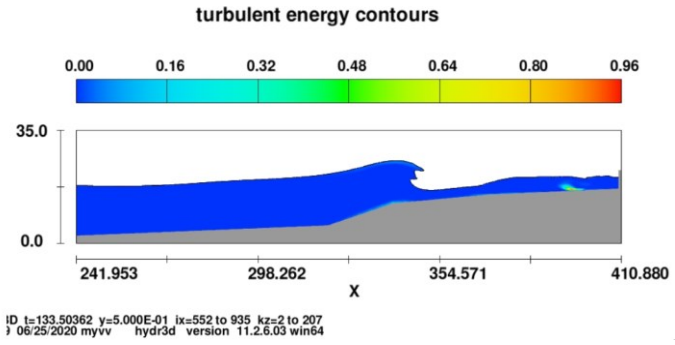

Figure 4.7.3 turbulent energy of TEST1 at instant t=133.5s (k-ω Model)

The effects of choice of turbulence closure model evaluated in term of overtopping volume show a relative error lower than 10%.

Table 4.7.1 volume error of turbulence closure model of TEST1

		relative error V_{fin}	MEAN	DEV.ST	(95%)
TEST1	k-ε_RNG	5%	3%	0.03	3%
TEST1	k-ε_K-ω	2%	4%	0.04	4%
TEST1	K-ω_RNG	7%	5%	0.05	5%

- analysis of TEST2

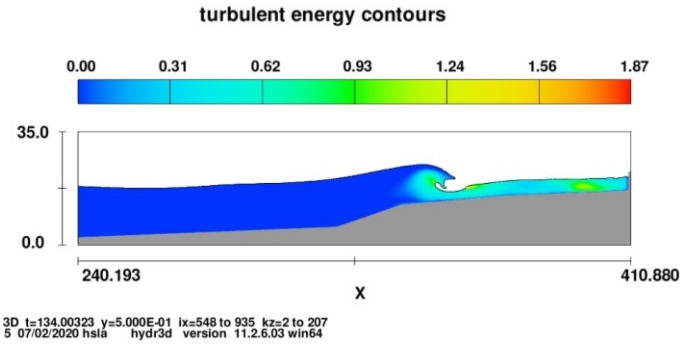

Figure 4.7.4 turbulent energy of TEST2 at instant t=134s (k-ε Model) during wave breaking process

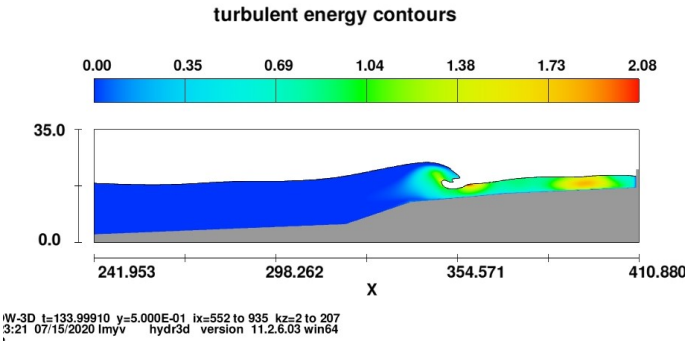

Figure 4.7.5 turbulent energy of TEST2 at instant t=134s (RNG Model) during wave breaking process

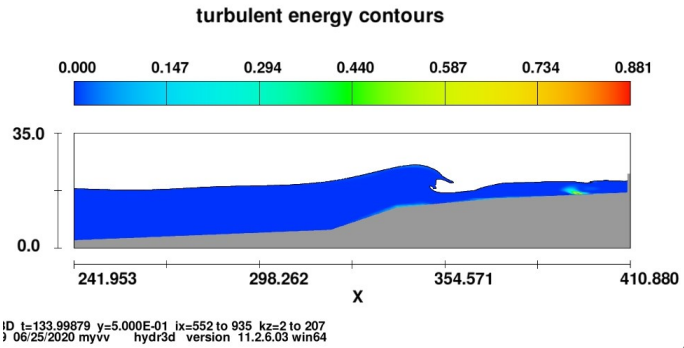

Figure 4.7.6 turbulent energy of TEST2 at instant t=134s (k-ω Model) during wave breaking process

Also is represented the turbulent energy distribution after breaking for all models.

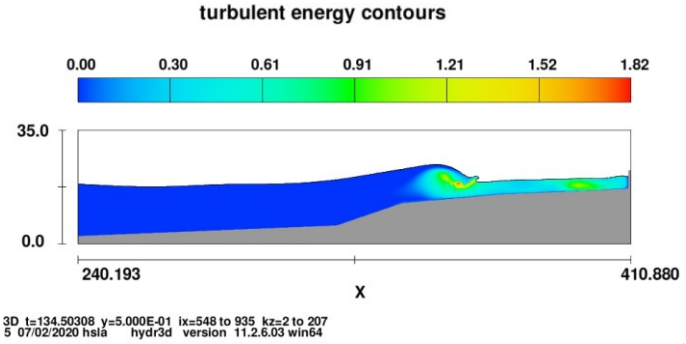

Figure 4.7.7 turbulent energy of TEST2 at instant t=134.5 s (k-ε Model) after wave breaking process

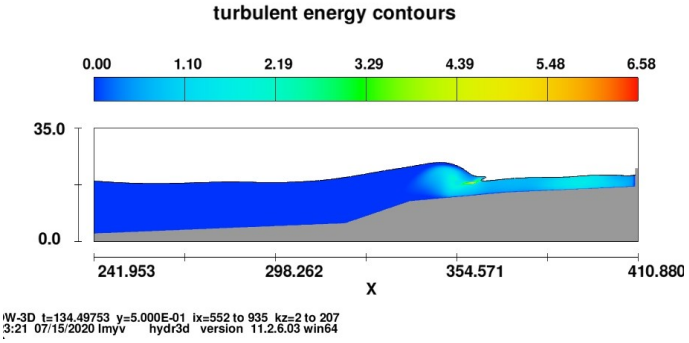

Figure 4.7.8 turbulent energy of TEST2 at instant t=134.5 s (RNG Model) after wave breaking process

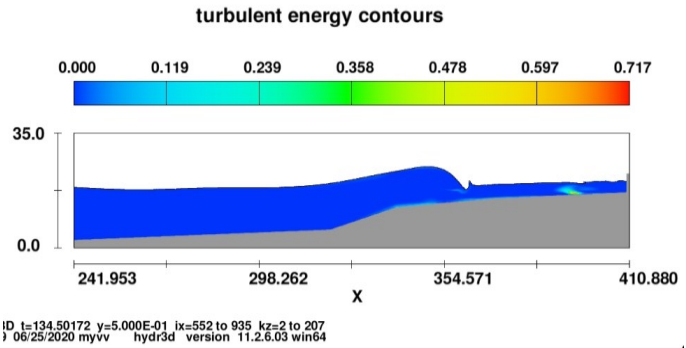

Figure 4.7.9 turbulent energy of TEST2 at instant t=134.5s (k-ε Model) after wave breaking process

The behaviour of breaking wave shown in the previous figures is consistent with Bradford (2000), in which a discussion of influence of turbulence closure model for breaking wave is addressed.
According to Bradford (2000), the two equation turbulence models yielded better predictions of surf zone properties. The RNG improves the standard k-ε model for simulating waves prior to breaking RNG model also generally yielded values of k that more closely matched the measurements.
Also, in this case the difference in terms of final volume is close to 10%.

Table 4.7.2 volume error of turbulence closure model of TEST2

		relative error V_{fin}	mean	DEV.ST	(95%)
TEST2	k-ε_RNG	10%	10%	0.10	10%
TEST2	k-ε_K-ω	8%	6%	0.06	6%
TEST2	K-ω_RNG	1%	7%	0.07	7%

The volume error related to turbulence closure model is around 10% as indicated for both tests in the previous tables; also, the standardized *log-residuals,* calculated as discussed in the previous paragraph, are not relevant compared to CLASH dataset (Table 4.7.3). Hence the study will be done with RNG.

Table 4.7.3 Standardized log-Residual of mean overtopping discharge for turbulence closure model.

	Test1	Test2
RNG	-0.08	-0.08
k-ε	0.02	0.13
k-ω	0.06	-0.05

The ReNormalized Group (RNG) extension of the k-ε model has been selected, which is particularly suited to describe the wave evolution in the area of the breaking point (Ting and Kirby 1994, Bradford 2000).

4.7.2 Effect of free surface boundary condition

Models with free surfaces have several options for volume-of-fluid methods. For this specific study two method have been setting:

- The One fluid, free surface option, in which the donor cell is always on the F = 1 side of the interface.
- The Split Lagrangian method (also known as TruVOF), that are suitable for both one- and two-fluid flows. Generally, the Lagrangian method exhibit good accuracy in tracking sharp interfaces. The Split Lagrangian method typically produces lower cumulative volume error than the other methods in FLOW-3D.

Two quantities have been employed as indicators of the convergence of results:

$$Rs = \frac{StDev[\eta_{TruVof}(t) - \eta_{OneFluid}(t)]}{\max(\eta_{OneFluid})} \quad (56)$$

The standard deviation of the difference between the eta signals, divided by the maximum eta measured with one fluid model:

$$R^2 = \frac{E[\eta_{TruVof} \cdot \eta_{OneFluid}]}{StDev[\eta_{TruVof} \cdot \eta_{OneFluid}]} \quad (57)$$

These quantities have been calculated in three positions of the flume as reported in the follow table.

Table 4.7.4 Positions xi (in m) used for analysis of temporal variation of η for Test1 and Test3.

	TEST1		TEST3	
	Rs	R^2	Rs	R^2
x1=5m	0.003	0.97	0.003	0.96
x2=195m	0.001	0.94	0.002	0.91
x3=407.5	0.016	0.79	0.004	0.96

The correlation index is lower for breaking wave in a section x=407.5m near the wall.
The wave profile for Test1 in different position are showed in the follow figures.

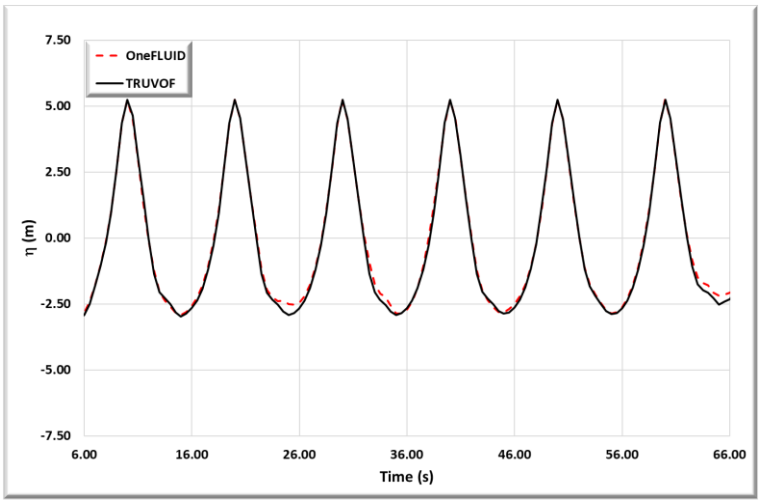

Figure 4.7.10 Time variation of water surface of TEST_1 in section of x=5m.

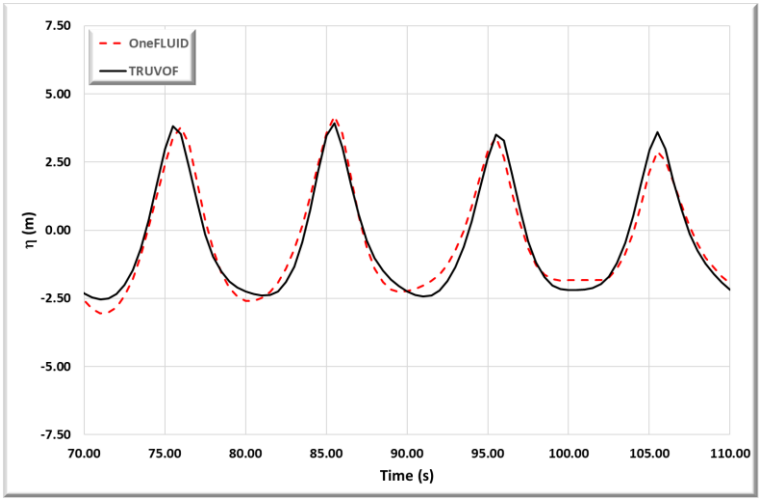

Figure 4.7.11 Time variation of water surface of TEST_1 in section of x=195m.

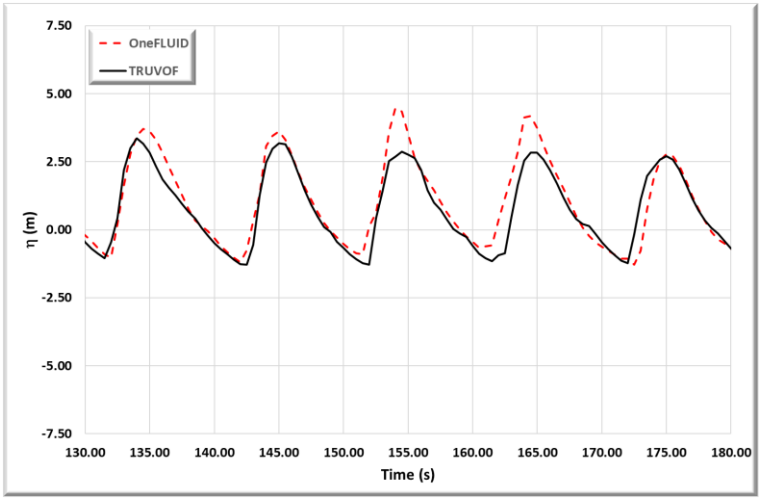

Figure 4.7.12 Time variation of water surface of TEST_1 in section of x=407.5m.

The wave profile for Test3 in different position are also showed in the follow figures.

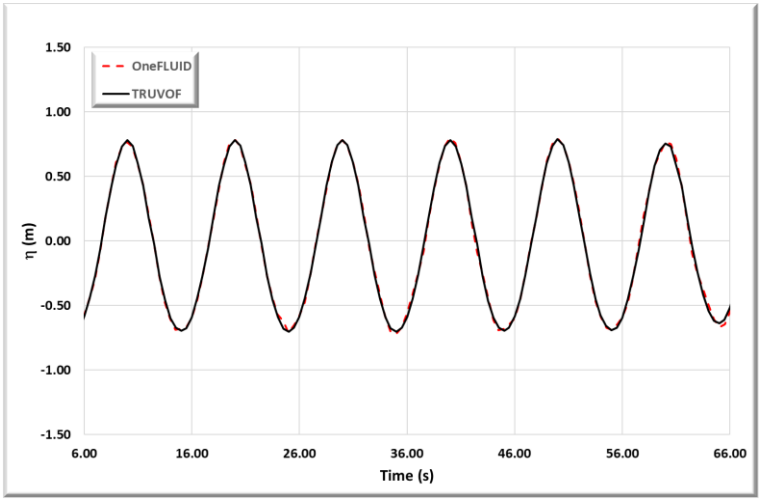

Figure 4.7.13 Time variation of water surface of TEST_3 in section of x=5m.

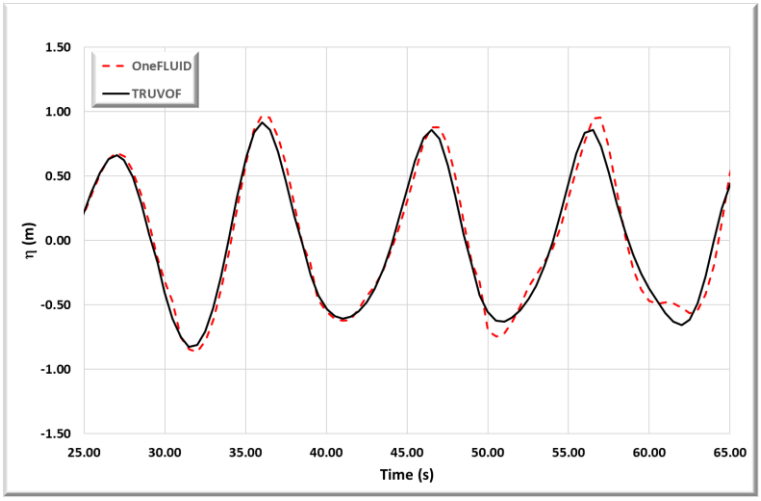

Figure 4.7.14 Time variation of water surface of TEST_3 in section of x=195m.

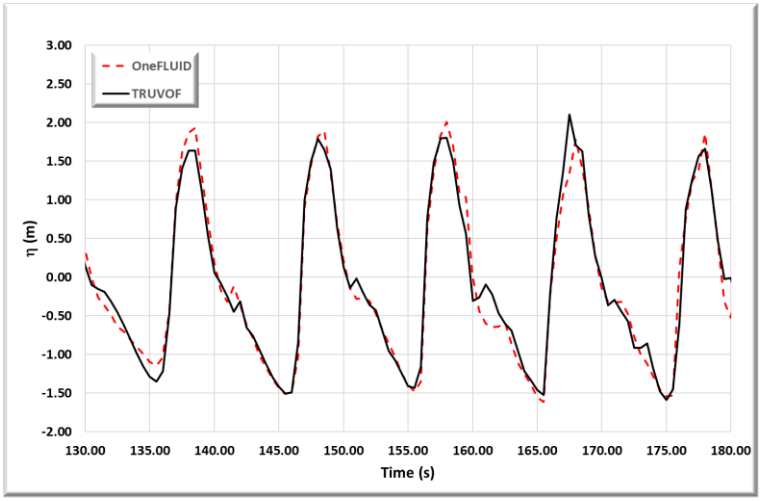

Figure 4.7.15 Time variation of water surface of TEST_3 in section of x=407.5m.

However, the analysis of wave overtopping volume (mean discharge) has been developed.

The analysis of overtopping volume error shows that the influence of model surface tracking is more pronounced for breaking wave and the study of spatial variation of wave signal give information of different influence of the model in section near the wall.

Table 4.7.5 Overtopping volume difference between two model of free surface tracking.

		relative error V_{fin}	**(mean)**	**DEV.ST**	**(95%)**
TEST1	truVoF_onefluid	12%	8%	0.08	8%
TEST3	truVoF_onefluid	0.4%	10%	0.10	10%

However, the analysis in terms of overtopping volume has not shown great errors between the two methods, same holds for standardized *log-residuals* that as shown in

Table 4.7.6 are not relevant compared to error of CLASH dataset.

Table 4.7.6 Standardized log-Residual of mean overtopping discharge for free surface boundary condition

	Test1	Test3
TruVof	-0.14	-0.005
One fluid	0.13	0.005

Then the analysis is carried out with TruVof, the most accurate method as described in Barkhudarov, M.R., 2004.
The standard donor-acceptor algorithm (one fluid method) produces very similar results in terms of free-surface motion, however also a considerably larger convective volume error. The split Lagrangian method produces lower cumulative volume error as indicated by Flow3D developer; below is reported for the specific case the convective volume error.

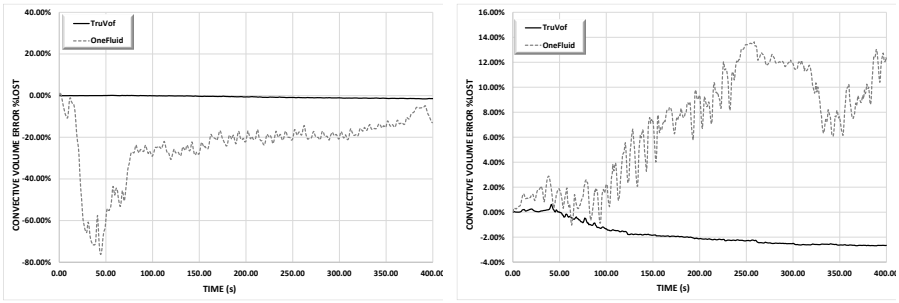

(a) (b)

Figure 4.7.16 Convective volume error - %LOST of (a)TEST_1, (b) TEST_3.

Convective volume error (% lost) represents the amount of fluid gained (negative value) or lost (positive value) due to advection errors in percent. Usually much less than 1%, and should always be less than 3%.
In Figure 4.7.16 the convective volume error of two model of free surface as function of time are reported and the improvement resulting using the TruVoF method is clear.

5 CFD ANALYSIS ON MALECÒN SEAWALL

5.1 NUMERICAL ANALYSIS WITH IRREGULAR WAVE CONDITION

5.1.1 Numerical domain

Generating waves through a boundary and at the same time absorbing reflected waves is a challenging task for both laboratory experiments and numerical modeling. For a numerical model based on Navier-Stokes's equations or Reynolds averaged Navier-Stokes (RANS) equations, it is even more difficult to treat the wave absorbing-generating boundary. An innovative procedure present in literature for generating waves using internal mass-source functions has been implemented in the present study. This method is very useful for a long duration simulation of coastal wave dynamics.

The influence of the test duration on the overtopping variability has also been investigated by Romano et al. (2014) that, by performing a sensitivity analysis carried out on the partial overtopping time series, have pointed out that shorter time series (e.g. 500 waves) can be used for overtopping tests obtaining the same order of accuracy with respect to the longer ones (e.g. the recommended 1000 waves).

500 waves are necessary to evaluate wave overtopping and so the simulation duration has been set at 5000s.

Following the experimental model scale of Malecòn seawall, developed in laboratory as discussed previously, the length of wave generation zone and wave structure interaction (Figure 5.1.1) is 410m in X direction, 1 m in Y direction and 40 m in Z direction (2D numerical domain). The water depth at the entrance (d) is 20.45m; the geometry of beach profile is the same described in paragraph 4.2. A damping zone defined by a special geometry

component, properly dimensioned as a function of a wavelength, called wave-absorber is added in numerical domain. It is completely open to fluid flow but applies damping to wave motion.
The size of general mesh for all the computations was chosen 0.40x1.00x0.15 m, the grid size of dissipation region is set as 0.5x1.0x0.5.

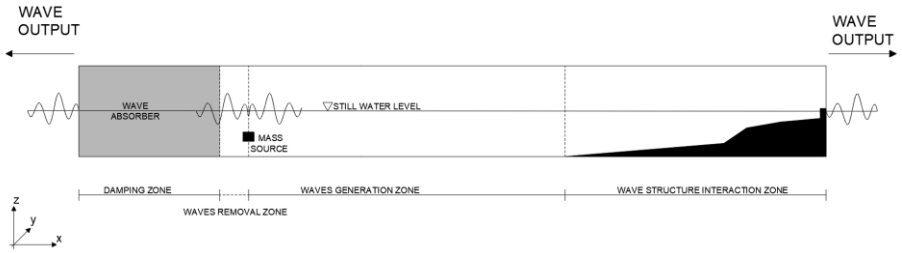

Figure 5.1.1 Scheme of numerical domain with mass-source implementation.

In Figure 5.1.2 boundary conditions have been shown, where "S" representing lateral and upper symmetry, "W" standing for wall and "P" shows pressure condition that allows fluid to outflow but with specific distribution, this is necessary to keep constant fluid level in the flume, the waves are generated through the mass source.

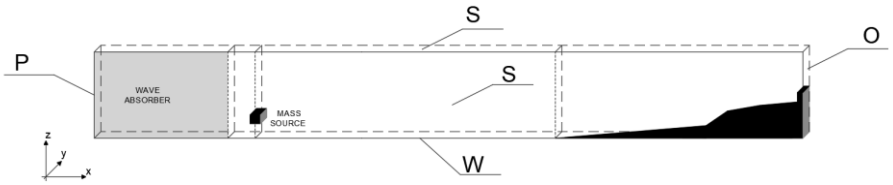

Figure 5.1.2 Boundary condition of numerical domain of irregular wave.

5.1.2 Wave generation

The aim of the research activity carried out is to implement simulations that return acceptable values of the parameters of wave motion.
The flow motion of a fluid can be described by Navier-Stokes's equations, (14) - (15) mass and momentum conservation respectively described in the previous paragraph.

To generate numerically a desired wave through an internal mechanism, there are several options.

One option is to introduce a mass source function in the continuity equation [(14)] inside the computational domain and it is the method applied in this research.

To generate a wave using a mass source function, we should modify (14) as follows:

$$\frac{\partial u}{\partial x} + \frac{\partial w}{\partial z} = s(x, z, t) \tag{58}$$

where s (x, y, t) = nonzero mass source function within the source region Lin and Liu (1999) provide s(t) expressions for incompressible fluid which produce waves of Stokes to the first order, to the second order, to the fifth order, irregular, solitary, cnoidal, assuming that the wavelength λ and the depth of the mean level of the sea *d* are much larger than the size of the generator. If irregular wave trains are considered s(x,t) for a wave of n components is expressed as:

$$\iiint s(x, z, t)\, dW = \sum_{i=1}^{n} [2C_i \eta_i(t)] \tag{59}$$

where C = phase velocity of the target wave. The factor 2 is used on the right side of because waves are generated on both sides of the source region.

According to Lin and Liu (1999), the corresponding mass source term is given by:

$$s_p(t) = \frac{2C\ \eta(t)}{A} \tag{60}$$

With A the area of the source region in x-z plane, η(t) is the free surface elevation at the rectangular source region with area A.

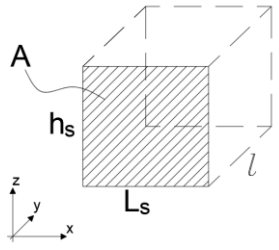

Figure 5.1.3 geometry of Mass source region.

It is noted that in a 2D model, for example x-z plane, the length *l* in y direction is 1 m.

In the simulations, the random waves (Jonswap spectrum shape) are generated from a solid element (Mass-source), located below still water level. Through the mass source, associated with a geometry component, fluid enters the computational domain at a user-specified volume flow rate from its open surface (surface not blocked by other components or by the boundary of the computational domain).

For a known energy spectrum of an irregular wave train, the inverse Fourier transformation can be used to reconstruct the wave train with a finite number of wave modes. Therefore, we can generate an irregular wave train by superposing different wave modes from i = 1 to n

$$s_p(t) = \sum_{i=1}^{n} [C_i H_i \sin(\omega_i t + \varphi_i] \tag{61}$$

Where φ_i is the phase of the *i*-th wave mode and ωi wave frequency.

This way to introduce wave in numerical domain give the opportunity to add the wave damping zone at the boundary to reduce the effects of re-reflection in numerical simulations and so allows generating longer and stable wave signal.

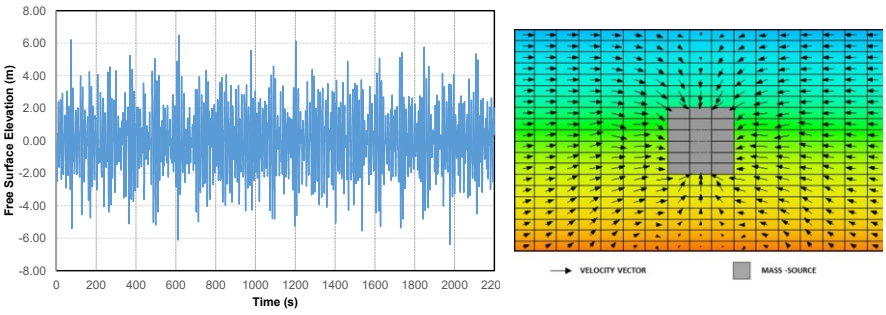

(a) **(b)**

Figure 5.1.4 (a) Free surface time series in numerical domain; (b) Velocity field around mass source.

A mass source releases fluid when flow rate is positive and removes it when flow rate is negative (Figure 5.1.4).

The waves generated are the same as those used in laboratory experiments and the main parameters are indicated in the follow table.

Table 5.1.1 irregular wave conditions for CFD analysis

Test	Hs (m)	Tp (s)	S (m)
IRR_CFD_9	2.7	12	1.73
IRR_CFD_10	4.0	12	1.73
IRR_CFD_11	5.4	12	1.73
IRR_CFD_12	6.5	12	1.73
IRR_CFD_13	2.7	10	1.73
IRR_CFD_14	4.0	10	1.73
IRR_CFD_15	5.4	10	1.73
IRR_CFD_16	6.5	10	1.73

As explained previously, is necessary to define a mass source flow rate (m^3/s) associated to the spectral parameters H_s and T_p of irregular wave trains. In the follow figures have been reported the mass source flow rate for different irregular wave conditions.

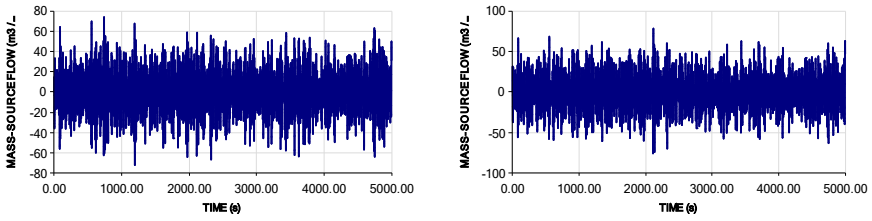

(a) (b)

Figure 5.1.5 Mass source flow rate (m^3/s) for TEST H=2.7m; panel (a)T=10m, panel (b)T=12m.

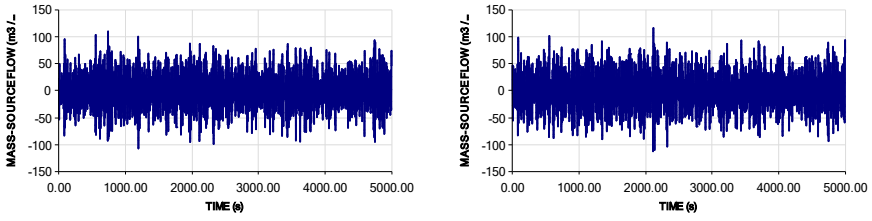

(a) (b)

Figure 5.1.6 Mass source flow rate (m^3/s) for TEST H=4.0 m; panel (a)T=10m, panel (b)T=12m.

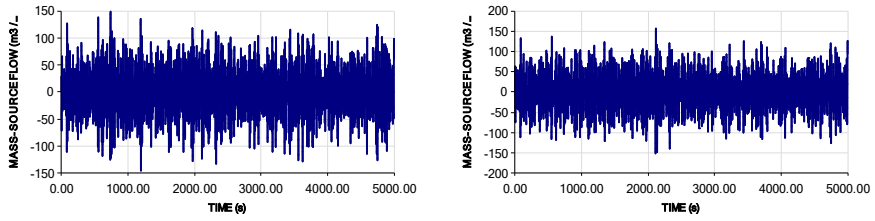

(a) (b)

Figure 5.1.7 Mass source flow rate (m^3/s) for TEST H=5.4 m; panel (a)T=10m, panel (b)T=12m.

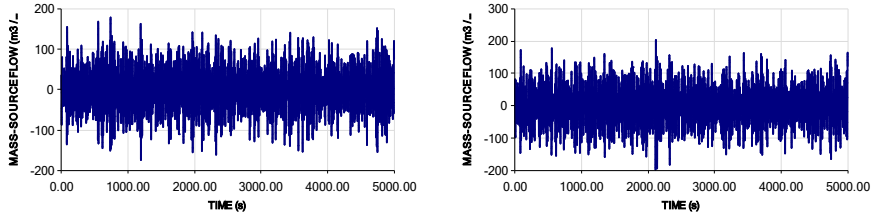

(a) (b)

Figure 5.1.8 Mass source flow rate (m^3/s) for TEST H=6.5 m; panel (a)T=10m, panel (b)T=12m.

5.1.3 Reflection analysis of irregular wave condition

In order to properly measure the incoming wave field at the flat floor seaward the foreshore, the effect of the reflection must have been separated by using the weighted least squared method proposed by Zelt & Skjelbreia (1992).

Fluctuations of the free surface were acquired in six positions in flat part of the domain in front of the structure as reported in Figure 5.1.9.

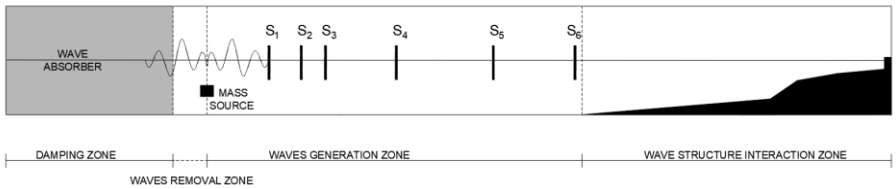

Figure 5.1.9 Position of wave probes for reflection analysis (irregular wave conditions.

Following that, the incoming Power Spectral Density Function, $S(f)$, has been compared with the desired one.

The moments of order -1 (m_{-1}), 0 (m_0) and 1 (m_1) of the measured spectrum and of theoretical one have been also evaluated (an example is given in Figure 5.1.10.

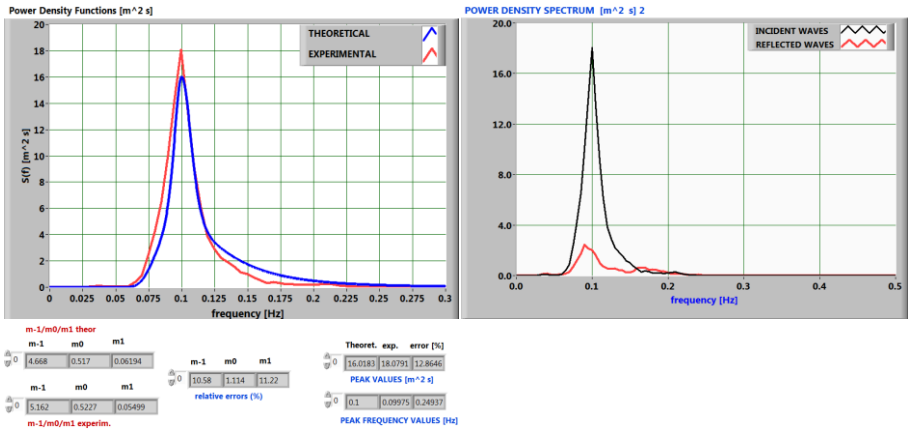

(a) **(b)**

Figure 5.1.10 Theoretical Jonswap spectrum vs measured (a) and Spectral density of incident and reflected waves (b) for TEST H=2.7m T=10s.

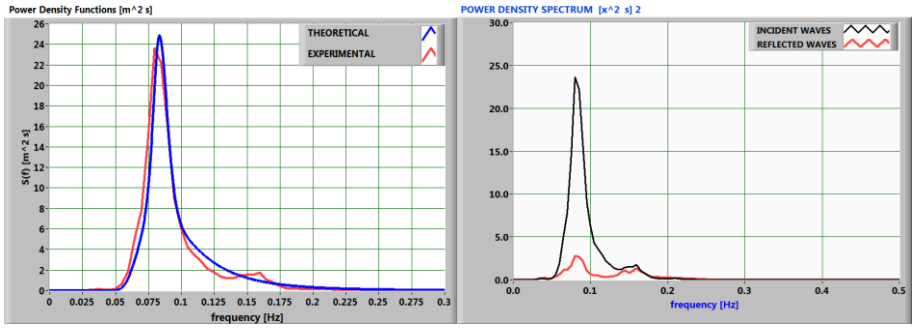

(a) (b)

Figure 5.1.11 Theoretical Jonswap spectrum vs measured (a) and Spectral density of incident and reflected waves (b)for TEST H=2.7m T=12s.

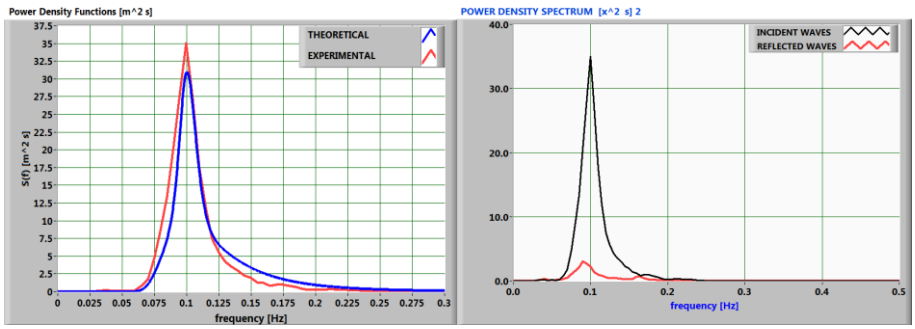

(a) (b)

Figure 5.1.12 Theoretical Jonswap spectrum vs measured (a) and Spectral density of incident and reflected waves (b) for TEST H=4.0m T=10s.

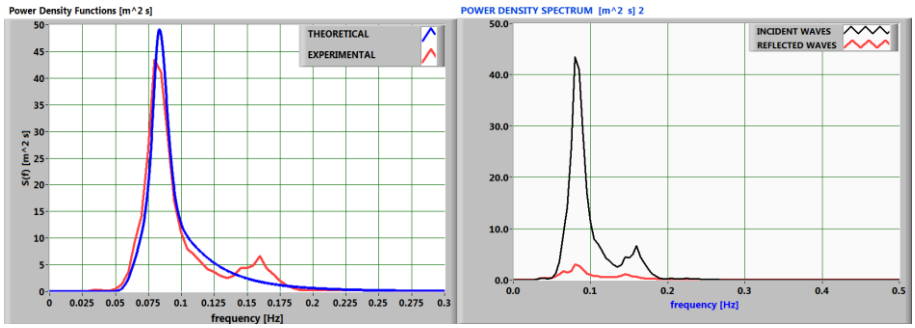

(a) (b)

Figure 5.1.13 Theoretical Jonswap spectrum vs measured (a) and Spectral density of incident and reflected waves (b) for TEST H=4.0m T=12s.

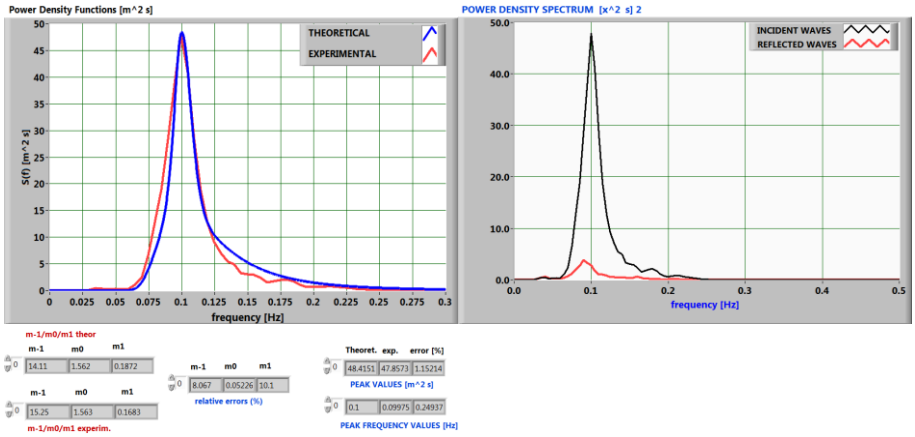

(a) (b)

Figure 5.1.14 Theoretical Jonswap spectrum vs measured (a) and Spectral density of incident and reflected waves (b) for TEST H=5.4m T=10s.

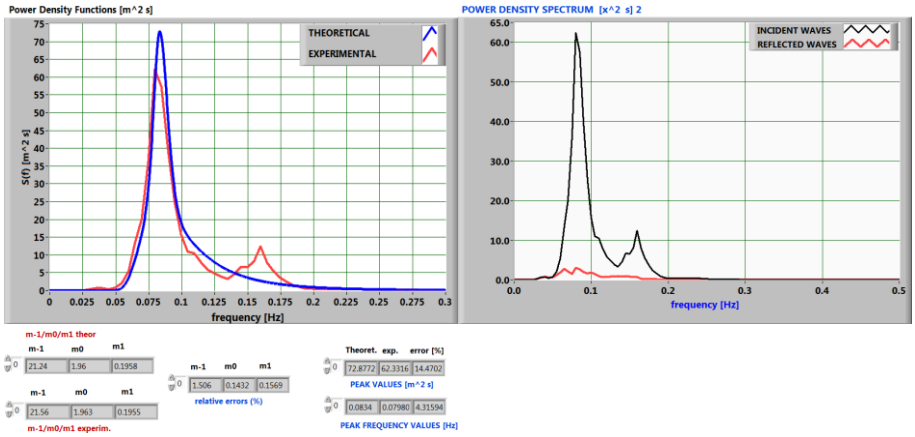

(a) (b)

Figure 5.1.15 Theoretical Jonswap spectrum vs measured (a) and Spectral density of incident and reflected waves (b) for TEST H=5.4m T=12s.

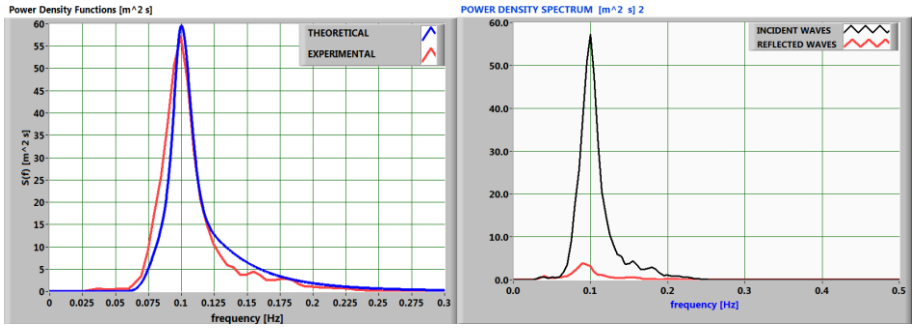

(a) (b)

Figure 5.1.16 Theoretical Jonswap spectrum vs measured (a) and Spectral density of incident and reflected waves (b) for TEST H=6.5m T=10s.

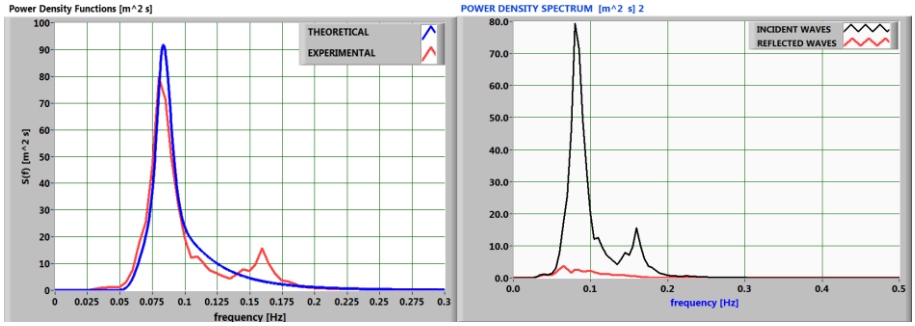

(a) (b)

Figure 5.1.17 Theoretical Jonswap spectrum vs measured (a) and Spectral density of incident and reflected waves (b) for TEST H=6.5m T=12s.

In addition, the wave signal envelope has been also evaluated, as shown in the Figure 5.1.18.

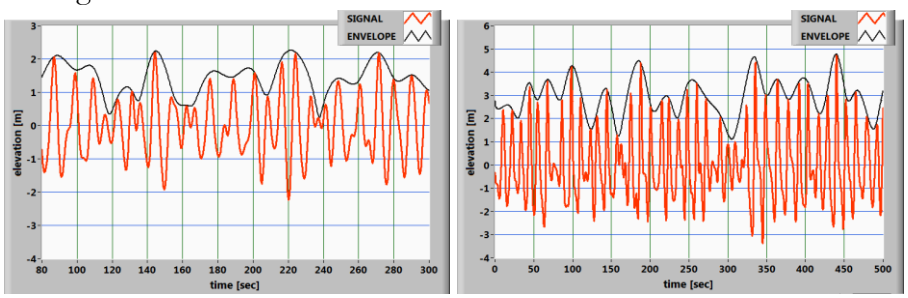

Figure 5.1.18 Example of irregular wave signal envelope for TEST H=4m T=10s (left) and TEST H=6.5m T=12s (right).

On this envelope the mean height and the RMS wave height have been estimated; finally, the analysis on the wave crest has been conducted to evaluate $Cr_{1/3}$. The parameter Cr 1/3 is defined as the significant value of wave peaks (crests) computed via zero up-crossing. This quantity takes into account the asymmetry between crest (which produces overtopping) and troughs (which doesn't).
All these quantities have been introduced to better evaluate their influence on the overtopping phenomenon.

Table 5.1.2 Wave reflection results of irregular wave conditions.

ID SIM	H_{m0} (m)	$H_{1/3}$ (m)	$T_{1/3}$ (s)	kr (-)	$Cr_{1/3}$ (m)	E_{mean} (m)	E_{rms} (m)
IRR_CFD_9	3.27	3.18	11.78	0.46	1.85	**1.41**	**1.52**
IRR_CFD_10	4.61	4.54	11.80	0.32	2.80	**2.14**	**2.33**
IRR_CFD_11	5.58	5.39	12.01	0.30	3.36	**2.63**	**2.78**
IRR_CFD_12	6.28	5.95	12.18	0.28	3.58	**2.98**	**3.08**
IRR_CFD_13	2.88	2.81	9.87	0.46	1.45	**1.10**	**1.18**
IRR_CFD_14	4.04	3.96	9.84	0.34	2.09	**1.58**	**1.70**
IRR_CFD_15	5.00	4.75	9.82	0.30	2.63	**1.97**	**2.10**
IRR_CFD_16	5.50	5.18	9.97	0.29	2.92	**2.26**	**2.38**

5.1.4 Comparison of laboratory and numerical irregular results

The numerical results have been compared with the same experimental results presented previously in the paragraph 4.2.
Figure 5.1.19 shown the mean overtopping discharge as a function of the spectral significant wave height nearshore $H_{m0,}$ for both the laboratory experiments and CFD simulations. The results have been also summarised in Table 5.1.3.

Table 5.1.3 mean overtopping discharge of laboratory measurements vs irregular CFD simulations.

Test	Hs (m)	Tp (s)	$H_{mo,lab}$ (m)	$q_{,lab}$ (m^3/sm)	$H_{mo,cfd}$ (m)	$q_{,irr\_cfd}$ (m^3/sm)
IRR_CFD_9	2.7	12	2.60	**0.185**	3.27	**0.190**
IRR_CFD_10	4.0	12	3.97	**0.339**	4.61	**0.347**
IRR_CFD_11	5.4	12	5.44	**0.557**	5.58	**0.555**
IRR_CFD_12	6.5	12	6.52	**0.800**	6.28	**0.795**
IRR_CFD_13	2.7	10	2.67	**0.183**	2.88	**0.140**
IRR_CFD_14	4.0	10	3.82	**0.294**	4.04	**0.222**
IRR_CFD_15	5.4	10	5.28	**0.467**	5.00	**0.342**
IRR_CFD_16	6.5	10	6.33	**0.667**	5.50	**0.456**

Laboratory and numerical data are supplementary distinguished by peak wave period Tp (10 and 12 seconds).

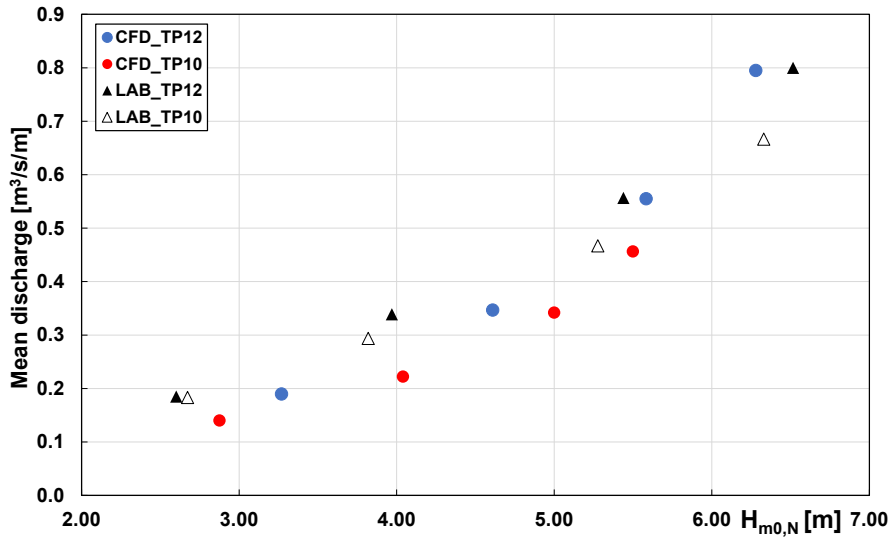

Figure 5.1.19 Mean discharge as function of H_{m0} of numerical and experimental results.

Results exhibit a smooth trend vs H_{m0} with wave period only playing a marginal role. This highlights that the nearshore wave conditions, beach profile (that govern wave evolution) and wall characteristics explain the overtopping response almost totally.
The best fit of all data is a third order polynomial with R^2=0.95.

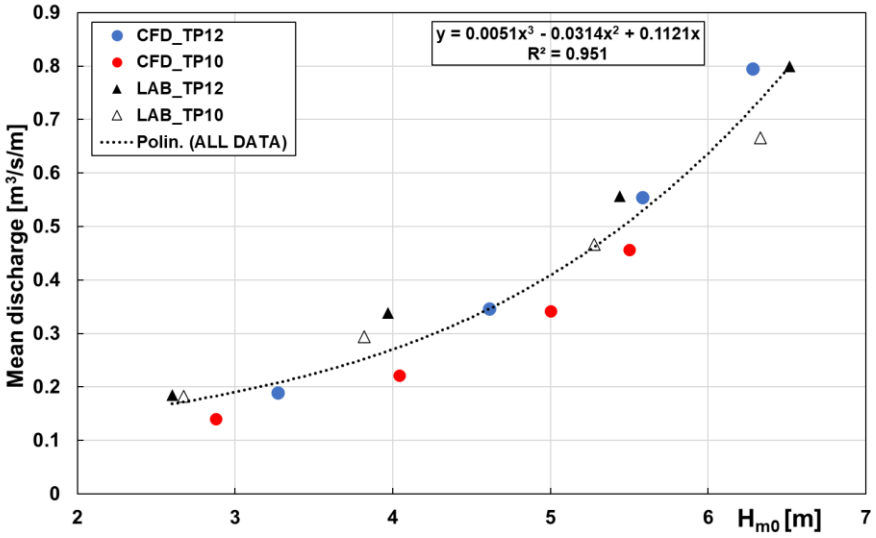

Figure 5.1.20 Mean discharge as function of H_{m0} of numerical and laboratory results of vertical seawall with Rc+3.96m

5.1.1 Analysis of volume distribution for irregular wave

In the previous paragraph the numerical model is used to evaluate average overtopping discharges over vertical seawall.
The time averaged wave overtopping rate is one of the important values in the seawall design. In addition to this, individual wave overtopping quantities generated by the random wave are also important, because the maximum values often reach several times of the time averaged value (Inoue et al. 1989). This explains the importance of investigating individual wave overtopping quantities.
Since no direct measures of the maximum overtopping volume Vmax are available, simulation results are validated against the literature outcome.

When the data are represented in a Weibull plot (considering [ln (- ln(1-F)] along the y-axis and [ln V] along the x-axis) the slope and the intercept of the fitted line allow to estimate the shape and scale factors of the Weibull distribution, respectively.
Individual overtopping volume from CFD experiments proved to be well described by a Weibull Cumulated distribution Function for threshold $1m^3$. The shape parameter, estimated by with the least square method ranges from 0.74 to 0.86 with a mean 0.8 according to literature that suggest value 0.85.

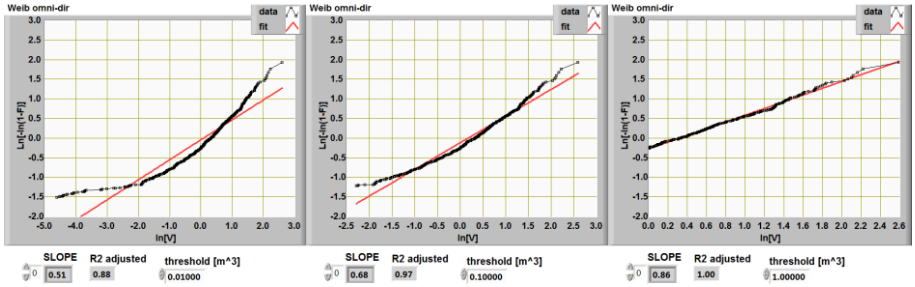

Figure 5.1.21Weibull distribution of wave overtopping volume of TEST H=2.7m T=10s.

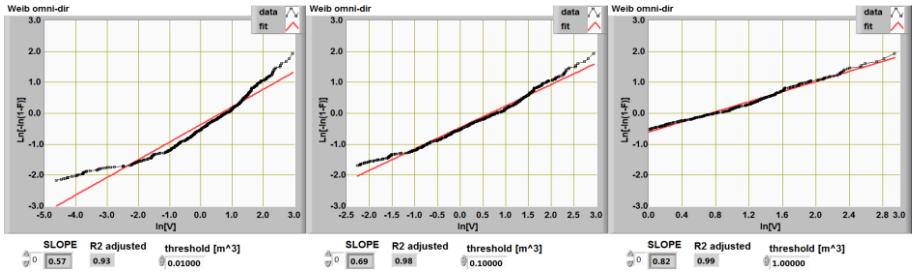

Figure 5.1.22 Weibull distribution of wave overtopping volume of TEST H=4.0m T=10s.

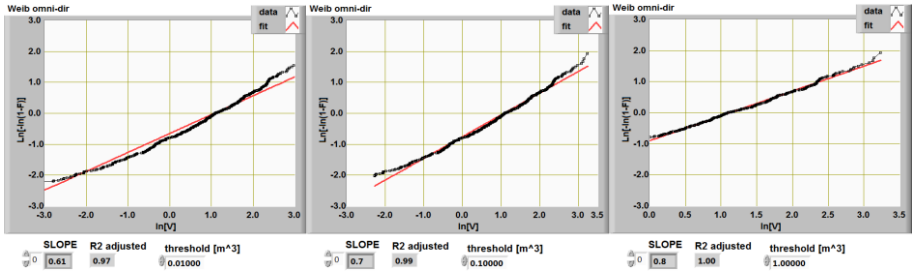

Figure 5.1.23 Weibull distribution of wave overtopping volume of TEST H=5.4m T=10s.

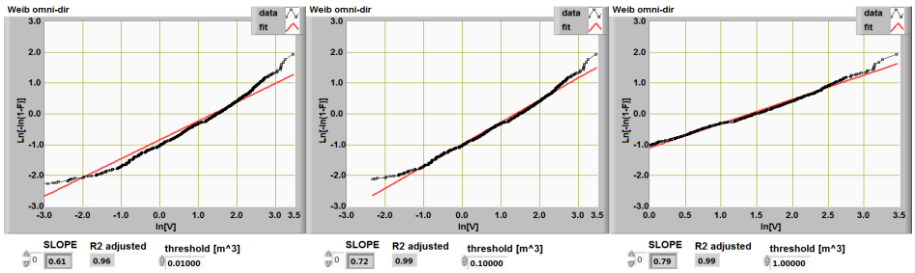

Figure 5.1.24 Weibull distribution of wave overtopping volume of TEST H=6.5m T=10s.

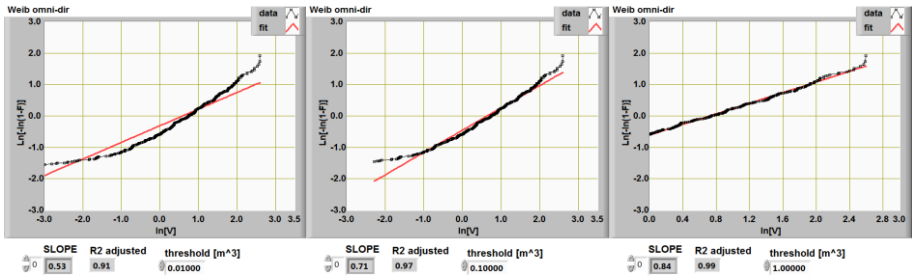

Figure 5.1.25 Weibull distribution of wave overtopping volume of TEST H=2.7m T=12s.

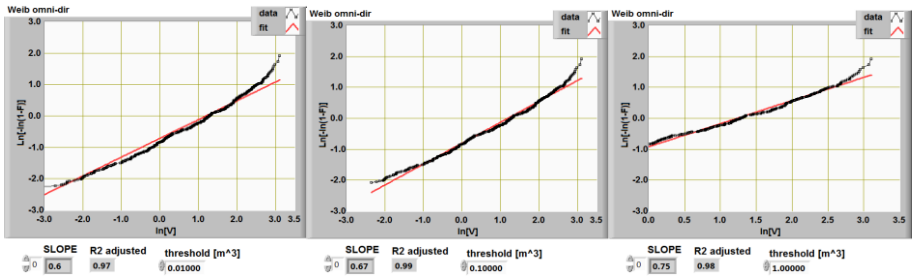

Figure 5.1.26 Weibull distribution of wave overtopping volume of TEST H=4.0m T=12s.

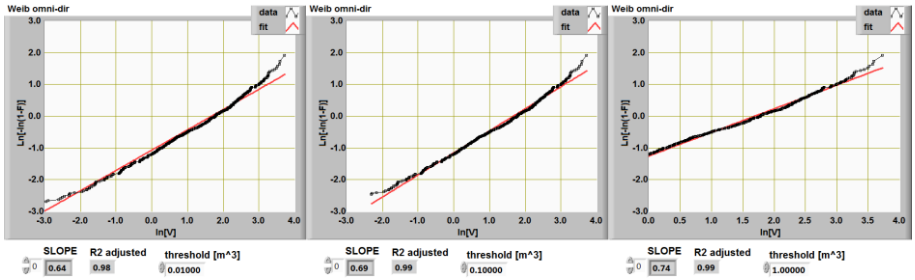

Figure 5.1.27 Weibull distribution of wave overtopping volume of TEST H=5.4m T=12s.

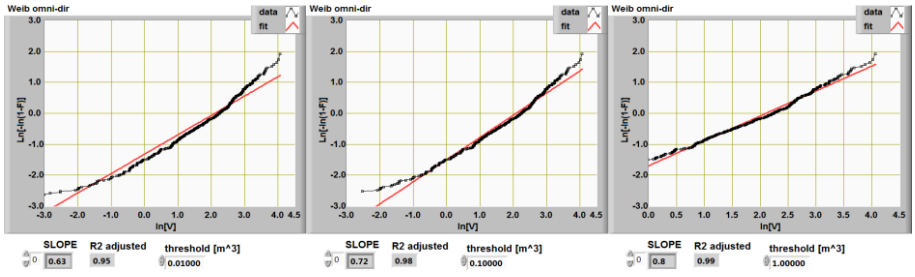

Figure 5.1.28 Weibull distribution of wave overtopping volume of TEST H=6.5m T=12s.

The results are summarized in the follow table.

Table 5.1.4 results of Weibull distribution on irregular CFD data.

T=10s				T=12s			
Id test	Threshold [m^3]	b	$R^2_{adjusted}$	**Id test**	Threshold [m^3]	b	$R^2_{adjusted}$
H=2.7m T=10s	0.01	0.51	0.88	H=2.7m T=12s	0.01	0.53	0.91
	0.1	0.68	0.97		0.1	0.71	0.97
	1.0	0.86	1.00		1.0	0.84	0.99
H=4.0m T=10s	0.01	0.57	0.93	H=4.0m T=12s	0.01	0.60	0.97
	0.1	0.69	0.98		0.1	0.67	0.99
	1.0	0.82	0.99		1.0	0.75	0.98
H=5.4m T=10s	0.01	0.61	0.97	H=5.4m T=12s	0.01	0.64	0.98
	0.1	0.70	0.99		0.1	0.69	0.99
	1.0	0.80	1.00		1.0	0.74	0.99
H=6.5m T=10s	0.01	0.61	0.96	H=6.5m T=12s	0.01	0.63	0.95
	0.1	0.72	0.99		0.1	0.72	0.98
	1.0	0.79	0.99		1.0	0.80	0.99

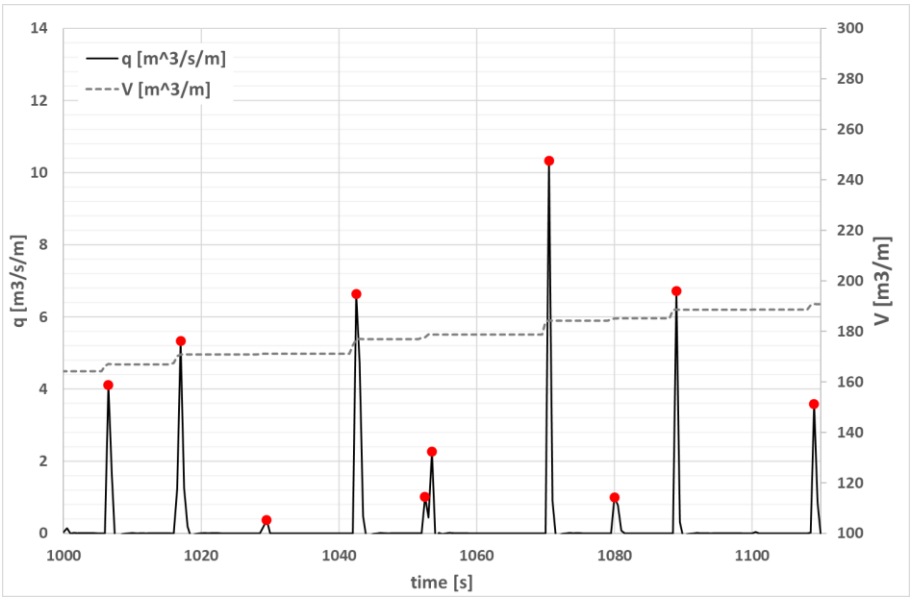

Figure 5.1.29 Time series of cumulated overtopping volume (V) and flow rate (q).

The results of maximum individual wave overtopping, and mean volume calculated trough CFD results of flow rate (Figure 5.1.29) are summarized in the follow table.

Table 5.1.5 Results of Vmax for Irregular CFD data.

Id test	Tm [s]	Vmax (in T_m)[m^3/m]	Vmean [m^3/m]	q_{mean} [$m^3/s/m$]
H=2.7m T=10s	9.567	13.37	1.62	0.140
H=4.0m T=10s	9.385	18.89	2.56	0.222
H=5.4m T=10s	9.384	25.32	3.88	0.342
H=6.5m T=10s	9.534	31.72	5.09	0.456
H=2.7m T=12s	10.913	13.38	2.16	0.190
H=4.0m T=12s	10.884	22.21	3.90	0.347
H=5.4m T=12s	10.769	41.41	6.17	0.555
H=6.5m T=12s	10.970	58.27	8.83	0.795

5.1.2 Overtopping volumes at plain vertical walls with Eurotop,2018 formula

In order to relate to existing practice, the individual wave overtopping volume are compared with methods recommended by the EurOtop Manual (Pullen et al., 2007).

To estimate the number of overtopping waves, the procedure explained in paragraph 2.3.2 is applied for this purpose.

Table 5.1.6 Input data for irregular CFD data.

Id test	H_{m0}	T_{m-10}	Rc_{eff}	$L_{m-10}(T_{m-10})$	s_{m-10}	$h^2/H_{m0}L_{m-10}$	*imp*
H=2.7m T=10s	3.27	10.9	2.23	185.94	0.02	0.019	IMP
H=4.0m T=10s	4.61	10.9	2.23	184.96	0.02	0.014	IMP
H=5.4m T=10s	5.58	10.8	2.23	181.07	0.03	0.012	IMP
H=6.5m T=10s	6.28	11.0	2.23	187.89	0.03	0.010	IMP
H=2.7m T=12s	2.88	9.6	2.23	142.90	0.02	0.029	IMP
H=4.0m T=12s	4.04	9.4	2.23	137.52	0.03	0.030	IMP
H=5.4m T=12s	5.00	9.4	2.23	137.49	0.04	0.021	IMP
H=6.5m T=12s	5.50	9.5	2.23	141.92	0.04	0.017	IMP

As shown in the previous table the impulsiveness parameter $h^2/(H_{m0}\ L_{m-1,0}) \leq 0.23$ and so the wave conditions are identified as impulsive.
Therefore, the following calculations have been developed for this condition as indicated in the paragraph 2.3.2., applying the equation (11)for Vmax and (12) for scale parameter *a*.
Note that for vertical structures for impulsive conditions, the value of shape parameter becomes 0.85.

The results are summarized in the following table:

Table 5.1.7 results of Vmax calculated with EurOtop, 2018.

Id test	H_{m0}	T_{m-10}	Now/ Nw	Nw	b	a	Vmax [m³/m] Eurotop
H=2.7m T=10s	3.27	10.9	1.00	427	0.85	1.045	**15.42**
H=4.0m T=10s	4.61	10.9	1.00	436	0.85	0.965	**28.16**
H=5.4m T=10s	5.58	10.8	1.00	436	0.85	1.064	**44.69**
H=6.5m T=10s	6.28	11.0	1.00	428	0.85	1.182	**64.96**
H=2.7m T=12s	2.88	9.6	1.00	374	0.85	1.138	**10.25**
H=4.0m T=12s	4.04	9.4	1.00	375	0.85	1.311	**16.03**
H=5.4m T=12s	5.00	9.4	1.00	379	0.85	1.161	**24.67**
H=6.5m T=12s	5.50	9.5	1.00	372	0.85	1.120	**33.32**

The value of Now/Nw has been fixed as minimum between value obtained with equation (9) and 1. This expedient has been adopted to

avoid that the formula for impulsive condition for this specific case giving several overtopping waves greater than the total waves in numerical domain.

5.1.3 Discussion on maximum volume distribution

The effectiveness of the predictor for maximum individual overtopping wave volumes under impulsive conditions can be evaluated in Figure 5.1.30.

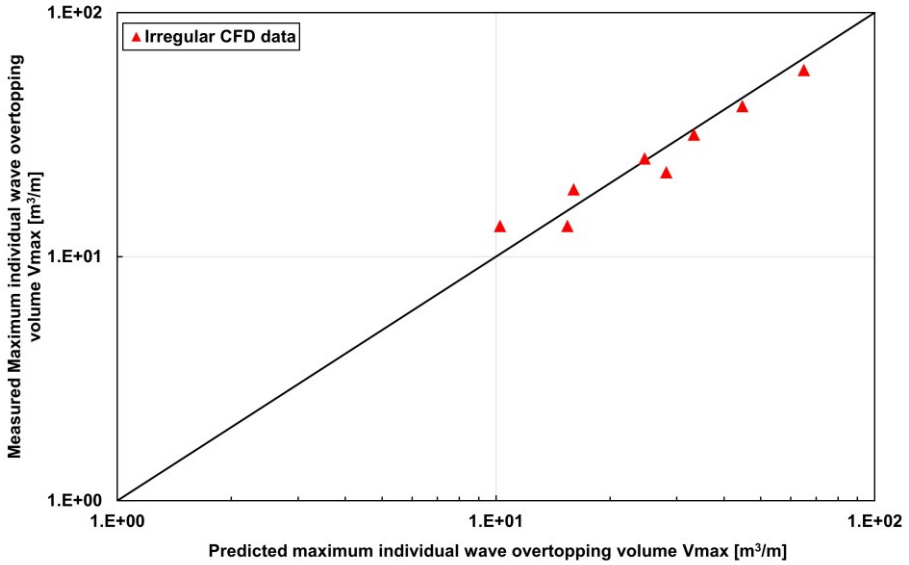

Figure 5.1.30 Predicted and measured maximum individual overtopping volumes. Irregular CFD tests.

The results indicate a reasonable correlation between predicted and measured volumes.
These results have been reported on the Eurotop,2018 graph to evaluate the fit of numerical results with literature data; in addition, for a better comparison, confidence bands have been drawn on EurOtop data.

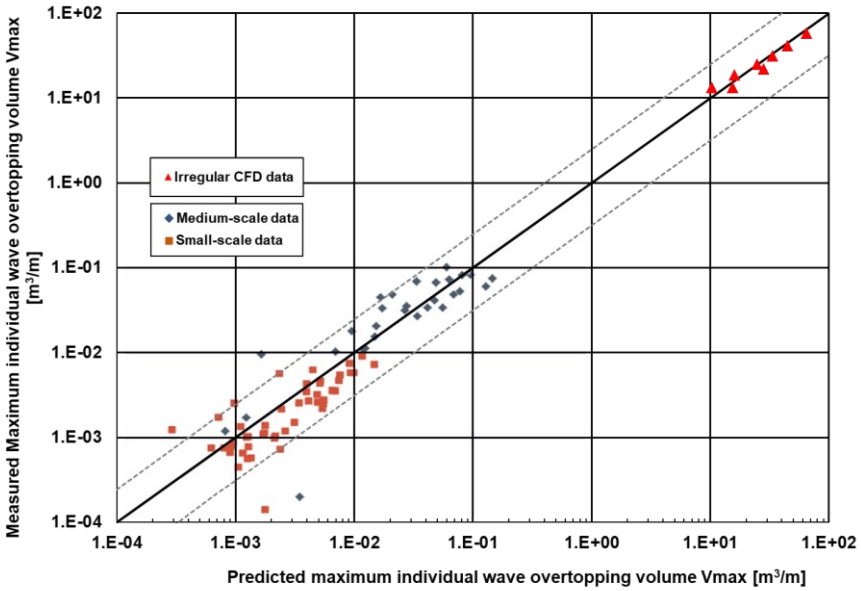

Figure 5.1.31 Irregular CFD vs Small and medium scale tests for plain vertical wall (Pearson et al., 2002-Eurotop,2018). Dashed grey lines mark the confidence band of literature data.

It is important to note that the Weibull distribution parameter "b" to bring exceeding $1m^3$ is in accordance with the value provided in Eurotop, 2018.

Table 5.1.8 shape parameter b of Weibull distribution function for individual overtopping volumes

Id test	b Eurotop,2018	b (Weibull CFDq>$1m^3$)
H=2.7m T=10s	0.85	0.86
H=4.0m T=10s	0.85	0.82
H=5.4m T=10s	0.85	0.80
H=6.5m T=10s	0.85	0.79
H=2.7m T=12s	0.85	0.84
H=4.0m T=12s	0.85	0.75
H=5.4m T=12s	0.85	0.74
H=6.5m T=12s	0.85	0.80

5.2 NUMERICAL ANALYSIS WITH REGULAR WAVE

In this paragraph the analysis of wave overtopping on Malecòn seawall is conducted with regular wave condition.
The first analysis was on current layout of seawall; afterwards, different geometrical seawall configurations have been simulated.
The aim of this analysis is evaluating the performance of regular wave train compared to irregular ones and laboratory measurements.
In detail, the objective is to analyze a smaller number of waves with less computation time than irregular waves. The aim is to provide a fast and efficient method to be used in the early stages of the design.

5.2.1 Numerical implementation

As discussed above, based on typical experimental arrangements the length of wave generation zone and wave structure interaction (Figure 5.2.1) is 410m in X direction, 1 m in Y direction and 40 m in Z direction. The water depth (d) is 20.45m; the geometry of beach profile is the same described in the paragraph 4.2.

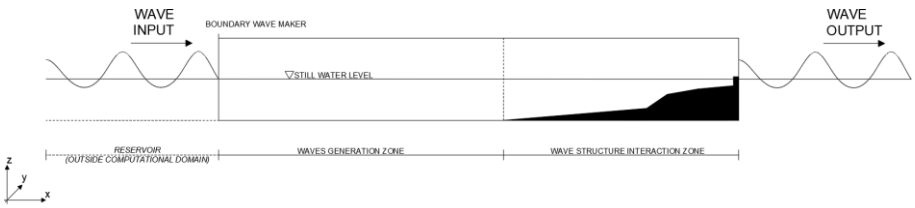

Figure 5.2.1 scheme of numerical domain with regular wave simulations.

In Figure 5.2.2 boundary conditions have been shown, where "S" representing lateral symmetry, "W" standing for wall and "O" shows outflow condition for fluid, "WV" standing for wave maker.

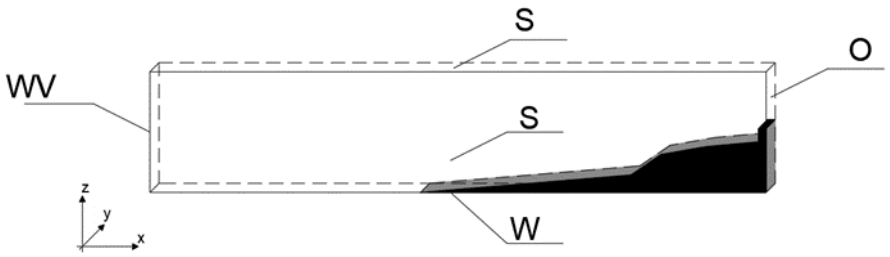

Figure 5.2.2 Boundary condition of 2D-numerical domain with seawall to evaluate wave overtopping.

In this specific case the regular wave condition generated with boundary wave maker are reported in the follow table:

Table 5.2.1. Regular wave condition.

SCENARIO T_R=50 YEARS			
ID SIM	**DEPTH (m)**	**Hs (m)**	**Tp(s)**
TEST1	20.45	8.00	10.00
TEST2	20.45	8.00	12.00
TEST3	20.45	1.50	10.00
TEST4	20.45	1.50	12.00
TEST5	20.45	3.20	10.00
TEST6	20.45	3.20	12.00
TEST7	20.45	1.10	10.00
TEST8	20.45	1.10	12.00
TEST9	20.45	5.40	10.00
TEST10	20.45	5.40	12.00
TEST11	20.45	7.20	10.00
TEST12	20.45	7.20	12.00

Numerical waves (approximately 40 wave) have been generated using the Stokes and cnoidal wave generator available in FLOW-3D.

In its current layout, the Malecòn seawall is a simple vertical wall with a crest freeboard, Rc of + 3.96m relative to the MWL (Figure 5.2.3 (a)). Along with 3.96m, one further has been tested and namely +4.96m. Additionally, on previous vertical seawall a curve layout has been

considered, as sketched in Figure 5.2.4 and Figure 5.2.5. Accordingly, 4 models of seawall (2 curve and 2 vertical) have been employed.

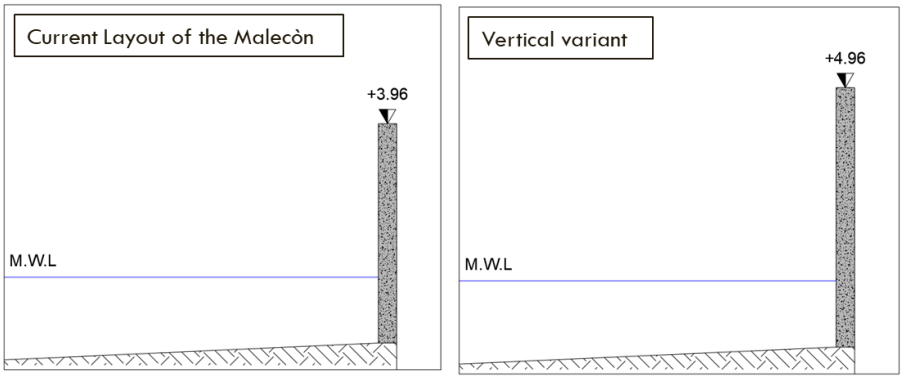

Figure 5.2.3 Geometrical configuration of a) current Layout of Malecòn seawall with Rc +3.96m, b) vertical variant with Rc+4.96m.

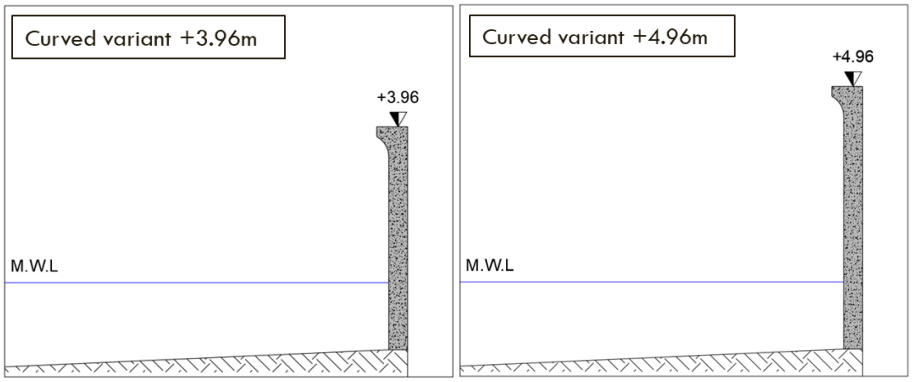

Figure 5.2.4 Geometrical configuration of a) curved variant of Malecòn seawall with Rc +3.96m, b) curved variant with Rc+4.96m.

Further details about curved seawall are indicated in the follow figure:

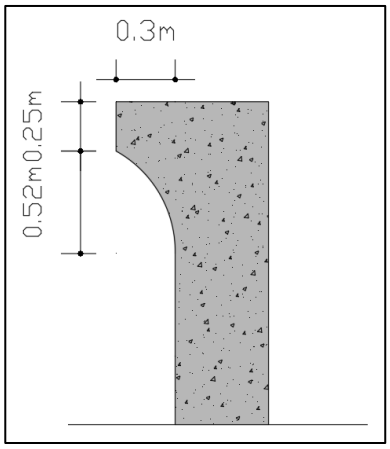

Figure 5.2.5 Geometrical details of curved variant of Malecòn seawall.

The horizontal extension of wave returns wall Br =0.3m, height of wave return hr=0.77m.

5.2.2 Discussion of numerical results

The incoming wave field at the flat floor seaward the foreshore, have been separated from the reflected by using the weighted least squared method proposed by Zelt & Skjelbreia (1992) and described above.
Fluctuations of the free surface were acquired in six positions in the flat part of the domain in front of the structure as reported in Figure 5.2.6.

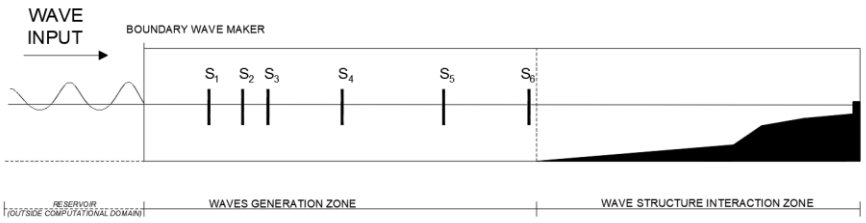

Figure 5.2.6 Position of wave probes for reflection analysis (regular wave conditions).

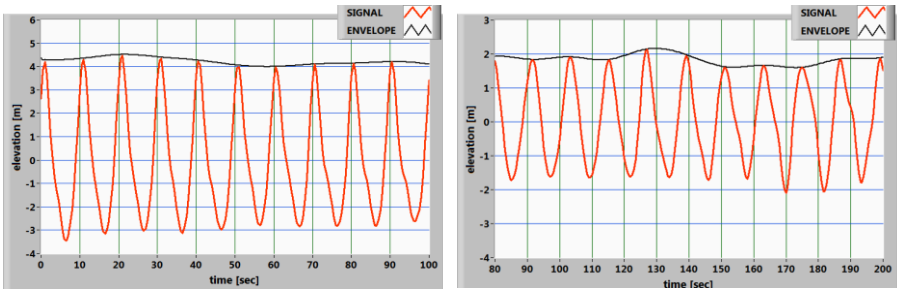

(a) (b)

Figure 5.2.7 Example of regular wave signal envelope (a) TEST1 H=8m T=10s and (b) TEST6 H=1.1m T=10s (Rc+3.96m).

The mean height and the RMS wave height have been estimated on this envelope; finally, the analysis on only wave crest has been conducted to evaluate $Cr_{1/3}$ (the highest third of the wave crest).

Table 5.2.2 results of wave reflection analysis of REGULAR CFD tests with Rc+3.96m.

	$H_{1/3}$(m)	$T_{1/3}$(s)	$Cr_{1/3}$(m)	kr (-)	E_{mean}(m)	E_{rms}(m)
TEST1	7.15	10.00	4.23	0.26	3.99	3.99
TEST2	8.00	12.00	4.99	0.18	4.78	4.79
TEST3	1.89	9.61	1.05	0.71	0.86	0.86
TEST4	1.76	11.61	0.96	0.78	0.80	0.80
TEST5	3.17	10.06	1.68	0.40	1.57	1.58
TEST6	3.68	11.86	1.97	0.42	1.81	1.82
TEST7	1.61	9.44	0.86	0.84	0.66	0.67
TEST8	1.18	8.50	0.75	0.92	0.57	0.58
TEST9	5.05	9.94	2.97	0.34	2.81	2.81
TEST10	5.82	12.00	3.73	0.23	3.33	3.34
TEST11	6.49	9.94	3.85	0.27	3.76	3.76
TEST12	7.40	12.07	4.71	0.19	4.41	4.43

5.2.2.1 Analysis of wave reflection of different seawall configurations

The analysis of wave reflection is also conducted for 3 other configurations of seawall described above.
For simplicity of exposure only the results of the plain and curved configuration of seawall with Rc+4.96m have been reported.

- ***Vertical seawall with Rc+4.96m***

Some results of wave reflection on vertical seawall +4.96m are shown in Figure 5.2.8 and Figure 5.2.9.

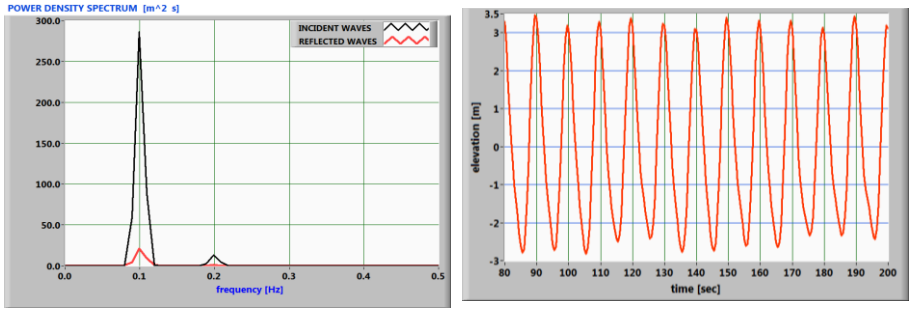

(a) **(b)**

Figure 5.2.8 TEST1 H=8m T=10s (Rc+4.96m vertical) (a) Spectral density of incident and reflected waves and (b) wave signal.

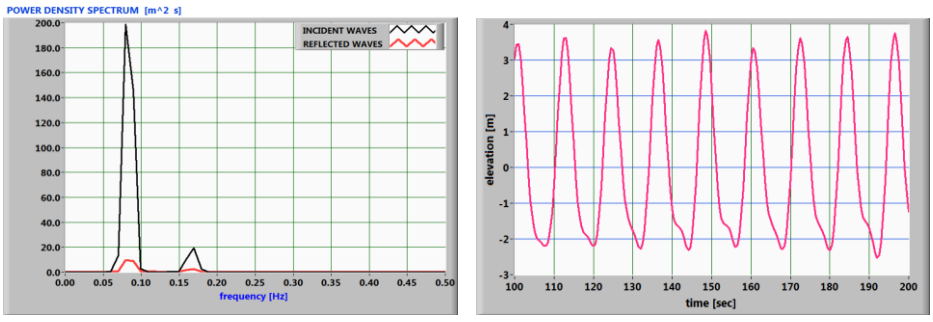

(a) **(b)**

Figure 5.2.9 TEST10 H=5.4m T=12s (Rc+4.96m vertical) (a) Spectral density of incident and reflected waves and (b) wave signal.

The main statistics of generated sea states are summarized in Table 5.2.3.

Table 5.2.3 results of wave reflection analysis of REGULAR CFD tests with Rc+4.96m.

	$H_{1/3}$(m)	$T_{1/3}$(s)	$Cr_{1/3}$(s)
TEST1	6.93	9.56	3.82
TEST2	8.29	12.14	4.95
TEST3	1.79	10.00	0.93
TEST4	1.96	10.94	0.93
TEST5	3.12	9.94	1.67
TEST6	3.77	12.07	2.05
TEST7	1.48	9.94	0.83
TEST8	1.16	9.25	0.68
TEST9	5.14	9.94	2.75
TEST10	6.02	12.07	3.69
TEST11	6.38	10.06	3.45
TEST12	7.51	12.07	4.56

- ***Curve seawall with Rc+4.96m***

In the follow the results of wave reflection analysis for Curve seawall configuration are reported.

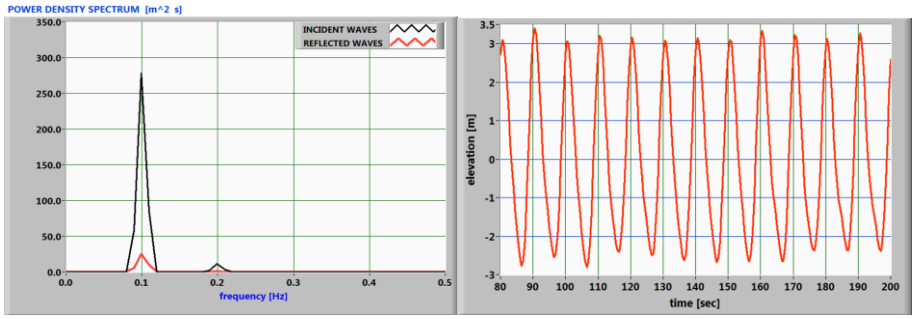

(a) (b)

Figure 5.2.10 TEST1 H=8m T=10s (Rc+4.96m CURVE) (a) Spectral density of incident and reflected waves and (b) wave signal.

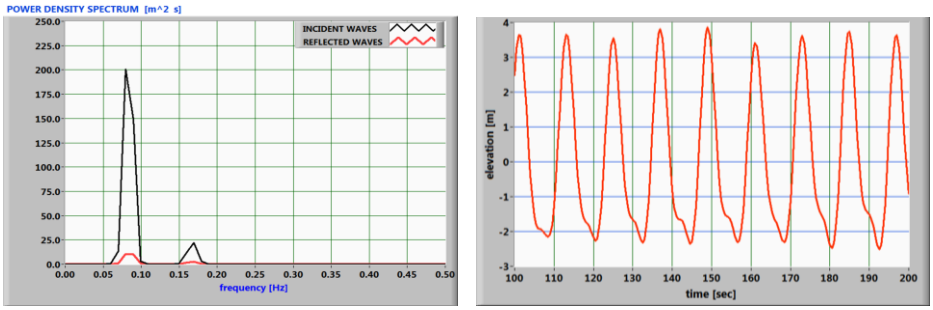

(a) (b)

Figure 5.2.11 TEST10 H=5.4m T=12s (Rc+4.96m CURVE) (a) Spectral density of incident and reflected waves and (b) wave signal.

The main statistics of generated sea states are summarized in Table 5.2.4.

Table 5.2.4 results of wave reflection analysis of REGULAR CFD tests of CURVE seawall Rc+4.96m.

	$H_{1/3}$(m)	$T_{1/3}$(s)	$Cr_{1/3}$(s)
TEST1	6.83	9.50	3.70
TEST2	8.11	12.07	4.86
TEST3	1.72	10.00	0.89
TEST4	2.14	11.56	0.97
TEST5	3.08	9.94	1.68
TEST6	3.84	12.07	2.10
TEST7	1.47	9.94	0.82
TEST8	1.21	8.94	0.67
TEST9	4.99	9.94	2.78
TEST10	6.12	12.07	3.75
TEST11	6.37	10.06	3.45
TEST12	7.66	12.00	4.58

It is also noted that the main statistic of generated sea state of curved configurations differs slightly from the same vertical configuration.

5.2.3 Regular vs irregular CFD results

For regular and irregular wave conditions comparison, different parameters of the wave profile were considered, as illustrated below.

The parameter $H_{1/3}$ is most useful for engineering purposes and therefore will be used for the validation.
The following graphs show the mean discharge as function of the main parameters calculated on nearshore wave profile ($H_{1/3,N}$, $Cr_{1/3,N}$, $E_{mean,N}$, $E_{rms,N}$).
The best trend model of all data has also been represented in the graphs.

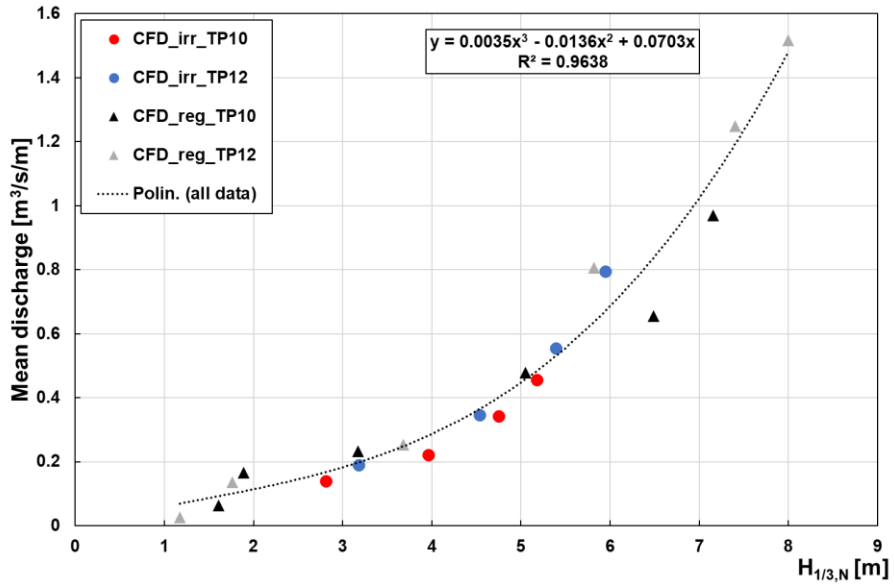

Figure 5.2.12 Regression model of CFD results of mean discharge related to $H_{1/3,N}$ for vertical seawall Rc+3.96m.

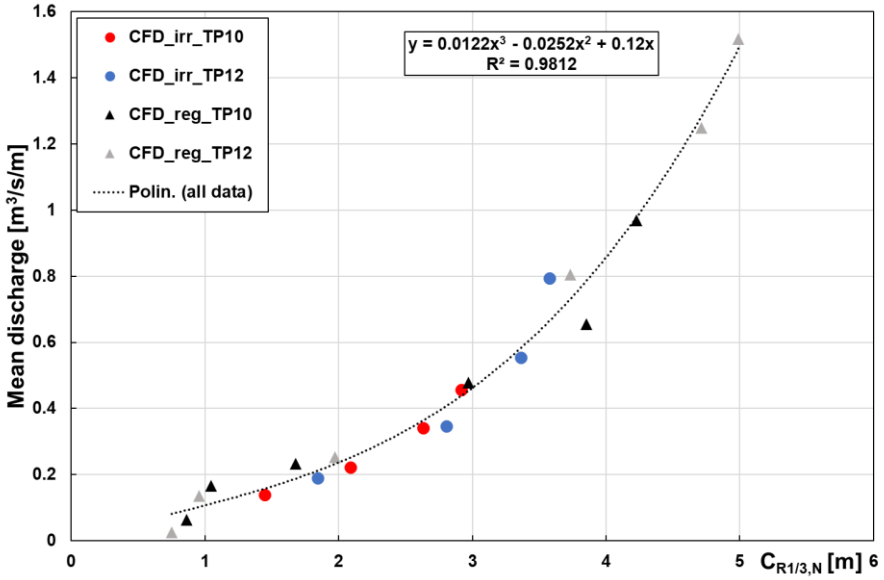

Figure 5.2.13 Regression model of CFD results of mean discharge related to $Cr_{1/3,N}$ for vertical seawall Rc+3.96m.

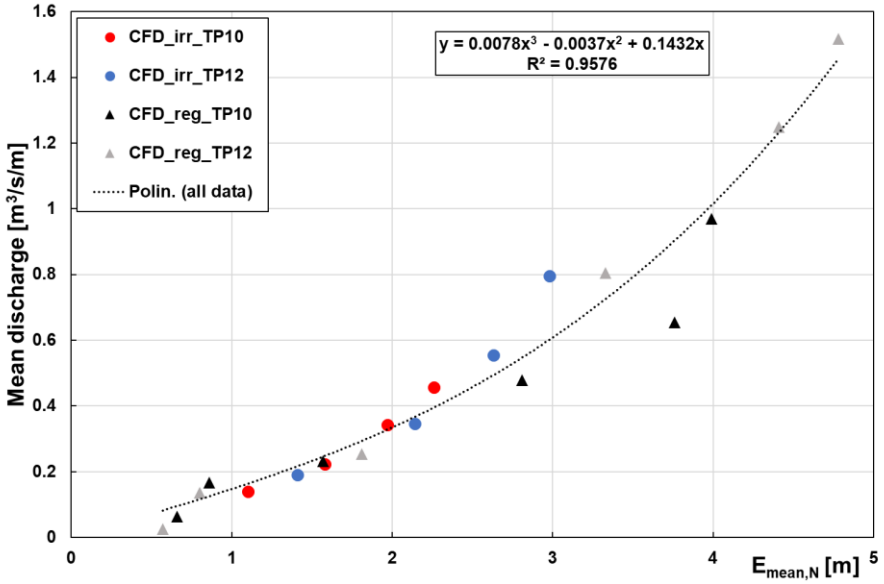

Figure 5.2.14 Regression model of CFD results of mean discharge related to E_{mean} for vertical seawall Rc+3.96m.

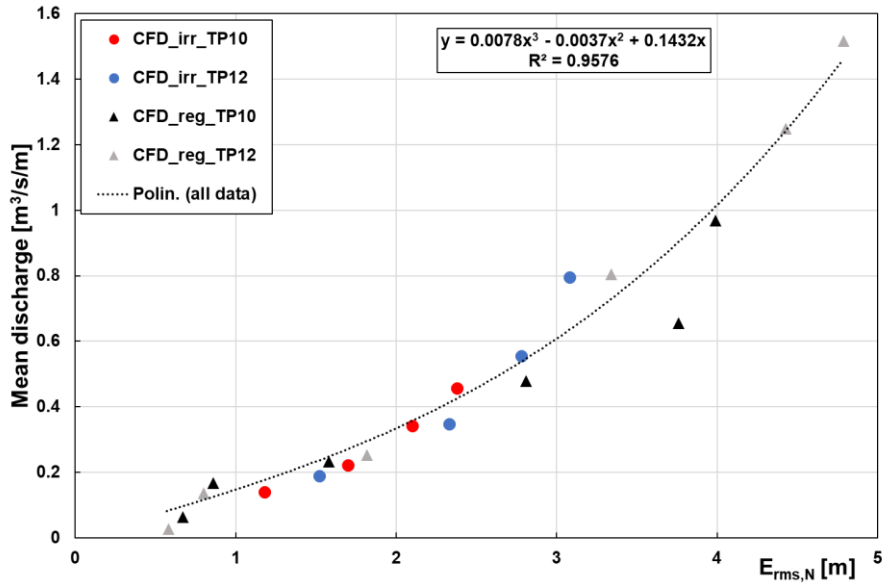

Figure 5.2.15 Regression model of CFD results of mean discharge related to E_{rms} for vertical seawall Rc+3.96m.

A further comparison of CFD results (regular vs irregular) is based on the assessment of the regression model on the two datasets separately and a comparison of the coefficients against the confidence intervals.
The form of regression model selected is a third order polynomial; the typical cubic function is:
$f(x)=ax^3+bx^2+cx+d$, $d=0$ (passing through origin)
The all parameters of wave profile have been used for the comparison; the coefficients value and the confidence level of 95% are summarized in the Table 5.2.5.

Table 5.2.5 Regression model on predictions of mean discharge with $H_{1/3}$- irregular vs regular wave condition.

	Third order polynomial (Irregular CFD data)			Third order polynomial (Regular CFD data)		
	Coefficients	*Inf. 95.0%*	*Sup.95.0%*	*Coefficient*	*Inferior 95.0%*	*Superior 95.0%*
d	0	-	-	0	-	-
c	0.188	0.082	0.294	0.091	-0.028	0.211
b	-0.080	-0.128	-0.033	-0.020	-0.066	0.027
a	0.012	0.007	0.017	0.004	0.000	0.008

Table 5.2.6 Regression model on predictions of mean discharge with $Cr_{1/3}$- irregular vs regular wave condition.

	Third order polynomial (Irregular CFD data)			Third order polynomial (Regular CFD data)		
	Coefficients	*Inf. 95.0%*	*Sup.95.0%*	*Coefficient*	*Inferior 95.0%*	*Superior 95.0%*
d	0	-	-	0	-	-
c	0.224	-0.050	0.498	0.155	0.042	0.267
b	-0.134	-0.343	0.075	-0.044	-0.113	0.026
a	0.036	-0.002	0.075	0.014	0.004	0.025

Table 5.2.7 Regression model on predictions of mean discharge with E_{mean}- irregular vs regular wave condition.

	Third order polynomial (Irregular CFD data)			Third order polynomial (Regular CFD data)		
	Coefficients	*Inf. 95.0%*	*Sup.95.0%*	*Coefficient*	*Inferior 95.0%*	*Superior 95.0%*
d	0	-	-	0	-	-
c	0.153	-0.027	0.333	0.179	0.007	0.351
b	-0.056	-0.224	0.112	-0.048	-0.157	0.061
a	0.031	-0.007	0.069	0.016	-0.001	0.033

Table 5.2.8 Regression model on predictions of mean discharge with Erms-irregular vs regular wave condition.

	Third order polynomial (Irregular CFD data)			Third order polynomial (Regular CFD data)		
	Coefficients	*Inf. 95.0%*	*Sup.95.0%*	*Coefficient*	*Inferior 95.0%*	*Superior 95.0%*
d	0	-	-	0	-	-
c	0.187	-0.063	0.438	0.176	0.007	0.346
b	-0.100	-0.324	0.124	-0.046	-0.153	0.061
a	0.039	-0.009	0.088	0.016	-0.001	0.032

The results showed that the trends of the regular data are consistent with the irregular ones and the results with good approximation can be identified by a single regression line. A further comparison is shown in Figure 5.2.17 for two period Tp=10s ad Tp=12s.

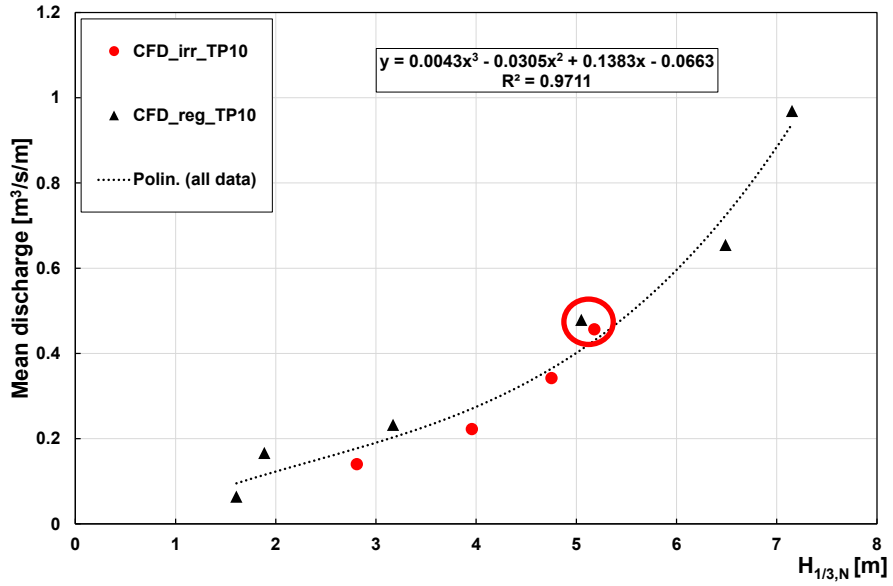

Figure 5.2.16 Regression model of CFD results of mean discharge related to $H_{1/3,N}$ for vertical seawall Rc+3.96m and Tp=10s.

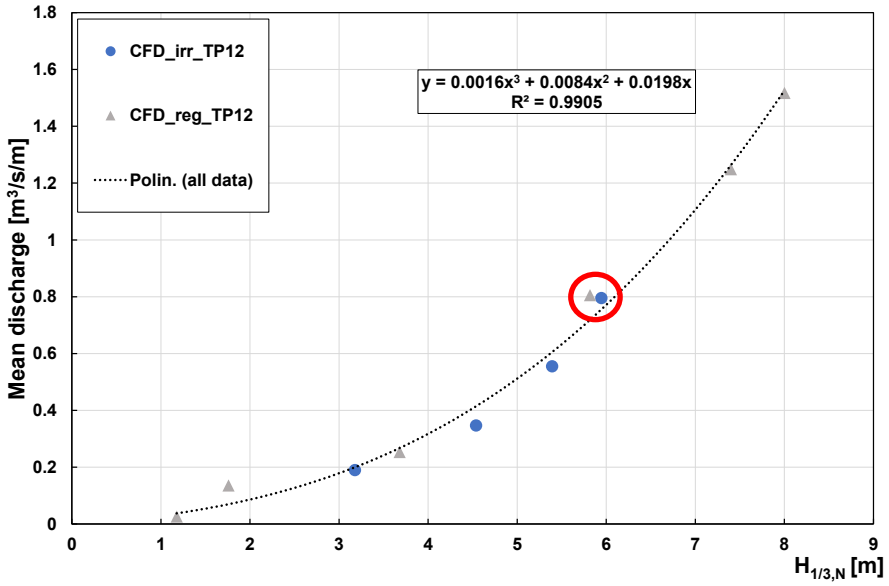

Figure 5.2.17 Regression model of CFD results of mean discharge related to $H_{1/3,N}$ for vertical seawall Rc+3.96m and Tp=12s.

The best fit model is a third order polynomial that give R^2=0.97 for Tp=10s and R^2=0.99 for Tp=12s.

The results obtained from the regular and irregular wave comparison showed for the two wave conditions circled in red that two waves with the same wave height nearshore produce the same mean overflow rate.

This is an interesting result and for this reason an analysis of the spectra occurring at the wall was developed.

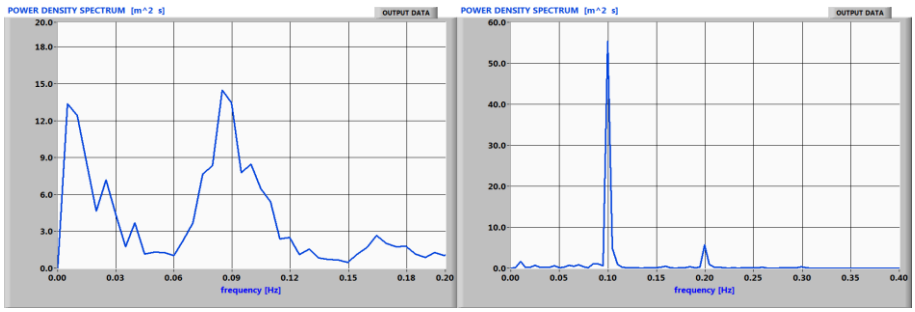

(a) **(b)**

Figure 5.2.18 Measured spectrum at wall (a) irregular wave train, (b) regular waves for Tp= 10s.

In the figure below the two wave spectra at seawall clearly show that the low frequencies that occur for irregular wave trains which are instead absent for regular waves, do not contribute to mean overtopping discharge.

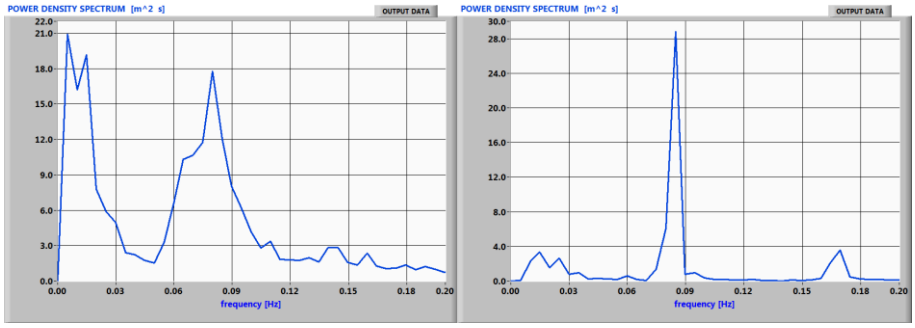

(a) **(b)**

Figure 5.2.19 Measured spectrum at wall (a) irregular wave train, (b) regular waves for Tp= 12s.

The comparison of regular vs irregular CFD data is reasonable and therefore the importance of low frequencies of the spectrum becomes relative.

5.2.4 Numerical results of different configuration of seawall and comparison with laboratory experiments.

The objective is to evaluate the extensibility of the results obtained for the wall in the current configuration (vertical with Rc+3.96m) to possible geometrical variations of the seawall.

An example is given in the Figure 5.2.20 in which is shown the effect of curve seawall.

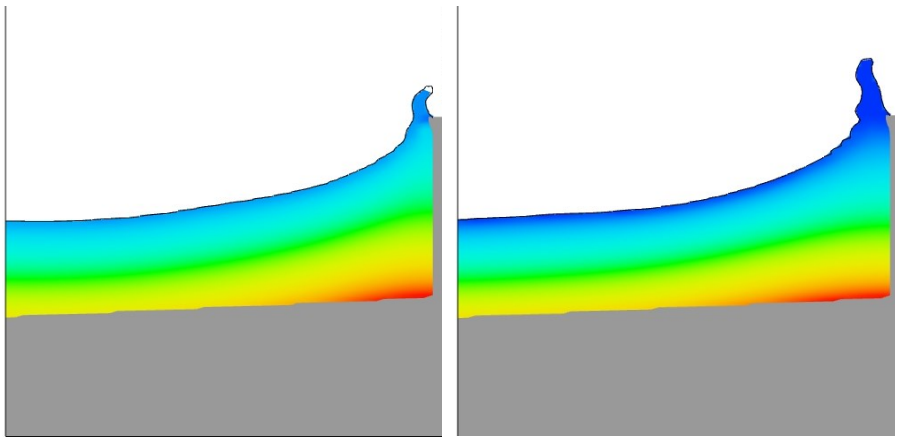

Figure 5.2.20 Effect of bullnose in numerical simulation.

For this purpose, regular CFD has been compared with laboratory measurements.

The regular CFD results and laboratory measurements of mean overtopping discharge relative to all configurations of seawall analysed are summarized in the follow tables and then compared in the following graphs.

Table 5.2.9 Regular CFD result of mean overtopping discharge of all seawall configurations.

				q (m³/s/m)			
				Vertical variant		Curved variant	
ID SIM	**Hs (m)**	**Tp (s)**	**$H_{1/3}$ (m)**	**+3,96 (m)**	**+4,96 (m)**	**+3,96 (m)**	**+4.96 (m)**
TEST1	8.00	10.00	7.15	0.969	0.551	0.738	0.341
TEST2	8.00	12.00	8.00	1.517	0.869	1.213	0.707
TEST3	1.50	10.00	1.89	0.167	0.036	0.071	0.002
TEST4	1.50	12.00	1.76	0.136	0.051	0.082	0.006
TEST5	3.20	10.00	3.17	0.232	0.110	0.110	0.023
TEST6	3.20	12.00	3.68	0.253	0.178	0.227	0.105
TEST7	1.10	10.00	1.61	0.064	0.015	0.031	0.000
TEST8	1.10	12.00	1.18	0.026	0.004	0.019	0.000
TEST9	5.40	10.00	5.05	0.479	0.237	0.279	0.117
TEST10	5.40	12.00	5.82	0.805	0.496	0.725	0.341
TEST11	7.20	10.00	6.49	0.655	0.328	0.570	0.161
TEST12	7.20	12.00	7.40	1.249	0.751	1.160	0.733

Table 5.2.10 Laboratory measurements of mean overtopping discharge of all seawall configurations.

				$q_{,LAB}$ (m³/s/m)			
				Vertical variant		Curved variant	
Id Test	**Hs (m)**	**Tp (s)**	**$H_{1/3,lab}$ (m)**	**+3,96 (m)**	**+4,96 (m)**	**+3,96 (m)**	**+4.96 (m)**
LAB _9	2.7	12	2.53	0.185	0.104	0.133	0.045
LAB _10	4.0	12	3.88	0.339	0.190	0.292	0.127
LAB _11	5.4	12	5.28	0.557	0.337	0.513	0.256
LAB _12	6.5	12	6.09	0.800	0.495	0.762	0.414
LAB _13	2.7	10	2.51	0.183	0.092	0.133	0.05
LAB _14	4.0	10	3.74	0.294	0.14	0.188	0.087
LAB _15	5.4	10	4.96	0.467	0.244	0.342	0.188
LAB_16	6.5	10	5.99	0.667	0.386	0.637	0.317

The mean overtopping discharge as function of $H_{1/3,N}$ has been shown in the follow graphs and all geometrical configuration has been considered.

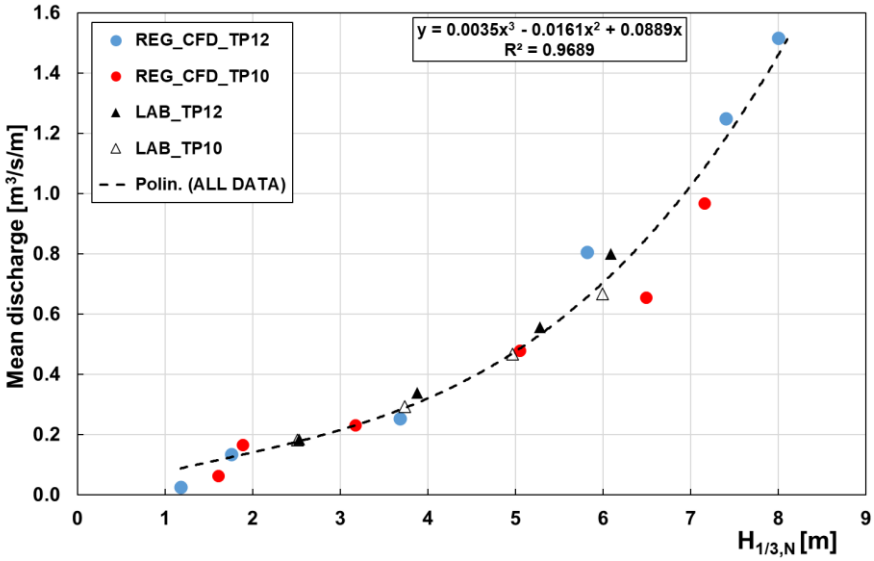

Figure 5.2.21 Mean discharge as function of $H_{1/3}$ of numerical and laboratory results of vertical seawall with Rc+3.96m.

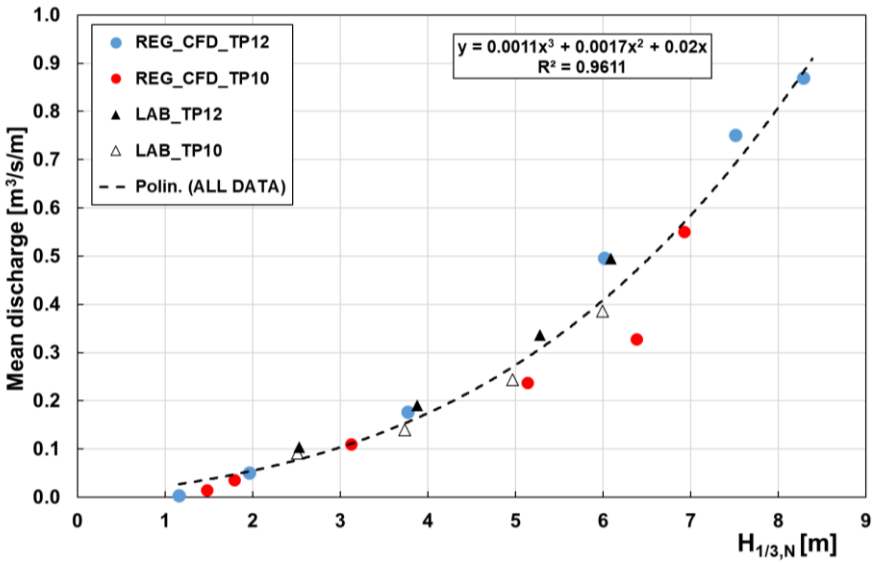

Figure 5.2.22 Mean discharge as function of $H_{1/3}$ of numerical and laboratory results of vertical seawall with Rc+4.96m.

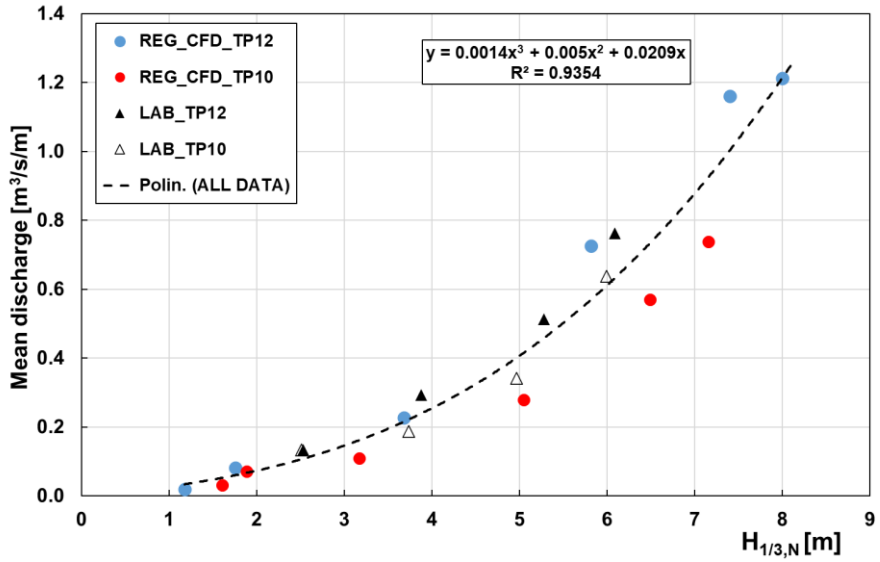

Figure 5.2.23 Mean discharge as function of $H_{1/3}$ of numerical and laboratory results of CURVE seawall with Rc+3.96m.

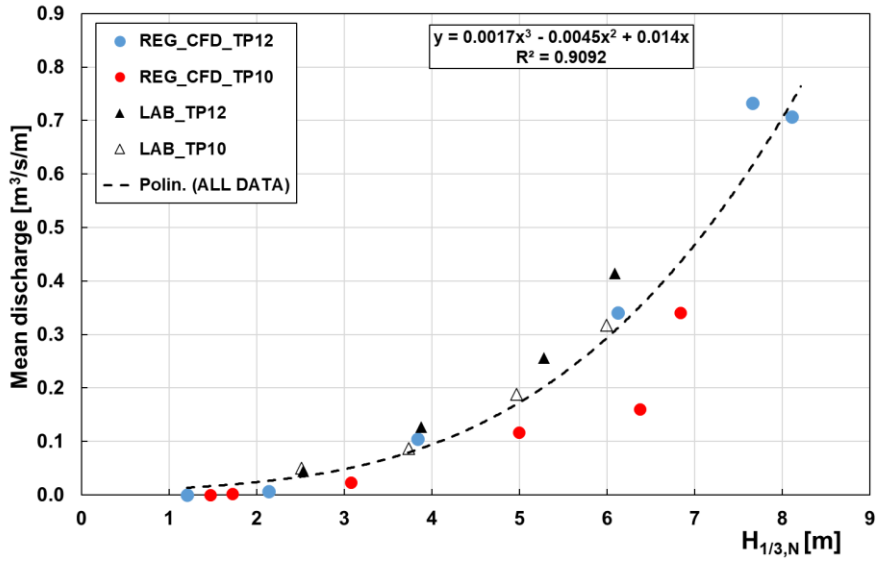

Figure 5.2.24 Mean discharge as function of $H_{1/3}$ of numerical and experimental results of CURVE seawall with Rc+4.96m.

The hypothesis of applicability of a reduced band spectrum also remains valid for other configurations. The results are consistent with laboratory measurements.
In the following paragraph a specific validation for all configurations of seawall is also carried out.

6 ANALYSIS OF LABORATORY DATA AND COMPARISON OF NUMERICAL METHOD

6.1 PRELIMINARY ANALYSIS OF LABORATORY DATA FOR VERTICAL SEAWALL WITH Rc+3.96

In this part of the research the laboratory data have been analysed to validate numerical results.

Given the shallow foreshore affecting the Malecòn, particular attention has been drawn to the role of wave set up and long wave components of the incident wave spectrum on the predictability of the mean overtopping discharge.

Calculations for wave overtopping for 4 conditions were performed using the empirical equations (EurOtop,2018) and the artificial neural network tool.

In details, 4 conditions have been considered:

1. high frequencies only: the wave setup is **not** included in the calculations.
2. high frequencies only: the wave setup is included in the calculations.
3. all frequencies: the wave setup is **not** included in the calculations.
4. all frequencies: the wave setup is included in the calculations.

The input data for different conditions are summarized in Table 6.1.1, Table 6.1.2, Table 6.1.3, and Table 6.1.4.

Table 6.1.1 Experimental data with High Frequencies only, the wave setup is not **included in the calculations.**

ID	Rc (m)	q_{mis} ($m^3/s/m$)	Surge (m)	Wave set-up (m)	Rc_{eff} (m)	h (m)	H_{m0} (m)	T_{m-10} (s)	T_p (s)
9	3.96	0.18	1.73	0.02	**2.23**	3.43	**1.82**	**9.39**	11.54
10	3.96	0.34	1.73	0.14	**2.23**	3.43	**2.09**	**10.01**	12.18
11	3.96	0.56	1.73	0.35	**2.23**	3.43	**2.32**	**10.18**	12.90
12	3.96	0.80	1.73	0.54	**2.23**	3.43	**2.63**	**10.62**	12.90
13	3.96	0.18	1.73	0.03	**2.23**	3.43	**1.65**	**7.60**	9.97
14	3.96	0.29	1.73	0.15	**2.23**	3.43	**1.80**	**8.39**	10.44
15	3.96	0.47	1.73	0.33	**2.23**	3.43	**2.11**	**8.82**	10.97
16	3.96	0.67	1.73	0.51	**2.23**	3.43	**2.28**	**9.23**	10.44

Table 6.1.2 Experimental data with High Frequencies only, the wave setup is included in the calculations.

ID	Rc (m)	q_{mis} ($m^3/s/m$)	Surge (m)	Wave set-up (m)	Rc_{eff} (m)	h (m)	H_{m0} (m)	T_{m-10} (s)	T_p (s)
9	3.96	0.18	1.73	0.02	**2.21**	3.45	**1.82**	**9.39**	11.54
10	3.96	0.34	1.73	0.14	**2.09**	3.57	**2.09**	**10.01**	12.18
11	3.96	0.56	1.73	0.35	**1.88**	3.78	**2.32**	**10.18**	12.90
12	3.96	0.80	1.73	0.54	**1.69**	3.97	**2.63**	**10.62**	12.90
13	3.96	0.18	1.73	0.03	**2.20**	3.46	**1.65**	**7.60**	9.97
14	3.96	0.29	1.73	0.15	**2.08**	3.58	**1.80**	**8.39**	10.44
15	3.96	0.47	1.73	0.33	**1.90**	3.76	**2.11**	**8.82**	10.97
16	3.96	0.67	1.73	0.51	**1.72**	3.94	**2.28**	**9.23**	10.44

Table 6.1.3 Experimental data with All Frequencies, the wave setup is not **included in the calculations.**

ID	Rc (m)	q_{mis} ($m^3/s/m$)	Surge (m)	Wave set-up (m)	Rc_{eff} (m)	h (m)	H_{m0} (m)	T_{m-10} (s)	T_p (s)
9	3.96	0.18	1.73	0.02	**2.23**	3.43	**1.91**	**17.49**	12.90
10	3.96	0.34	1.73	0.14	**2.23**	3.43	**2.30**	**25.26**	12.18
11	3.96	0.56	1.73	0.35	**2.23**	3.43	**2.63**	**31.85**	12.18
12	3.96	0.80	1.73	0.54	**2.23**	3.43	**2.93**	**24.38**	12.18
13	3.96	0.18	1.73	0.03	**2.23**	3.43	**1.72**	**12.99**	9.54
14	3.96	0.29	1.73	0.15	**2.23**	3.43	**2.01**	**24.01**	10.44
15	3.96	0.47	1.73	0.33	**2.23**	3.43	**2.42**	**33.75**	10.97
16	3.96	0.67	1.73	0.51	**2.23**	3.43	**2.67**	**32.62**	10.97

Table 6.1.4 Experimental data with All Frequencies, the wave setup is included in the calculations.

ID	Rc (m)	q_{mis} ($m^3/s/m$)	Surge (m)	Wave set-up (m)	Rc_{eff} (m)	h (m)	H_{m0} (m)	T_{m-10} (s)	T_p (s)
9	3.96	0.18	1.73	0.02	**2.21**	3.45	**1.91**	**17.49**	12.90
10	3.96	0.34	1.73	0.14	**2.09**	3.57	**2.30**	**25.26**	12.18
11	3.96	0.56	1.73	0.35	**1.88**	3.78	**2.63**	**31.85**	12.18
12	3.96	0.80	1.73	0.54	**1.69**	3.97	**2.93**	**24.38**	12.18
13	3.96	0.18	1.73	0.03	**2.20**	3.46	**1.72**	**12.99**	9.54
14	3.96	0.29	1.73	0.15	**2.08**	3.58	**2.01**	**24.01**	10.44
15	3.96	0.47	1.73	0.33	**1.90**	3.76	**2.42**	**33.75**	10.97
16	3.96	0.67	1.73	0.51	**1.72**	3.94	**2.67**	**32.62**	10.97

The wave period, $T_{m-1,0}$ and significant wave height, H_{m0}, are required at the toe of the structure. These are spectral parameters and low frequency energy in the surf zone causes, $T_{m-1,0}$ to be larger than, Tp/1.1, the usual approximation, and H_{m0}, to be larger than the probabilistic significant wave height $H_{1/3}$.

The literature formulas with H_{m0} and $T_{m-1,0}$, are applied to this purpose but pointing out that in practice are not always easy to determine.

6.1.1 Comparison of laboratory data with EurOtop formula

Using the formula of EurOtop, 2018 for vertical wall as discussed in paragraph 2.3.1, the mean overtopping flow rate was calculated for the 4 wave conditions described above.

Table 6.1.5 predicted value of mean discharge q with Eurotop,2018.

		VERTICAL SEAWALL Rc+3.96				
		$q_{mean}(m^3/s/m)$				
ID	**Rc (m)**	q_{MEAS}	$q_{CALC\_Eurotop}$ **COND_1**	$q_{CALC\_Eurotop}$ **COND_2**	$q_{CALC\_Eurotop}$ **COND_3**	$q_{CALC\_Eurotop}$ **COND_4**
9	3.96	0.185	0.036	0.037	0.082	0.083
10	3.96	0.339	0.068	0.077	0.243	0.272
11	3.96	0.557	0.100	0.133	0.489	0.625
12	3.96	0.800	0.164	0.239	0.534	0.744
13	3.96	0.183	0.019	0.020	0.039	0.041
14	3.96	0.294	0.031	0.036	0.137	0.159
15	3.96	0.467	0.061	0.083	0.389	0.501
16	3.96	0.667	0.086	0.131	0.526	0.747

These results are used below to evaluate the accuracy of all estimating methods.

6.1.2 Comparison of laboratory data with Neural Network

The different conditions have been applied in Neural Network as described in paragraph 2.3.3.. The all-input parameters (geometry and wave) are described in previous tables (Table 6.1.1 to Table 6.1.4) for different conditions analysed. As far as the foreshore slope, *m*, is concerned, an equivalent value has been calculated as the average bottom slope from the wall to one (peak) wavelength nearshore.

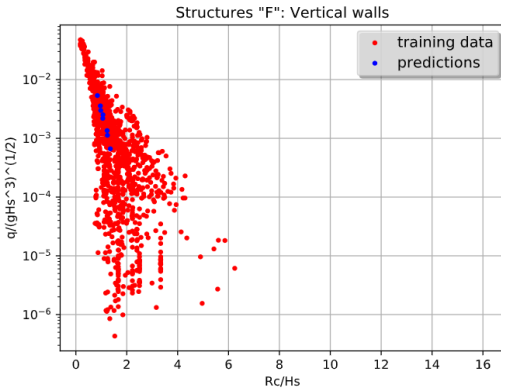

Test-ID	Average	Prototype	5.0%	95.0%	E
1_1	1.04e-02	1.04e-02	4.37e-03	2.29e-02	0.0000
1_2	2.39e-02	2.39e-02	9.93e-03	5.85e-02	0.0000
1_3	3.94e-02	3.94e-02	1.62e-02	9.95e-02	0.0000
1_4	7.15e-02	7.15e-02	2.92e-02	1.82e-01	0.0000
1_5	4.38e-03	4.38e-03	2.09e-03	8.44e-03	0.0000
1_6	8.50e-03	8.50e-03	4.09e-03	1.80e-02	0.0000
1_7	2.10e-02	2.10e-02	1.00e-02	4.62e-02	0.0000
1_8	3.21e-02	3.21e-02	1.45e-02	7.56e-02	0.0000

Figure 6.1.1 Results of ANN tool of CONDITION 1 (vertical seawall Rc+3.96).

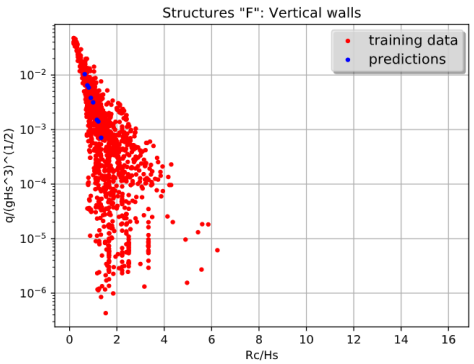

Test-ID	Average	Prototype	5.0%	95.0%	E
1_1	1.08e-02	1.08e-02	4.66e-03	2.35e-02	0.0000
1_2	2.99e-02	2.99e-02	1.24e-02	7.30e-02	0.0000
1_3	6.51e-02	6.51e-02	2.88e-02	1.51e-01	0.0000
1_4	1.39e-01	1.39e-01	6.02e-02	3.10e-01	0.0000
1_5	4.67e-03	4.67e-03	2.28e-03	8.89e-03	0.0000
1_6	1.14e-02	1.14e-02	5.56e-03	2.29e-02	0.0000
1_7	3.65e-02	3.65e-02	1.85e-02	7.71e-02	0.0000
1_8	6.97e-02	6.97e-02	3.45e-02	1.45e-01	0.0000

Figure 6.1.2 Results of ANN tool of CONDITION 2 (vertical seawall Rc+3.96).

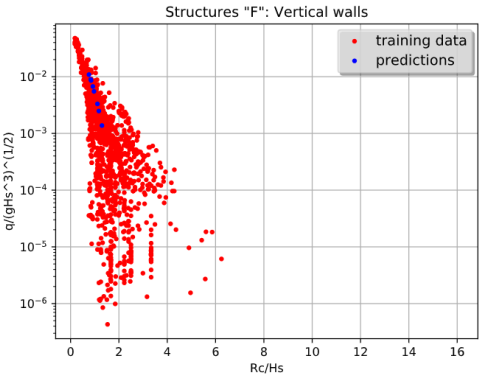

Test-ID	Average	Prototype	5.0%	95.0%	E
1_1	2.04e-02	2.04e-02	6.22e-03	7.18e-02	0.0000
1_2	6.02e-02	6.02e-02	1.55e-02	2.29e-01	0.0000
1_3	1.14e-01	1.14e-01	2.62e-02	4.63e-01	0.0000
1_4	1.71e-01	1.71e-01	4.18e-02	6.93e-01	0.0000
1_5	9.71e-03	9.71e-03	3.64e-03	2.82e-02	0.0000
1_6	2.95e-02	2.95e-02	8.09e-03	1.14e-01	0.0000
1_7	7.93e-02	7.93e-02	1.92e-02	3.26e-01	0.0000
1_8	1.22e-01	1.22e-01	2.74e-02	5.01e-01	0.0000

Figure 6.1.3 Results of ANN tool of CONDITION 3 (vertical seawall Rc+3.96).

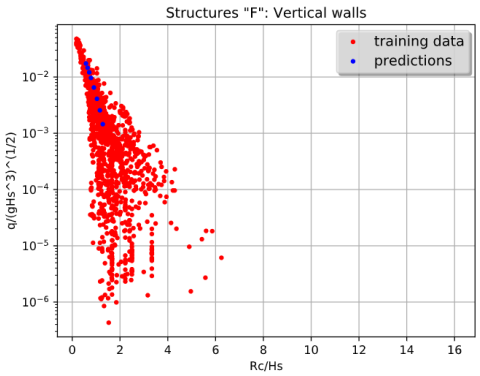

Test-ID	Average	Prototype	5.0%	95.0%	E
1_1	2.11e-02	2.11e-02	6.39e-03	7.37e-02	0.0000
1_2	7.11e-02	7.11e-02	1.87e-02	2.49e-01	0.0000
1_3	1.62e-01	1.62e-01	4.05e-02	6.42e-01	0.0000
1_4	2.74e-01	2.74e-01	7.42e-02	1.01e+00	0.0000
1_5	1.02e-02	1.02e-02	3.86e-03	2.97e-02	0.0000
1_6	3.64e-02	3.64e-02	1.04e-02	1.28e-01	0.0000
1_7	1.14e-01	1.14e-01	2.87e-02	4.27e-01	0.0000
1_8	1.99e-01	1.99e-01	5.25e-02	7.78e-01	0.0000

Figure 6.1.4 Results of ANN tool of CONDITION 4 (vertical seawall Rc+3.96).

The analysis was developed for the Current Layout of Malecòn with all the wave conditions previously described (Table 6.1.1 to Table 6.1.4.).
The comparison is carried out through the calculation of some statistical parameters to assess the validity of the estimators.
The mean overtopping discharge measured in laboratory experiment is compared with q calculated with different predictive method trough *Log Residuals*.
Log-residuals are defined as the logarithm of the measured to calculated q^*:

$$LR = log_{10} \frac{q^*_{meas}}{q^*_{calc}} \tag{62}$$

To compare the performances of predictive models, two statistics have been chosen, namely the mean (E) and the standard deviation (SD) of *Log-Residuals*; these two quantities have been then combined to give the *maximum semi-band amplitude*:

$$M_X = |E_{LR}| + 2 \cdot (SD)_{LR} \tag{63}$$

Also, Max LogResidual is evaluated and indicate as MaxLR.
The reliability indexes have been calculated in Table 6.1.6 for different datasets:

Table 6.1.6 statistical indicator of reliability of prediction.

VERTICAL SEAWALL Rc+3.96								
	EUROTOP,2018				ARTIFICIAL NEURAL NETWORK			
	mean	*st.dev*	*MX*	*MaxLR*	*mean*	*st.dev*	*MX*	*MaxLR*
Cond_1	0.82	0.125	1.07	0.98	1.303	0.197	1.70	1.62
Cond_2	0.73	0.148	1.03	0.97	1.134	0.270	1.67	1.59
Cond_3	0.24	0.206	0.65	0.67	0.856	0.208	1.27	1.28
Cond_4	0.16	0.250	0.66	0.66	0.740	0.272	1.28	1.25

The analysis of results of vertical seawall with Rc=+3.96m shows that the set-up has no influence and the condition with all spectral frequencies gives a better estimate.

But it should be noted that the distribution of all the frequencies of the spectrum is difficult to obtain. In fact, in engineering practice the parameters of the spectrum of the high frequencies alone are deducible through a standard analysis as opposed to the frequencies of the surf beats which are difficult to determine.

However, the analysis showed that the best estimate using the formulas is given by the presence of all frequencies of the spectrum. For these reasons, the study referring to the other geometric configurations of the wall, proceeds considering only condition_3 (*all frequencies and without set-up*).

Table 6.1.7 Results of Eurotop formula for vertical seawall with Rc =+4.96m.

ID	Rc (m)	q_{MEAS} ($m^3/s/m$)	$q_{CALC\_Eurotop}$ ($m^3/s/m$)
9	4.96	0.104	0.028
10	4.96	0.190	0.094
11	4.96	0.337	0.212
12	4.96	0.495	0.252
13	4.96	0.092	0.013
14	4.96	0.140	0.048
15	4.96	0.244	0.157
16	4.96	0.386	0.231

Table 6.1.8 Results of Eurotop formula for curve seawall with Rc =+3.96m.

ID	Rc	q_{MEAS} ($m^3/s/m$)	K_{bn}	$q_{CALC\_Eurotop}$ ($m^3/s/m$)
9	3.96	0.133	0.76	0.062
10	3.96	0.292	0.86	0.209
11	3.96	0.513	0.92	0.449
12	3.96	0.762	0.96	0.512
13	3.96	0.133	0.70	0.028
14	3.96	0.188	0.79	0.109
15	3.96	0.342	0.88	0.343
16	3.96	0.637	0.92	0.486

Table 6.1.9 Results of Eurotop formula for curve seawall with Rc =+4.96m.

ID	Rc	q_{MEAS} ($m^3/s/m$)	K_{bn}	$q_{CALC\_Eurotop}$ ($m^3/s/m$)
9	4.96	0.045	0.52	0.015
10	4.96	0.127	0.66	0.062
11	4.96	0.256	0.74	0.157
12	4.96	0.414	0.80	0.202
13	4.96	0.050	0.43	0.006
14	4.96	0.087	0.56	0.027
15	4.96	0.188	0.69	0.108
16	4.96	0.317	0.75	0.173

The application of ANN tool is limited to vertical seawall, therefore in the follow figure and table has been reported the results of vertical seawall with Rc=+4.96 s.w.l.

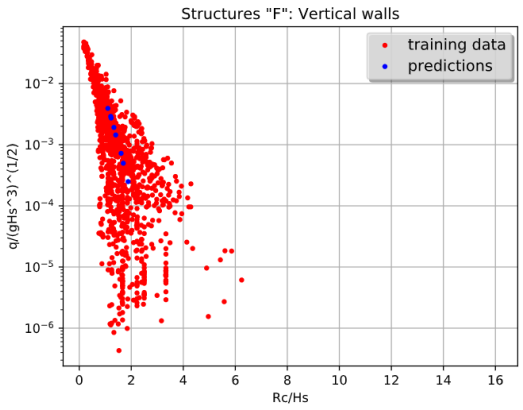

Test-ID	Average	Prototype	5.0%	95.0%	E
1_1	4.11e-03	4.11e-03	1.08e-03	1.52e-02	0.0000
1_2	1.58e-02	1.58e-02	3.77e-03	7.11e-02	0.0000
1_3	3.64e-02	3.64e-02	8.19e-03	1.67e-01	0.0000
1_4	6.18e-02	6.18e-02	1.44e-02	2.55e-01	0.0000
1_5	1.76e-03	1.76e-03	5.26e-04	5.99e-03	0.0000
1_6	6.43e-03	6.43e-03	1.53e-03	2.68e-02	0.0000
1_7	2.26e-02	2.26e-02	4.83e-03	1.04e-01	0.0000
1_8	3.97e-02	3.97e-02	8.94e-03	1.83e-01	0.0000

Figure 6.1.5 Results of ANN tool of CONDITION 3 (vertical seawall Rc+4.96).

Table 6.1.10 Results of ANN tool for vertical seawall with Rc =+4.96m.

ID	Rc (m)	q_{MEAS} ($m^3/s/m$)	$q_{CALC\_ANNtool}$ ($m^3/s/m$)
9	4.96	0.104	0.004
10	4.96	0.190	0.016
11	4.96	0.337	0.036
12	4.96	0.495	0.062
13	4.96	0.092	0.002
14	4.96	0.140	0.006
15	4.96	0.244	0.023
16	4.96	0.386	0.040

The resume of the results of the application of different predictive model has been reported in the follow tables for different seawall configurations and for two wave periods.

Table 6.1.11 Synthesis of Malecòn Traditional vertical seawall with Rc=+3.96m.

	MT vertical +3.96m (12s)				***MT vertical +3.96m (10s)***			
	E_{LR}	SD_{LR}	M_X	Max_{LR}	E_{LR}	SD_{LR}	M_X	Max_{LR}
EurOtop,2018	0.18	0.13	0.43	0.36	0.30	0.27	0.84	0.67
ANN TOOL	0.77	0.13	1.03	0.96	0.95	0.25	1.44	1.28

Table 6.1.12 Synthesis of Malecòn Traditional vertical seawall with Rc=+4.96m.

	MT vertical +4.96m (12s)				***MT vertical +4.96m (10s)***			
	E_{LR}	SD_{LR}	M_X	Max_{LR}	E_{LR}	SD_{LR}	M_X	Max_{LR}
EurOtop,2018	0.34	0.16	0.66	0.57	0.43	0.30	1.04	0.85
ANN TOOL	1.09	0.22	1.53	1.40	1.27	0.34	1.95	1.72

Table 6.1.13 Synthesis of Malecòn Traditional Curve seawall with Rc=+3.96m.

	MT CURVE +3.96m (12s)				***MT CURVE +3.96m (10s)***			
	E_{LR}	SD_{LR}	M_X	Max_{LR}	E_{LR}	SD_{LR}	M_X	Max_{LR}
EurOtop,2018	0.18	0.11	0.40	0.33	0.26	0.30	0.86	0.69
ANN TOOL	-	-	-		-	-	-	

Table 6.1.14 Synthesis of Malecòn Traditional Curve seawall with Rc=+4.96m.

	MT CURVE +4.96m (12s)				***MT CURVE +4.96m (10s)***			
	E_{LR}	SD_{LR}	M_X	Max_{LR}	E_{LR}	SD_{LR}	M_X	Max_{LR}
EurOtop,2018	0.33	0.11	0.56	0.49	0.49	0.33	1.14	0.94
ANN TOOL	-	-	-		-	-	-	

The results of vertical and curved walls are also summarized in the follows tables.

Table 6.1.15 Synthesis of Malecòn Traditional Vertical seawall with Rc=+3.96m.

	MT vertical+3.96m				***MT vertical +4.96m***			
	E_{LR}	SD_{LR}	M_X	Max_{LR}	E_{LR}	SD_{LR}	M_X	Max_{LR}
EurOtop,2018	0.24	0.21	0.65	0.67	0.39	0.23	0.85	0.85
ANN TOOL	0.86	0.21	1.27	1.28	1.18	0.28	1.74	1.72

Table 6.1.16 Synthesis of Malecòn Traditional Curved seawall with Rc=+3.96m.

	MT CURVE +3.96m				***MT CURVE +4.96m***			
	E_{LR}	SD_{LR}	M_X	Max_{LR}	E_{LR}	SD_{LR}	M_X	Max_{LR}
EurOtop,2018	0.22	0.21	0.65	0.69	0.41	0.24	0.89	0.94
ANN TOOL	-	-	-		-	-	-	

The preliminary results of use existing methods/tool shown as the statistic parameters of ANN tool are greater than Eurotop,2018 one.

6.1.3 Comparison of laboratory data with Irregular CFD simulations

To assess the quality of CFD predictions compared to laboratory data, numerical data has been fitted with a simple regression model based on which laboratory data have been estimated. A third order polynomial function has been used for Irregular CFD data giving R^2=0.98.
The irregular CFD simulations have been carried out for only vertical seawall with Rc+3.96m

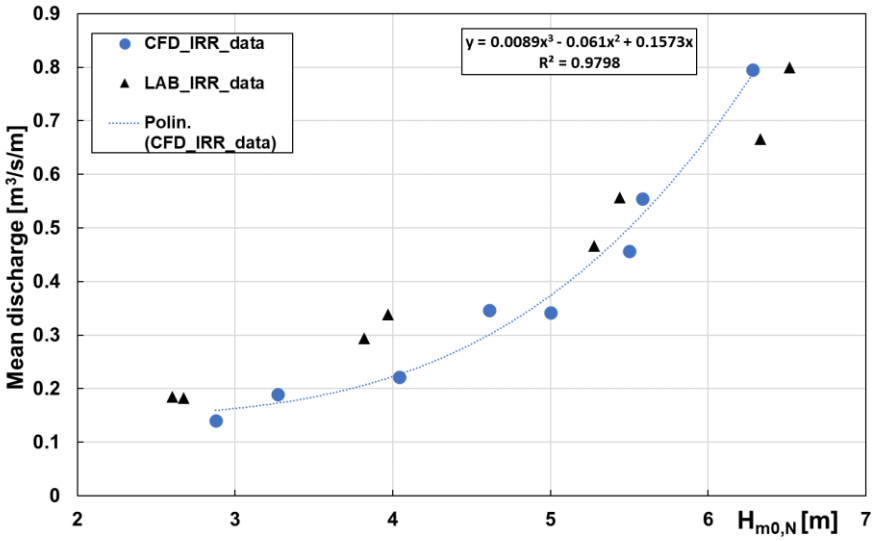

Figure 6.1.6 Third order polynomial regression model of numerical irregular results.

The results summarized in Table 6.1.17 show that the performance of Eurotop Model is function of incident wave parameters H_{m0} and $T_{m-1,0}$ as already discussed in the previous paragraph.

Table 6.1.17 Predictive method for vertical seawall +3.96.

	MT +3.96m			
	E_{LR}	SD_{LR}	M_X	*MaxLogResidual*
EurOtop,2018 (all freq.)	0.24	0.21	0.65	0.67
EurOtop,2018 (Heigh freq.)	0.82	0.13	1.07	0.98
Irregular CFD (third order polynomial)	**0.06**	**0.09**	**0.24**	**0.19**
ANN TOOL (all freq.)	0.86	0.21	1.27	1.28
ANN TOOL (Heigh freq.)	1.30	0.20	1.70	1.62

As can be seen from the results in the Table 6.1.17, the condition with the whole spectrum improves the performance of the EurOtop model.

6.1.4 Comparison of laboratory data with REGULAR CFD tests

The results obtained with regular waves suggest that a simpler method to assess the flowrate for preliminary analysis could be provided.
A validation of the laboratory data with the regression models built on the regular CFD data has therefore been addressed.
In the following table the results of laboratory are compared to the results of regular CFD simulations tests of the same seawall configuration.

Table 6.1.18 Results of overtopping discharge for laboratory tests.

				q (m^3/s/m)			
				Vertical wall		Curved variant	
Test	Hs (m)	Tp (s)	S (m)	+3,96 (m)	+4,96 (m)	+3,96 (m)	+4.96 (m)
9	2.7	12	1.73	0.185	0.104	0.133	0.045
10	4.0	12	1.73	0.339	0.190	0.292	0.127
11	5.4	12	1.73	0.557	0.337	0.513	0.256
12	6.5	12	1.73	0.800	0.495	0.762	0.414
13	2.7	10	1.73	0.183	0.092	0.133	0.050
14	4.0	10	1.73	0.294	0.140	0.188	0.087
15	5.4	10	1.73	0.467	0.244	0.342	0.188
16	6.5	10	1.73	0.667	0.386	0.637	0.317

The analysis has been conducted separately for wave periods. A third order polynomial is selected as regression model of regular CFD; the results of all seawall configurations has been plotted in the following figures:

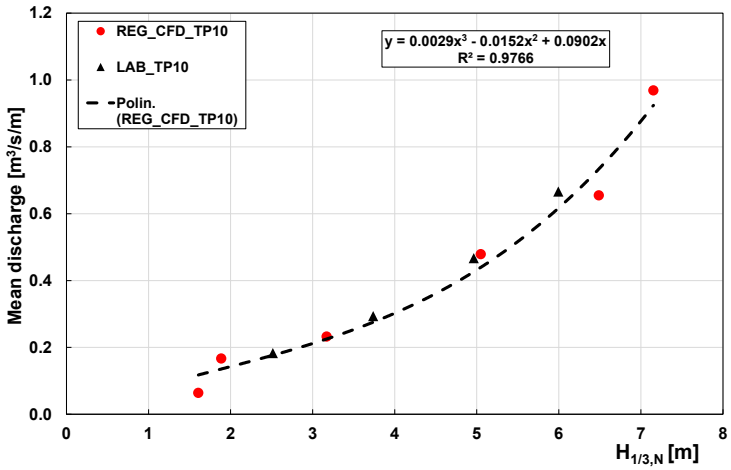

Figure 6.1.7 Regression model of Regular CFD data for Tp=10s of vertical seawall with Rc+3.96m.

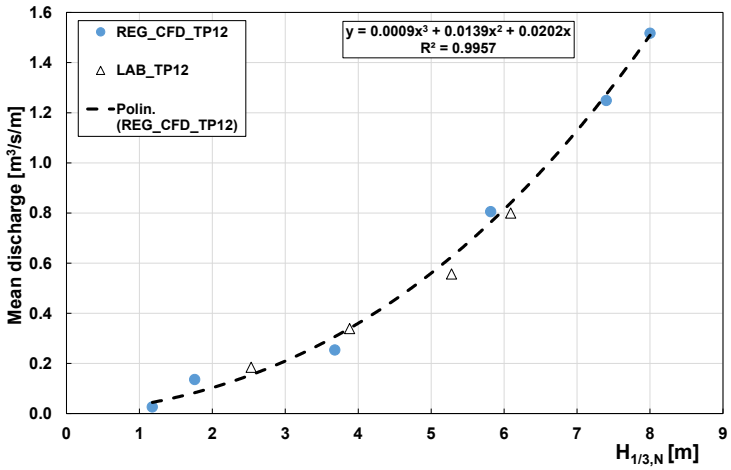

Figure 6.1.8 Regression model of Regular CFD data for Tp=12s of vertical seawall with Rc+3.96m.

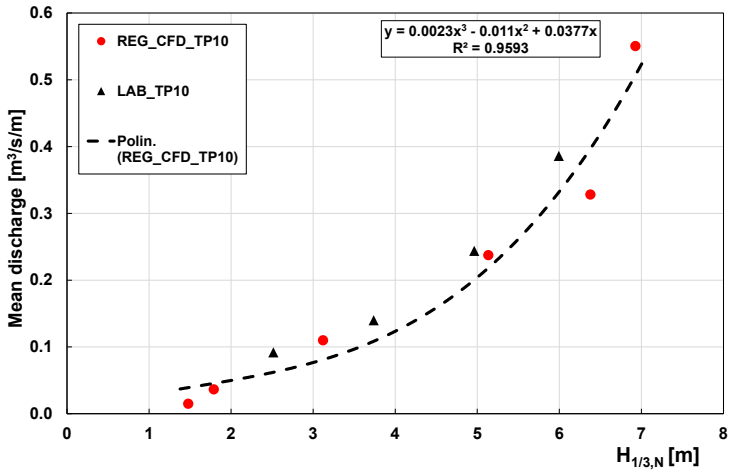

Figure 6.1.9 Regression model of Regular CFD data for Tp=10s of vertical seawall with Rc+4.96m.

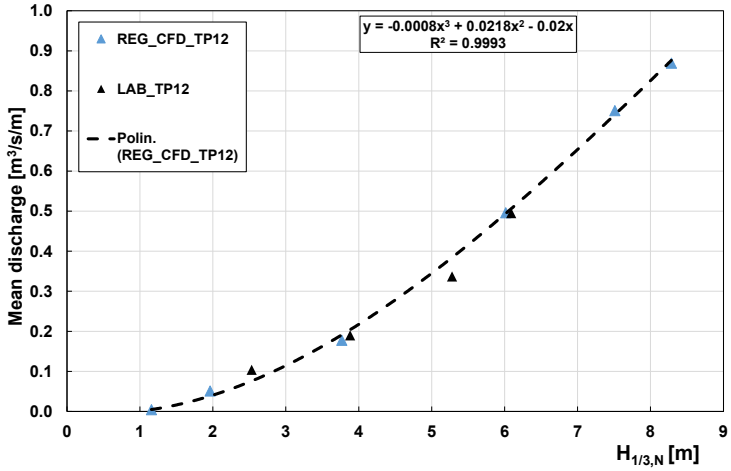

Figure 6.1.10 Regression model of Regular CFD data for Tp=12s of vertical seawall with Rc+4.96m.

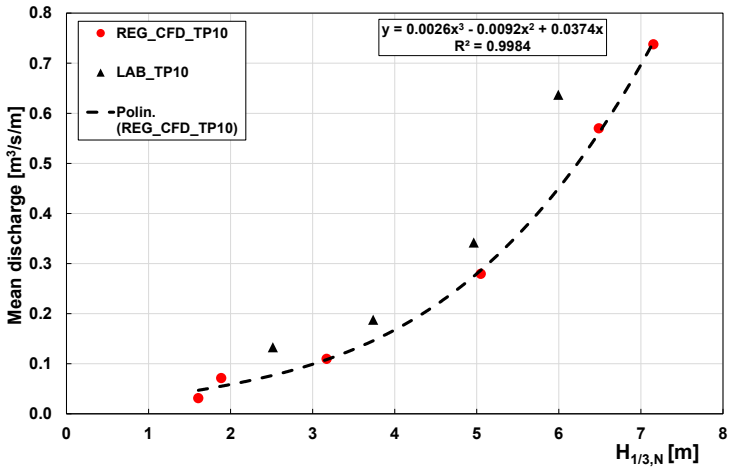

Figure 6.1.11 Regression model of Regular CFD data for Tp=10s of CURVE seawall with Rc+3.96m.

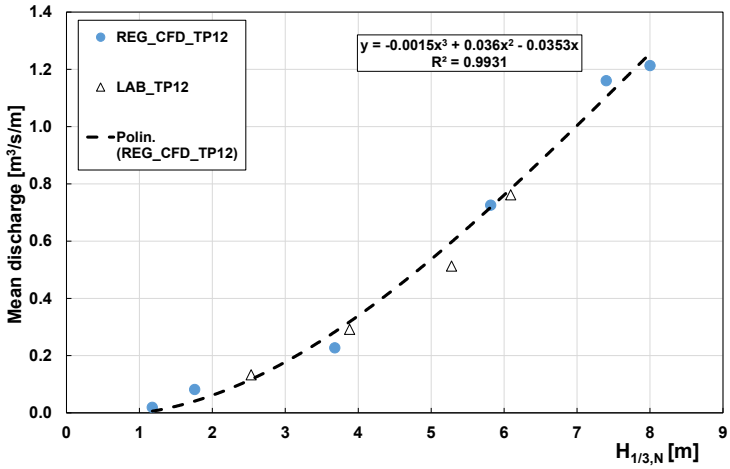

Figure 6.1.12 Regression model of Regular CFD data for Tp=12s of CURVE seawall with Rc+3.96m.

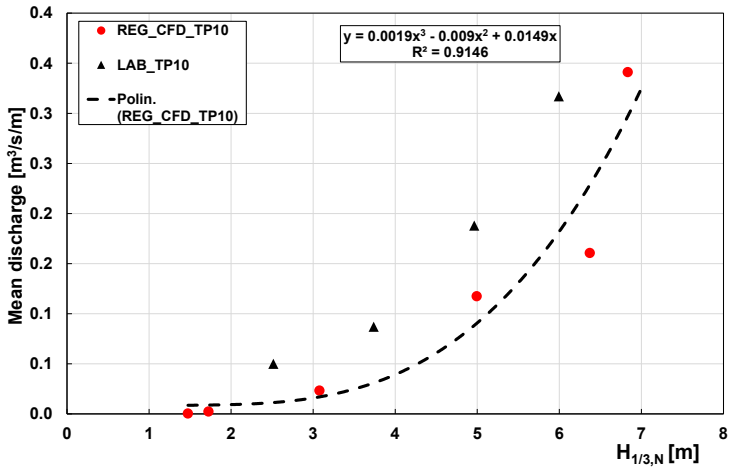

Figure 6.1.13 Regression model of Regular CFD data for Tp=10s of CURVE seawall with Rc+4.96m.

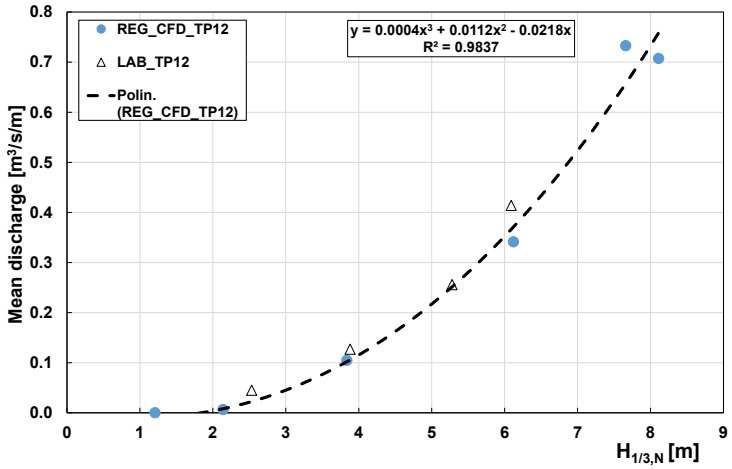

Figure 6.1.14 Regression model of Regular CFD data for Tp=12s of CURVE seawall with Rc+4.96m.

These regression models have been used as tool to predict mean overtopping discharge and compared with laboratory measurements as plotted in the Figure 6.1.15 and for vertical and curve seawall, respectively.

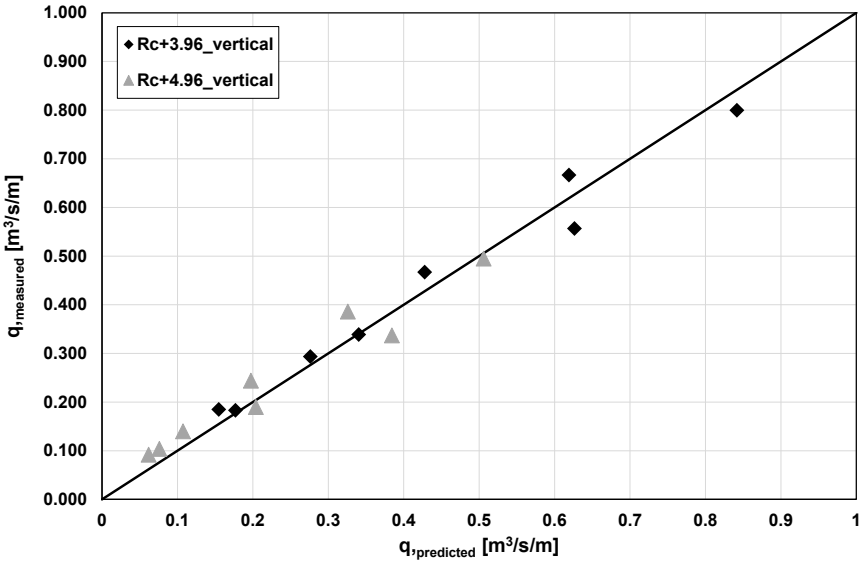

Figure 6.1.15 Mean overtopping discharge predicted with regression model of regular CFD data vs laboratory measurements - VERTICAL seawall configurations.

With the same procedure described above the statistical parameters of *LogResidual*, calculated as ratio of $q_{measured}$ in laboratory experiments and $q_{predicted}$ with regression model of regular CFD data, have been evaluated for both vertical configurations and for the various periods.

Table 6.1.19 Results of predictive models for Malecòn Traditional vertical seawall with Rc=+3.96m.

	MT +3.96m (12s)				***MT +3.96m (10s)***			
	E_{LR}	SD_{LR}	M_X	Max_{LR}	E_{LR}	SD_{LR}	M_X	Max_{LR}
EurOtop,2018	0.18	0.13	0.43	0.36	0.30	0.27	0.84	0.67
Regular CFD (third order polynomial)	-0.01	0.05	0.12	0.06	0.15	0.06	0.28	0.24
Artificial Neural Network	0.77	0.13	1.03	0.96	0.95	0.25	1.44	1.28

Table 6.1.20 Results of predictive models for Malecòn Traditional vertical seawall with Rc=+4.96m.

	MT +4.96m (12s)				***MT +4.96m (10s)***			
	E_{LR}	SD_{LR}	M_X	Max_{LR}	E_{LR}	SD_{LR}	M_X	Max_{LR}
EurOtop,2018	0.34	0.16	0.66	0.57	0.43	0.30	1.04	0.85
Regular CFD (third order polynomial)	0.01	0.09	0.18	0.14	0.11	0.04	0.20	0.17
Artificial Neural Network	1.09	0.22	1.53	1.40	1.27	0.34	1.95	1.72

The curved seawall configurations have been also studied; the results are plotted in the Figure 6.1.16 and the statistic summarized Table 6.1.21 and Table 6.1.22.

The regular CFD results of recurve wall consistently leads to underestimates for Curve seawall with Rc+4.96 as shown in the Figure 6.1.16.

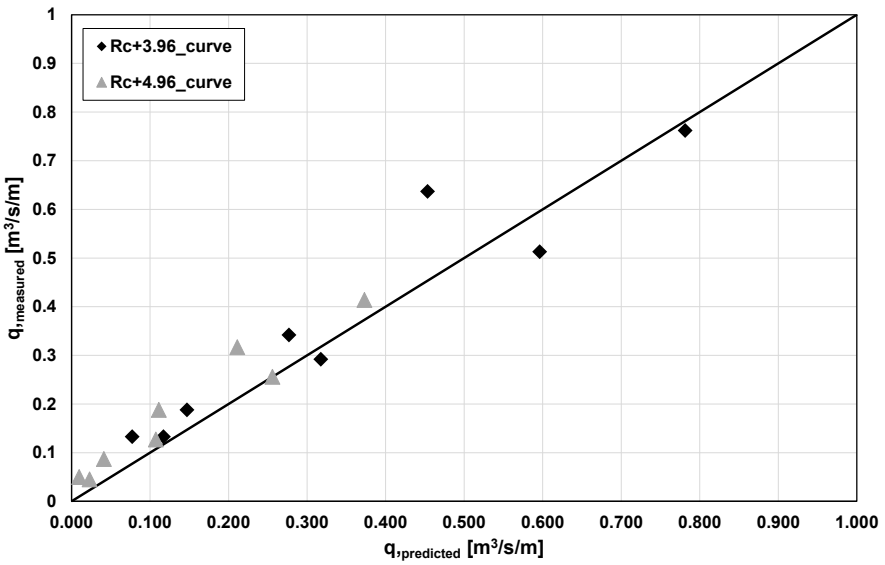

Figure 6.1.16 Mean overtopping discharge predicted with regression model of regular CFD data vs laboratory measurements – CURVE seawall configurations.

The results of maximum amplitude Mx, compared to Eurotop 2018, are reported below:

Table 6.1.21 Results of predictive models for Malecòn Traditional CURVE seawall with Rc=+3.96m.

	MT CURVE +3.96m (12s)				***MT CURVE +3.96m (10s)***			
	E_{LR}	SD_{LR}	M_X	Max_{LR}	E_{LR}	SD_{LR}	M_X	Max_{LR}
EurOtop,2018	0.18	0.11	0.40	0.33	0.26	0.30	0.86	0.69
Regular CFD (third order polynomial)	-0.01	0.05	0.12	0.06	0.15	0.06	0.28	0.24
Artificial Neural Network	-	-	-		-	-	-	

Table 6.1.22 Results of predictive models for Malecòn Traditional CURVE seawall with Rc=+4.96m.

	MT CURVE +4.96m (12s)				***MT CURVE +4.96m (10s)***			
	E_{LR}	SD_{LR}	M_X	Max_{LR}	E_{LR}	SD_{LR}	M_X	Max_{LR}
EurOtop,2018	0.33	0.11	0.56	0.49	0.49	0.33	1.14	0.94
Regular CFD (third order polynomial)	0.10	0.13	0.36	0.29	0.44	0.18	0.79	0.67
Artificial Neural Network	-	-	-		-	-	-	

The results of RegularCFD of curve seawall with Rc+4.96m presents an outlier that probably influences the performance of the model. Nevertheless, when these results are used to compare predictive models, it is seen that numerical model provides the same performances as the EurOtop model (Table 6.1.21and Table 6.1.22).

In conclusion the results show that the predictive models built on Regular CFD data yield the best performance of all tools applied for the calculation of q. In some cases (e.g. Curved configuration) the prediction given by regular CFD model yields the same performance of EurOtop still remaining the best prediction.

These results confirm the negligibility of low frequency waves and the possibility of using waves with a reduced spectral band (also indicated as Regular) having reliable estimates of mean overtopping discharge.

6.2 DISCUSSION OF OVERTOPPING RATE ESTIMATION METHODS

As shown in the previous paragraphs Eurotop Model is based principally on the spectral parameters H_{mo} and $T_{m-1,0}$ or spectral band. The influence of the spectral band contributes to the value assumed by H_{m0} but significantly to the value of $T_{m-10.}$

The aim was to verify the real need to use the whole spectral band to estimate the overtopping flow rate; this objective was pursued by comparing CFD simulations with irregular and regular waves (reduced spectral band).

The data were consistent with each other and with the laboratory data.

Table 6.2.1 Results of predictive method for Malecòn Traditional Vertical seawall.

	MT +3.96m				***MT +4.96m***			
	E_{LR}	SD_{LR}	M_X	Max_{LR}	E_{LR}	SD_{LR}	M_X	Max_{LR}
EurOtop,2018	0.24	0.21	0.65	0.67	0.39	0.23	0.85	0.85
Regular CFD (third order polynomial)	0.01	0.04	0.09	0.08	0.06	0.08	0.23	0.17
Irregular CFD (third order polynomial)	**0.06**	**0.09**	**0.24**	**0.19**	-	-	-	-
ANN TOOL	0.86	0.21	1.27	1.28	1.18	0.28	1.74	1.72

It is seen regular CFD results reduce the large bias on vertical *MaleconTraditional* data, keeping the same performances as the EurOTOP models on the remaining datasets (Curve Seawall).

Table 6.2.2 Results of predictive method for Malecòn Traditional Curve Seawall

	MT CURVE +3.96m				***MT CURVE +4.96m***			
	E_{LR}	SD_{LR}	M_X	Max_{LR}	E_{LR}	SD_{LR}	M_X	Max_{LR}
EurOtop,2018	0.22	0.21	0.65	0.69	0.41	0.24	0.89	0.94
Regular CFD (third order polynomial)	0.07	0.10	0.27	0.24	0.27	0.23	0.73	0.67
ANN TOOL	-	-	-	-	-	-	-	-

It is also remarkable that the CFD predictor exhibits a drop of accuracy for Curve seawall configurations with Rc+4.96m.
The limits of the neural network are closely linked to the configuration. Some of the configurations analysed in this work turned out beyond the range of training of the NN tool, influencing the predictions of q.

The type of foreshore is an important parameter for the wave overtopping phenomenon.

Table 6.2.3 Type of foreshore.

$h/H_{m0,deep}$	**Area**
$h/H_{m0,deep} < 0.3$	Extremely shallow
$0.3 < h/H_{m0,deep} < 1$	Very Shallow
$1 < h/H_{m0,deep} < 4$	Shallow
$h/H_{m0,deep} > 4$	Deep

All the numerical wave conditions analyzed in this work are affected by very shallow and shallow conditions ($0.43<h/H_{m0,deep}<3.12$) and the excellent fit of the CFD data and laboratory experiments can help fill the literature gap for these particular conditions.
The empirical formulations are not calibrated for this specific case of foreshore.

7 EFFECT OF WIND ACTION ON WAVE OVERTOPPING

In this part of research, the influence on overtopping phenomenon under wind influence has been investigated.
The influence of wind on overtopping has often been neglected, but recently a number of research results have shown that this effect cannot be neglected.
Some research studies have suggested that the effects of onshore winds on green water overtopping discharges are small, but that overtopping well below q = 1 l/s per m might increase by up to 4 times under strong winds (EurOtop Manual 2018).
Wind affects the overtopping discharge through two actions: wave deformation of the water surface in front of the seawall, and the convection of the water particles behind the seawall (Masami Kiku and Koji Kawasaki, 2014).
The effects of wind on the overflow phenomenon thus seem to be important in the design of seawalls but it is difficult to quantify their effects through hydraulic models. In the following some results are presented of numerical simulation of the phenomenon at the field scale.

7.1 LITERATURE REVIEW

The influence of wind on overtopping can be described as consequence of strong onshore wind pushing cause part of the upwards projected water to be transported landwards over the crest.
It is therefore widely assumed that onshore winds significantly increase runup and overtopping (Ward et al., 1996; De Waal et al. 1996).

In particular De Wall et al. 1996 clarified that the wind causes the overtopping of the part of the breaker spray which would have fallen back into the sea in a situation without wind.

Physical models have been conducted by Pullen et al. (2009) and de Waal et al.(1996) who experienced similar challenges with regards to scaling wind as the surface tension, viscosity and droplet sizes are the same for both the prototype and model.
The problem of wind scaling remains a difficult task and the use of Froude scale in physical model, where the gravity is the predominant factor, is incorrect because the spray phenomenon is turbulent and will be modelled with Reynold's scaling.
For the influence of wind, a factor between defined as the ratio between the overtopping discharge q_{wind} including the effect of the wind and q , the same discharge without the wind $f_{wind} = q_{wind}/q$

f_{wind} varies according to q, and is normally higher when q is small, and becomes closer to 1 for high values of q.

De Waal et al. (1996) took an innovative approach to the problem, seeking to quantify the maximum possible wind transport effect by using a paddle wheel to "push" all water that reached the height of the crest over the wall. The results by De Waal et al. (1996) suggest that the wind effect was found to be 3.2 times the mean overtopping discharge without wind (q_{wind}, max = 3.2 q)

As reported in De Rouck et al. 2005, the factor on wind effects is related to amount of mean overtopping discharge and for cases in which q is greater than 0.01 m^3/sm is close to 1.

De Rouck et al. 2005 using the output from small scale model test results or the output from a Neural Network for wave overtopping predictions, propose a procedure to take into account wind effects.

For the influence of wind, a factor between 1 (10 l/s/m) and 4 (0.01 l/s/m) is proposed compared to the situation without wind.

As reported in Pullen et al. (2009), to study the effects of the wind in the laboratory, 4 fans were placed in front of the seawall in a manner analogous to the paddle wheel of De Wall et al. 1996. However, they proposed a wind transport factor f_{wind} based on field observations and laboratory measurements as a method to obtain the mean overtopping discharge including wind. The factor on possible wind effects can be calculated by:

$$f_{wind} = 1.0 + 3 \cdot \left(\frac{-log\ q - 2}{3}\right)^3 \quad for\ \ 10^{-5} < q < 10^{-2}\ m^3/s/m \tag{64}$$

where q is in $m^3/s/m$, and the wind adjusted discharge q_{wind} is simply $q_{wind} = q\ f_{wind}$

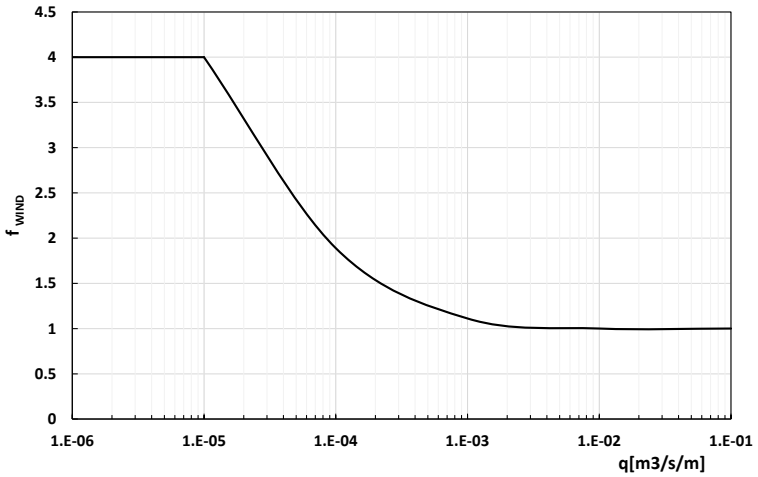

Figure 7.1.1 The factor on possible wind effects (Pullen et al. 2009).

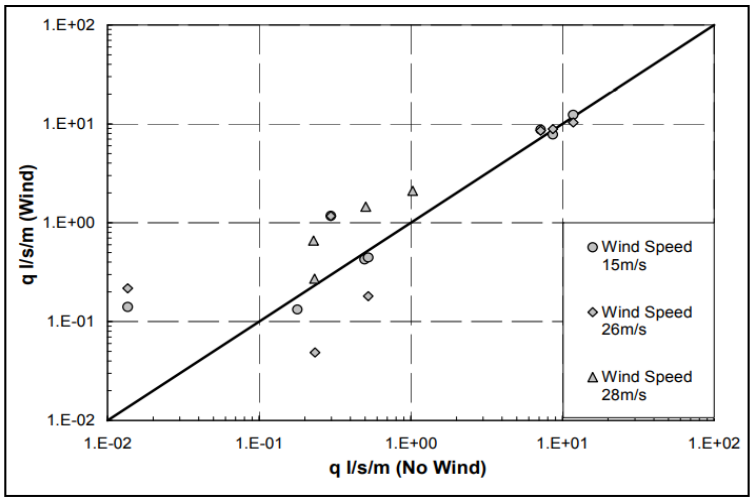

Figure 7.1.2 The results of HRW overtopping discharges (b) (Pullen et al. 2009) (on vertical seawall of Samphire Hoe) with and without wind.

7.2 WIND STRESS MODEL

The approach followed here is different from the previous work described above: the influence of the wind is assumed to depend upon the surface stress acting on the water surface in the stretch of water closer to the shore.

A two-dimensional numerical model has therefore been implemented at field scale in order to evaluate the effect of wind induced shear stress on the sea surface, without taking into account the convective flux over the crest of the seawall.
Effects of wind and generation of spray have not often been modelled due to the problem of wind scaling.
A simple wind model is employed to evaluate the stress induced by the wind on the sea surface as a function of the wind speed U_{10}at 10 meters over the sea level.
The wind model is then used to apply a fixed shear stress tangential to the free surface.

If the vertical distribution of the sea wind follows the logarithmic law, the wind shear stress τ acting on the sea surface is typically estimated by Eq. (65). This estimation utilizes the wind speed U_{10} at an elevation of 10 m above sea level and the sea surface drag coefficient C_{D10}. The wind shear stress is calculated using the quadratic law:

$$\overrightarrow{\tau_s} = \rho_a C_{D10} |\overrightarrow{U_{10}}| U_{10} \tag{65}$$

where:

- ρ_a is the density of air (1.225 kg m-3),
- U_{10} is the wind velocity at 10m above water surface,
- C_{D10} is the wind shear coefficient (or drag coefficient)

To calculate C_{D10} the predictive equation suggested by Andreas et al. 2012 has been employed:

$$\sqrt{C_{D10}} = \frac{0.239 + 0.0433 \cdot \{(U_{10} - 8.271) + [0.120 \cdot (U_{10} - 8.271)^2 + 0.181]^{0.5}\}}{U_{10}} \tag{66}$$

The wind stress model can be applied in Flow-3D, the CFD model selected for this study, defining wind velocity (U_{10}) and wind shear parameters (ρ_a;C_{D10}).

7.3 WIND MODEL IMPLEMENTATION

In the first phase of the research, the effects of wind were evaluated on wave conditions and geometric configuration of the wall as in the cases previously for the Current Layout of Malecòn (Rc=+3.96m on mean water level 18.72m). The wave characteristics are summarized in Table 7.3.1, in detail regular incident wave were generated using wave boundary condition.

Table 7.3.1 Wave characteristics used for wind model implementation.

H(m)	T(s)	Wave celerity c (m/s)
8	12	18.74
1.5	10	15.61
5.4	10	15.61

Wave celerity *c* is calculated in deep water as follow:

$$c = \frac{gT}{2\pi} \tag{67}$$

A parametric study with different ratio U_{10}/c has been implemented and the main characteristics are reported in Table 7.3.2 in which C_{D10} is function of U_{10} and has been calculated with the equation (66).

Table 7.3.2 Wind model characteristics.

Wind model characteristics for TEST2			Wind model characteristics for TEST3, TEST9		
U_{10}	U_{10}/c	C_{D10}	U_{10}	U_{10}/c	C_{D10}
30	1.9	0.0025	**31.2**	2.0	0.0026
18.7	1.0	0.0021	**19**	1.2	0.0021
9.4	0.5	0.0011	**12.5**	0.8	0.0015
6.1	0.3	0.0009	**5.2**	0.3	0.0009
1.9	0.1	0.0010	**3.1**	0.2	0.0009

However, it has been necessary reduce the wave overtopping discharge with increment of relative crest freeboard Rc (Figure 7.3.1) and using the wave condition H=1.5m T=10s (unbreaking wave). Finally, the effect of wind is also studied for a breaking wave H=8m T=10s and Rc=+10.00m.

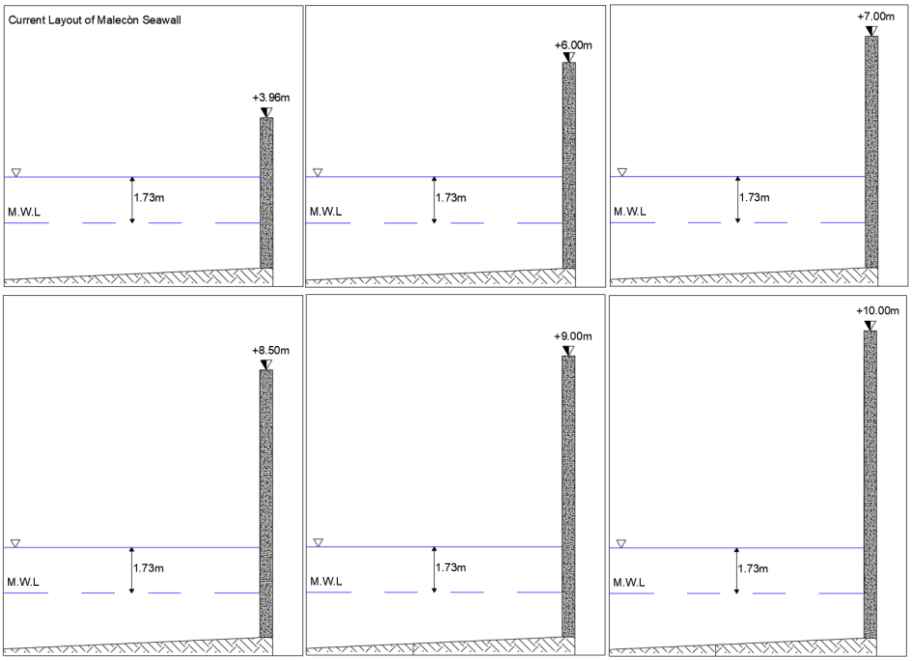

Figure 7.3.1 Geometric configurations with increased Rc of the wall to reduce wave overtopping.

7.4 DISCUSSION OF RESULTS

In the analysis carried out with real values of the relative crest freeboard Rc, the increase of overtopping discharge was found to be very low (fw~ 1).

In order to investigate into more relevant situations, lower discharges were considered by increasing Rc.

Since low overtopping volumes have been found to be most affected by wind, the experiments are focussed on the lower overtopping regime.

Practically these low overtopping volumes are relevant for the safety of pedestrians and vehicles and can already cause structural damage to buildings.

As represented in the figure below, the presence of wind shear stress in the simulation gives a greater elevation of confined flow that directly influenced the wave overtopping.

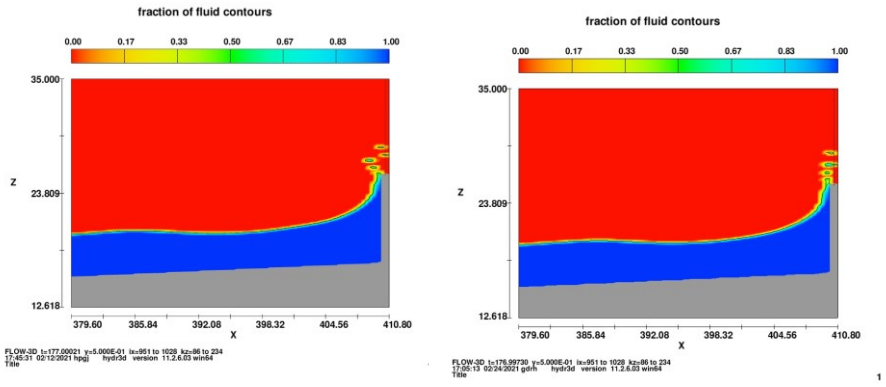

(a) no wind **(b) U_{10}=31.2 m/s**

Figure 7.4.1 Up-rushing jet of instant (177.0 s) on wave overtopping for different simulation; panel a) no wind panel b) wind velocity U_{10}=31.2 m/s for H=1.5m T=10s and Rc=+7.00m.

Up-rushing jet in presence of wind stress induces greater overtopping compared to the no wind condition. The difference of height of the up-rushing jets is about 40cm (the water drops are not considered).
The following graph shows the sequence of wave overtopping discharge at the same instant represented in Figure 7.4.1 for both the U_{10}=31.2m/s wind and for the no-wind condition.

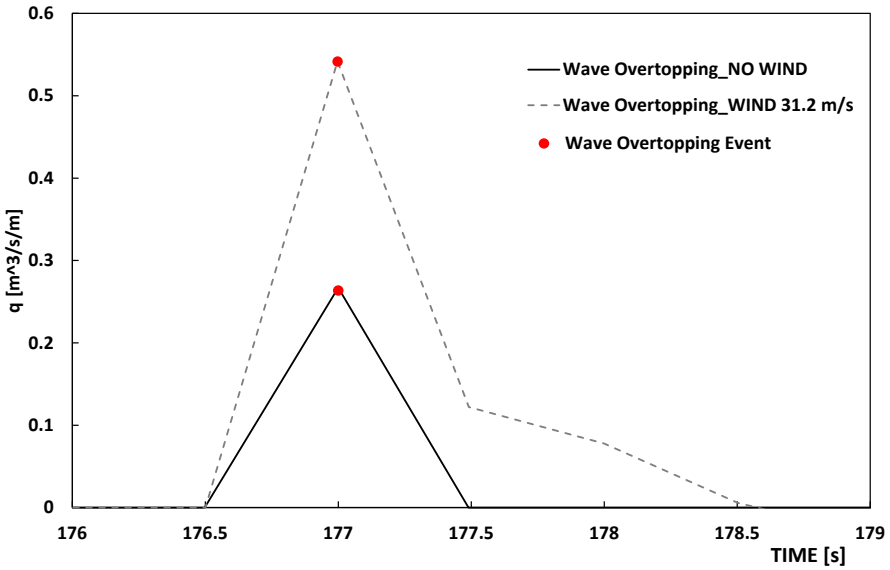

Figure 7.4.2 Effects of wind stress on wave overtopping and maximum height of water level at wall of TEST H=1.5m T=10s and Rc=+7.00m.

A further example of wind effect is shown in Figure 7.4.3

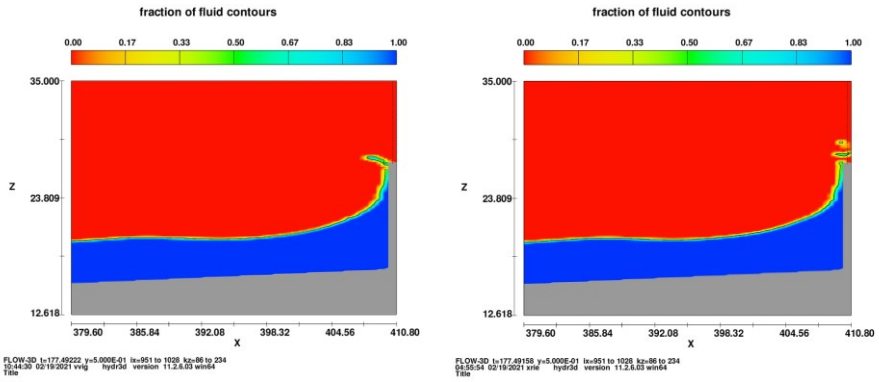

(a) no wind **(b) U_{10}=19 m/s**

Figure 7.4.3 Up-rushing jet of instant (177.5 s) on wave overtopping for different simulation; panel a) no wind panel b) wind velocity U_{10}=19 m/s for H=1.5m T=10s and Rc=+8.50m.

Furthermore, the next graph shows the cumulative overtopping volume by varying wind velocity.

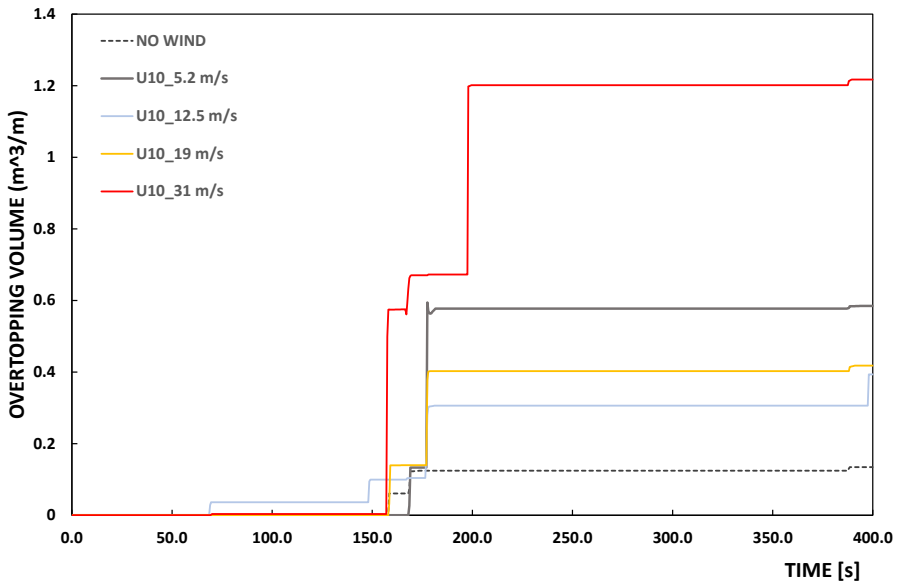

Figure 7.4.4 Cumulative overtopping volume for different wind velocity of TEST H=1.5m T=10s and Rc=+8.50m.

A further case has investigated for a breaking wave: H=8m T=10s and Rc=+10.00m. Figure 7.4.5 to 7.4.7 provide some examples of the spatial profile of the water surface surrounding the vertical seawall without wind and in presence of wind stress.

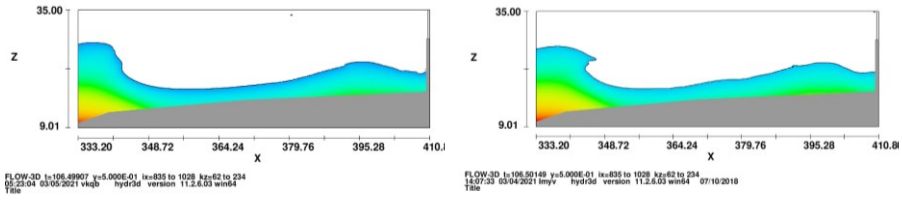

(a) no wind **(b) U_{10}=31 m/s**

Figure 7.4.5 Change in water surface at the instant t=106.5s (TEST H=8.0m T=10s and Rc=+10.00m).

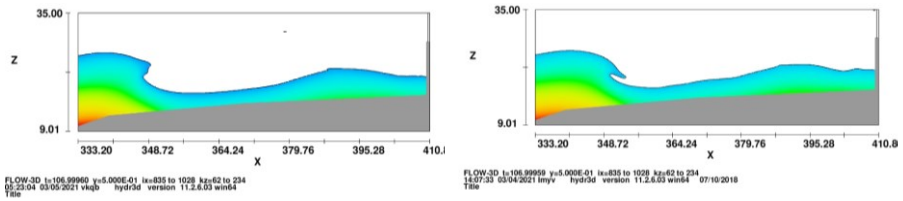

(a) no wind **(b) U_{10}=31 m/s**

Figure 7.4.6 Change in water surface at the instant t=107s (TEST H=8.0m T=10s and Rc=+10.00m).

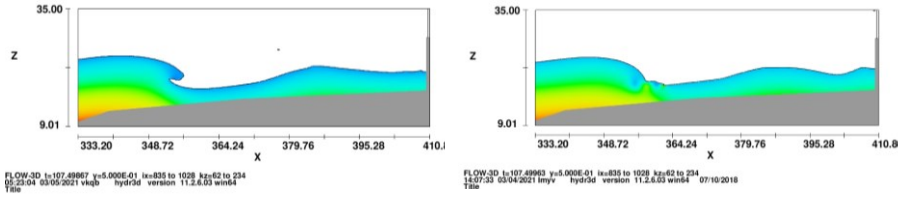

(a) no wind **(b) U_{10}=31 m/s**

Figure 7.4.7 Change in water surface at the instant t=107.5s (TEST H=8.0m T=10s and Rc=+10.00m).

The presence of wind stress clearly modifies the propagating wave shape.

In the following figures the turbulent energy TKE is considered for different instant of simulation of the propagating wave, again with and without the wind shear stress.

TKE increases near to the breaking zone, but the wind shear stress modifies the process of wave breaking and the distribution of wave energy. The wind stress on water surface induces a higher rise to the wall that does not always turn into overtopping however it reduces the energy of the downhill flow that will propagate backwards towards the open sea (Figure 7.4.8, Figure 7.4.9, Figure 7.4.10, Figure 7.4.11, Figure 7.4.12.)

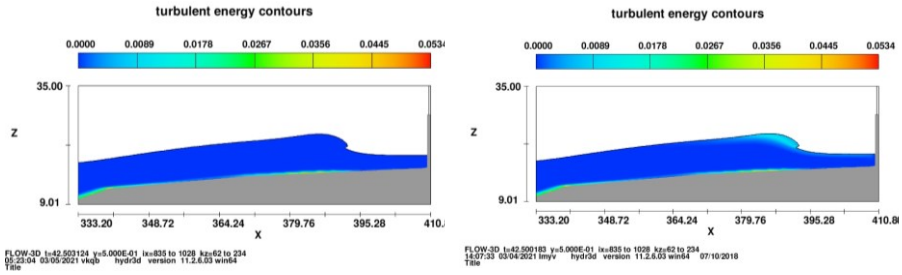

(a) no wind **(b) U_{10}=31 m/s**

Figure 7.4.8 Turbulent energy for instant t=42.5s of TEST H=8.0m T=10s and Rc=+10.00m.

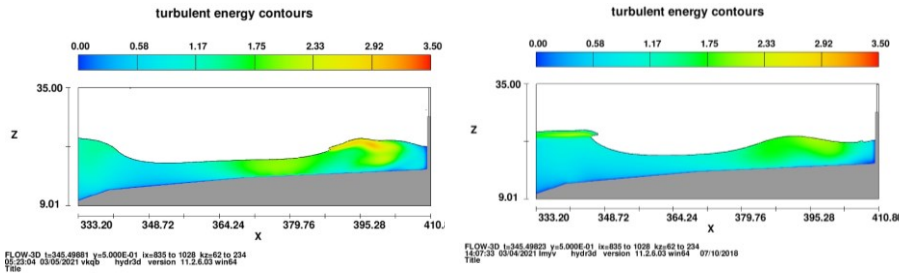

(a) no wind **(b) U10=31 m/s**

Figure 7.4.9 Turbulent energy for instant t=345.5s of TEST H=8.0m T=10s and Rc=+10.00m.

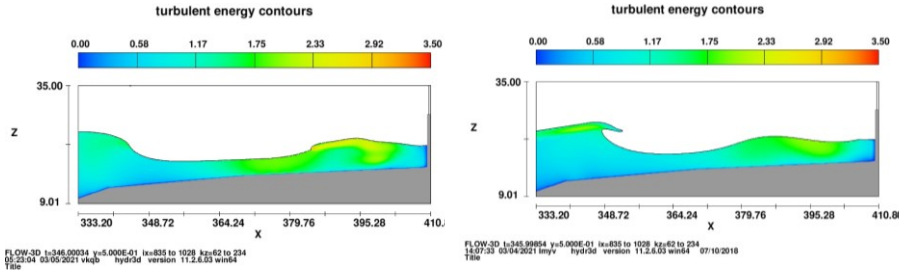

(a) no wind **(b) U10=31 m/s**

Figure 7.4.10 Turbulent energy for instant t=346s of TEST H=8.0m T=10s and Rc=+10.00m.

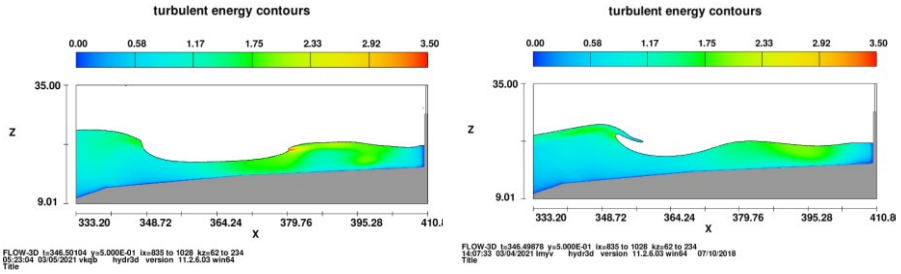

(a) no wind **(b) U10=31 m/s**

Figure 7.4.11 Turbulent energy for instant t=346.5s of TEST H=8.0m T=10s and Rc=+10.00m.

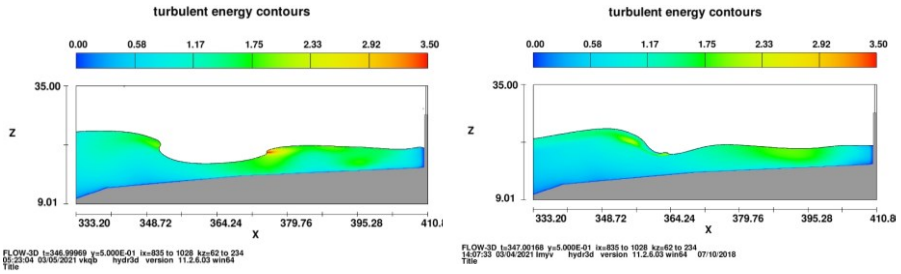

(a) no wind **(b) U_{10}=31 m/s**

Figure 7.4.12 Turbulent energy for instant t=347s of TEST H=8.0m T=10s and Rc=+10.00m.

As referred Perlin et al. 2013 the wave profile at the onset of the breaking is highly dependent on the way the breaking is achieved. In this regard the x-velocity component is also represented during breaking process in Figure 7.4.13.

The breaking and reforming processes are clearly different; the velocity on the wave crest induces different propagation, as shown in the following plots.

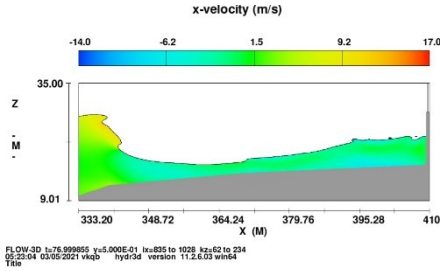

no wind (t=77.0s)

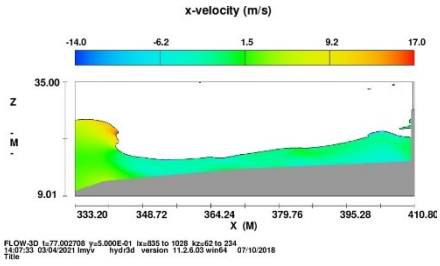

U_{10}=31 m/s (t=77.0s)

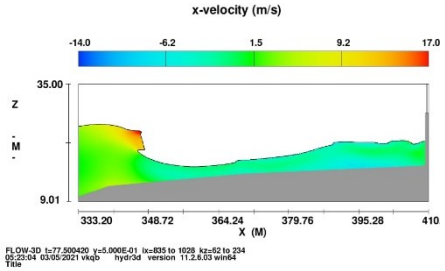

no wind (t=77.5s)

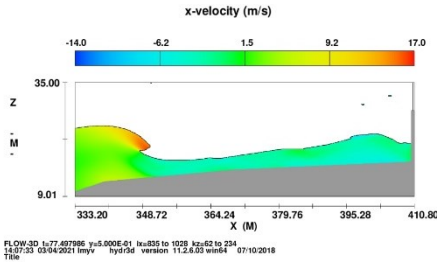

U_{10}=31 m/s (t=77.5s)

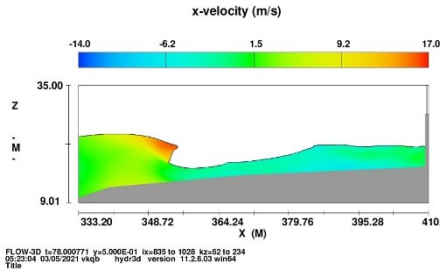

no wind (t=78.0s)

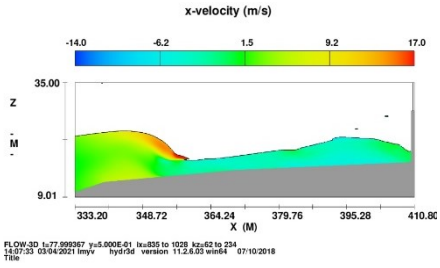

U_{10}=31 m/s (t=78.0s)

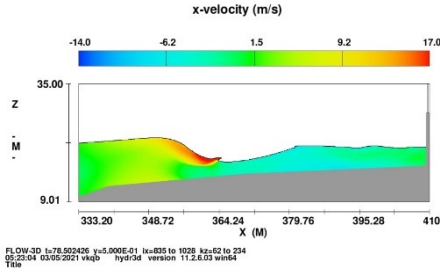

no wind (t=78.5s)

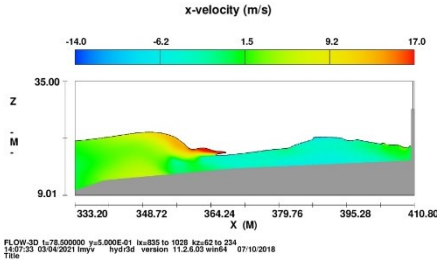

U_{10}=31 m/s (t=78.5s)

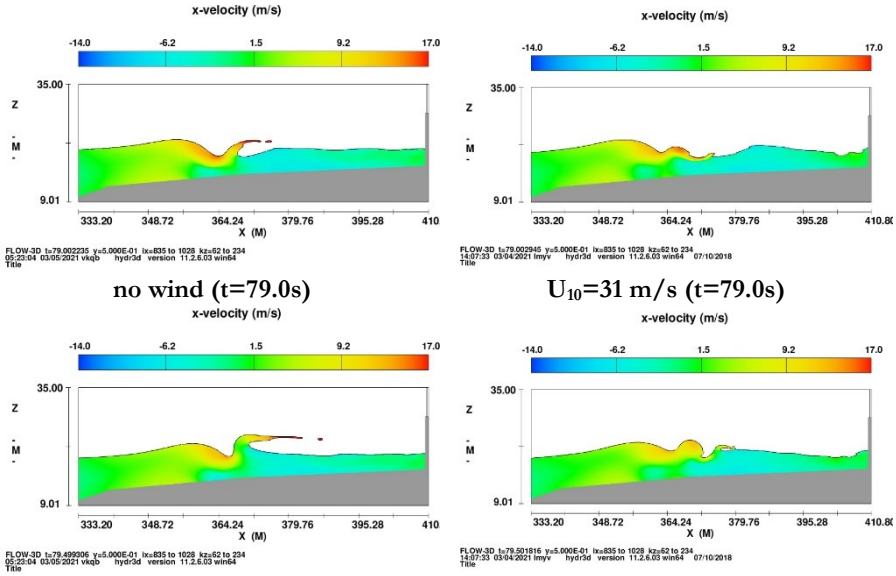

Figure 7.4.13 x-velocity for Test: H=8.0m T=10s and Rc=+10.00m.

In the following graph (Figure 7.4.14) is possible to see that in some situations, when the waves break before reaching the wall, the application of wind surface shear stress reduces wave overtopping. It appears that when no wind is present, more energy is dissipated at the early stage of the breaking so that fewer overtopping events appear, but with greater intensity, thus increasing the mean discharge.

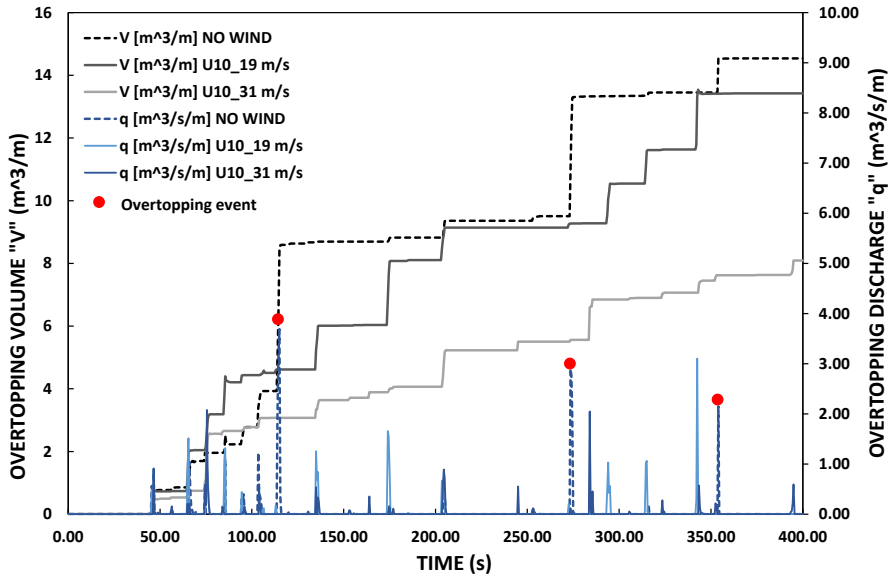

Figure 7.4.14 Cumulative overtopping volume for different wind velocity of TEST H=8.0m T=10s and Rc=+10.00m.

This behaviour is probably a consequence of a different energy distribution during wave breaking process and a different redistribution of the rising flow near the wall.
The results of a single test for breaking waves cannot be considered reliable. A further investigation is required.

The all results were also represented (Figure 7.4.15) as function of mean overtopping discharge in order to evaluate the influence of wind stress.

The results showed that for large flow rates (q>100 l/s/m) the wind factor f_{wind} is close to 1, while for higher Rc and therefore for lower q values f_{wind} may increase sensibly. Data, however, appear to be more scattered as the overtopping flow rate decreases.

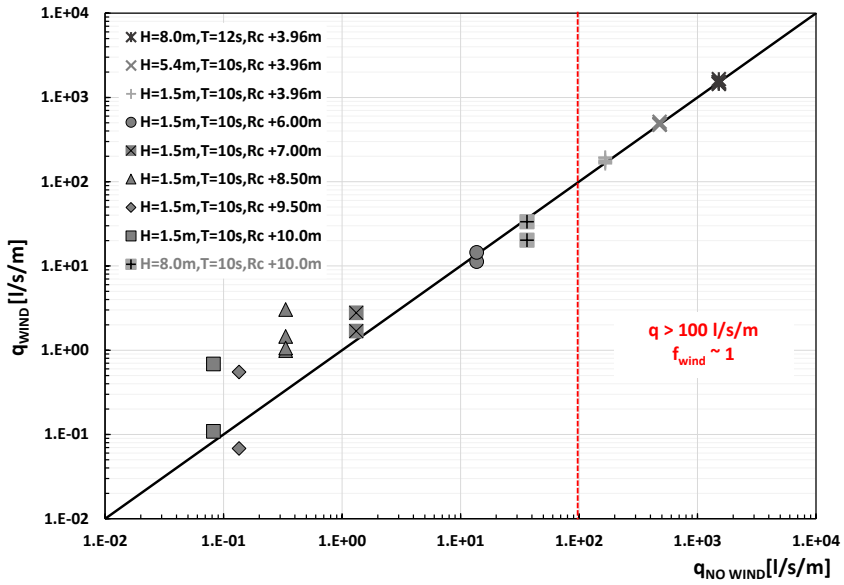

Figure 7.4.15 Numerical results of wind influence with different wave conditions and different Rc.

The same results have been plotted as function on wind velocity and excluding tests for which q> 100 l/s/m.

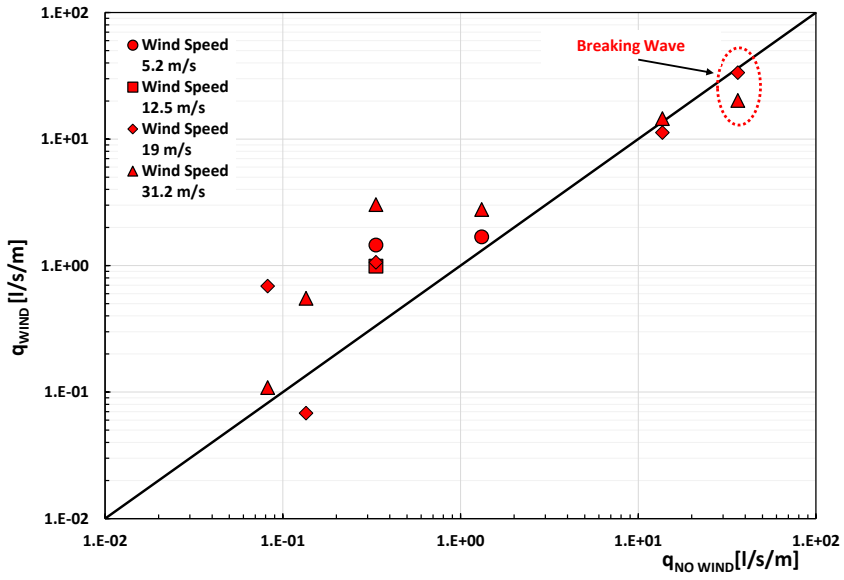

Figure 7.4.16 Numerical results of wind influence with different wind speed.

The comparison of the data shown previously with the literature data of the laboratory experiments reported in Pullen et al. 2009 is shown below.

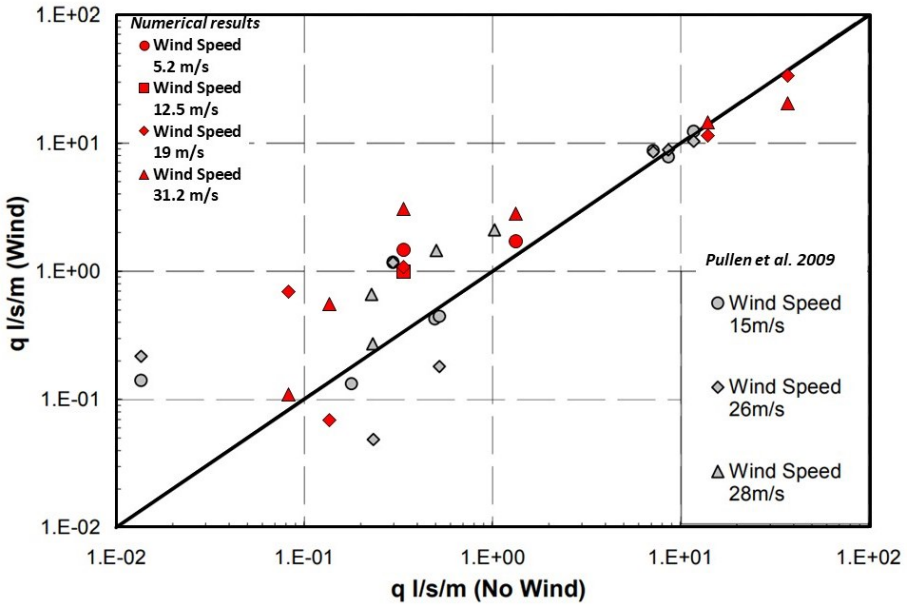

Figure 7.4.17 Numerical results vs HRW laboratory experiments of overtopping discharges (Pullen et al. 2009) with and without wind (note different wind speed have been applied).

The numerical results are in agreement with the laboratory data of the literature (Pullen et al. 2009) as reported in the Figure 7.4.17.
The conclusion is that the increase due to wind is large when the discharge is small and its effect decreases as the discharge increases, which agrees with de Waal et al. (1996) and Ward et al. (1996).

Although it has not been possible to quantify the convective effects of water transport over the wall numerically, it has been shown how the presence of the wind, as shear stress only, induces an increase of up-rushing jet near the wall.

In some cases, wave overtopping does not occur. However, according to the numerical computation, the probability of wave overtopping is assumed to be higher in the presence of wind than without it.
The results shown agree with literature data for which, however, only the convective transport over the seawall due to the wind was considered.

8 CONCLUSION and FUTURE DEVELOPMENT

8.1 CONCLUSION

The work exposed in the thesis has shown that CFD can provide a reliable estimate of the wave overtopping over seawalls and it is therefore a useful tool for the analysis and the design of such structures. An extensive comparison has been carried out with existing and reliable formulas such as those provided by the EurOtop Manual as well as with the results of an experimental campaign carried out by CUGRI and led by Prof. Mariano Buccino and Luis Cordoba at the laboratory of the "Federico II" University of Naples within a research project for the design of the "Malecón Tradicional" seawall in Habana.

While it is well known that CFD procedures are heavily reliant upon the choice of the computational grid and of the turbulence models, experiments are affected by parameters such as the scale and the nature of the wave generators. Particular care has therefore been taken in comparing the uncertainties and the error that inevitably affect both numerical analysis and experimental results.
This involved an extensive series of tests on the effect of grid size and shape on the results.
As far as the wave profile is concerned, several statistics have been considered, such as set-up(m) energy(σ), skewness(s)) and zero up-crossing wave average and significant height (H_m, $H_{1/3}$), as well as a Coefficient of Variation Cv for each of the relevant quantities.

It has been shown that the results do not indicate a clear grid effect except for "skewness- s". For this reason, it was concluded that the results are grid independent, with random fluctuating around the mean value.
It was also possible to retrieve a relationship between the coefficient of variation Cv and the Ursell number of the wave.
As Ur increases (i.e. the waves tends to become nonlinear, and particularly after wave breaking), so does the Cv.
A clear difference between non-breaking and breaking waves has been identified.
Finally, a comparison between rectangular and square grid suggests that the shape bears little influence on the variability of results for set-up, while for the other most relevant engineering quantities (wave energy and zero-up crossing waves) the use of square grids is beneficial only at low Ursell numbers.

By carrying out a convergence analysis on the overtopping, an envelope region was found characterized by the degree of accuracy of the solution as a function of the wave and geometric parameters (H, T, Rc/ H) and the cell size.
It is thus possible to determine a convergence area on the diagram where the grid related error does not exceed 10-15%.
Finally, it was assessed that the uncertainty estimated for laboratory experiments within EurOtop data set for vertical seawall is greater than the error relative to the grid.
The reliability of the CFD model has then been evaluated by reproducing a large set of laboratory experiment carried out for the "Malecón Tradicional" seawall with spectral wave trains and different seawall configurations, of which 2 straight vertical and two curved. These latter experiments however only provide the mean overtopping discharge; in order to validate the computed maximum overtopping volume Vmax, we have made use of the relevant EurOtop formulas. The comparison between spectral laboratory and CFD results for overtopping discharges are satisfactory.

A further set of CFD tests have been implemented, aimed at evaluating the possibility of using regular wave trains rather than spectral series, in order to reduce and simplify the computations and to provide expedite tool for engineer at the early stage of the design process.
The results have shown that a monochromatic wave causes a similar mean overtopping discharge as spectral wave train with a peak period equal to the period of the single wave. The comparison of experimental data with CFD monochromatic wave results, for various geometric configurations of the seawall, has also yielded satisfactory results.
However, it should be noted that these results only apply to large flow rate, higher than 30l/s/m. For smaller flow rates the extreme randomness of overtopping events requires a larger number of waves to have a stable mean overtopping flow rate.

A final comparison has been carried out between the CFD results, the EurOtop formulas, and the Artificial Neural Network (ANN)algorithm. CFD has proved to be more accurate than the other methods for all the wall shapes, except for the curved wall, for which the EurOtop formulas are equivalent.
The reliability of ANN tool is limited by the configuration of the foreshore that, for the configuration of case study, is beyond of the range of training.

An important and relatively new effect which has been successfully studied by making use of CFD techniques is the influence of the wind on the overtopping. The use of a numerical model overcomes the limits due to scale effects in experimental tests, and it has therefore been possible to consider the action of wind induced shear stress on the increase of up-rushing jet near the wall. The results show a good agreement to the literature.
Prediction results of the overtopping from numerical modelling have in conclusion been shown to be as good as those provided by existing and well proven empirical methods, while at the same time allowing an ample flexibility in shape and wave conditions.

CFD has thus proven to be an important design tool for vertical structures in shallow water.
In general, the CFD approach showed excellent predictive abilities of different parameters of interest in the coastal engineering.

REFERENCES

1. Akbari H., 2017. Simulation of wave overtopping using an improved SPH method. Coastal Engineering, Volume 126, Pages 51-68.

2. Andreas E.L., Mahrt L., and Vickers D., 2012. A New Drag Relation for Aerodynamically Rough Flow over the Ocean. Journal of the Atmospheric Sciences Page(s): 2520–2537.

3. Antonini, A., Archetti, R., Lamberti, A., 2017. Wave simulation for the design of an innovative quay wall: the case of Vlorë Harbour. Nat. Hazards Earth Syst. Sci. 17 (1), 127–142.

4. Borsboom, M., Jacobsen, N.G., 2021. A generating-absorbing boundary condition for dispersive waves. International Journal for Numerical Methods in Fluids.
   URL https: //onlinelibrary.wiley.com/doi/abs/10.1002/fld.4982

5. Barkhudarov, M.R., 2004. Lagrangian VOF advection Method for FLOW-3D. Technical Report FSI-03-TN63-R. Flow Science, Inc. (USA).

6. Bradford, S.F., 2000. Numerical simulation of surf zone dynamics. Journal of Waterway, Port, Coastal, And Ocean Engineering", Vol. 126, N. 1, Jan./Feb.

7. Buccino, M., Dentale, F., Salerno, D., Contestabile, P., Calabrese, M., 2016. the use of CFD in the analysis of wave loadings acting on seawave slot-cone generators. Sustainability, 2016, 8, 1255

8. Buccino, M., Daliri M., Dentale, F., Di Leo A., Calabrese M.,2019. CFD experiments on a low crested sloping top caisson breakwater. Part 1. nature of loadings and global stability. Ocean Engineering Volume 182, 15 June 2019, Pages 259-282.

9. Celik, I.B., Ghia, U., Roache, P.J., Freitas, C.J., Coleman, H., Raad, P.E.,2008. Procedure for estimation and reporting of uncertainty due to discretization in CFD applications. J. Fluids Eng., 130, 078001.

10. Chopakatla, S.C., Lippmann, T.C., Richardson, J.E., 2008. Field verification of a computational fluid dynamics model for wave transformation and breaking in the surf zone. J. Watarw. Port, Coast. Ocean Eng. 134 (2), 71-81.

11. CLASH, 2004. Crest Level Assessment of coastal Structures by full scale monitoring, neural network prediction and Hazard analysis on permissible wave overtopping. EC-contract EVK3-CT2001-00058. ⟨www.clash-eu.org⟩

12. De Rouck J., Geeraerts J., Troch P., Kortenhaus A., Pullen T., Franco L., 2005. New results on scale effects for wave overtopping at coastal structures, Proc. International Conference on Coastlines, Structures and Breakwaters 2005 in London, UK, on 19-21 April 2005, Thomas Telford Publishing, London

13. De Waal J.P., Tönjes P. and van der Meer J., 1996, Wave overtopping of vertical structures including wind effect, Proceedings of the 25th Int. conf. on Coastal Engineering, ASCE, 2216-2229.

14. Dentale, F., Donnarumma, G., Pugliese Carratelli, E., 2014a. Simulation of flow within armour blocks in a breakwater. J. Coast. Res. 2014, 30, 528–536.

15. Dentale, F., Donnarumma, G., Pugliese Carratelli, E., 2014b. Numerical wave interaction with Tetrapods breakwater. J. Naval Arch. Ocean Eng. 2014, 6, 800–812.

16. Di Leo A., Reale F., Dentale F., Viccione G., Pugliese Carratelli E. 2017. Wave-structure interactions a 2D innovative numerical methodology. AIMETA 2017 - Proceedings of the 23rd Conference of the Italian Association of Theoretical and Applied Mechanics.

17. Didier, E., Neves, M., 2009. Coastal flow simulation using SPH: Wave overtopping on an impermeable coastal structure. 4th Int. SPHERIC Work.

18. Dieter Vanneste, 2013 Experimental and Numerical Study of Wave-Induced Porous Flow in Rubble-Mound Breakwaters.

19. EurOtop (2007) Wave overtopping of sea defenses and related structures: assessment manual, Die Kuste, Archive for research and technology of the North Sea and Baltic coast.

20. Fenton J. D., 1999 Numerical methods for nonlinear waves. In P.L.F. Liu, editor, Advances in Coastal and Ocean Engineering, Vol. 5, pages 241–324. World Scientific.

21. Flow Science, Inc. (2009). FLOW-3D user's manual, 11.2-12(hydro) edition, Flow Science, Inc., Santa Fe, N.M.

22. Formentin S.M., Zanuttigh B. & Van der Meer J.W. (2017). A neural network for predicting wave reflection, overtopping and transmission, Coastal Engineering Journal, 59, No. 2 (2017).

23. Goda Y., 2009 Derivation of unified wave overtopping formulas for seawalls with smooth, impermeable surfaces based on selected CLASH datasets. Coastal Engineering 56 (2009) 385–399.

24. Harlow Francis H. and Nakayama Paul I.,1967. Turbulence Transport Equations. The Physics of Fluids 10, 2323.

25. Higuera, P., Lara, J.L., Losada, I.J., 2013. Realistic wave generation and active wave absorption for Navier–Stokes models: Application to OpenFOAM®. Coast. Eng. 71, 102–118.

26. Hirt C.W. and Nichols B.D., 1981. Volume of fluid (VOF) method for the dynamics of free boundaries, Journal Comp. Physics, Vol.39, pp. 201-225.

27. Hirt C. W. and Sicilian J. M.,1985. A porosity technique for the definition of obstacles in rectangular cell meshes.

28. Inoue, M., Shimada, H., Tonomo,K. 1989. Quantitative Study on Overtopping of Irregular Waves, Proc. Coastal Engineering, JSCE, vol 36, pp 618-622.

29. Jacobsen, N.G., Fuhrman, D.R., Fredsøe, J., 2012. A wave generation toolbox for the opensource CFD library: OpenFoam. International Journal for Numerical Methods in Fluids, 70(9), pp. 1073-1088.

30. Launder B.E., Spalding D.B., 1974., The numerical computation of turbulent flows. Computer Methods in Applied Mechanics and Engineering, Volume 3, Issue 2, Pages 269-289.

31. Le Mehaute B., 1976. An introduction to hydrodynamics and water waves. Springer Verlag.

32. Li, T., Troch, P., De Rouck, J., 2004. Wave overtopping over a sea dike. J. Comput.Phys. 198, 686-726.

33. Lin P., Liu P.L.F.,1999. Internal wave-maker for Navier-Stokes equation models. Journal of Waterway, Port, Coastal, and Ocean Enginnering, 125, No. 4.

34. Lopez, L.F.C., Salerno, D., Dentale, F., Capobianco, A., Buccino, M., 2015. Experimental campaign on the overtopping of the seawall Malecon Tradicional. In: 25th International Ocean and Polar Engineering Conference, ISOPE 2015 Kona, Big Is-land, United States, 21e26 June 2015, pp. 1499e1505. Volume 2015-January

35. Martínez Pés, V., 2013. Validation of Swash for wave overtopping.

36. Masami Kiku and Koji Kawasaki, 2014. Proposal of numerical wave flume for wave overtopping computation considering wind external force. Conference Proceedings of of Coastal Engineering. No34

37. McCabe M., Stansby P., and Apsley D., 2013. Random wave runup and overtopping a steep sea wall: Shallow water and boussinesq modelling with generalised breaking and wall impact algorithms validated against laboratory and field measurements. Coastal Engineering, 74:33–49.

38. Miquel, A.M., Kamath, A., Chella, M.A., Archetti, R., Bihs, H., 2018. Analysis of different methods for wave generation and absorption in a CFD-based numerical wave tank. J. Mar. Sci. Eng. 6 (2) art. no. 73.

39. Pearson J., Bruce T., and Allsop N.,2002. Prediction of wave overtopping at steep seawalls–variabilities and uncertainties. In

Proceedings of Fourth International Symposium on Ocean Wave Measurement and Analysis, volume 1, pages 1797–1808

40. Pearson, J., Bruce, T., Allsop, N. W. H. & Gironella, X., 2002. Violent wave overtopping – measurements at large and small scale. Proc. ICCE, ASCE, pp 2227–2238.

41. Perlin M., Wooyoung C, Zhigang T., 2013. Breaking Waves in Deep and Intermediate Waters. Annual Review of Fluid Mechanics, Volume45, n1, pp.115-145.

42. Pullen T., Allsop N., Bruce T., Kortenhaus A., Schüttrumpf H., and Van der Meer J., 2007. Wave overtopping of sea defences and related structures: assessment manual. Environment Agency, UK.

43. Pullen T., Allsop W., Bruce T., Pearson J., 2009. Field and laboratory measurements of mean overtopping discharges and spatial distributions at vertical seawalls. Coastal Engineering.

44. Romano A., Williams H E., Bellotti G., Briganti R., Dodd N., Franco L., 2014. About some uncertainties in the physical and numerical modeling of wave overtopping over coastal structures. Coastal Engineering Proceedings-July 2014.

45. Saad, Y., 1996. Iterative methods for sparse linear systems. Soc. for Industrial and Applied Mathematics 1–520.

46. Scholte S.I.O, 2020. The validation of wave overtopping over complex dikes using CFD. Master Project Applied Mathematics.

47. Schultz M.P. John F. & Callow, Callow M., Callow JA. (2003). Three Models to Relate Detachment of Low Form Fouling at Laboratory and Ship Scale. Biofouling. 19 Suppl. 17-26.

48. Schüttrumpf H., Kortenhaus A., and Oumeraci H.,1998. Application of Overtopping Models to Vertical Walls against Storm Surges. 26th International Conference on Coastal Engineering June 22-26, Copenhagen, Denmark.

49. Ting, F.C.K., Kirby, J. T., (1995). Dynamics of surf-zone turbulence in a strong plunging breaker. Coastal Engineering 24: 177-204.

50. Van der Meer J., Janssen H.,1995. Wave run-up and wave overtopping at dikes.

51. Van der Meer J., Allsop N., Bruce D. R., Kortenhaus A. J., Pullen T., Schüttrumpf H., Troch P., and Zanuttigh B. EurOtop, 2018. Manual on wave overtopping of sea defences and related structures. An overtopping manual largely based on European research, but for worldwide application. page 320, 2018. URL www.overtopping-manual.com.

52. Viccione, G., Bovolin, V., Pugliese Carratelli, E., 2012. Simulating fluid-structure interaction with SPH. AIP Conf. Proc. 1479 (1), 209-212.

53. Vicinanza, D., Dentale, F., Salerno, D., Buccino, M., 2015. Structural response of seawave slot-cone generator (SSG) from random wave CFD simulations. In: Proceedings of the International Offshore and Polar Engineering Conference (ISOPE 2015). 2015-January, pp. 985–991.

54. Ward D.L., Zhang J., Wibner C.G., Cinotto C.M., 1996, Wind effects on runup and overtopping, Proc. of the 25th International Conference on Coastal Engineering (ICCE 1996) in Orlando, Florida, ASCE, New York, 2206-2215

55. Wilcox, D. C., Turbulence Modeling for CFD, 2nd edition, DCW Industries, Inc., La Canada CA, 1998.

56. Wilcox, D. C., "Formulation of the k-omega Turbulence Model Revisited," AIAA Journal, Vol. 46, No. 11, 2008, pp. 2823-2838.

57. Yakhot V., and Orszag S. A., 1986 Renormalization group analysis of turbulence. J. Sci. Comput. 1, 3.

58. Yakhot V. and Smith L. M., 1992. The renormalization group, the ε-expansion and derivation of turbulence models. J. Sci. Comput. 7, 35.

59. Yazid Maliki A., Azlan Musa M., Ahmad M. F., Zamri I., Omar Y., 2017. Comparison of Numerical and Experimental Results for Overtopping Discharge of the Obrec Wave Energy Converter. Journal of Engineering Science and Technology Vol. 12, No. 5 (2017) 1337 – 1353.

60. Zanuttigh B., Formentin S.M., & Van der Meer J.W. (2016). Prediction of extreme and tolerable wave overtopping discharges through an advanced neural network, Ocean Engineering, 127, 7-22.